Analysis and design of compact antennas in cavity based on metasurfaces for multiband GNSS applications

Laura Garcia Gamez

To cite this version:

Laura Garcia Gamez. Analysis and design of compact antennas in cavity based on metasurfaces for multiband GNSS applications. Electronics. Université Rennes 1, 2020. English. NNT : 2020REN1S014 . tel-03045846

HAL Id: tel-03045846
https://theses.hal.science/tel-03045846

Submitted on 8 Dec 2020

THESE DE DOCTORAT DE

L'UNIVERSITE DE RENNES 1

ECOLE DOCTORALE N° 601
Mathématiques et Sciences et Technologies
de l'Information et de la Communication
Spécialité : *Electronique*

Par

Laura GARCIA GAMEZ

Analysis and Design of Compact Antennas in Cavity based on Metasurfaces for Multiband GNSS Applications

Thèse présentée et soutenue à Saint-Louis, le 27 Mai 2020
Unité de recherche : UMR CNRS 6164
Thèse N° :

Rapporteurs avant soutenance :

Thierry MONEDIERE	Professeur des universités | Université de Limoges
Jean-Marc RIBERO	Professeur des universités | Université Nice Côte d'Azur

Composition du Jury :

Président :	Sylvain LECLER	Professeur des universités | INSA Strasbourg
Examinateurs, -trices :	Anne-Claire LEPAGE	Maître de conférences | Télécom ParisTech
	Sylvain COLLARDEY	Maître de conférences, co-encadrant | Université de Rennes 1
	Loïc BERNARD	HDR, co-encadrant | ISL
Dir. de thèse :	Ronan SAULEAU	Professeur des universités | Université de Rennes 1

Invités :

Nicolas CAPET	CEO Anywaves
Philippe POULIGUEN	DGA, responsable du domaine ondes acoustiques et radioélectriques
Patrick POTIER	DGA-MI

ANALYSIS AND DESIGN OF COMPACT ANTENNAS IN CAVITY BASED ON METASURFACES FOR MULTIBAND GNSS APPLICATIONS

Laura GARCIA GAMEZ

27th May 2020

Acknowledgments

Même si ces deniers trois mois de stress, incertitude, solitude et travail ont ressorti de l'ensemble de ma thèse (aussi pour le monde entier), je voudrais surtout baser mes remerciements sur les autres 41 mois de chemin. Une thèse est une cours long distance où chaque personne croisée a apporté sa pierre à l'édifice. Je vous remercie.

Tout d'abord, je voudrais remercier les membres du jury d'avoir accepté ce rôle dans une soutenance un peu particulaire et pour les questions et remarques très intéressants afin d'améliorer mon travail: Sylvain LECLER comme président du jury, Thierry MONEDIERE et Jean-Marc RIBERO en tant que rapporteurs et Anne-Claire LEPAGE comme examinatrice. Merci aussi aux membres invités Nicolas CAPET, Philippe POULIGUEN et Patrick POTIER. A ces deux derniers je présente un spécial merci pour le financement et le soutien pendant la thèse.

Une thèse ne peut pas toucher à sa fin sans l'aide des encadrants. Merci à Ronan SAULEAU pour accepter la direction de cette thèse et pour m'inculquer son savoir et sa rigueur. Je voudrais remercier aussi à Kourosh MAHDJOUBI, qui profite maintenant de sa retraite bien mérité. Il est toujours plein de bonnes idées et c'était un plaisir pour moi apprendre de son expérience et amour pour la science. Un spécial merci à Sylvain COLLARDEY pour son excellence, son aide constante et pour me soutenir avec calme dans les moments plus stressants. Finalement, merci à Loïc BERNARD pour croire en moi (plus que moi-même) depuis le début. Il a été mon pilier et mon confident pendant ces années, je n'ai pas des mots suffisants pour lui remercier. L'effet de partager le bureau avec lui a fait qu'il soit disponible pour moi de manier constant et, même si je lui demande mil questions par jour, il est toujours disponible pour me répondre avec la bonne humeur (même si mon calme le stressait). Un grand merci à tous pour votre professionnalité.

Je ne pourrais jamais oublier de remercier les collègues de l'ISL. La team STC-GNC m'a donné la dose journalière de bon humeur (et de café), très nécessaire pour la réussite de ma thèse. Votre aide scientifique comme humaine a été la clé de mon travail à l'ISL depuis que j'ai commencé en tant que stagiaire. Un sincère et grand merci à tous ! Vous êtes beaucoup mais je voudrais mentionner der Leiter ARMIN, ETIENNE, MANU P., HRVOJE, CLEMENT, JONATHAN, MANU M., qui m'ont démontré sa tendresse jour à jour et de qui je vais garder un spécial souvenir.

J'ai eu la chance de partager le temps entre Bretagne et Alsace, ce qui m'a donné l'opportunité de connaître deux belles régions, mais aussi d'avoir une famille à chaque côté de la France, personnes que j'espère garder pour toujours. Mi super coloc, JESSICA, que ha sido como una hermana y con la que he compartido momentos increíbles (incluyendo caídas, fiestas improvisadas e inundaciones en el piso). Les nombreux soirées, marchés, sorties avec CLAUDIA, FABRICE, DAVID, CARLOS, CLAU, CLARA en las que no sabíamos cómo iba a acabar la noche después de un buen viernes de B&V. Y no me puedo olvidar de mis "chicas de la merienda", FATIMA Y ROSA, que han sabido darme todo su cariño desde el minuto uno. El tiempo en el IETR me ha permitido cruzarme con personas formidables (ALVARO, MARIA, IOANNIS...). Infine, la mia squadra italiana merita una menzione speciale, MICHELE e NICOLA (mi buenorro), da quando sono arrivati hanno rivoluzionato la mia vita, e lo adoro. Siamo riusciti ad avere una connessione speciale dall'inizio (anche se a volte rara) che ci ha fatto vivere momenti molto speciali, e continueremo *il volo*, sono sicura.

Estos últimos casi dos años en Mulhouse han sido menos duros gracias a mi TUCA family, gracias por aparecer CAMI, PEDRO, COPITO, EMI, MANU, y sobre todo DENIS, que se convirtió en la mugre de mi uña de la noche a la mañana (me hubiera puesto más sentimental, pero a los alemanes no le van esas cosas). ¡El campeonato mundial de Uno nos espera! Un merci énorme aussi à BASTIEN pour son soutien infatigable pendant cette année.

No me podía olvidar de unas personas que han estado, están y estarán siempre ahí; lejos o cerca, los llame o no, pero siempre fundamentales: mis NIÑAS POCEÑAS, DANI, RAQUEL, ALICIA, gracias por quererme y demostrármelo cada día. Tengo a los mejores.

Y quiero acabar con mi familia. PAPÁ, MAMÁ, ALVARO, gracias por estar a mi lado siempre. Aunque haya estado lejos estos años y me haya perdido muchos momentos con vosotros, sois mi motor, sin vosotros no hubiera llegado hasta aquí ni estaría escribiendo estas palabras. Os quiero mucho y no hay suficiente tinta para agradecer todo lo que habéis hecho por mí. Este trabajo también es vuestro. Y por supuesto mis titos y titas, primos y primas, abuelitos, y a todos ¡gracias!

Merci Danke Gracias Hvala Grazie Thank you

"Dans la vie, rien n'est à craindre, tout est à comprendre"

Marie Curie

Contents

List of Figures

List of Tables

Nomenclature

2D	two-dimensional
3D	three-dimensional
AltBOC	Alternate Binary Offset Carrier
AR	Axial Ratio
ARC	Active Radiation Coefficient
ARNS	Aeronautical Radio Navigation Service
BOC	Binary Offset Carrier
BPSK	Binary Phase Shift Keying
BW	Bandwidth
CDMA	Code Division Multiple Access
CP	Circular Polarization
CS	Commercial Service
DAB	Digital Audio Broadcasting
DNG	Double-NeGative
DPS	Double PoSitive
EBG	Electromagnetic Band-Gap
EM	ElectroMagnetic
ENG	Epsilon-NeGative
FDMA	Frequency Division Multiple Access
FSS	Frequency Selective Surface
Glonass	GLObal NAvigation Satelite System
GNSS	Global Navigation Satellite Systems
GPS	Global Position System
IGSO	Inclined Geosynchronous Orbits

ISS	International Space Station
ITU	International Telecommunications Union
LHCP	Left-Hand Circular Polarization
LHM	Left-Handed Metamaterial
LP	Linear Polarization
MBOC	Multiplexed Binary Offser Carrier
MEO	Medium Earth Orbit
MNG	Mu-NeGative
MTS	Metamaterials
NavIC	Navigation with Indian Constellation
OS	Open Service
PEC	Perfect Electric Conductor
PMC	Perfect Magnetic Conductor
PRN	Pseudo-Random-Noise
PRS	Public Regulated Service
QHA	Quadrifilar Helix Antenna
QPSK	Quadrature Phase Shift Keying
QZSS	Quasi-Zenith Satellite System
RCA	Resonant Cavity Antennas
RHCP	Right-Hand Circularly Polarized
RIS	Reactive Impedance Surface
RNSS	Radio Navigation Satellite Service
SAR	Search and Rescue Service
SATNAV	SATellite NAVigation system
SoL	Safety-of-Life
TARC	Total Active Radiation Coefficient
UTC	Universal Time Coordinated
XPD	Cross-Polarization Discrimination

Résumé des travaux. Analyse et conception d'antennes compactes en cavités basées sur des métasurfaces pour des applications GNSS multi-bandes

Introduction et objectifs

La nécessité de communication avec et entre des systèmes en vol est en augmentation constante, accompagnée de demandes de débits plus élevés, besoin de localisation, de distances de communications plus importantes, d'une fiabilité et d'une discrétion accrue en environnements perturbés ou hostiles. Ces objectifs impliquent le développement d'antennes compactes large bande ou multi-bandes. Ces antennes peuvent être utilisées dans différentes plateformes telles que des projectiles de petits, moyens et gros calibres ou des micro-drones, dont les applications peuvent concerner le domaine de la défense (transmission de données de capteurs embarqués, transmissions d'ordre de guidage, mise à jour de données de poursuite de cibles, etc.). Le cas de cette étude, qui aborde notamment la problématique de l'intégration de petites antennes sur le corps des projectiles, est centré sur l'utilisation d'un projectile en particulier. Ceux-ci sont construits avec des matériaux métalliques ce qui fait que les antennes doivent être généralement intégrées dans des cavités métalliques. Profitant de cela, des avantages importants peuvent être obtenus grâce à l'intégration des antennes imprimées en cavités, telles que la rigidité, la compacité, l'isolation de l'environnement ou la réduction des ondes de surface [26]. La conséquence principale de cette intégration en cavité métallique est la réduction de la bande passante des antennes [15].

De plus, une antenne présente une bande passante plus étroite lorsque sa taille devient plus petite. La limitation des dimensions des antennes intégrées dans les cavités métalliques, elles-mêmes contraintes par la géométrie de la plateforme, devient alors un facteur limitant pour obtenir des bandes passantes suffisamment larges pour couvrir les applications visées, c'est à dire la réception de signaux GNSS (Global Navigation Satellite Systems). Les bandes de fréquences considérées s'étendent de 1164 MHz à 1610 MHz.

La limitation la plus importante à respecter concernant les dimensions de l'ouverture de la cavité est sa largeur, qui ne peut pas dépasser 50 mm (0,26λ_0 à 1578 MHz), car il est envisagé à terme de construire un réseau d'antennes en forme d'anneau autour du cylindre métallique comme montré à la Figure 1. Par contre, la limitation de longueur est légèrement plus grande, jusqu'à 60 mm (0,31λ_0). La cavité peut être carrée ou rectangulaire si nécessaire, mais l'effort de miniaturisation de l'antenne doit être poussée au maximum tout en respectant les contraintes de bande passante des systèmes GNSS.

Le sujet est divisé en trois étapes. Dans un premier temps, afin de couvrir les fréquences utilisées par Galileo E1, GLONASS G1 et GPS L1 avec une seule antenne, un dispositif avec une bande passante d'au moins 60 MHz est nécessaire à la fréquence centrale de 1578 MHz. Comme on vise une plate-forme volant en altitude, la propagation radio ne souffre pas de trajets multiples, et la polarisation linéaire est choisie pour simplifier les premières études. Dans un second temps, pour mieux adapter le dispositif aux

Figure 1: Modèle de plateforme pour intégrer les antennes: section de projectile 155 mm

exigences de la technologie GNSS, une étude en polarisation circulaire est menée.

Dans un troisième temps, une antenne en cavité est étudiée avec l'objectif de couvrir l'ensemble de bandes GNSS, c'est-à-dire, de 1164 MHz jusqu'à 1610 MHz. Dans ce cas, l'étude est centrée sur une antenne à double résonance. Cette structure excite une première résonance basse pour les fréquences basses du spectre GNSS et une deuxième résonance plus haute en fréquence pour la partie haute du spectre GNSS. Les bandes GNSS sont présentées à la Figure 2.

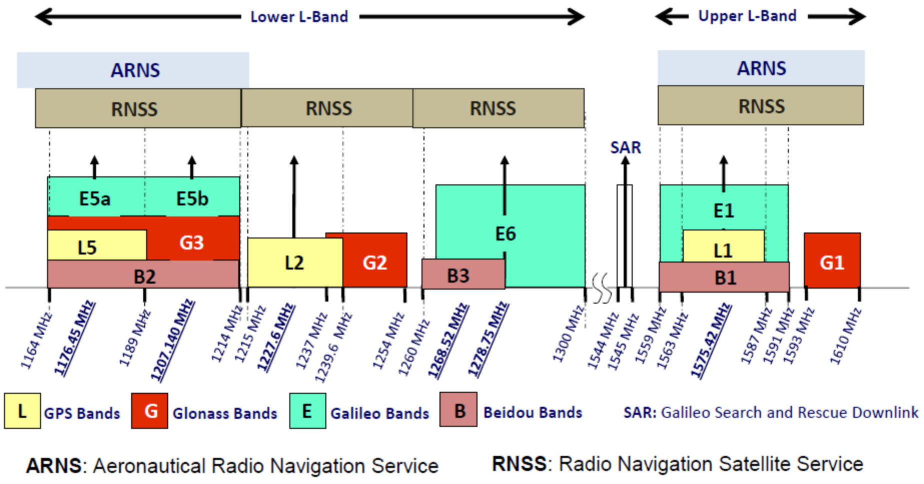

Figure 2: Répartition des bandes GNSS dans le spectre de fréquence de la bande L [1]

Il a été démontré au début de ces travaux qu'il n'était pas possible d'obtenir les exigences mentionnées ci-dessus avec une antenne patch standard en raison des dimensions réduites de la cavité. Une autre option pour obtenir la bande passante souhaitée consiste à utiliser des patchs superposés. Cette configuration peut offrir une augmentation substantielle de la bande passante par rapport à un patch simple [27]. Au cours de ce travail de thèse, une configuration à base de patchs empilés est considérée, mais il est démontré qu'il n'est pas possible non plus d'atteindre les spécifications souhaitées en matière de bande passante pour une taille d'ouverture de cavité inférieure à $0{,}26\lambda_0$, soit l'objectif de cet étude. L'utilisation d'une métasurface dans l'ouverture de la cavité est également une solution intéressante : il est alors possible d'augmenter la bande passante sans augmenter les dimensions de la cavité, en d'autres termes, l'utilisation de métasurfaces permet de miniaturiser la taille de l'ouverture de la cavité. Par conséquent, l'objectif est de développer une structure compacte basée sur une métasurface avec la bande passante la plus large possible. Dans des études précédentes, une antenne à polarisation linéaire en cavité carrée basée sur des métasurfaces a été présentée en [3]. La métasurface est constituée de petits patchs de même taille imprimés sur la même surface. Ce concept conduit à une diminution de l'inductance de la surface à l'ouverture de la cavité et le système devient purement capacitif. Dans l'étude mentionnée ci-dessus, l'empilement de ces métasurfaces a également été étudié. Ce processus contribue à augmenter fortement l'effet capacitif. Ce concept fut introduit par Martinis dans [21].

Objectifs généraux de la présente étude

Selon la problématique présentée précédemment, les objectifs généraux de cette thèse sont résumés ci-dessous:

- Intégration de l'antenne dans une cavité métallique
- Antenne compacte la plus petite possible
- Polarisation linéaire et circulaire
- Développer une antenne capable de couvrir l'ensemble de bandes GNSS avec comportement large bande ou multi-bande

Objectifs pratiques et spécifiques

Pour que les objectifs généraux soient atteints, différents critères pratiques sont pris en compte. Les exigences dépendent du nombre de bandes de fréquence nécessaires pour couvrir l'ensemble des besoins GNSS.
Les objectifs et spécifications pour l'antenne à une seule résonance sont les suivants:

- Antennes à polarisation linéaire, dans un premier temps, puis, à polarisation circulaire
- Couverture des bandes L1, E1 et G1, centrés à 1578 MHz
- Bande passante minimal de 60 MHz
- La profondeur maximale de la cavité est fixée à 20 mm ($0.11\ \lambda_0$)
- Dimensions de l'ouverture sohuaitées: 50×50 mm^2 ($0{,}26\ \lambda_0\times0{,}26\ \lambda_0$), 40×45 mm^2 ($0{,}21\ \lambda_0\times0{,}24\ \lambda_0$) et 40×40 mm^2 ($0{,}21\ \lambda_0\times0{,}21\ \lambda_0$).
- Utilisation de métasurfaces
- Réalisation de prototypes et caractérisations expérimentales

Les objectifs et spécifications pour l'antenne à double résonance sont énumérés ci-dessous:

- Polarisation circulaire
- Résonance inférieure capable de couvrir de 1164 MHz jusqu'à 1300 MHz

- Résonance supérieure qui couvre de 1559 MHz à 1610 MHz
- Dimensions de la cavité retenues 60×60×20 mm^3 (0.26 λ_0×0.26 λ_0×0.09 λ_0 à 1400 MHz). Dimensions de la cavité souhaitées 50×50×20 mm^3 (0.23 λ_0×0.23 λ_0×0.09 λ_0 à 1400 MHz).
- Utilisation de métasurfaces
- Réalisation de prototypes et caractérisations expérimentales

État de l'art

Systèmes de géolocalisation GNSS

Un système de navigation satellitaire (SATNAV) est une constellation de satellites qui tournent autour de la Terre. Aujourd'hui, ces systèmes sont largement utilisés pour déterminer la position (trois dimensions) d'objet quelconque sur la surface terrestre. Une quatrième information est déduite des signaux: il s'agit du temps. Mis à part la constellation de satellites, un système GNSS est composé de deux autres parties, le segment de contrôle à la surface de la Terre et le segment des utilisateurs. Ce dernier inclue tous les appareils qui nous informent sur la position en temps réel.

Il y a quatre systèmes GNSS, deux qui sont complètement développés et deux qui sont en voie de développement/déploiement. GPS (Global Position System) est le système américain de géolocalisation qui opère de façon complète depuis la fin des années 80. Les signaux émis sur les bandes L1, L2 et L5 dépendent de GPS. Galileo est la constellation propriété de l'Union Européen, dont les signaux sont émis dans les bandes E1, E5 et E6. Également, la Russie dispose du système Glonass qui gère les bandes de fréquences G1, G2 et G3. Enfin, la République de Chine possède son propre système, Beidou (bandes B1, B2 et B3), qui est ouvert à son utilisation dans le monde entier depuis décembre 2018. Les différentes fréquences pour chaque bande sont exposées Figure 2.

Divers types de structures d'antennes peuvent être utilisés pour applications GNSS : antennes hélicoïdales, antennes imprimées, antennes bow-tie, ou même des réseaux. Idéalement, pour éviter les réflexions multi-trajet lors de l'utilisation au sol, les antennes sont conçues en polarisation circulaire.

Antennes en cavité

Les antennes en cavité sont basées sur un résonateur tridimensionnelle contenant une ouverture à travers laquelle l'antenne rayonne. Une cavité peut être modélisée comme une ligne de transmission. Considérons une cavité rectangulaire dans un plan de masse infini remplie d'un matériaux homogène (permittivité ε_r et perméabilité $\mu_r = 1$), comme montré sur la Figure 3. Cette cavité peut être modélisée par une ligne de transmission en court-circuit plus une charge correspondant à l'ouverture. Ce modèle est considéré comme un guide d'ondes rectangulaire, et le mode TE10 est le mode dominant.

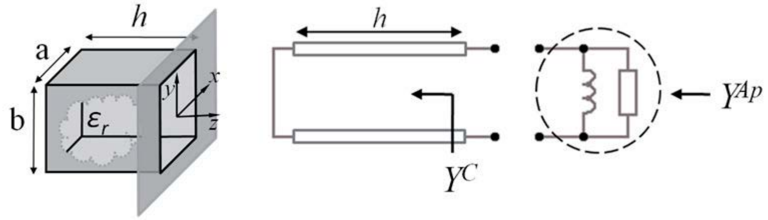

Figure 3: Cavité de dimensions $a \times b \times h$ dans un plan masse infini et son modèle de ligne de transmission

L'analyse du système précédent ([3]) détermine qu'il oscille lorsque les réactances dans le circuit s'annulent conformément à l'équation 1.

$$jB^{AP}(k) - j\frac{k_{TE}}{k\eta_0}\cot\left(k_{TE}h\right) = 0 \tag{1}$$

où $B^{AP}(k)$ est la susceptance de l'ouverture, $k_{TE}^2 = \varepsilon_r k^2 - k_c^2$ soit $k^2 = \omega^2\mu_0\epsilon_0$, $k_c = \pi/a$, a est la taille de l'ouverture carrée et h la profondeur de la cavité.

L'insertion d'une antenne dans une cavité métallique offre divers avantages comme l'isolation, la réduction d'ondes de surface, la miniaturisation, la rigidité et la compacité ou la réduction du rayonnement latéral. Néanmoins, cette isolation provoque la forte réduction de la bande passante de l'antenne et de l'efficacité. Cohen [28] et Counter [29] étaient les pionniers dans la recherche de ces effets des cavités sur les antennes.

Une solution pour l'amélioration de la bande passante est la catégorie des antennes imprimées à base de métasurface

Antennes en cavité à base de métasurfaces

Un métamatériau est un matériau artificiel constitué d'inclusions périodiquement placées, microscopiquement homogènes et qui présente des propriétés électromagnétiques particulières qui n'existent pas dans la nature. Une métasurface est définie comme un métamatériau en deux dimensions ou en version planaire.

L'utilisation de métasurfaces offre des avantages telles que coûts de fabrication réduits, légèreté, capacité de bloquer, absorber, concentrer, disperser et guider des ondes, etc [30]. Une antenne métasurface est en général composée d'une structure périodique de patchs métalliques. Grâce à ses propriétés, les métasurfaces peuvent être utilisées pour la miniaturisation et l'amélioration de la bande passante si elles sont placées dans l'ouverture d'une cavité.

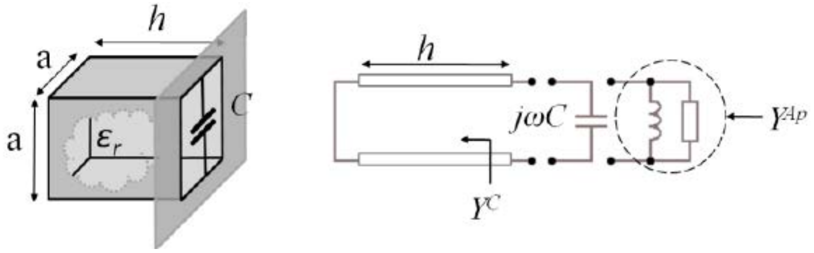

Figure 4: Cavité de dimensions $a \times a \times h$ avec une capacité parasite à l'ouverture et son modèle de ligne de transmission [2]

Quand une métasurface est mise au niveau de l'ouverture de la cavité, une capacité C est ajoutée au modèle d'une cavité simple, comme montré Figure 4. A partir de ce modèle, permettant C d'attendre la bande passante maximale doit être recherchée. La condition de résonance est à présent donnée par l'équation 2.

$$jB_{AP}(k) - j\frac{k_{TE}}{k\eta_0}\cot\left(k_{TE}h\right) + jc_0kC = 0 \tag{2}$$

où k est le nombre d'onde tel que $k_{TE}^2 = \varepsilon_r k^2 - k_c^2$ et c_0 la vitesse de la lumière dans le vide. Si la permittivité ε_r est fixée à une valeur connue, la capacité C est considérée comme une fonction de la hauteur h de la cavité.

Dans un sens pratique, C est obtenu à partir d'un patch coupé en différents parties de plus en plus petites, jusqu'à atteindre la valeur optimale de la capacité C. La Figure 5 montre l'évolution d'un patch classique vers une métasurface.

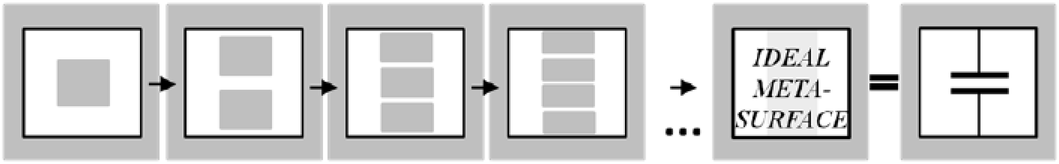

Figure 5: Processus de création d'une métasurface dans l'ouverture d'une cavité à partir d'un patch simple [3]

Antennes en cavité pour applications GNSS en polarisation linéaire

Le placement d'un patch simple à l'ouverture d'une cavité n'est pas suffisant pour atteindre la bande passante demandée pour les bandes GNSS. Dans ce première cas, les bandes L1, G1 et E1 doivent être couvertes avec les spécifications exposées ci-dessus. Est-il possible d'obtenir une bande passante de 60 MHz avec des antennes patchs empilés ou une métasurface?

Structure composée de patchs empilés

Pour démontrer s'il est possible ou non de satisfaire les exigences énoncées ci-dessus, une antenne à base patchs superposés a été étudiée.

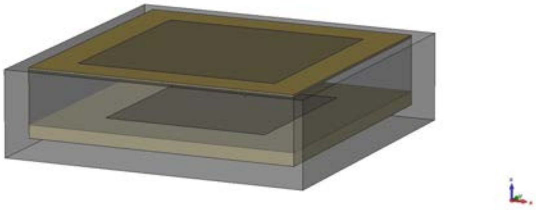

Figure 6: Vue 3D de la structure à base de patchs empilés en cavité métallique

La Figure 6 montre la vue 3D d'une antenne en cavité carrée basée sur deux pièces empilées avec une taille de cavité $a \times a \times h$, soit a la taille de l'ouverture et h la hauteur. La structure de l'antenne est composée comme suit. La profondeur de la cavité a une valeur fixe, et les patchs sont imprimés sur un substrat $\varepsilon_r = 10{,}2$. Il convient de noter que le patch supérieur est légèrement plus large que celui situé dessous. Le volume entre les deux patchs est rempli d'air. L'antenne est alimentée par une sonde coaxiale fixée au patch inférieur.

Une étude a été menée consistant à varier la largeur a, en optimisant chaque design à la fréquence centrale de 1578 MHz et d'estimer la largeur de bande pour chaque dimension d'ouverture. Les résultats de cette étude sont résumés sur la Figure 7 qui montre la largeur de la bande passante maximale réalisable en fonction de la taille d'ouverture de la cavité. Ces résultats montrent que jusqu'à une cavité de taille $0.43\ \lambda_0 \times\ 0.43\ \lambda_0$ (soit $81 \times 81\ \text{mm}^2$), il n'est pas possible d'obtenir 60 MHz de bande passante. On aurait besoin d'une cavité deux fois plus large pour répondre aux exigences de l'étude.

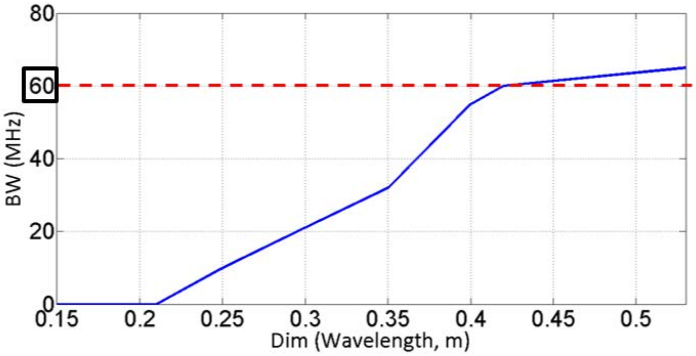

Figure 7: Bande passante en fonction de la taille de l'ouverture d'une antenne carrée en cavité à base de patchs empilés

Structure à base de métasurfaces

Comme mentionné plus haut, avec l'utilisation d'une métasurface il est possible d'augmenter la bande passante sans augmenter les dimensions de la cavité. La métasurface choisie est montrée sur la Figure 8. Il s'agit de deux couches superposées et composées de trois rectangles identiques imprimés sur un substrat diélectrique Rogers ε_r = 10,2 [31].

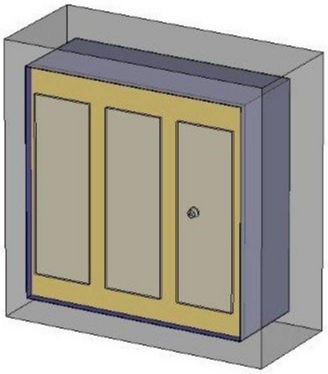

Figure 8: Vue en 3D de l'antenne en cavité rectangulaire à base de métasurfaces

Plusieurs conceptions ont été menées en utilisant cette technique en polarisation linéaire. Premièrement les résultats numériques ont montré qu'une cavité carrée de 40 × 40 mm^2 (0,21λ_0 × 0,21λ_0) n'atteignait pas la bande passante spécifiée de 60 MHz ; en revanche, une cavité rectangulaire de 40 × 45 mm^2 (0,21 × 0,24 λ_0) [32] peut être suffisante pour obtenir une bande passante d'un peu plus de 60 MHz (68 MHz), ce qui est montrée à la Figure 9.

Avec l'objectif d'observer le comportement d'une antenne carrée, un modèle de 50 × 50 mm^2 (0,26λ_0 × 0,26λ_0) a été étudiée. Des bons résultats sont obtenus en simulation avec une bande passante de 87 MHz. Ensuite, des prototypes des deux versions, rectangulaire et carré ont été fabriqués et mesurés. Les prototypes valident les résultats obtenus en simulation pour une antenne à polarisation linéaire. La Figure 10(a) montre une photographie du prototype de l'antenne à ouverture carrée et la Figure 10(b) les résultats obtenues en mesure et en simulation.

Par rapport à la configuration de patchs empilés montrée dans la section précédente, la réduction

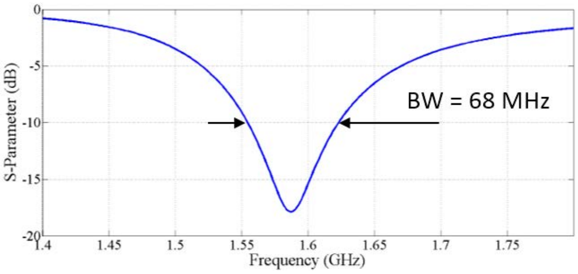

Figure 9: Coefficient de réflexion simulé de l'antenne à base de métasurface en cavité rectangulaire de taille 0.21 × 0.24 × 0.11 λ_0 (40 × 45 × 20 mm^3)

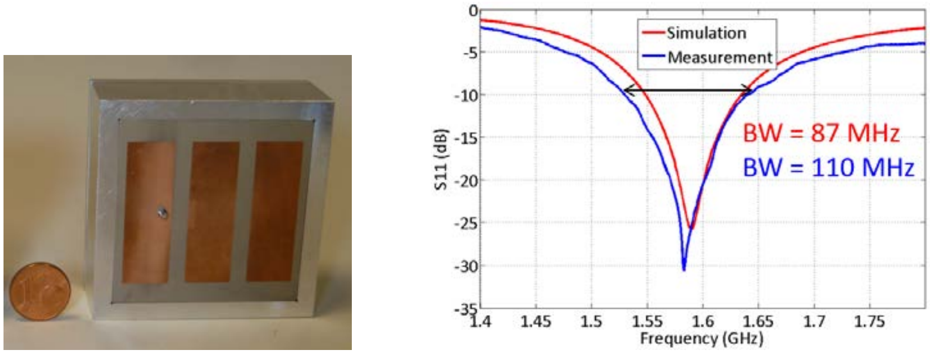

(a)

(b)

Figure 10: (a) Prototype et (b) coefficient de réflexion simulé et mesuré de l'antenne à base de métasurface en cavité carrée de taille 0,26 × 0,26 × 0,11 λ_0 (50 × 50 × 20 mm^3)

d'ouverture est d'environ 50% pour obtenir une bande passante de 68 MHz (bande passante de l'antenne la plus petite). Ce résultat illustre l'intérêt de développer une antenne dont la géométrie est inspirée par les métasurfaces pour l'intégration dans une cavité métallique.

Antennes en cavité pour GNSS en polarisation circulaire

L'émission des signaux GNSS est faite en polarisation circulaire. C'est pourquoi la structure précédente a été modifiée pour la polarisation circulaire mais en conservant les conditions requises mentionnées au début de ce document. Deux designs sont optimisés, un de dimensions 50 × 50 mm^2 (0,26λ_0 × 0,26λ_0) [33] et un autre de dimensions 40 × 40 mm^2 (0,21λ_0 × 0,21λ_0) à 1578 MHz [34]. La différence par rapport à l'antenne à polarisation linéaire est la forme de la métallisation. Dans ce cas, on a une métallisation en deux couches composées de neuf carrés imprimés sur un substrat diélectrique Rogers ε_{r2} = 1,2, comme montré sur l'image de la Figure 11(a). Elles sont alimentées par quatre points d'alimentation, ce qui assure un bon rapport axial. L'intérieur de la cavité métallique est représenté dans le schéma de la Figure 11(b). Le fond de la cavité est rempli de polypropylène pour assurer la tenue mécanique et conférer une rigidité suffisante à la structure, notamment à cause des fortes accélérations que les projectiles doivent supporter lors du tir.

Des bons résultats sont obtenus en simulation pour les deux cas. La bande passante est très supérieure aux 60 MHz souhaités. Elle est autour de 180 MHz pour la plus petite antenne (Figure 12(a)) et de 240

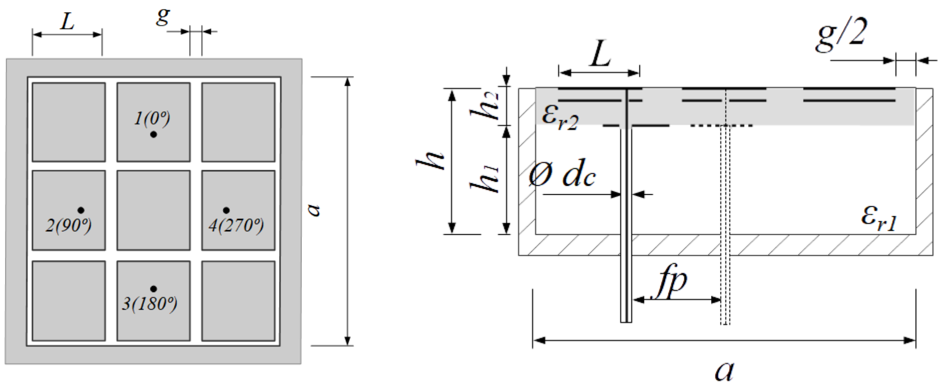

(a) (b)

Figure 11: (a) Vue de dessus et (b) coupe transversale de l'antenne en cavité à polarisation circulaire

MHz pour l'ouverture plus grande (Figure 12(b)). Le rapport axial en simulation est presque idéal pour toute la bande, et les antennes présentent un bon rayonnement. Par contre, à cause de la petite taille des ouvertures (40 × 40 mm^2 et 50 × 50 mm^2), le gain est peu élevé. De plus, un couplage important entre les ports est noté, qui peut être aussi attribué à la petit taille des structures.

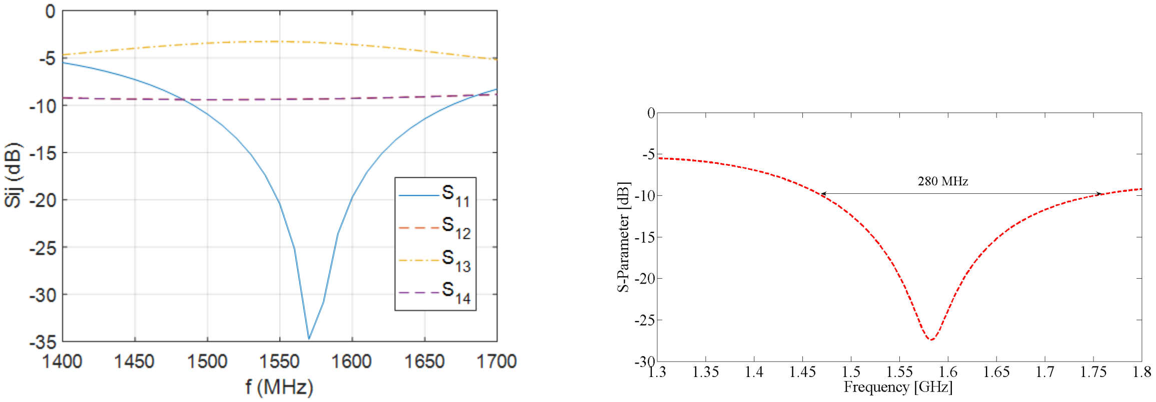

(a) (b)

Figure 12: Coefficient de réflexion simulé des antennes à base de métasurface en cavité et à polarisation circulaire de taille (a) 0.21 × 0.21 × 0.11 λ_0 (40 × 40 × 20 mm^3) et (b) 0.26 × 0.26 × 0.11 λ_0 (50 × 50 × 20 mm^3)

Suite aux bons résultats obtenus en simulation, les deux structures ont été fabriquées. Les photographies des prototypes sont montrées sur la Figure 13. Le principal problème de cette antenne est le faible gain qu'elle présente due à la petite taille de l'antenne. De plus, le couplage existant entre les ports est très élevé (d'autant plus que l'antenne est petite), surtout pour les ports qui se trouvent face à face (voir Figure 12). La réduction de ce couplage est l'objectif de travaux futurs.

Associée à un circuit de répartition actif (incluant un amplificateur faible bruit), l'antenne de dimensions 50 × 50 mm^2 a été caractérisée en champs lointains. Les diagrammes de rayonnement sont

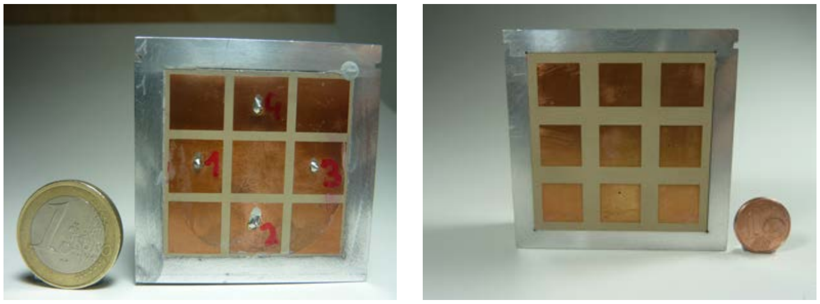

(a) (b)

Figure 13: Prototypes manufacturés pour l'antenne de (a) petite ouverture de 40×40 mm^2 et (b) large ouverture de 50×50 mm^2

satisfaisant (Figure 14), le rapport axial est inférieur à 3 dB sur toute la bande visée de 1550 à 1610 MHz et le gain supérieur à 15 dBic sur cette bande (Figure 15 [33]).

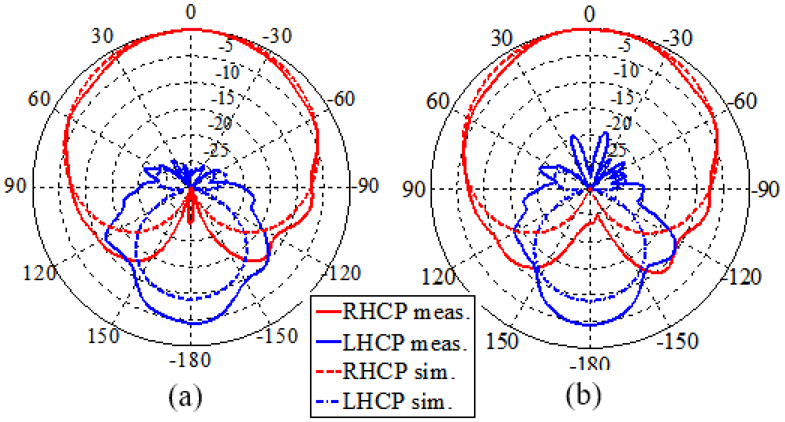

Figure 14: Antenne à polarisation circulaire: mesuré (ligne continue) et simulé (ligne pointillée) diagrammes de rayonnement à 1578 MHz dans deux plans coupe verticaux: (a) φ=0°, (b) φ=90°. RHCP en rouge, et LHCP en bleu

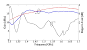

Figure 15: Performances de l'antenne avec le système d'alimentation (Figure 3.23b). Gauche: gain mesuré et simulé. Droite: rapport axial mesuré

Antennes multibandes pour GNSS

Avec l'objectif de couvrir l'ensemble de bandes GNSS ([1164-1610] MHz), notamment de rajouter les bandes E5 et E6 de Galileo, L2 et L5 de GPS et puis G2 et G3 de Glonass, une antenne multibande ou très large bande est nécessaire. Le principal but est de créer une deuxième résonance capable de couvrir la bande L inférieure ([1164-1300] MHz), ou une large bande qui couvre toutes bandes GNSS.

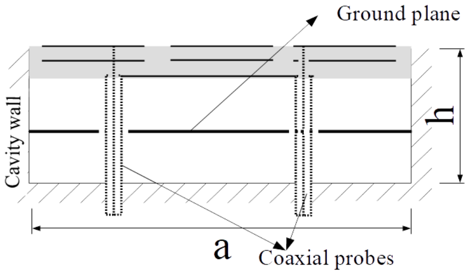

Figure 16: Position du plan masse dans la cavité

Après plusieurs études basées sur des simulations numériques de différentes structures potentielles, un second plan masse est ajouté au milieu de la cavité, ce qui a pour conséquence de générer une deuxième résonance plus bas en fréquence, avec une bande passante suffisante pour couvrir toutes les bandes manquantes. Le plan masse est une plaque métallique placée au milieu de la cavité de manière horizontale, parallèle au plan XY. Cette plaque est connectée directement avec les parois de la cavité, comme illustré à la Figure 16. La division de la cavité en deux sous-cavités de tailles différentes, mais connectées entre elles à travers des trous circulaires, permet l'excitation d'une autre résonance. Les trous réalisés dans la plaque métallique sont montrés à la Figure 17a. Les câbles coaxiaux ne sont pas en contact avec le plan de masse intérieur.

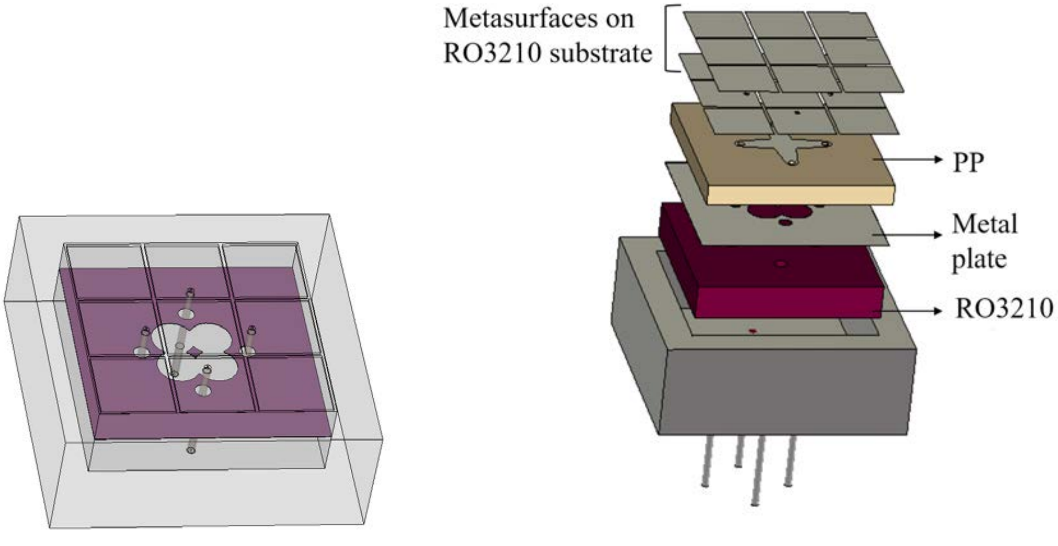

(a) (b)

Figure 17: Modèle de l'antenne multibande GNSS à base de métasurface et insérée dans une cavité métallique. (a) Position et forme des ouvertures dans le plan métallique. (b) Vue éclatée des pièces

La Figure 17b expose le découpage des parties de l'antenne à l'intérieur de la cavité. Sous le plan métallique se trouve un bloc de diélectrique de haute permittivité (ε_r=10,2) qui permet l'excitation de la résonance. La sous-cavité supérieure est composée de deux métasurfaces imprimées sur le même matériau diélectrique, puis le reste est remplie d'un bloc de polypropylène ($\varepsilon_{r_{pp}}$=2,23).

Au final, une bande passante de plus de 500 MHz est atteinte en simulation, comme montré à la Figure 18. La taille de l'ouverture de la cavité a dû être augmentée jusqu'à 60 × 60 mm^2 (0,28λ_0 × 0,28λ_0) à la fréquence centrale de 1400 MHz, alors que la profondeur de la cavité est restée de 20 mm (0,09λ_0 à 1400 MHz).

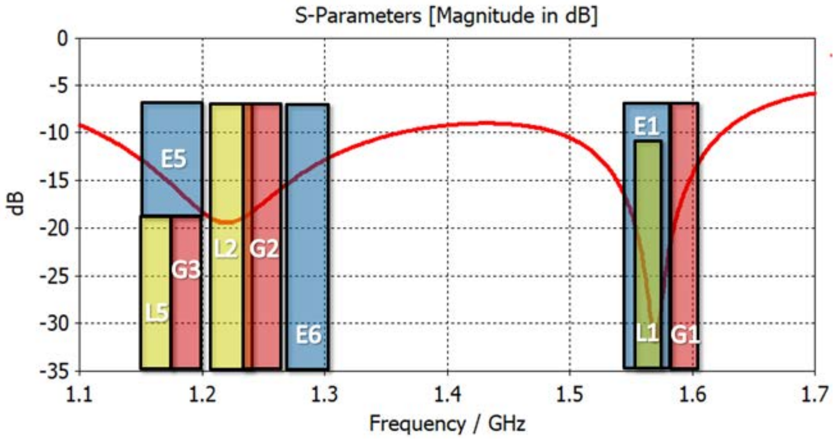

Figure 18: Coefficient de réflexion mesuré pour l'antenne multibande de double résonance

Un prototype a été fabriqué, démontrant les potentialités de cette structure, et en particulier l'apparition des deux résonances. Des études complémentaires doivent être menées pour réduire le couplage entre les ports et améliorer l'efficacité de l'antenne.

Conclusion

Le but de ce travail de recherche était l'étude d'antennes compactes en cavité pour des applications GNSS, dans un premier temps à simple résonance et dans un second temps à double résonance pour couvrir l'ensemble des bandes GNSS. La forme cylindrique du porteur de l'antenne (projectile) fait que les dimensions de la cavité sont limitées. Différents design à polarisation linéaire et circulaire avec une seule résonance ont été conçus et fabriqués, avec un bon accord entre simulation et mesures. Ces antennes sont capables de recevoir les signaux des bandes L1, E1 et G1 de GNSS avec des bonnes performances. Finalement, une structure à double résonance capable de couvrir l'ensemble des bandes GNSS est designée et fabriquée. Les potentialités de cette structure double bande sont montrées, malgré des différences entre simulation et mesure. Cependant cette antenne présente un fort couplage qui dégrade en partie les performances de l'antenne. La principale nouveauté de cette étude est l'utilisation d'une cavité pour créer des multi-résonances. De nouvelles investigations pourraient être menées dans ce sens, comme l'utilisation d'une cavité conique (pour antenne cylindrique) ou pyramidale (pour antenne carrée) pour obtenir une bande passante maximale

C'est pourquoi les travaux futurs autour de cette structure doivent porter notamment sur la réduction du couplage entre ports. De plus, des études de miniaturisation sont également à envisager car cette dernière structure est plus large que les dimensions initialement spécifiées.

Par conséquence, les travaux futurs sont centrés sur l'amélioration du couplage de cette antenne, ainsi que la validation des prototypes. Une miniaturisation de l'antenne multi-bande est également recherchée car ce dernier design dépasse les dimensions souhaitées.

General introduction

PhD history

The thesis work presented in this manuscript has lasted 3 years and 8 months. It has been developed between the Institute of Electronics and Telecommunications of Rennes IETR (Rennes, 35) and the French-German Research Institute of Saint-Louis ISL (Saint-Louis, 68), with equivalent time spent in each place. This work was funded by the DGA (Direction Générale de l'Armement) and ISL. During the first year a solid theoretical base was developed on antenna theory and specific topics, such as metasurfaces, GNSS, cavities, among others. The first year has also been devoted to the study and the development of the linear polarization antennas. Prototypes were manufactured at the beginning of the second year.

Next, the circularly polarized structures were investigated and designed, and then built during the second year and part of the third year. Finally, the last months of the PhD have been dedicated to the investigations and the implementation of the multiband antenna.

Context and objectives

Communication between flying systems and ground stations or even other systems in deployment is essential for the exchange of data (onboard or ground sensor data, initialization data, target update, etc.) and for the correct geolocation of the object, as well as its navigation and guidance. Nowadays, communications require high data rates accompanied by discretion, especially in disturbed or hostile environments. These requirements involve the development of compact broadband or multi-band antennas, also to be usable by multiple services/standards at a time. These antennas can be used on multiple platforms, such as small, medium or large caliber projectiles or on micro-drones. Specifically, this study addresses the integration of small antennas in the body of a projectile. These carriers are made of metallic materials, which causes the antennas to be integrated in metallic and conductor environments. Unfortunately, a cavity backed antenna causes strong bandwidth reduction. However, it has numerous advantages, such as miniaturization, isolation, reduction of surface waves, among others [26].

An antenna has a narrower bandwidth as smaller is the size of the antenna. Limits in size are the main challenge to obtain enough bandwidth, because the cavity aperture is limited by the dimensions and the geometry of the carrier. The applications targeted in this study focus on the reception of GNSS (Global Navigation Satellite Systems) signals. The frequency band range considered goes from 1164 MHz to 1610 MHz.

The most important limit to respect for the aperture sized is the width, which cannot exceed 50 mm (0.26 λ_0 at 1578 MHz). This limit is imposed because it is foreseen at terms to constitute a ring-shaped antenna array around the metallic cylinder, as Figure 19 shows. On the other hand, the length limitation is slightly longer, up to 60 mm (0.31 λ_0). The antenna can be rectangular if necessary, but the maximum miniaturization of the antenna should be considered. In short, a small square or rectangular cavity

Figure 19: Carrier model to embedded antennas: 155 mm projectile section

antenna is required. This antenna must be able to receive signals from several GNSS systems at the same time.

The subject is divided into three main stages. Initially, in order to cover the frequencies used by Galileo E1, GLONASS G1 and GPS L1 with a single antenna, a device with a bandwidth of at least 60 MHz is necessary at the central frequency of 1578 MHz. As we are targeting a platform flying in altitude, radio propagation is not affected by multipaths. The linear polarization of the receiving antenna is adapted to collect the GNSS signals. In a first time, the polarization of the antenna to be designed is chosen to be linear. Then in a second time, to better adapt the device to the characteristics of the GNSS technology, the circular polarization will be investigated (in fact, the signals emitted by the satellites are circularly polarized).

In a third stage, a cavity antenna is studied with the objective of covering the whole GNSS bands, i.e., from 1164 MHz to 1610 MHz. In this case, the study is focused on designing a double resonance antenna. This structure should have a low resonance for the low L-band frequencies and a second resonance for the GNSS bands placed in the upper L-band range. GNSS bands are shown in Figure 20.

At this level, the reader could wonder, why it is not possible to buy some GNSS antennas « from the shelf » and simply fix them on a projectile? The answer is multiple : first of all, there is no « compact antenna » on the market covering all the GNSS bands, with dimensions small enough to be properly integrated into a projectile. Secondly, the presence of conductor wall around the antenna will degrade its performances (frequency shift, polarization). Lastly, the integration has to ensure the respect of the carrier profile and also the mechanical withstanding of the antenna to the high accelerations during the firing (typically around 15000 g). For all these reasons, the work presented in this manuscript constitute a real need for flying objects with small dimensions.

Ones of the most-known and appreciated antennas are the patch antenna and its enhanced version, the stacked patches antenna. This last configuration can offer a substantial increase in bandwidth compared to a single patch [35].

The use of metasurfaces at the cavity aperture is also an interesting solution [3]: it is possible to increase the bandwidth (in comparison to a patch configuration) without increasing the dimensions of the cavity; in other words, the use of metasurfaces allows to miniaturize the cavity aperture size.

In previous studies [3], a square cavity antenna based on metasurfaces was introduced with linear polarization [21]. In comparison to a single patch in a cavity of same size ($<0.4\ \lambda_0$), the bandwidth was

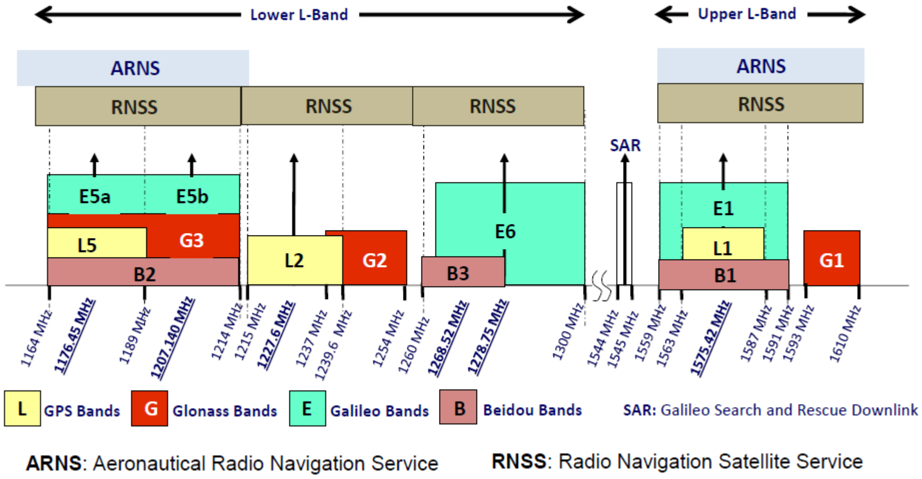

Figure 20: GNSS frequency spectrum [1]

significantly larger for the metasurface (the enhancement was larger for larger cavities). The metasurface is composed of small metallic strips with equal size printed on the same surface. This work was extended to circular cavity. Multiple layers of metasurface, arranged as the example of Figure 21, can be stacked to reach the maximum achievable bandwidth for very small cavity sizes. However, too many layers decrease the bandwidth performances. The work performed by Mario Martinis [3] considered a single resonance antenna on circular and square cavities. Only linear polarization was addressed, and the difficulties to design circularly-polarized antennas were pointed out.

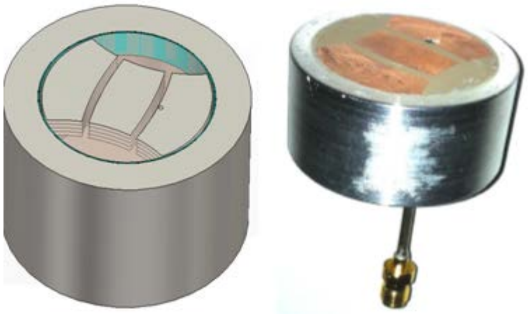

Figure 21: Multilayer metasurface design: 3D model and prototype [3]

From theses basis, it is proposed in the present work to extend the previous work to rectangular cavities, as well as to circularly-polarized antennas and to multi-resonances compact structures.

General objectives

According to the problematic presented above, the general objectives of this thesis are summarized below:

- Integration of the antenna in a metal cavity
- Compact antenna as smaller as possible

- Linear and circular polarization
- Develop an antenna capable of covering all GNSS bands

Practical objectives

In order to achieve the general objectives, different practical objectives are taken into account. Objectives and requirements are divided according to the number of resonances.

Objectives and specifications for the single resonance antenna:

- Linearly-polarized antennas, first, then circularly-polarized
- Band to cover: L1, E1 and G1 centered at 1578 MHz
- Minimum bandwidth of 60 MHz
- The maximum depth of the cavity is fixed at 20 mm (0.11 λ_0)
- Dimensions of the aperture used: 50×50 (0.26 $\lambda_0 \times 0.26$ λ_0) mm^2, 40×45 (0.21 $\lambda_0 \times 0.24$ λ_0) mm^2 et 40×40 (0.21 $\lambda_0 \times 0.21$ λ_0) mm^2.
- Use of metasurfaces
- Prototypes manufacture and experimental characterizations

The objectives and specifications for the double resonance antenna are the following:

- Circular polarization
- Lower resonance to cover from 1164 MHz up to 1300 MHz
- Upper resonance to cover from 1559 MHz to 1610 MHz
- Dimensions of the cavity used 60×60×20 (0.26 $\lambda_0 \times 0.26$ $\lambda_0 \times 0.09$) at 1400 MHz. Wanted cavity dimensions 50×50×20 (0.23 $\lambda_0 \times 0.23$ $\lambda_0 \times 0.09$) at 1400 MHz.
- Use of metasurfaces
- Prototype manufacturing and experimental characterizations

Manuscript outline

This manuscript is divided into four chapters preceded by an introduction and finalized by a general conclusion. The introduction presents the subject of this investigation and the objectives to reach. The topic of this investigation is remembered throughout the chapters.

Chapter 1 focuses on the theoretical background necessary to carry out this work and follow this thesis manuscript. Each of the topics exposed in this chapter are merged and further investigated in the following chapters. Section 1.1 introduces GNSS and the systems that comprise it. The knowledge of the satellite constellations, the type of signals used or the frequency bands are fundamental in this thesis. Next, different types and designs of antenna are considered, in order to choose the best solution to achieve the requested requirements. Section 1.2 lists different antennas that can be used in GNSS applications, as well as the characteristics that these must have for the good reception of signals. Compact antennas are necessary in the context of this work. For this reason Section 1.3 is dedicated to microstrip antennas. They are interesting due to the low price, miniaturization capacity or lightness. Section 1.4 presents the advantages and disadvantages of cavity antennas. Metasurfaces are a good solution to circumvent the cavity drawbacks. Metasurfaces antennas are presented in Section 1.5. Examples and characteristics of multiband antennas are discussed in Section 1.6. Finally, antenna arrays are briefly exposed in Section 1.7. The conception of a ring array is foreseen at terms of this project, however, it will not be investigated in this thesis.

Chapter 2 presents the first results in linear polarization. Microstrip antennas and metasurfaces are joined to create a linearly polarized antenna embedded into a metal cavity. Firstly, a single patch microstrip antenna has been investigated in Section 2.1. Secondly, the possible use of stacked patches is discussed in Section 2.2. Section 2.3 focuses on the design of the linearly-polarized metasurface antenna in cavity. Antennas into a rectangular and a square aperture are designed. Section 2.4 presents the manufactured prototypes and Section 2.5 the numerical results obtained for each prototype. Section 2.6 shows a study carried out about the integration of the antenna in the carrier.

Chapter 3 presents circularly-polarized structures. Section 3.1 is based on the process of creating a circular polarized meta-surface antenna in cavity, as well as the results obtained in simulation. Two different sizes for the aperture are developed. Concerning the antenna feeding, two main methods are investigated thoroughly: 2-port feeding and 4-port feeding. Finally the last one is retained for the rest of the work. Section 3.2 presents the manufacturing of the prototypes and the materials used. The polarization circuit used and its behavior are also explained in this section. Finally, the experimental results obtained from the measurements of the antennas are discussed in Section 3.3.

Chapter 4 develops the study of a multiband antenna for GNSS. In Section 4.1 several methods are tested to obtain two resonances. Section 4.2 presents the development and design for the multiband antenna with double ground plane. Numerical results are also presented in this section. Section 4.3 focuses on the development of an external decoupling and matching networks. Finally, Section 4.4 shows the manufactured prototype and the experimental results for the structure achieving the best performances.

As already mentioned above, a general conclusion as well as an outlook are given at the end of this document.

Chapter 1

State of the art and theoretical basis

This chapter aims to provide a theoretical background for the correct understanding of the proposed work. Several previous studies, which have had a special interest and inspiration for the development of this work, are listed.

First, section 1.1 of this chapter is about Global Navigation Satellite Systems (GNSS). Specifically, it talks about the use, operation mode and the systems involved. Section 1.2 is based on the antennas used for GNSS applications. Different antenna design techniques are used to receive signals from geolocation satellites. The concepts of multiband and multiport antennas applied to GNSS is presented in this section. Then, section 1.3 focus on the concept of patch antennas. This kind of antennas is widely used and they are the type of antennas developed in the course of this work. Concretely, the case of patch antennas integrates into a cavity. For that, section 1.4 is completely focused on cavity properties and their use on antennas. Then, metasurface antennas are addressed in section 1.5. During this investigation, metasurface-inspired antennas are developed to mitigate the drawbacks given by the dimensions of antennas and the use of cavity. This interesting concept may be useful to receive signals from different GNSS bands with a single antenna. Therefore, a brief section on antenna arrays focused on the use for GNSS is developed in section 1.6.

1.1 Global Navigation Satellite Systems (GNSS)

A (SATNAV) is a constellation of satellites orbiting Earth. Nowadays, these systems are widely used to determine the three-dimensional (3D) position of a point anywhere on the planet. Known the position and timing of the satellites, it is necessary the signal of three of them to make a two-dimensional (2D) triangulation, and four to obtain also the altitude of the point, so the 3D position [1]. The more satellite signals are locked, the more accurate the assessment.

1.1.1 GNSS systems

Talking about GNSS is not just referring to the set of constellations; the systems are composed of two more parts. Apart from the space segment (satellites), the systems also need the ground control section and the user segment. This last part includes all receiving devices that inform us about positioning in real time.

There are four different systems form GNSS, two of them fully developed and two under development. (GPS) is the system belonging to the US, which has been the only one operating completely for several years. The Russian GLObal NAvigation Satelite System (Glonass) began with the launch of its first satellite by the Soviet Union in 1982. Until 2011 the whole system was not put in operation. The

European Union develops its own positioning system called Galileo. The first satellite of this project was put into orbit in 2005, and in 2016 the system has begun to operate. But it will not be until 2020 when the constellation is complete and fully operational. Finally, Beidou is the constellation implanted by the Federal Republic of China. At the beginning, this system only covered China and its surroundings. The first experimental generation has been operation since 2000. The global expansion called Compass or Beidou-2 has planned to be completed in 2020 with a total of 30 satellites. Japan's Quasi-Zenith Satellite System (QZSS) or the India's Navigation with Indian Constellation (NavIC) are other existing satellite navigation systems. However, these systems offer only regional operation, so can not be classified as global SATNAVs. Figure 1.1 shows the position of the GNSS orbits with respect to other orbits, such as the International Space Station (ISS), and the size of Earth.

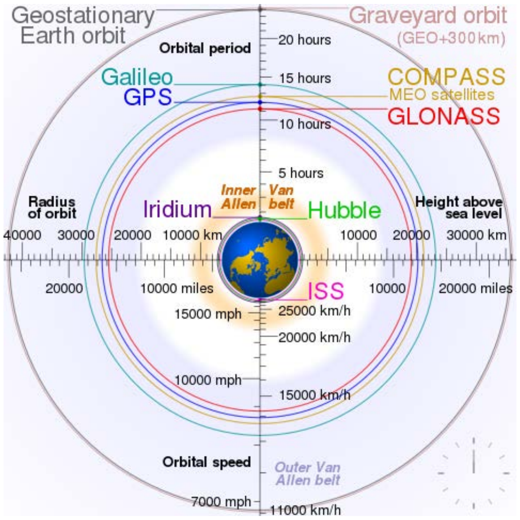

Figure 1.1: Comparison between the orbits from GNSS, ISS, among others, with the nominal Earth size (*CC BY-SA 3.0 by cmglee - Own work)*

1.1.2 GNSS signals

The frequencies used to emit the signals from GNSS satellites belong to the L-band. This microwave frequency range includes the bands between 1000 MHz and 2000 MHz. This frequency set of the radio spectrum is also used by mobile communications service, such a 4G, operations radio amateurs, the Digital Audio Broadcasting (DAB), among others.

The spectrum frame assigned by the International Telecommunications Union (ITU) for the Radio Navigation Satellite Service (RNSS) is divided into two parts. In the upper L-band, from 1559 MHz to 1610 MHz, are placed GPS L1, Galileo E1, Glonass G1 and Beidou B1. The rest of GNSS bands are in the lower L-bands between 1164 MHz and 1300 MHz, as shown in Figure 1.2. Similarly, there are two bands used by the Aeronautical Radio Navigation Service (ARNS).

GNSS signals are composed of the following parts: the carrier centered at the desired frequency, the ranging code and the navigation code. The ranging code is a binary sequence that allows to mark the time of the signal traveling from the receiver to the satellite. The navigation code is also a binary message which reports satellite telemetry, such as clock parameters, velocity or position.

The temporal synchronization of the signal is done by atomic clocks, the most accurate time and frequency method (an atomic clock is a device with a counter using the frequency of the electromagnetic radiation emitted by an electron moving between two energy levels). Satellites are equipped with three or

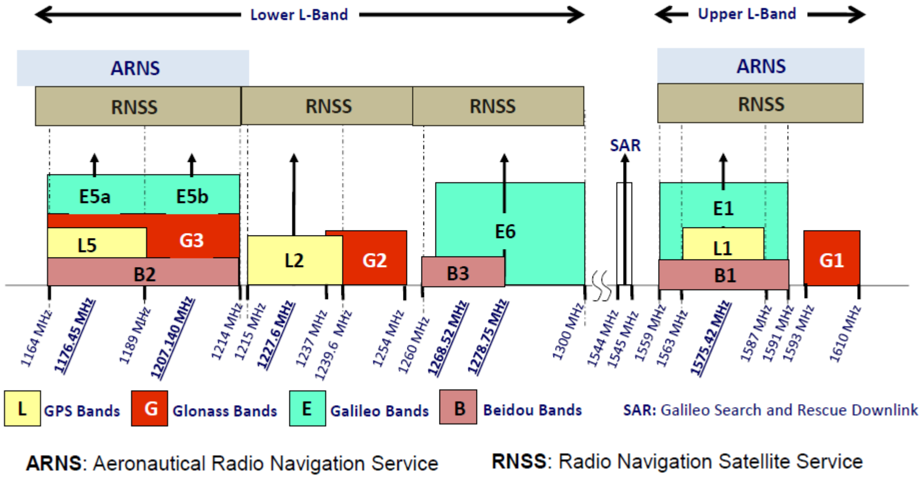

Figure 1.2: GNSS frequency bands distribution [1]

four of them. They are fabricated with rubidium, cesium or hydrogen masers (Microwave Amplification by Simulated Emission of Radiation) but the first one offers the best performances [36]. All clocks placed on satellites are synchronized with international standards (as UTC).

1.1.2.1 GPS

GPS offers military and government services (Precise Pointing Service or PPS) and civil and commercial bands opened worldwide (Standard Positioning Service or SPS) [37]. 24 satellites placed in 6 MEO (Medium Earth Orbit) orbital planes currently form the GPS constellation. Several improvements are carried out continuously both in the ground control segment and in the space segment.

GPS signals are divided into two groups, legacy signals and modernized signals. The first group refers to the set of signals which are operational since the program was launched. The second includes the signals that have been added later to the constellation. All of them are right-hand circularly polarized (RHCP).

Legacy signals Legacy GPS signals transmit information on two different radio frequencies. These signals are called L1 (Link 1) and L2 (Link 2). L1 is centered at the frequency 1575.42 MHz and L2 at 1227.6 MHz. The frequencies are derived from the nominal frequency of the aforementioned atomic clocks. In this case, the fundamental frequency of the clock material is $f_0 = 10.23$ MHz. The CDMA (Code Division Multiple Access) technique allows two signals to use the same carrier frequency. As we can see in the Figure 1.2, L2 is $120 \times f_0 = 1227.6$ MHz and L1 is $154 \times f_0 = 1575.42$ MHz, both using BPSK (Binary Phase Shift Keying) modulation method.

Figure 1.3 represents the synthesis of the Legacy GPS signals and use these three types of PRN (Pseudo-Random-Noise) codes:

- C / A code (Coarse / Acquisition): It is the code developed for civil use and its chipping rate is 1.023 Mchips/s ($= f_0/10$). This code only modulates L1.
- P code (Precision): The chipping rate of this code is 10.23 Mchips/s ($= f_0$) and its use is mainly military including some authorized civil users. To restrict this civil access, a protection called Anti-Spoofing (A / S) is implemented. When A / S on is the mode of operation, the P code is combined

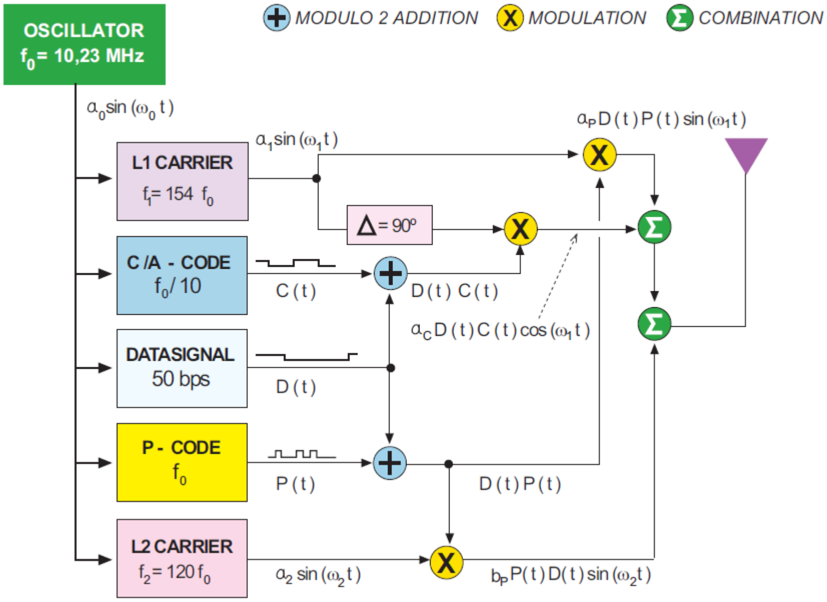

Figure 1.3: L1 and L2 signal structure (source [4])

with a secret W code, which results in the Y code. P(Y) is only available for PPS users because it is modulated over L1 and L2.

- Navigation data message (D): Both C / A and P codes are modulated with the 50-bps navigation message over both L1 and L2 signals. As explained above, this kind of message offers information about the time-of-transmission of each signal, the location of the satellite, its status, among other data. In the same way, the message contains user help information such how to translate from GPS time system to UTC time system.

Modernized signals The signals modernization phase includes a new signal called L5 (Link 5) and some new codes. L1C and L2C signals contains the new civil codes modulated over the previous L1 and L2 signals. This phase also includes the M code for military exclusive use also added to L1 and L2. The modernization of the civil code aims to improve the robustness and the accuracy with respect to the C / A code. This improvement also allows the interoperability of GPS with signals from other GNSS systems (e. g., Galileo) operating at the same carrier frequency.

The military use code M has been designed for autonomous without the need to access via C / A or P(Y), although it is compatible with them. In this way security is improved. The M code uses BOC (Binary Offset Carrier) modulation with a chip rate of 5 × 1.023 Mchips/s.

New L5 signal uses a QPSK modulation in order to combine the two signal components; in-phase (L5-I) component and quadra-phase (L5-Q) component. This band is centered at 1176.45 MHz ($115 \times f_0$). This third civil GPS signal has the main objective of covering SoL (Safety-of-Life) services.

1.1.2.2 Glonass

Glonass has a constellation of 24 satellites spread over three MEO orbited planes of 8 satellites each. It also has another 7 among spare, maintenance or testing. First satellites were placed in orbit in 1982, but it was not until 2007 that Russia removed the restrictions of use. This caused the manufacture of receivers capable of capturing GPS and Glonass signals at the same time. Glonass signals development follow a similar structure as GPS. First, two signals and two codes were developed, both with civil and military version. In a second phase, another signal was launched along with an improvement of the previous codes.

Legacy signals In the first phase, Glonass transmits FDMA (Frequency Division Multiple Access) signals in G1 and G2 bands (see Figure 1.2). Because of that, the legacy signals are derived from the channel number k, with $k = -7, ..., 6$, following this two expressions, where the first term corresponds to the central frequency of the band:

$$G1 : f_1(k) = 1602 + k \times 9/16 = (2848 + k) \times 9/16\text{MHz}$$

$$G2 : f_1(k) = 1246 + k \times 7/16 = (2848 + k) \times 7/16\text{MHz}$$

As in GPS, C / A civil code is modulated over G1 and the P military code is modulated over both, G1 and G2. These codes and the navigation message D are modulated using the BPSK (Binary Phase Shift Keying) technique.

Modernized signals In the modernization phase of Glonass a new frequency band is added. This band called G3 provides other civil C / A code and other P military code. CDMA technique is used for this band which is centered at 1202.025 MHz and is mostly used for SoL services.

1.1.2.3 Galileo

The development of Galileo system allows the European Union to have its own system and act independently of GPS and Glonass. At this time Galileo has a constellation of 26 satellites divided into three MEO orbital planes, of which 22 are fully operational. Spare satellites are included. In the next few years it is planned to put 8 more satellites into orbit. Galileo is designed to provide users with five different services:

- Open Service OS: This service provides worldwide public and free access. The service is used for personal navigation and allows everyone to possess a GNSS receiver, usually into a smartphone or car. Normally these receivers also use GPS as support.

- Safety-of-Life SoL: It is designed for critical applications, when human life is endangered if the radionavigation service suffers an error, such as aviation. This service is guaranteed due to the use of dual frequency receivers. It will be available in future phases of the program.

- Public Regulated Service PRS: Different encrypted code are part of this robust service, as it is intended for security authorities, such as police, military or customs. Governments are responsible for controlling the access to the service, which is independent from other services to prevent malicious interference or signal hacking.

- Commercial Service CS: Commercial access can be considered as a service that complements the OS service. By paying a fee, commercial applications that require more features have access to two additional signals. These signals are protected by commercial encryption.

- Search and Rescue Service SAR: Galileo provides a complement to the existing SAR service (Cospas-Sarsat system). Galileo's SAR is responsible for the real-time reception of distress messages and the precise location of them from anywhere on the planet. For this, the detection is carried out with multiple satellites.

Galileo transmits signals in three frequency bands in the L-band; E1, E5 and E6. As GPS, satellites differentiate the signals using the CDMA technique. Data and raining codes are also provided by the signals channels.

E1 signal is centered on frequency 1575.42 MHz, as GPS L1. This signal is divided into three sub-signals. Only PRS users have access to E1-A signal, that is, it is encrypted for the use by security authorities. On the other hand, E1-B and E1-C signals have access for all users with encrypted raining codes. These two signals are modulated by MBOC (Multiplexed Binary Offser Carrier). E1 also supports OS, CS and SoL services.

E5 signal is centered at 1191.795 MHz and consists of two individual signals, E5a and E5b. These signals can be captured together performing a larger bandwidth or separately and they are modulated using AltBOC (Alternate Binary Offset Carrier). E5a is at 1176.45 and E5b at 1207.14, running into L5 and G3 (slightly shifted) respectively. Both E5a and E5b support OS service but E5b is used also for CS and SoL.

Finally E6 signal, which is centered at 1278.75 MHz, supports CS and PRS services. E6 signal follows the same structure as E1. It is divided into 3 sub-signals where E6-A is dedicated to users with PRS service permissions.

1.1.2.4 Beidou

The Chinese GNSS system is composed of three phases. The first constellation (Beidou-1) has only three satellites with limited coverage. The second one (Compass or Beidou-2), with 10 satellites in orbit, is limited to the region of Southeast Asia and East Asia. Finally, Beidou-3 completes the global coverage phase of the system. When this constellation will be complete, it will have 35 satellites and reach pinpoint accuracy. They will be located in three different orbits: the geostationary orbital plane (GEO), some 55-degree Inclined Geosynchronous Orbits (IGSO) and several MEO orbits.

The second and third phase of Beidou emit in three radio frequencies in L-band called B1, B2 and B3. The signals are transmitted in RHCP. For Beidou-2, QPSK and BPSK are the modulation used but the BOC modulation type is also included for the global version or the system.

Taking into account only the global system, B1 signal is centered at 1575.42 MHz, sharing carrier frequency with GPS L1 and Galileo E1. B1 has both open and authorized restricted access. B2 signal is placed at 1191.795 MHz and offers full public access. Finally, B3 band at 1298.52 MHz is used exclusively by authorized users.

The Table 1.1 shows a summary of all GNSS signals and their characteristics. The signals from GPS, Glonass and Galileo are the signals used in this thesis.

1.2 Antennas for GNSS applications

The use of antennas is the first step to receive signals from navigation systems. For this, the antennas must be designed according to certain specifications. The current GNSS systems are set between 1100 MHz and 1610 MHz, which require wideband antennas to capture the whole set. The antenna has to ensure other criteria, such as a good polarization axial ratio or an efficient rejection of multipath and interference [6]. A linearly-polarized antenna for GNSS is also possible, for example for onboard flying platform in multipath-free environments, with the inconvenient to have a worse carrier-to-noise ratio C_0/N_0. All these requirements will be addressed in detail throughout this section. Apart from the specifications imposed by the GNSS signals, the application requirements must also be taken into account. Nowadays, more compact, lightweight or low cost antennas are demanded. Another fundamental element is the platform where the antenna needs to be placed. The carrier adds other environmental conditions that may determine the size, materials used or design techniques.

Table 1.1: Characteristics of GNSS signals

System	Band name	Carrier frequency	BW (MHz)	Services
GPS	L1	1575.42 MHz	24	Civil/Military
	L2	1227.6 MHz	24.6	Civil/Military
	L5	1176.45 MHz	25	Civil
Glonass	G1	1602 MHz	17	Civil/Military
	G2	1246 MHz	17	Civil/Military
	G3	1202.025 MHz	25	Civil/Military
Galileo	E1	1575.42 MHz	32	PRS, OS, CS, SoL
	E5a	1176.45 MHz	25	OS
	E5b	1207.14 MHz	25	OS, CS, SoL
	E6	1278.75 MHz	40	PRS, CS
Beidou	B1	1575.42 MHz	32	Open/Authorized
	B2	1191.795 MHz	50	Open
	B3	1268.52 MHz	18.75	Authorized

1.2.1 Requirements for a GNSS antenna

1.2.1.1 Polarization and axial ratio

According to Balanis [5], the polarization of a wave arriving to an antenna is defined as the "polarization of a plane wave, incident from a given direction and having a given power flux density, which results in maximum available power at the antenna terminals". In general, the vector that described electric field at a point in space as a function of time traces an ellipse, Figure 1.4a. So we can say that circular polarization is a special case of elliptical polarization when the ellipse have equal axes. Following the standard IEEE 149-1979 and [6], if the turn is counterclockwise we have right-hand circular polarization (RHCP) and if it turns clockwise we have a left-hand circular polarization (LHCP).

GNSS satellites antennas emit in CP, specifically in RHCP. Because of this, the receiving antennas should also be designed in CP, although linear polarization (LP) is also possible. Due to the circularity of the Earth's magnetic field, a LP signal can change the polarization properties. In the same way, the use of circular polarization makes possible to distinguish between signals coming from satellites and multipath signals reflected from surface elements. Multipath signals cause a change in the polarization state becoming left-hand circular polarization (LHCP). Consequently, if an antenna is in circular polarization it may discriminate the interference captured filtering only RHCP signals.

The shape of the ellipse formed (Figure 1.4b) is determined by the axial ratio (AR). The AR is defined as the ratio between the major and the minor axis following Equation (1.1). If $|AR| = \infty$ the polarization is linear and when $|AR| = 1$ (0 dB) the ellipse is a circle: the polarization becomes circular. Axial ratio needs to be less than 3dB to perform a good circular polarization for an antenna.

$$|AR| = \frac{Major\ Axis}{Minor\ Axis} = \frac{OA}{OB}; \qquad AR(dB) = 20log\,|AR| \tag{1.1}$$

Therefore, AR is useful for determining different factors of a GNSS antenna; like the efficiency of the RHCP polarization of the GNSS signal receiving antenna or the ability to reject multipath signals. However, it should be borne in mind that the AR of the receiving antennas can vary with the angles (elevation and azimuth) so an adapted design must be performed. The axial ratio of an antenna at certain elevation and azimuth angles can be calculated using the cross-polarization discrimination (XPD). This magnitude can be defined as the minimum value measured over the beamwidth in a certain angular deviation from the main beam direction. The XPD is related to the AR as follow [6]:

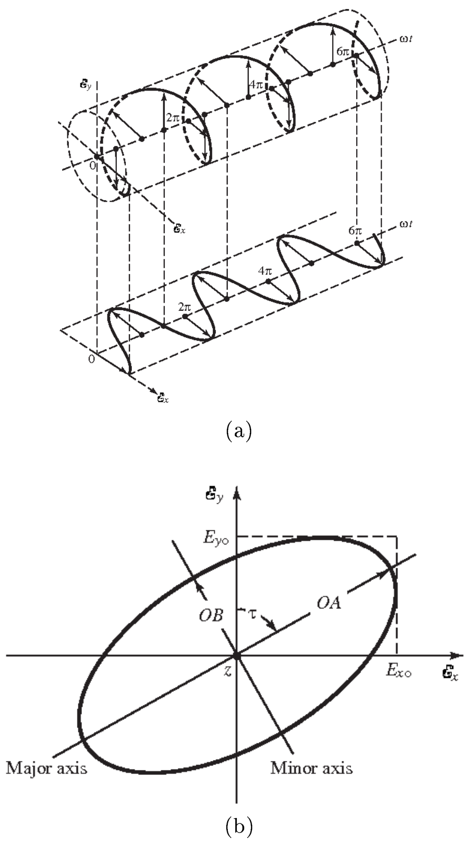

Figure 1.4: (a) Schema of the rotation of an electromagnetic wave. (b) Polarization ellipse [5]

$$XPD = \left[\frac{|AR| + 1}{|AR| - 1}\right]^2 \tag{1.2}$$

1.2.1.2 Directivity and gain

Two of the most characteristic values of an antenna are gain and beamwidth. Especially for GNSS antennas, an adequate C_0/N_0 is essential for receivers to use efficiently the signals from the satellites. For that, a minimum criteria must be imposed on gain. The directivity of a GNSS antenna can be defined as the directive gain, that is, the concentration of RHCP radiation in the maximum direction of the main lobe. This parameter describes the shape of the radiation pattern, in other words, the distribution of radiated energy by the antenna in the space. However, this definition of directivity or directive gain does not include any of the different losses that can be found. Therefore, the realized gain is described in the Equation (1.3), where η_{tot} is the total antenna efficiency (total losses). The realized gain is the term used for the efficient calculation of the C_0/N_0.

$$G = \eta_{tot} D \tag{1.3}$$

$$\eta_{tot} = \eta_{imp} \cdot \eta_{fn} \cdot \eta_p \cdot \eta_{ohm} \cdot \eta_w \tag{1.4}$$

where

η_{imp} = impedance mismatch loss between the antenna and the feeding connector
η_{fn} = losses caused by the feed polarization network to generate RHCP
η_p = polarization mismatch between the receiving and the transmitting antennas
η_{ohm} = ohmic losses
η_w = losses from dielectric and surface waves

If we assume an uniform antenna radiation pattern, the directivity is also equal to the area of a sphere ($4\pi r^2$) divided by the cross section area of the sector represented by the radiated beam [6]. Considering a circular shape, the directivity could be defined as follow:

$$D = \frac{4\pi r^2}{Antenna\, Pattern\, Area} = \frac{const}{beamwidth^2} \tag{1.5}$$

Since beamwidth is proportional to the wavelength λ and inversely proportional to the antenna aperture size d, Equation (1.5) becomes Equation (1.6)

$$D = const \left(\frac{d}{\lambda}\right)^2 \tag{1.6}$$

It should be pointed out that GNSS reception antennas require a wide beamwidth to cover the entire upper hemisphere. Taking into account the above equations, the requirement of needing a wide beamwidth causes a strong loss in gain. Gain is reduced to minimums especially for low elevations angles, where the width of the lobe is crucial to acquire the satellites of that area. The current minimum gain required for a GNSS antenna with 5° of elevation angle is estimated to -4.5 dBic [6]. Figure 1.5 shows a scheme of the minimum gain necessary for a beamwidth as wide as possible.

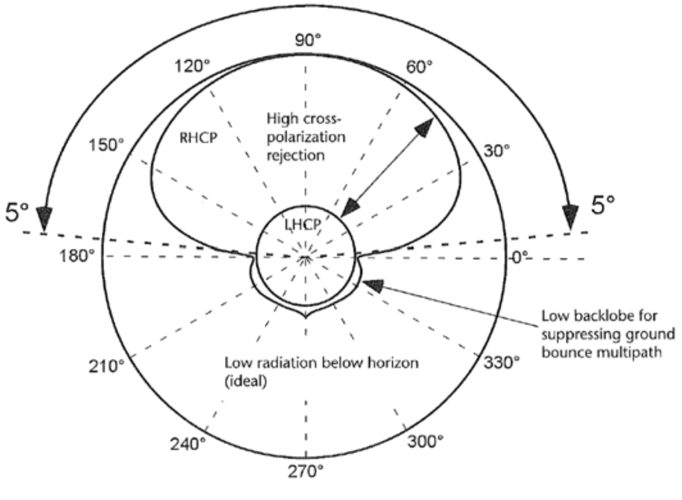

Figure 1.5: Radiation pattern with the ideal minimum gain [6]

1.2.2 Types of GNSS antennas

Various methods of antenna design can be used to achieve the previously mentioned requirements. The platform, the bands to cover, the applications or the dimension constraints will determine the type of antenna chosen. Some types of antennas used for GNSS applications are microstrip antennas, spiral antennas or helix antennas. The use of reflectors or beam forming arrays is also very common. Some of them will be detailed below and in the following sections.

1.2.2.1 Quadrifilar Helix antenna

A helical antenna consists of one or more conducting wires (monofilar, bifilar, quadrifilar, hexafilar, etc.) rolled up in the form of a helix. These antennas operate in axial mode to obtain circular polarization. However, the use of the quadrifilar version achieves a pure circular polarization over a wide angular sector. The Quadrifilar Helix Antenna or QHA consists of an array of four helix-shaped metal filaments around a cylindrical support. These elements have a certain curvature and they are rotated 90° from each other, as Figure 1.6 shows, to generate RHCP. Nowadays, more compact QHA antennas are created. For example in [38, 39], the filaments are converted into strip lines printed on a dielectric material.

Figure 1.6: Classic Quadrifilar Helix Antenna

These type of antennas are widely used for GNSS applications, especially for portable receivers and mobile terminals. The main advantages that QHA offers for GNSS are:

- Small dimensions. QHA are light in weight and small in size, especially the most current ones manufacture by the technique called photolithography. As QHA do not need a ground plane, they are even more compact.
- Wide beamwidth. The QHA antenna has a conical radiation pattern that provides a wide beamwidth. This feature is useful for receiving multiple satellites in the upper hemisphere.
- Miniaturization. In the same way as in patch antennas, the size can be even more reduce if the cylindrical support is made by a dielectric material with high permittivity, such as a ceramic. The negative effect is the bandwidth reduction.

QHA antennas have certain disadvantages for the use in GNSS applications:

- High profile. The antennas used in avionics should have a very low profile and to be very light in weight. The QHA antennas do not have a low profile due to their cylindrical shape, which makes them unadapted for this application.
- Coaxial baluns (balanced to unbalanced). These antennas are used with baluns, which cause a narrow bandwidth and a poor front-to-back ratio. Although there are currently designs that can improve this ratio, the use of baluns makes the antenna susceptible to multipaths.

- Single band. They are generally used to cover a single band of frequencies, which is a drawback for the recent multi-frequencies requirements.

1.2.2.2 Planar and drooping bow-tie antenna

The standard bow-tie antennas consists of two triangular-shaped metal sheets confronted and fed by their narrowest part, as can be seen in the Figure 1.7. They are a miniaturization of the biconical antenna. These antennas are well known for their broadband but the structure is so massive for certain applications. The use of bow-tie reduce the size but also the bandwidth. Anyway, this compromise make them useful for GNSS applications. The RHCP is obtained by crossing two of these antennas forming 90º between its flaps. These two dipoles have to be placed on a ground plane and they must have different sizes. A trick to improve the gain in reception for satellites located at low elevation angles is drooping the dipoles. Both, planar and drooping bow-tie antennas for GNSS are investigated in [40] and [41].

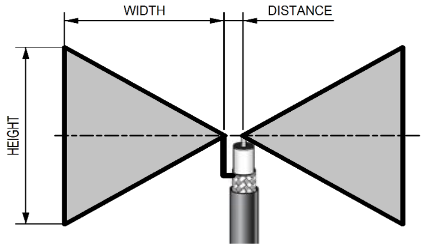

Figure 1.7: Schema of a standard bow-tie antenna

1.2.2.3 Printed antennas for GNSS

Printed antennas (called microstrip antennas or patch antennas) will be extensively explained in the dedicated Section §1.3, but a brief about them is provided below. This type of antennas are the most used for the reception of GNSS signals. Its main advantages are the compact size, the low profile and the low cost. A standard microstrip antenna consists of a radiator patch printed on a dielectric substrate and placed on a ground plane to make the antenna resonate. The patch is made of a conducting material (copper generally), considered as PEC (perfect electric conductor) in simulation, and it can be designed with different shapes. Usually, classical patch antennas operate for a single frequency. However, it is common in GNSS to use stacked patches to cover two or more resonances, for example to cover L1 and L2 bands of GPS.

The use of microstrip antennas for GNSS applications has numerous advantages, listed below:

- Very low profile. This antennas are useful for applications in avionics to not interfere with aerodynamic drag due to the small weight. Due to this, they are very easily integrated into GNSS reception circuits.

- High permittivity dielectrics. The use of these materials allows the miniaturization of the antenna. Also, this entails obtaining antennas more compact and with better performances; such as bandwidth, directivity and gain at low elevation angles or the suppression of surface waves radiation.

- Low cost. Photolithography is the technique used to print the metallizations on the substrates. This method combined with other engraving techniques led to mass production and, therefore, costs are reduced.

- Flexibility. Patch antennas are easily integrated into conical or cylindrical surfaces. The use of flexible substrates and patches favors integration on conformal surfaces without affecting aerodynamics.
- Circular polarization. As mentioned above, GNSS antennas have better performances in circularly-polarized, specifically RHCP. Circular polarization is easily achieved in patch antennas because they tolerate different feeding techniques, such as coaxial probes, apertures or microstrips lines. The use of single or multiple feeding points is possible to reach the circular polarization.

Like all technologies, the use of patch antennas for GNSS suffer also disadvantages to consider:

- Narrow bandwidth. Many times it is required to go beyond a simple patch to enhance the bandwidth. The use of stacked patches, parasitic patches or metasurfaces is very common.
- Multipath and interference increase. The use of substrates with very high permittivity increases the radiation by surface waves for low elevation angles and the diffraction from the ground plane edges. Although this increase the beamwidth, the backlobes created are sensitives to interference and multipath. These phenomena affect the gain and phase at higher elevation angles, due to interference with the main patch radiation.

1.2.3 Multiband antennas

1.2.3.1 Definition and characteristics

There could be an interest in operating in two or more frequency bands with a single antenna. Multiband or multi-frequency antennas are commonly used to resonate at frequencies with a considerable separation between them. These antennas may have lower gains or needs to be physically larger in comparison to single-band antenna, but they are less costly and smaller in total size than a solution using one antenna for each frequency. In GNSS, it is very useful to cover several bands from the same system without the need to design antennas with extremely large dimensions.

Multi-frequency antennas can be divided into three types: classic antennas, arrays and fractal antennas.

Classical multiband antennas

Depending on the number of feeding points or resonators, multiband antennas can be divided into the following categories.

1. *Multiband antennas with single feed and single resonator.* The extra resonances obtained are due to the excitation of other modes in a single resonator. This type of design is more compact but it has some disadvantages. The bandwidth for the lowest band is smaller than the bandwidth for the band placed at higher frequency. In this type of antennas, this issue is impossible to control. In fact, if three or more modes want to be excited, the design becomes complex. The field polarization is also hard to control. However these limitations, some classical miniaturization techniques such as the use of dielectrics, short circuits and ground planes, can be applied. Some examples of this method are given in [42, 43, 44, 45, 46]. Many of them use this technique together with others, such as the use of slots or unusual patch shapes.
2. *Multiband antennas with single feed and multiple resonators.* The classical method uses in this case is the coupled parallel patches. The upper patch is fed directly from the probe and the lower one is therefore coupled only through the fringing field. Although the two radiators have the same dimensions, the fringing fields are different and two resonances appear. The main advantage of having a common feed point is the attenuation of mutual coupling problems. Different patch-shapes

may be used, as traditional square patches, circular patches [47] or annular-rings [48]. Another example of the use of single feeding point and several resonators are the periodic structures [49].

3. *Multiband antennas with multiple feeds (equal or less than frequency bands).* Contrary to the previous case, mutual coupling is the main drawback. This design is used if each service provided requires different chip sets or if it is not possible to adapt the antenna to the desired frequencies with a simple power point. This system is useful when frequency bands are very far apart. These types of antennas usually require an external decoupling network. In [50, 51] some examples can be found.

Numerous ways to generate dual-frequency antennas have been researched. For example, Figure 1.8 extracted from [7] shows several methods for patch antennas.

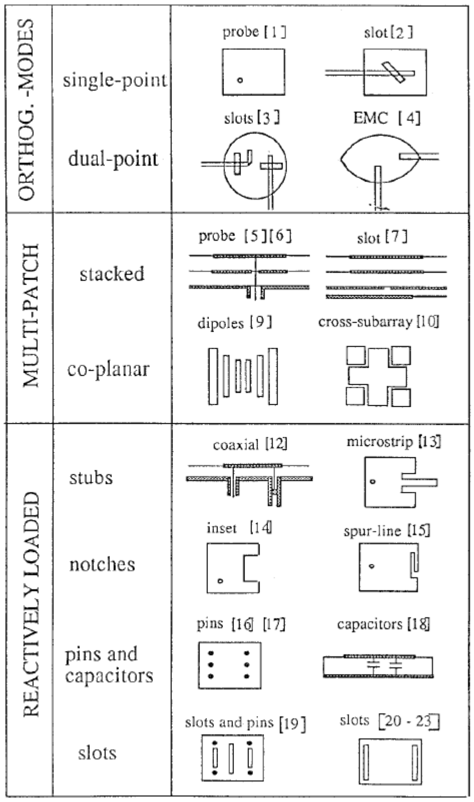

ORTHOG. -MODES	single-point	probe [1]	slot [2]
	dual-point	slots [3]	EMC [4]
MULTI-PATCH	stacked	probe [5][6]	slot [7]
	co-planar	dipoles [9]	cross-subarray [10]
REACTIVELY LOADED	stubs	coaxial [12]	microstrip [13]
	notches	inset [14]	spur-line [15]
	pins and capacitors	pins [16] [17]	capacitors [18]
	slots	slots and pins [19]	slots [20 - 23]

Figure 1.8: Summary-table with different methods to generate dual-frequency antennas [7]

Multiband with arrays

Arrays are useful for multiband applications. In this case, the entire array is used for one band and another section of the array for another frequency band. The arrays will be explained in more detail in Section §1.6. Some examples of arrays for multiband applications, such as 5G or GNSS are given in [52, 53, 54].

Fractal antennas

A fractal antenna is an antenna that uses a fractal-shaped design, with the aim of maximizing the distance or perimeter that it can receive or transmit, on a given volume or surface. The general concept of fractals was defined by the mathematician Benoît Mandelbrot in 1975 [55]. The fractal shape is based on the repetition of a pattern over different scales. The fractal-shape for antennas is useful because of their self-similarity and space-filling properties. Due to these properties, fractal antennas are very compact, multiband or ultra-wide band and they have numerous utilities in mobile telephony and microwave communication. Similarly, mass fractals and boundary fractals are useful to obtain high-directivity antennas, undersampled arrays and low-side lobes arrays [56].

The design process of a fractal antenna begins with the choice of a base fractal shape. This form is iterated until the desired results are obtained. Figure 1.9 corresponds to an example of a fractal antenna design given by [8]. Different shapes offer different properties for the antenna. In this case, the hexagonal design allows the increase of the electrical trajectory, the improvement of the bandwidth and the reduction of manufacturing costs. Other examples of printed antennas with fractal structures providing multiband behaviors are given in [56, 57, 58, 59].

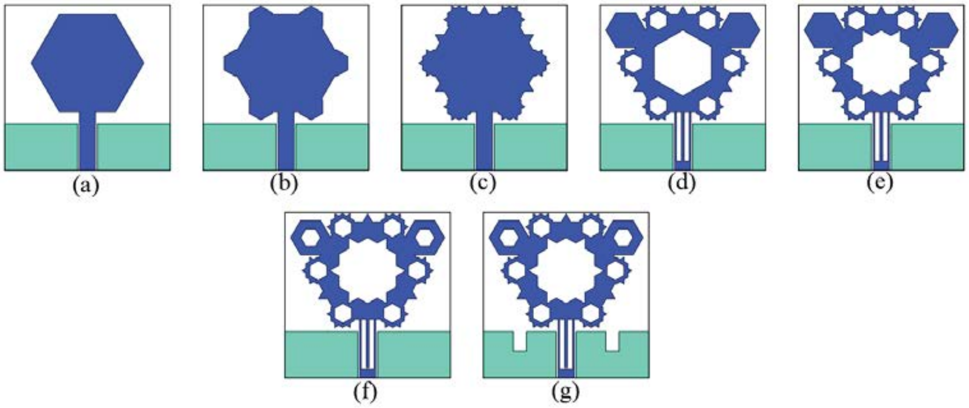

Figure 1.9: Evolution of the design process for a fractal antenna. From the initial hexagonal shape (a) to the final design (g) after six iterations [8]

1.2.3.2 Multiband GNSS antennas

In the early days of satellite navigation, the antennas were designed only to cover L1 and L2 of GPS or G1 and G2 of Glonass. Only a few antennas had been designed to cover both Glonass and GPS. With the passage of time and the evolution of the system, new changes need to be made. Today, GPS and Glonass have been modernized and new bands as L5 and G3 have been included into the system. Similarly, new constellations such as Galileo and Compass were included. GPS and Galileo, for example, may require triple- and even quadruple-band antennas for the optimum use of all their bands. But one of the most interesting offers by multiband antennas for GNSS is the geodetic-grade, multiband antennas that cover all GNSS systems.

What are the advantages of covering multiple GNSS? By using several signals, i.e., GPS P(Y) and M on L1 and L2 or PRS on E1 and E6, greater accuracy is obtained. In the same way, the satellite availability in challenging environments is improved. Low availability satellite signals can be replaced by other system signal with better performances in this environment. Due to the collective detection allows the receiver location to be tracked with higher sensitivity and in a short time. Also, the effect to have less vulnerability to interference and jamming from narrow band sources since several alternate frequency, is quite interesting. Finally, interoperability between GNSS systems may enhance the integrity, reliability and security of the whole system.

Numerous of the above-mentioned techniques may be applied for the design of multiband antennas for GNSS application. One of the main objectives of the research presented in this thesis is precisely the design of an antenna capable of covering all satellite navigation systems. Other designs as arrays [60, 54, 61, 62], spiral antennas [63, 64, 65] or microstrip antennas [44] are some examples. The creation of new ground plane shapes is a recent technique using to generate multiband in GNSS. Some examples applying this technique are: a 2D choke-ring ground planes using FSS (frequency selective surface) [66], 3D conical choke-ring ground plane, resistivity tapered ground plane [67] or AMC/EBG (electromagnetic band-gap) ground plane [68].

1.2.4 Multiport antennas

Numerous communication applications as GNSS require large bandwidths and multiple polarizations. For this, the use of antennas with multiple ports is a solution, since each port can be assigned different phases and amplitudes. Manteghi and Rahmat-Samii introduce in [69] the concept of TARC (Total Active Radiation Coefficient) to find an appropriate measure for multiport antennas. They shown that the single port scattering parameters or the ARC (Active Radiation Coefficient) do not represent the radiation performance and the frequency BW of a multiport antenna. The ARC is presented below.

Considering a single port antenna, the scattering parameter (S_{11}) provides the information between the reflected and accepted powers. Commonly, the bandwidth of an antenna is measured for $S_{11} < -10$. Accepted power is fully radiated if a lossless antenna is considered. Thus, any microwave network is defined by its scattering matrix. Considering a N-port, the scattering matrix, or $[S]$ matrix is defined as

$$\begin{bmatrix} V_1^- \\ V_2^- \\ \vdots \\ V_N^- \end{bmatrix} = \begin{bmatrix} S_{11} & S_{12} & \cdots & S_{1N} \\ S_{21} & & & \vdots \\ S_{N1} & \cdots & & S_{NN} \\ \vdots & & & \end{bmatrix} \begin{bmatrix} V_1^+ \\ V_2^+ \\ \vdots \\ V_N^+ \end{bmatrix}$$

or

$$\left[V^-\right] = [S]\left[V^+\right] \tag{1.7}$$

where V_N^- is the amplitude of the voltage wave reflected from port N and V_N^+ is the amplitude of the voltage wave incident on port N.

Any scattering parameter of the matrix can be determined as

$$S_{ij} = \left.\frac{V_i^-}{V_j^+}\right|_{V_k^+=0\; for\; k\neq j} \tag{1.8}$$

In summary, (1.8) states that S_{ij} is calculated driving an incident wave with voltage V_j^+ into port j and the reflected wave of amplitude V_i^- is measured at the output of port i [70]. To avoid reflections, all ports should end up in matched loads (incident waves are set to zero except the jth port). This means that S_{ii} is the reflection coefficient measured into port i when the other ports terminated in matched loads. Similarly, S_{ij} is the transmission coefficient from port j to i with the same ending ports conditions and it provides coupling information.

Due to the lack of relationship between the radiated power and the reflection coefficient of each port (or the scattering matrix in multiport systems), the TARC is introduced to characterize the frequency bandwidth and radiation performances of a multiport antenna.

As defined in [69], TARC is defined “as the square root of the sum of all incident powers at the ports (available power) minus radiated power divided by the sum of all incident powers at the ports. The TARC is a function of the frequency and is a real number between zero and one”, (1.9).

$$\Gamma_a^t = \sqrt{\frac{available\,power - radiated\,power}{available\,power}} = \sqrt{\frac{P_a - P_r}{P_a}} \tag{1.9}$$

The TARC is calculate following Equation (1.10) when the N-port antenna is excited at the ith port and the others are connected to a matched load (50Ω).

$$\Gamma_{ai}^t = \sqrt{1 - P_{ri}} = \sqrt{\sum_{i=1}^{N} \left| S_{ij} \right|^2} \qquad \forall\, i = 1, ..., N \tag{1.10}$$

For a given excitation $[a]$, the TARC as a function of frequency is calculated with Equation (1.11).

$$\Gamma_a^t = \frac{\sqrt{\sum_{i=1}^{N} |b_i|^2}}{\sqrt{\sum_{i=1}^{N} |a_i|^2}} \tag{1.11}$$

where

$$[b] = [S_p] \cdot [a] \tag{1.12}$$

Identically to a reflection coefficient, if the value of the TARC obtained is equal to zero, all the delivered power is radiated. However, if the coefficient is equal to one, the total of the power is either reflected back or sent towards other ports.

If we consider the example of a 4-ports antenna in linear polarization, as in [69], the TARC is calculated using (1.11) and setting (1.13) as the excitations for (1.12).

$$\begin{bmatrix} b_1 \\ b_2 \\ b_3 \\ b_4 \end{bmatrix} = \frac{1}{\sqrt{2}} \begin{bmatrix} s_{11} & s_{12} & s_{13} & s_{14} \\ s_{21} & s_{22} & s_{23} & s_{24} \\ s_{31} & s_{32} & s_{33} & s_{34} \\ s_{41} & s_{42} & s_{43} & s_{44} \end{bmatrix} \begin{bmatrix} 1 \\ 0 \\ -1 \\ 0 \end{bmatrix} \tag{1.13}$$

For the circular polarization case and a 4-port feeding antenna, the excitation based on (1.14).

$$\begin{bmatrix} b_1 \\ b_2 \\ b_3 \\ b_4 \end{bmatrix} = \frac{1}{2} \begin{bmatrix} s_{11} & s_{12} & s_{13} & s_{14} \\ s_{21} & s_{22} & s_{23} & s_{24} \\ s_{31} & s_{32} & s_{33} & s_{34} \\ s_{41} & s_{42} & s_{43} & s_{44} \end{bmatrix} \begin{bmatrix} 1 \\ -i \\ -1 \\ i \end{bmatrix} \quad or \quad \begin{bmatrix} 1 \\ i \\ -1 \\ -i \end{bmatrix} \tag{1.14}$$

Solving the matrix, the values for $[b]$ are as follows

$$b_1 = (s_{11} + s_{12} \cdot (-i) - s_{13} + s_{14} \cdot (i))\,\frac{1}{2} \tag{1.15}$$

$$b_2 = (s_{21} + s_{22} \cdot (-i) - s_{23} + s_{24} \cdot (i))\,\frac{1}{2} \tag{1.16}$$

$$b_3 = (s_{31} + s_{32} \cdot (-i) - s_{33} + s_{34} \cdot (i))\,\frac{1}{2} \tag{1.17}$$

$$b_4 = (s_{41} + s_{42} \cdot (-i) - s_{43} + s_{44} \cdot (i))\,\frac{1}{2} \tag{1.18}$$

As mentioned above, the reflection coefficient into port i is measured when the other ports terminated in matched loads. However, there are multiport designs (or arrays) in which all ports are active at the same time. In that case, the passive S-parameters are substituted by the active S-parameters. Using the passive Sii parameters, it is not possible to discriminate the ohmic losses from the radiation losses. These parameters take into account the coupling due to the influence of the other ports. Therefore, the calculation of the TARC is performed using the active scattering matrix. They are calculated from the passive parameters as follow

$$s_{11act} = (s_{11}a_1 + s_{12}a_2 + s_{13}a_3 + s_{14}a_4)\,\frac{1}{a_1} \tag{1.19}$$

$$s_{22act} = (s_{21}a_1 + s_{22}a_2 + s_{23}a_3 + s_{24}a_4)\,\frac{1}{a_2} \tag{1.20}$$

$$s_{33act} = (s_{31}a_1 + s_{32}a_2 + s_{33}a_3 + s_{34}a_4)\,\frac{1}{a_3} \tag{1.21}$$

$$s_{44act} = (s_{41}a_1 + s_{42}a_2 + s_{43}a_3 + s_{44}a_4)\,\frac{1}{a_4} \tag{1.22}$$

1.3 Microstrip antennas

The first concept of a printed antenna was proposed by Deschamps [71] in the middle of the 20th century. Nowadays, patch antennas are widely used for countless applications, especially in the aeronautical and defense sectors. Airplanes, satellites, rockets, projectiles or missiles use this technology to achieve accurate communication. This is due to its numerous advantages. Some of them have been mentioned above for the special case of GNSS. A more in-depth analysis of microstrip antennas is presented throughout this section.

As mentioned before, microstrip antennas are characterized by low weight, low volume and small profile. In turn, they have low manufacturing costs so they are good candidates for mass production. Due to their thinness and flexibility, microstrip antennas are ideal for integration into platforms where aerodynamics is critical. In terms of design, it is easy to generate circular polarization, linear polarization or double resonance. Finally, patch antennas are compatible with modules soldered on printed circuits, such a oscillators, amplifiers, modulators, etc [72].

However, microstrip antennas also have some disadvantages compared to other types of antennas. The bandwidth tends to be narrow and the gain lower. Another disadvantage is that the most patch antennas radiate only in one hemisphere, which is beneficial for some applications. Microstrip antennas also have poor isolation between the radiator and the feed, in the same way, there is a risk of exciting surface wave. Later we will explain how the use of cavities can improve this disadvantage. Finally, it should be noted as a disadvantage that microstrip antennas have low efficiency, low power and a high Q.

1.3.1 Fundamental characteristics

1.3.1.1 Geometry

As explained above, microstrip antennas consist of a dielectric material or substrate with a metal patch printed (photoetched) on one side and a ground plane in the other side, as shown in Figure 1.10. The shape of the radiator can have multiple shapes and it varies depending on the application and the characteristic of the antenna. Square, rectangular, circular or strip-shape are the common patches used. The range of substrates that can be used is very varied. They usually have permittivities from ε_r= 2.2 to ε_r= 12, but recently it is being investigated with ceramic materials that exceed these numbers.

The most popular methods for microstrip antennas analysis are the transmission line model, cavity model and full-wave model. The first is the most used for its simplicity, however it is less accurate.

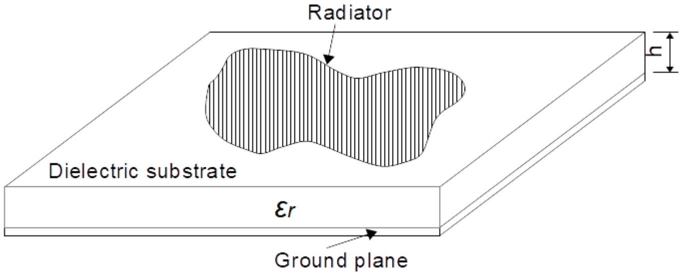

Figure 1.10: Microstrip antenna general configuration

Rectangular patch

The rectangular or square shape for the radiator is the most used due to the simplicity. The fundamental design parameters are the width (W) and length (L) of the patch and the thickness (h) and the relative permittivity of the substrate (ε_r). By playing with the parameters following the design equations, it is possible to get an antenna adapted to the desired frequency. These equations come from the development of the transmission line model described in [5, 72]. As the TM010 mode is the dominant one in a microstrip antenna, the resonant frequency is the given by Equation (1.23).

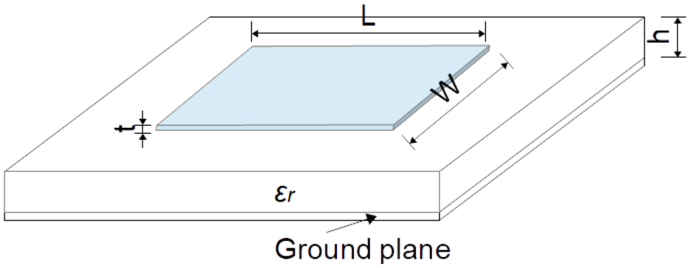

Figure 1.11: Square patch antenna configuration

$$f_{r010} = \frac{c}{2\left(L_e\right)\sqrt{\varepsilon_e}} \tag{1.23}$$

where c is the velocity of light and ε_e is the effective dielectric constant. For low frequencies ε_e can be considered constant. However, if the frequency increases, the effective dielectric constant increases to even approximate the value of the substrate permittivity. This parameter is determined using Equation (1.24). L_e is the effective length of the patch that corresponds to the Equation (1.25), where ΔL is the electrical extension of L, because the patch is electrically larger than its physical dimensions. The distance ΔL is a function of the effective dielectric constant ε_e and the width-to-height radio, W/h, and can be approximated by the Equation (1.26).

$$\varepsilon_e = \frac{\varepsilon_r + 1}{2} + \frac{\varepsilon_r - 1}{2}\left[1 + 12\frac{h}{W}\right]^{-\frac{1}{2}} \qquad \frac{W}{h} > 1 \tag{1.24}$$

$$L_e = L + 2\Delta L \tag{1.25}$$

$$\frac{\Delta L}{h} = 0.412\frac{\left(\varepsilon_e + 0.3\right)\left(\frac{W}{h} + 0.264\right)}{\left(\varepsilon_e - 0.258\right)\left(\frac{W}{h} + 0.8\right)} \tag{1.26}$$

Once the values of the substrate and the operation frequency of the antenna are known, the design process begins by calculating the dimensions of the patch. For an efficient radiator the width is calculated with the Equation (1.27). In the same way, the length is giving by the Equation (1.28). The design of an antenna width other dimensions is also right, but the behavior will be less efficient and the field may be distorted.

$$W = \frac{1}{2f_r\sqrt{\varepsilon_0\mu_0}}\left(\frac{\varepsilon_r+1}{2}\right)^{-\frac{1}{2}} = \frac{c}{2f_r}\left(\frac{\varepsilon_r+1}{2}\right)^{-\frac{1}{2}} \tag{1.27}$$

$$L = \frac{1}{2f_r\sqrt{\varepsilon_0\mu_0}\sqrt{\varepsilon_e}} - 2\Delta L = \frac{c}{2f_r\sqrt{\varepsilon_e}} - 2\Delta L \tag{1.28}$$

Circular patch

The patch with circular shape is another of the most used configurations in microstrip antennas, as shown in Figure 1.12. As well as the rectangular patch, it is used not only as a single element [73, 74, 75, 76], but also being part of an array [77] or metasurface [78]. Circular patches also active TM modes when $h \ll \lambda$ and z is chosen perpendicular to the patch. However, in this case there is only one degree of freedom to regulate and only cavity model can be used properly to analyze this type of microstrip antenna. Based on the fields analyzed that can be find in [79, 72, 76], the dominant mode in a circular patch microstrip antenna is TM110 and the resonant frequency is given by the Equation (1.29).

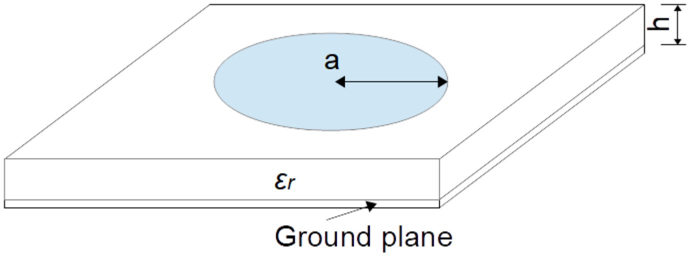

Figure 1.12: Circular patch antenna configuration

$$f_{r110} = \frac{1.8412c}{2\pi a\sqrt{\varepsilon_r}} \tag{1.29}$$

where c is the velocity of light in free space and ε_e the relative permittivity of the substrate.

One the resonance frequency, relative permittivity and substrate height are known, the radius of the patch is design using the following approximation

$$a = \frac{K}{\left\{1 + \frac{2h}{\pi\varepsilon_r K}\left[\ln\left(\frac{\pi K}{2h}\right) + 1.7726\right]\right\}^{\frac{1}{2}}} \tag{1.30}$$

where h must be in cm and K is

$$K = \frac{8.794}{f_r\sqrt{\varepsilon_r}} \tag{1.31}$$

1.3.1.2 Q factor and efficiency

When it comes to optimizing an antenna, other parameters must be taken into account, such as quality factor, bandwidth of efficiency. Sometimes there is the interest to make the design based on the enhancement of some of them.

Q-factor determines the frequency selectivity of a radiating element and is representative of the antenna losses. In general, it is the sum of all losses as equation (1.32) represents.

$$\frac{1}{Q} = \frac{1}{Q_{rad}} + \frac{1}{Q_{ohm}} + \frac{1}{Q_d} + \frac{1}{Q_w} \tag{1.32}$$

where
Q = total Q-factor
Q_{rad} = Q-factor from space wave losses (radiation)
Q_{ohm} = Q-factor from ohmic losses (conduction)
Q_d = Q-factor from dielectric losses
Q_w = Q-factor from surface waves

Some approximations to calculate the different Q-factors for very thin substrates are given by [80] and [81]. When the substrates are very thin $h \ll \lambda$, the losses due to surface waves can be omitted. The use of cavities is a common solution to remove them, as we will explain in a dedicate section. Q-factor from radiation losses is

$$Q_{rad} = \frac{2\omega\varepsilon_r}{hG_t/l}K \tag{1.33}$$

$$K = \frac{L}{4} \tag{1.34}$$

where G_t is the total conductance per unit length of the radiation aperture and K is determined by Equation (1.34) for a rectangular aperture operating in the dominant TM010 mode. The quality factor due to ohmic and dielectric losses is given by the following equations.

$$Q_{ohm} = h\sqrt{\pi f \mu \sigma} \tag{1.35}$$

$$Q_d = \frac{1}{\tan\delta} \tag{1.36}$$

where $\tan\delta$ is the loss tangent of the substrate material, σ is the conductivity and μ the permeability.

The antenna radiation efficiency is the power radiated over the input power and can be calculate using the quality factor as shown in Equation (1.37).

$$\eta_{rad} = \frac{1/Q_{rad}}{1/Q} = \frac{Q}{Q_{rad}} \tag{1.37}$$

1.3.1.3 Excitation techniques

The two most used methods to feed a microstrip antenna are through a coaxial probe and a microstrip line (Figure 1.13). In the same way, the antenna excitation by coupled aperture or proximity coupling are also typically used configurations. Whichever the feed configuration is chosen, the antenna has to be matched with the excitation system. The position of the feeding point also influences the radiation characteristics of the antenna and determines which mode is excited.

In the first two cases, the process of adjust the feeding point position begins by placing it centered on the patch. The antenna must be adapted again and the feeding point displaced to obtain a good match.

The variation of the position of the power probe may produce a frequency shift due to the coupling between the antenna and the feed. However, the radiation pattern remains unchanged [82]. Coaxial connector type N or SMA are the most used for microstrip antennas.

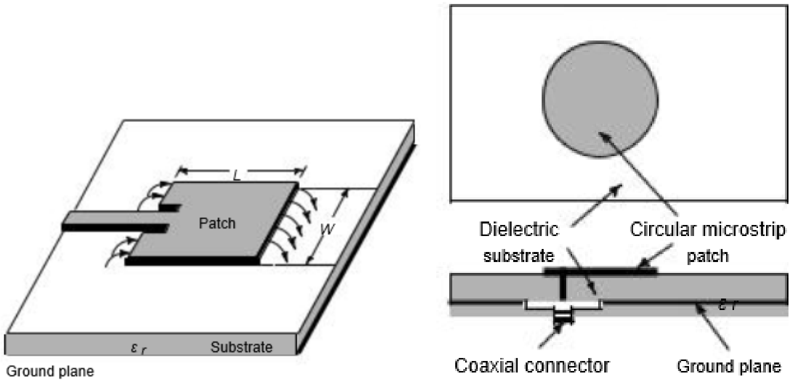

(a) (b)

Figure 1.13: Feeding techniques [5]. (a) Antenna feds by a microstrip line. (b) Antenna feds by a coaxial probe

1.3.1.4 Circular polarization techniques

If the previous feeding methods are used with the classic, both circular and rectangular patches, the radiated waves will be in linear polarization. However, there are different techniques to modify them and obtain a circular polarization. Physically, circular polarization is achieve when two orthogonal modes are activated with 90° phase difference between them. The techniques for generating circular polarization in microstrip antennas are divided into two groups: a single feeding point and two (or four) feeding points.

Different techniques for obtaining circular polarization with a single feeding point are presented in Figure 1.14. The principle of this feeding method is based on the fact that the excited mode can be separated in two orthogonal ones. The 90 ° shift is obtained by a small asymmetry in the structure, which causes a small frequency difference between the two resonances. For example in (a) and (d), the feeding point is placed 45 ° to search this orthogonality. The aforementioned perturbation is more visible in images (b), (c), (e) and (f). In the two examples located in the center, a slot rotated 45 ° causes the division of the mode into two orthogonal modes. Another example is given by the images in the right. The edges or corners of the patches are trimmed to cause the mode excitation. It should be noted that in all cases, the direction of polarization may be controlled by changing the position, of the point or sections, to the opposite side.

Figure 1.15 shows two different techniques to generate circular polarization with 2 excitation points, one for each mode. In this case, the patches are fed with the same amplitude and 90 ° out of phase using an external polarizer [83].

Other techniques such as the combination of the previous two are also used. For example in [84], a patch with slots and double feeding is presented. The use of four feeding points is also a widely used technique [51, 85]. The use of four feeding points is also a widely used technique. This allows the generation of a sequential polarization or the circular polarization generation for two different frequencies, such as in the design shown in Figure 1.16.

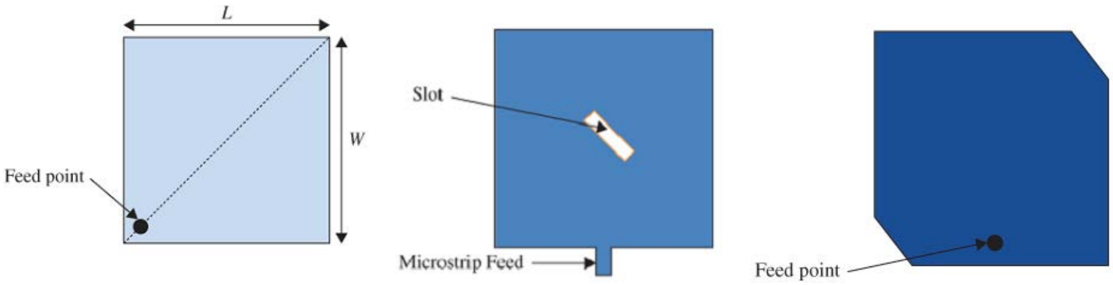

(a) Patch fed in a corner (b) Square patch with a thin slot (c) Trimmed square patch

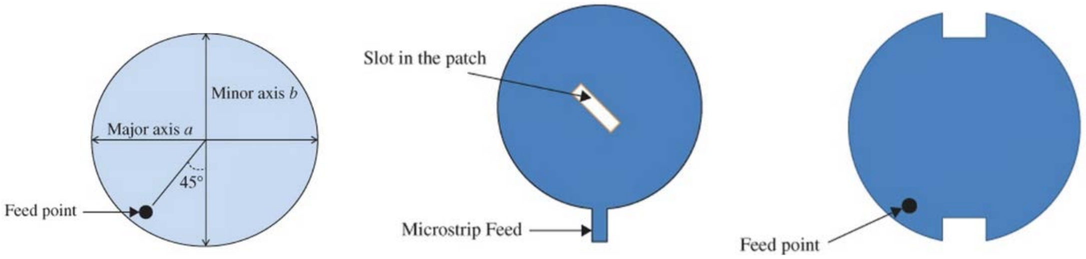

(d) Elliptical patch with feed point in 45° (e) Circular patch with thin slot in the center (f) Trimmed circular patch

Figure 1.14: Examples of circular polarization generation with a single feeding point in circular and square patches [9]

Circularly-polarized antennas with two and four feeding points will be the object of study in next chapters.

1.3.2 Small antennas

At the beginning of the 20th century, electronic devices depended on vacuum tubes until 1940. The discovery of the transistor was a revolution for technological miniaturization. Later, the development of the integrated circuit and the microprocessor allowed the devices to be even smaller and to consume less energy. The size has been reduced over the years to reach molecular levels. Nowadays, nanotechnology is booming with the development of devices at atomic, molecular and supramolecular scales. Research does not only seek miniaturization, it is also sought cheaper, lighter, and more efficient technologies. Microstrip antennas are the best candidates to miniaturize the antenna size.

Antennas are also undergoing the same miniaturization process. However, the antennas are based on physical laws that limit them. An antenna is responsible for transforming the incident wave into a radiated wave. That transformation is performed efficiently when the size of the antenna is equal or larger than half a wavelength. When an antenna is smaller than half a wavelength, the performances are affected. Finding the compromise between miniaturization and performances is the issue of numerous investigations.

Definition

A compact or small antenna is the antenna which has an electrical size much smaller than 1. Generally, the electrical volume or electrical size is defined by kr, where k is the free space wavenumber defines by $2\pi/\lambda_0$ and r is the radius of the imaginary sphere that surrounds the antenna touching it maximum dimension, as shown in Figure 1.17. λ_0 is the free space wavelength, one of the fundamental parameters

(a) Two excitation points for square-shape patches

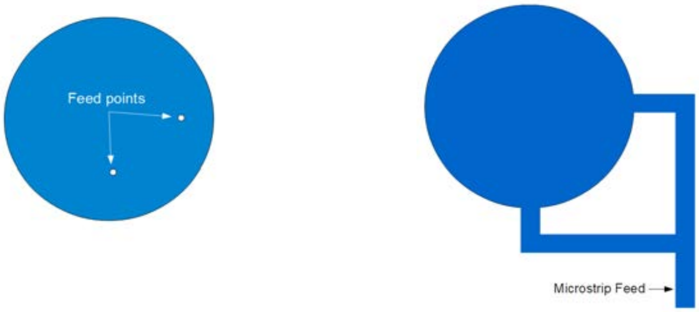

(b) Two excitation points for circular-shape patches

Figure 1.15: Examples of circular polarization generation with two feeding points in circular and square patches

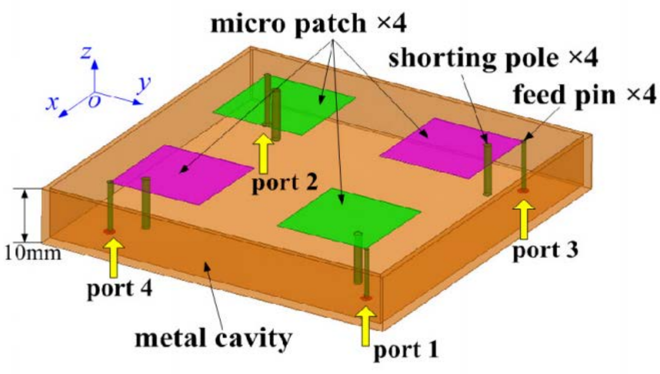

Figure 1.16: Example of CP antenna feeds by four ports [10]

of the antenna radiation characteristics. In fact, Wheeler [86] proposed that a electrically small antenna can be enclosed in a sphere smaller than $1/2\pi$ wavelength. This radius enclosing the antenna may be interpreted as the bound between the near and far field of the antenna [87]. In conclusion, a small antenna is an antenna much shorter than the wavelength at it working frequency.

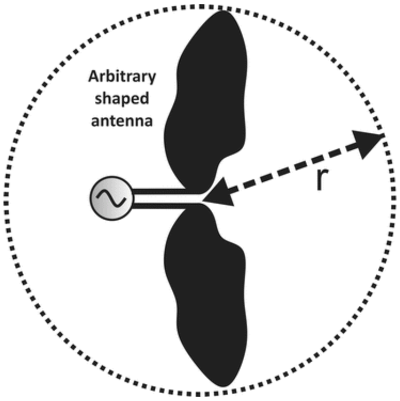

Figure 1.17: Smallest sphere enclosing an arbitrary shape antenna

Bandwidth limitations in small antennas

In this type of antennas, the propagation modes become evanescent modes with a high Q-factor. This is because the far-field radiation of an antenna is the sum of the spherical modes of the near field. Simplifying, they can be considered as omnidirectional radiation diagrams without variation in the azimuth plane. That is, one antenna inside a sphere with radius r have additional energy storage and in consequence a higher Q-factor.

Chu [88] obtained the smallest possible Q (1.38) for a linearly-polarized antenna where the TE01 mode is excited, using equivalent circuits. Then, Fano [89], Collin [90], Fante [91], McLean [92], among others, arrived to the same estimation applying different methods based on field considerations.

$$Q = \frac{1}{(kr)^3} + \frac{1}{kr} \tag{1.38}$$

McLean arrived in [92] to the same result of Chu estimating the radiated power and the energy stored in the reactive field. Following the same procedure, he obtained also the Q factor for a circularly-polarized antenna using TE01 and TM01 modes with a phase shift of 90°, Equation (1.39).

$$Q = \frac{1}{2}\left[\frac{1}{(kr)^3} + \frac{2}{kr}\right] \tag{1.39}$$

Gain limitations

In an electrically small antenna the gain by itself is not limited. Gain practical limit or gain-bandwidth product limit are more correct ways to define it [87]. This limit was approach by Harrington in [93]. The gain bound obtained in this approximation is given by Equation (1.40), where N is the hightest mode radiated by the antenna. From this equation it can be concluded that the gain is limited by the number of modes excited by the antenna. Harringthon in his study limits the number of modes to $N < kr_s$, where r_s is the radius of the sphere.

$$G_{max}\left(\pi/2, 0\right) = N^2 + N \tag{1.40}$$

Finally, from this study it may be extract the following conclusion. If the mode is $n < kr$, it goes quickly to cut off and the mode n is not naturally excited on the field. In the same way, this mode will increase the reactive energy stored, but without impact on the radiated power. Therefore, the limit on gain is given by Equation (1.41).

$$G_{max} = (kr)^2 + kr \tag{1.41}$$

An antenna can have a higher gain, but paying the price of losing in bandwidth. In fact, if a lossless antenna is considered and the minimum possible N in Equation (1.40) is 1, the maximum gain obtained for a significant bandwidth is $G_{max} = 2\ (3dB)$.

Applications and examples of small antennas

Microstrip antennas are the most used for the realization of electrically small antennas because of their low profile, but they are not the only one. Some examples are loop antennas, dipoles and monopoles or PIFA antennas (Planar Inverted-F Antenna).

A loop antenna is made up a loop-shape wire feds by a differential source. The radiation resistance of the loop antenna may be enhanced if the diameter is larger or more loops are added. This antenna is a good candidate for reception but is not for transceivers. The circumference is around λ. Loop antennas are studied in [5, 94] and summarized in [87], among others. Numerous studies have been performed in this topic, some examples are presented in [95, 96].

Dipoles, monopoles, helix antennas [5, 97, 98], ILA (Inverted-L Antenna) or IFA (Inverted-F Antenna) [99] are very popular antennas, specially for mobile terminal applications. PIFA antennas may be considered as a short microstrip antenna or as a folded monopole-type antenna where the wire is replace by a sheet [87]. These antennas are widely used for the low profile, small losses and good bandwidth, if the ground plane is not so large. They are fully analyzed in [100, 101, 102].

GNSS antennas usually require the geolocation of small devices and compact microstrip antennas could be a solution. Some examples are presented in [103, 104, 105]. Nevertheless, none of these solutions are integrated into cavities. A microstrip small antenna undergoes changes in its performances if it is inserted into a cavity. Cavity antennas and their applications are presented below.

1.4 Cavity antennas

Research on the use of small cavities in antenna designs has started since the 50s. Cohen [28] and Counter [29] were the pioneers in investigating the effect of these cavities on antennas. It is nowadays well known that a cavity reduces the radiation back radiation and side lobes, improves the forward gain and helps the miniaturization of the antenna. Cavity antennas can be divided in two main groups: dual reflector antennas and other cavity backed antennas. Dual reflectors antennas are based on open resonators and consist of two reflectors, plane or curved, facing each other and having a resonance field between them.

The first type of double reflector antennas are called backfire antennas, which one of the reflector is much larger then the other. Figure 1.18 depicts the backfire antennas classification depending on the distance between reflectors, proposed by Kumar in [11]. The backfire short-type comprises a space between reflectors of half wavelength, so a structure between them is unnecessary. However, the backfire long-type antennas have a surface wave structure between both reflectors, usually excited by a crossed dipole or a waveguide aperture.

On another hand, one of the reflectors can also be semitransparent, acting as an end-mirror in a laser cavity. It is the case of the beam waveguide antennas, classified in Figure 1.19. These antennas represent quasioptical open resonators, so their dimensions are several times larger than the wavelength. The semitransparency effect can be performed by a perforated metal, for example. In this case, the end-reflectors are not only plane, they can be spherical, in a confocal configuration, depending on the profile of the reflector.

The other group of antennas above-defined as "other cavity-backed antennas", includes the 3D apertures or 3D cavity resonators. A metal aperture is made of a multitude of small holes of various shapes.

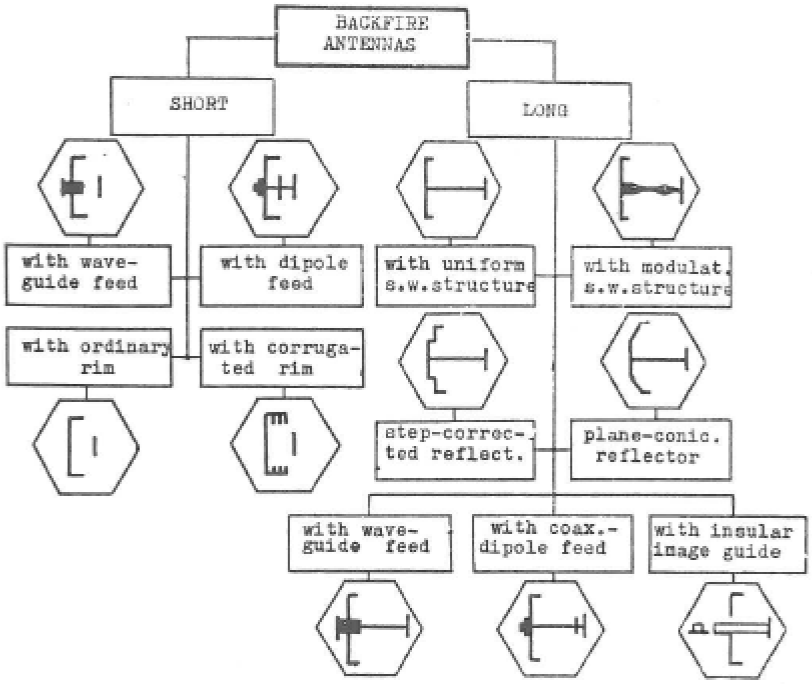

Figure 1.18: Classification of backfire antennas with a cavity [11]

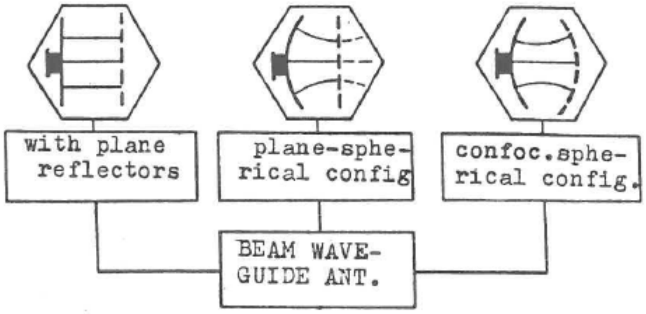

Figure 1.19: Beam waveguide quasioptical antenna configurations [11]

These types of apertures can be considered as an array or a semi-transparent opening closed by a resonator cavity. Some examples are shown in Figure 1.20. For these first cavity antennas, a crossed dipole feed located in the aperture of the backing cavity was used to create circular polarization. The disadvantage of the cavities mentioned above was their size. Usually the cavity dimensions were larger than half a wavelength, at least for the aperture size.

Over the years, new types of cavity antennas have been created with the aim of improving defects from the first original configurations. The structure based on cavity-backed microstrip antennas is very interesting, because the dimensions of the cavity can be significantly reduced. Even if patch antennas have some limitations, their encrustation in a cavity has been investigated to improve some of the drawback of classical microstrip antennas, explained in detail in the previous section. The main interest of this thesis

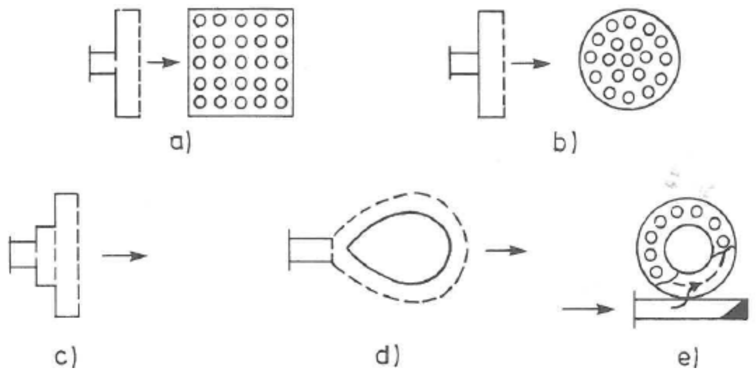

Figure 1.20: Examples of semitransparent radiating apertures. (a) Rectangular single-cavity. (b) Circular single-cavity. (c) Double cavity. (d) double-bounded cavity. (e) ring-shaped cavity [11]

is focused on microstrip patch antennas in cavity, therefore, this type of antennas has a dedicated section below.

A more modern example of resonant cavity antennas (RCA) is given in [12, 13, 106]. These antennas, also known as Fabry-Perot resonator antennas, are typically formed between two parallel reflecting surfaces. One of the surface is a partially reflecting surface (PRS) place on a distance $\lambda_0/2$ from the ground plane to perform an standing wave pattern in the cavity. The ground plane is the other reflector which holds a feed antenna exciting electromagnetic waves inside the cavity [107]. The main drawbacks of this type of cavities are the narrow band and the profile dimensions. To reduce the distance between both reflector, Wang *et al.* [12] proposed the use of an artificial magnetic conductor (AMC) as a reflector, instead of a perfect electric conductor (PEC), as depicted in Figure 1.21a. The use of the artificial material can reduce the distance between reflectors from $\lambda_0/2$ to $\lambda_0/4$, thereby reducing the antenna profile. One of the techniques investigated to improve bandwidth in RCAs is to generate multiple resonances close to each other. For them in [13], a double layer of PRS has been created. The layers are composed of a dielectric material where the cells have different sizes in each layer (Figure 1.21b). For the case presented in [106], the double resonance is created with the ground plane, which allows to have a single PRS and reduce the total antenna profile. In that case a conventional RCA is used, but the height of the cavity is changing using a non-uniform ground plane. Other example using AMC loaded backed aperture have been investigated in [108] to design a low profile CP antenna, with a thickness lower than $0.1\lambda_0$.

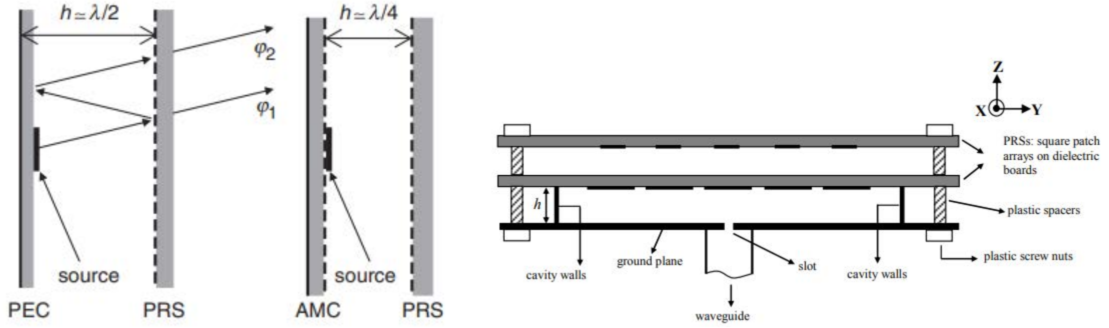

(a) (b)

Figure 1.21: (a) Resonant cavity antenna formed by PEC-PRS, and by AMC-PRS [12]. (b) Double-layer resonant cavity antenna[13]

Magneto-electric dipole antennas are composed of an horizontal planar dipole and a vertically oriented folded shorted patch antenna. These type of antennas are interesting because combining a magnetic and an electric dipole we obtained good electrical performances such as low back radiation, stable gain and symmetric radiation patterns. The inclusion of these antennas in a metallic cavity gives them low back radiation and stable pattern beamwidth. Some examples are giving in [109, 14, 110, 111]. Figure 1.22 depicted the magneto-electric antenna investigated in [14]. The metallic cavity acts like the ground plane of the antenna. The main problem of these structures is the total size. Even if the cavity can make them more

and they have a low profile, the distance between the dipole and the reflector plane need to be at least quarter wavelength ($\lambda_0/4$), which makes them antennas of considerable size.

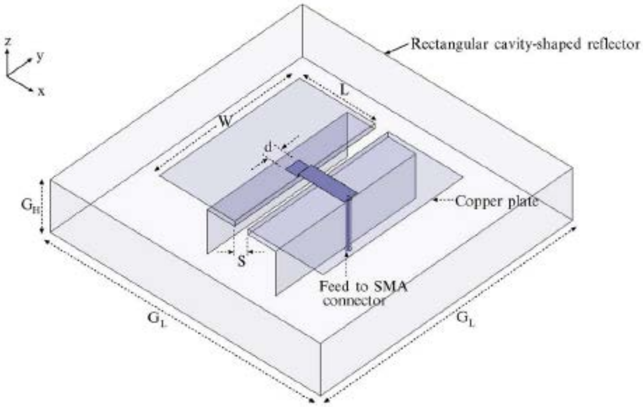

Figure 1.22: Geometry of a magneto-electric antenna in a cavity [14]

The utilization of parasitic patch is also a technique to improve cavity antennas performances. For example in [112] a microstrip antenna over a resonant cavity with a parasitic patch is developed for axial ratio enhancement.

1.4.1 Cavity modeling

Modeling of a small open ended cavity is shown in this section to analyze the theoretical behavior and limitations of a cavity. Following the works performed by Cohen [113] and Martinis [3] the transmission line model is used. The analysis with infinite and finite ground plane is exposed.

1.4.1.1 Rectangular cavity in an infinite ground plane

If we consider a rectangular cavity with dimensions $(a \times b \times h)$ inserted into an infinite ground plane and filled with an homogeneous material with permittivity ε_r and permeability equal to one ($\mu_r = 1$), as depicted in Figure 1.23. The cavity can be analyze like a waveguide, concretely an short-circuit waveguide open ended toward a half space. The transmission line model of this cavity consist of a short-circuit on one side and a load at the other side which corresponds to the cavity aperture.

For this analysis the dominant mode TE$_{10}$ is assumed. The propagation constant in a waveguide is given by

$$k_{TE}^2 = \varepsilon_r k^2 - k_c^2 \tag{1.42}$$

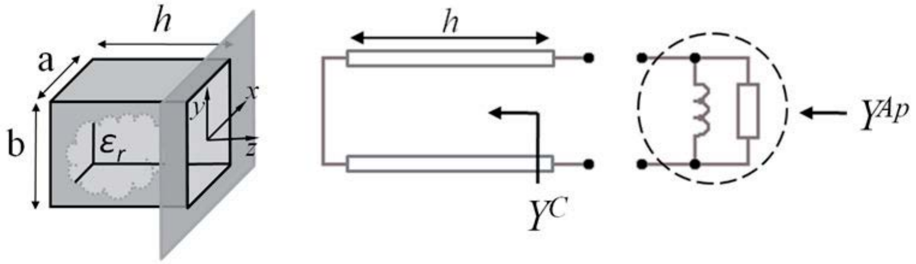

Figure 1.23: Square cavity modeling with an infinite ground plane and the transmission line model

where $k^2 = \omega^2\mu_0\epsilon_0$ is the wave-number and $k_c = \pi/a$ is the cutoff wave-number for the dominant mode. Considering $Y_{TE} = k_{TE}/\omega = k_{TE}/k\eta_0$ as the characteristic admittance for TE modes, the input admittance for a cavity is defined as follows

$$Y^C(k) = Y_{TE}\frac{Y_{TE} + jY_T \tan\left(k_{TE}h\right)}{Y_T + jY_{TE}\tan\left(k_{TE}h\right)} = -j\frac{k_{TE}}{k\eta_0}\cot\left(k_{TE}h\right) \tag{1.43}$$

where $Y_T = \infty$ is the short circuit admittance. As we can see in the plot Figure 1.24 representing the input admittance against cavity height for different values of relative permittivity ($\varepsilon_r = 3.66, 6.15, 10.2$), the input admittance if inductive (negative) for short cavities. The admittance crosses zero at a quarter of the guided wavelength inside the waveguide.

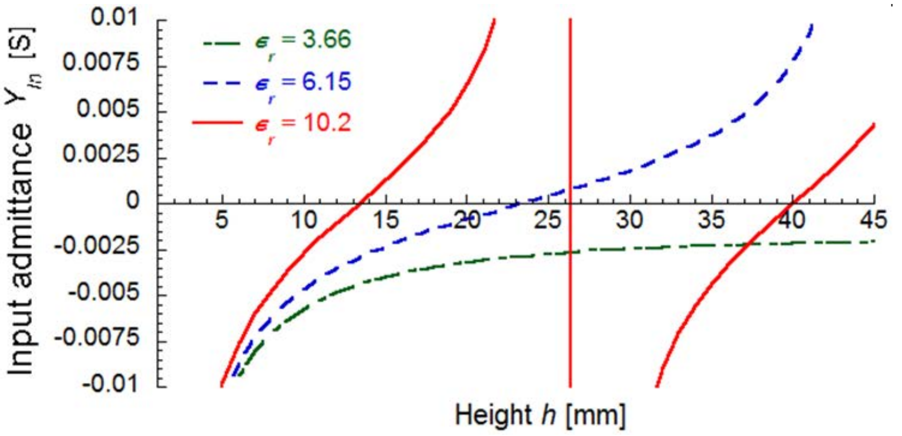

Figure 1.24: Input admittance against cavity height h for tree different values of permittivity in a square cavity filled with homogeneous material [3]

On the other side of the circuit, the open en of the structure is modeled by the aperture admittance Y^{AP}. The full calculation for the general mode TEmn using the spectral domain approach can be found in [3]. The result for the mode TE10 is given by (1.44).

$$Y^{AP}(k) = G^{AP} + jB^{AP} = \frac{ab}{8k\eta_0}\iint_{\mathbb{R}^2}\frac{k^2 - k_x^2}{\sqrt{k^2 - k_x^2 - k_y^2}}\left(\frac{cos\left(\frac{k_x a}{2}\right) sinc\left(\frac{k_y a}{2}\right)}{\left(\frac{\pi}{2}\right)^2 - \left(\frac{k_x a}{2}\right)^2}\right)dxdy \tag{1.44}$$

The equation (1.44) need to be solved numerically for each value of k. The results of equation (1.44) for a square cavity where $a = b$ was reported by Cohen in [113] in a Taylor series form as follows,

$$\begin{aligned} G^{AP}(x) &= g^0x^2 + g^1x^4 + g^2x^6 + ..., \\ B^{AP}(x) &= b^0x^{-1} + b^1x + b^2x^3 + ..., \end{aligned} \tag{1.45}$$

where $x = a/\lambda_0 = ka/2\pi$. Solving the equations for a square cavity, the figure shows the admittance of the aperture as a function of its size in wavelength. As in the previous case, the admittance is inductive (negative) in all cases when the size of the cavity is less than half a wavelength, that is, for small aperture cavities. An approximation for the series (1.45) taken from [3] is developed below.

$$\begin{aligned} G^{AP}(x) = {} & 0.0090x^2 - 0.01522x^4 + 0.01436x^6 - 0.00848x^8 + 0.00342x^{10} - \\ & -0.00101x^{12} + 0.00023x^{14} - 0.00004x^{16} \\ B^{AP}(x) = {} & -0.000809x^{-1} + 0.00537x + 0.01278x^3 - 0.01596x^5 + 0.01161x^7 + \\ & +0.00559x^9 - 0.00193x^{11} + 0.00049x^{13} + 0.0001x^{15} \end{aligned} \tag{1.46}$$

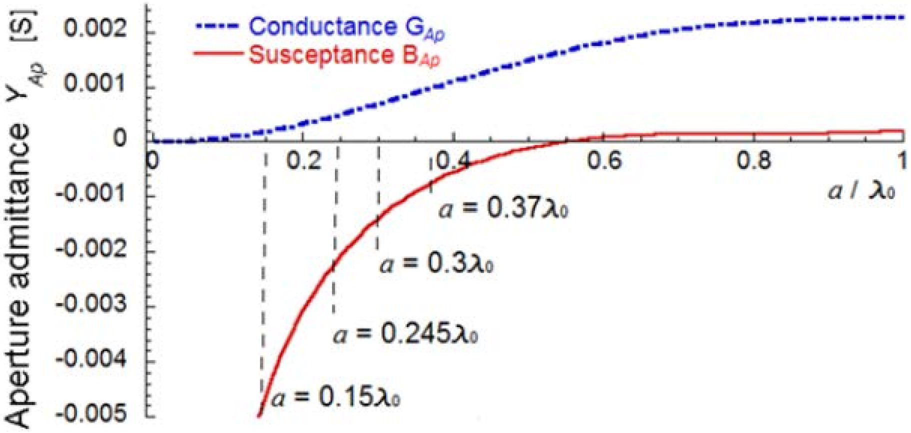

Figure 1.25: Real and imaginary part of aperture admittance against aperture dimensions in wavelength, from the polynomial approximation (1.46) [3]

The system presented in Figure 1.23 oscillates when the following equation is true,

$$jB^{AP}(k) - j\frac{k_{TE}}{k\eta_0}\cot(k_{TE}h) = 0 \tag{1.47}$$

where $B^{AP}(k)$ is the aperture susceptance, k_{TE} is calculated using (1.42), a is the side of a square aperture and h the cavity height. The two degrees of freedom of (1.47) are the permittivity ε_r and the cavity height h. Therefore, one can be treat as a function of the other to adjust them and achieve resonance.

If the resonant height is known, the Q factor can be calculated. The full Q factor calculation can be found in [3].

$$Q_{Ant} = \frac{\omega_0}{2G^{AP}(\omega_0)}\left|\frac{\partial Y(\omega)}{\partial \omega}\right|_{\omega=\omega_0} = \frac{k_{0r}}{2G^{AP}(k_{0r})}\left|\frac{\partial Y(k)}{\partial k}\right|_{k=k_{0r}} \tag{1.48}$$

where ω_0 is the resonant frequency, k_{0r} the resonant wave-number. The fractional bandwidth is calculated directly from the Q factor,

$$FBW = \frac{2\sqrt{\beta}}{Q} \tag{1.49}$$

where $\beta = \alpha/(1-\alpha)$ and $\alpha = |\Gamma_0(\omega)|^2$ being $\Gamma_0(\omega)$ the reflection coefficient.

Therefore, using the expressions (1.47), (1.48) and (1.49) the bandwidth of a cavity antenna can be predicted.

1.4.1.2 Rectangular cavity in a finite ground plane

The cavities with finite ground plane are of great interest for this work. This thesis is focused on the design of apertures surrounded by a narrow wall, which makes the ground plane not infinite. When it comes to small cavities, the aperture admittance changes due to the different boundary geometries. Because of that, analytical procedures to obtain the aperture admittance are extremely complex. However, there are electromagnetic simulation software that help for obtaining these results, for example CST Studio Suite [114] or HFSS [115]. CST has been chosen as the microwave simulator to perform the numerical results of this thesis work.

The steps to follow to design and simulate numerically a rectangular cavity in a finite ground plane are listed below:

1. A rectangular square metallic box is create in the free space with dimensions $(a+x) \times (b+x) \times (h+x)$,where x is the wall width.
2. Then, the aperture is created by inserting a vacuum box of the desired cavity dimensions, i.e. $(a \times b \times h)$ into the previous metallic element.
3. The cavity is excited by a waveguide port placed at the bottom of the cavity.
4. After fixing the frequency range, the simulation obtain the S11 parameter. To get the rest of the information

An example performed by [3] of simulation of a finite metallic cavity is presented in Figure 1.26.

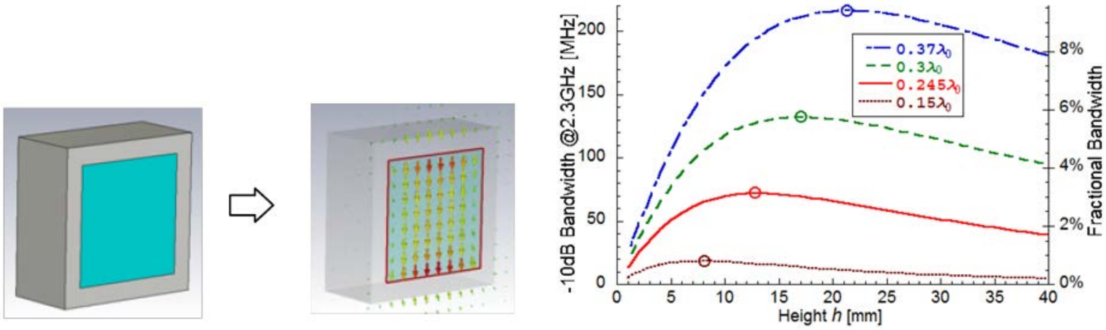

(a) (b)

Figure 1.26: (a) Simulation geometry design of a square cavity and E-field representation. (b) Bandwidth behavior of square cavity antenna for different aperture sizes. Example taken from [3]

Different excitation methods can be used to feed cavity antennas. A short dipole at the aperture of a cavity was used by Cohen in [113] for his experiments. He probed that a dipole much shorter than half wavelength can excite the fundamental mode. Others methods can be utilized to excite cavities, however, a patch antenna inside a cavity have a huge interest for this work. A special section dedicated to microstrip antennas in cavity is presented below.

1.4.2 Cavity-backed microstrip antennas

The integration of microstrip antennas into cavities does not only serve as an excitation method. The inclusion of patches in cavities also allows to solve some of microstrip antennas drawbacks. Some advantages, summarized in [26], are listed below:

- Bandwidth increasing through the use of a thick substrate
- Metal walls dodge surface waves modes supported by grounded dielectrics materials.
- Cavity make antenna more compact and rigid
- Isolation from surroundings
- Backward radiation reduction
- Suppression of scan-bandwidth trade-off for microstrip patch arrays

However, fabrication of cavity-backed patch antennas have some disadvantages despite the above-listed benefits.

- Limitations on efficiency and bandwidth
- Increase in manufacturing cost
- Complicated assembly of the structure comparing with a classic microstrip antenna
- Complex boundary conditions which entails complex analytical approaches
- If the cavity is too small, coupling problems may appears

Nevertheless, many advances have been made today to improve these inconveniences, like the use of substrate integrate (SIW) technology to reduce fabrication cost in cavity-backed antennas and arrays. An example of good performances, including bandwidth enhancement, using this technique for an array is presented in [116]

Zavosh and Aberle present various papers showing cavity-backed structures to improving microstrip-patch antennas. In [74] and [73] they demonstrate that a dielectric layer above the patch reduces the resonant frequency. This frequency shift is basically depending on the material and the height. However, they found a decrease on the impedance bandwidth that forces to look for an agreement between impedance and resonance shift. Singhai *et al.* demonstrate in [117] that by cavity backing a conventional microstrip antenna, the bandwidth increases many times.

1.4.2.1 Bandwidth behavior for microstrip antennas in cavity

To investigate the behavior of a cavity-backed patch antenna, Martinis, in [3] and [118] conducts a study based on a microstrip antenna square patch microstrip antenna backed in a square cavity. This study is performed for both finite and infinite cavities. The designs studied are presented in Figure 1.27, where Figure 1.27a and Figure 1.27c show the dimensions for the infinite ground plane; Figure 1.27b and Figure 1.27d for a finite ground plane on the aperture. The entire study is adapted to 2.3 GHz. Independent optimizations have been made for each variation in cavity height, each opening dimension and each permittivity value, following the rules listed below:

- Different aperture sizes (a): 20 mm (0.15 λ_0), 32 mm (0.245 λ_0), 40 mm (0.3 λ_0) and 48 mm (0.37 λ_0)
- Discrete increments of cavity height Δh =1 mm

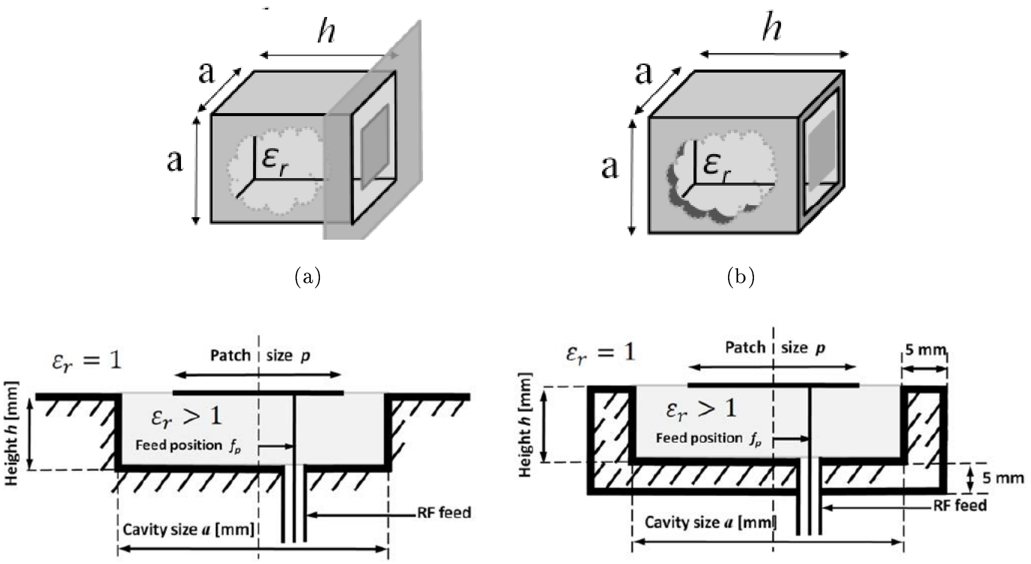

(a) (b)

(c) (d)

Figure 1.27: (a) Infinite ground plane cavity design. (b) Finite ground plane cavity design. (c) Schema of an infinite ground plane patch antenna. (d) Schema of a finite ground plane patch antenna [3]

- Values for permittivity corresponding to $\varepsilon_r = 3.66, 6.15, 10.2$; corresponding to available Roger materials
- Cavity walls of 5 mm
- Excitation with a coaxial cable at 50Ω characteristic impedance
- Best optimization values for patch length and feed point position

The following conclusions for bandwidth behavior have been drawn.

Influence of cavity aperture size

The different values for the aperture size show that the cavity motives a miniaturization of the antenna. This is because the antenna continues resonating even for the smallest cavities, where the size of the patch is restricted. In cases where almost the total aperture is taken up by the patch, the bandwidth is narrower. However, the aperture size allows a larger bandwidth because the antenna is bigger, but a exact relationship is not found.

As classic patch antennas, increasing the thickness of the substrate (cavity height) allows the antenna length to be reduced (aperture size).

Influence of cavity height

If the depth of the cavity increases, the cavity is transformed into a waveguide portion. This affects to the modes and the maximum bandwidth is achieved when $h \simeq \lambda_g/4$ (where λ_g is the guide wavelength), unless the waveguide is below cut-off.

Patch size decrease when cavity height increase, where it may be the case that the feeding point is place outside the patch. In that case the antenna is operating like a cavity antenna, unless the waveguide is below cut-off.

Influence of material permittivity
When the antenna operates in the above-mentioned waveguide mode, the permittivity of the substrate determines whether the waveguide is above or below cut-off. As a consequence, it determines if there is a maximum for the antenna height. Classic patch antennas have a inversely relationship between bandwidth and permittivity, larger bandwidth is achieved with lower permittivity. This relationship is also true for cavity antennas. However, for very small cavities $a \simeq 0.15\lambda_0$, the patch can cover the total aperture, which results in a bandwidth reduction. Therefore, if the permittivity is increased, the path dimensions is reduced, which increases the bandwidth.

Influence of ground plane
After studying the antenna with infinite and finite ground plane, it can be concluded that the finite ground plane offers larger bandwidth. This is because the infinite ground plane behaves as a barrier making the antenna only radiate in half-space. However, the finite ground plane allows the antenna to radiate into the whole space. This extra radiation increases radiation losses, hence increase the bandwidth.

Martinis also performs this study with similar conclusions for a circular cavity-backed microstrip patch antenna [15]. The design used for simulation is depicted in Figure 1.28.

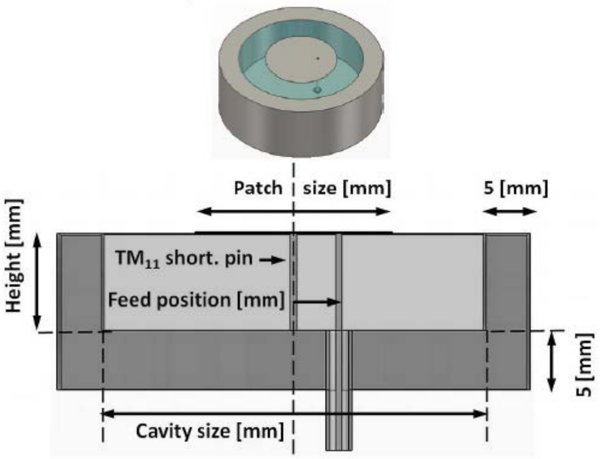

Figure 1.28: Design and dimensions of a circular patch antenna backed on a circular metallic cavity [15]

Throughout this section we determine that microstrip cavity-backed antennas have numerous advantages depending on applications. However, the narrow bandwidth limits the miniaturization of the antenna and the possible applications. New type of antennas based on metasurfaces may be very useful to circumvent this drawback. For that, metasurfaces are studied and presented below.

1.5 Metasurfaces for cavity antenna

Today, research on metasurfaces has taken quantum leaps due to its adaptability to work with electromagnetic waves in both microwaves and optical frequencies. The metasurfaces are generally composed of metallic patches with thickness less than the wavelength. The main advantages that make them very interesting are their light weight, easy manufacturing and the ease of controlling surface waves and free space waves. Metamaterials are used in various applications, such as antenna properties enhancement, absorbers, cloaking, among others. In this section various examples of metasurface applications will be presented.

1.5.1 General concepts

A metasurface can be defined as a metamaterial in two dimensions or as a planar version of it. But what is a metamaterial? Although this work is dedicated to metasurfaces, metamaterials are the basis of these types of surfaces. Therefore, this section is focused on metamaterials and their use in electromagnetism.

1.5.1.1 Definition of metamaterial

Metamaterial is an artificial material realized by inclusions periodically displaced, microscopically homogeneous, that exhibits anomalous electromagnetic properties that do not exist in nature. Metamaterials achieve electromagnetic (EM) performance beyond the limitation of the individual constituents [119]. Metamaterials are made from assemblies of multiple elements arranged in repeating patterns, at scales that they are smaller than the wavelengths of the phenomena they influence. Metamaterials are created by artificial inclusions that affect electromagnetic waves, inducing electrical and magnetic moments, which affects the permittivity and permeability. The creation of these inclusions gives the design more degrees of freedom, such as the properties of the main material, the size and shape of the inclusions, the density, the arrangement, etc [16]. A medium can be classified according to its permeability μ and permittivity ε as shown in Figure 1.29. If the permittivity and permeability are greater than zero ($\varepsilon > 0,\ \mu > 0$), the medium is called double positive (DPS), such as dielectric materials. On the contrary, if only permittivity is greater than zero ($\varepsilon > 0,\ \mu < 0$), it is a mu-negative material (MNG). This characteristic is possessed by some gyrotropic materials for certain frequency bands. A medium with negative permittivity and positive permeability ($\varepsilon < 0,\ \mu > 0$) is designated an epsilon-negative medium (ENG). Many plasmas have this property for certain frequencies. Finally, a double-negative medium (DNG) has both permittivity and permeability smaller than zero ($\varepsilon < 0,\ \mu < 0$). These materials can only be obtained artificially: metamaterials.

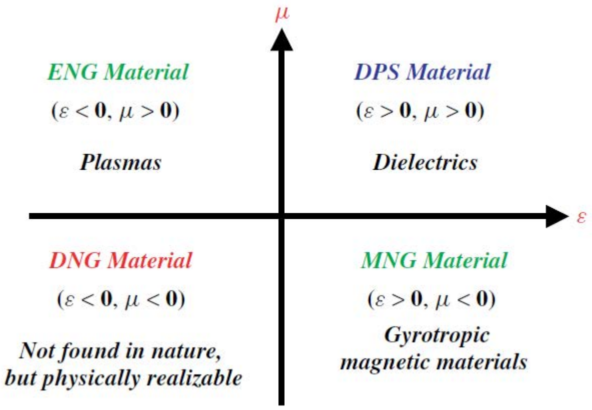

Figure 1.29: Material classification depending on the permittivity and permeability [16]

The first left-handed metamaterial (LHM, terminology also used to name the first DNG materials) was predicted in [120] and demonstrated and reported more than 30 years later in [17]. They created a negative-refractive-index medium to experimentally demonstrate negative refraction. The metamaterial consists of a 2D array of copper strips and split ring resonators, depicted in Figure 1.30. By irradiating with a microwave beam thought the medium, the scattering angle and the effective index of refraction n were determined, appropriate to Snell's law. This index was negative and confirm the predictions of Maxwell's equations that n is given by the negative square root of $\varepsilon \cdot \mu$ for the frequencies where permittivity and permeability are negative [17].

Figure 1.30: Wire-SRR metamaterial to verify negative refraction[17]

1.5.1.2 Metamaterials for antennas

The use of metamaterials for small antennas brings benefits to the antenna performances. One of the advantages of using metamaterials in antennas is miniaturization and bandwidth enhancement. Metamaterials for antennas are designed to control the dispersion relation on the near-field boundary conditions. This may result in antenna size reduction maintaining good radiation results. Metamaterials can overcome bandwidth and efficiency limitations of small antennas, as mentioned in subsection 1.3.2.

Metamaterial-based antennas can be classifies in the four following categories according to [121]:

- *CRLH-based (Composite Right/Left Handed)*: These antennas are based on CRLH transmission line, which can be applied to generate dominant modes. This method possesses characteristics of low insertion loss, broad bandwidth, and low profile, which are interesting for antenna application. Antennas with negative-order modes and zeroth-order resonators are in this group [122, 123].
- *Metamaterial loading*: [124, 125, 126] are some examples of metamaterial loading antennas. This category includes antennas loaded by negative permeability and permittivity materials, as mentioned above. Magnetic photonic crystals or high permeability shells are also included on it.
- *Antennas loaded with metasurfaces*: Due to the capacity of miniaturization and bandwidth enhancement, this technique is chose for the present thesis work, and therefore, they have this dedicated section, where a large number of examples are exposed. Electromagnetic Band Gap (EBG) as mushroom structures, or patch-based Reactive Impedance Surfaces (RIS) [127], among others, are part of this category. Metasurfaces are further described below.
- *Metaresonator antennas*: These antennas are based on the split-ring resonators or the complementary version of it. Some examples found in the literature are [128, 129, 130].

1.5.2 Metasurfaces for antennas

Metasurfaces have a big interest in research community due to the large number of benefits they provides to antennas and microwave circuits. In [131] can be found a review on MTS with a set of more than 200 references that proves the relevance of the subject in recent years.

1.5.2.1 Presentation

MTS are generally composed by a periodic 2D structure of metallic patches or printed dielectrics, in planar or multi-layer configurations. They are common name as High Impedance Surfaces (HIS) or Artificial Magnetic Conductors (AMC). As metamaterials, metasurfaces have a sub-wavelength thickness. MTS are divided in two main groups: EBG and RIS. Band gap structures were introduced by Sievenpiper in his PhD thesis [132] and are composed of a mushroom periodic structure with metallic patches as depicted in Figure 1.31a. The concept of RIS was introduced in [19]. A reactive impedance surface is composed only of periodic metallic patches, as shown in Figure 1.31b. The biggest difference between the two is the absence of vias in the case of RIS. The mushroom structure presents high surface impedance for both normally indicent and surface waves at the same frequency band. The type of surface chosen depending on the application of the antenna.

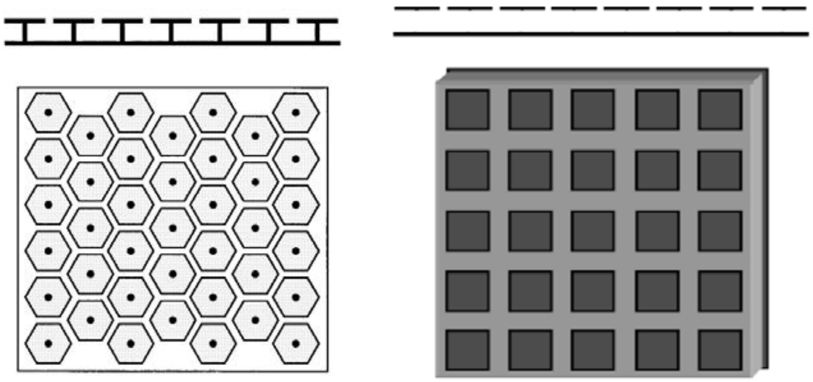

(a) (b)

Figure 1.31: (a) High impedance surface EBG mushroom-type ground plane. Cross section and top view [18]. (b) RIS type ground plane. Cross section and top view [19]

In general, the use of metasurfaces in antenna applications offers the following benefits:

- Light weight and ease of fabrication.
- They can blocking, absorbing, concentrating, dispersing and guiding waves both on the surface at grazing incidence and in space at normal and oblique incidence, from microwave through visible frequencies [30].
- Metasurfaces are very versatile. They can be tuned at any point between the electrical surface (PEC) and the magnetic surface (PMC) to obtain the optimal bandwidth and a good miniaturization factor.
- Reactive impedance surfaces have the capacity of store energy (magnetic or electric) which can be used to compensate near-field energy of the radiating structure. This ability results in a size reduction.
- A metasurface provides a total reflection of power resulting in a front-to-back ratio enhancement.
- In metasurfaces the mutual coupling between the antenna and the substrate is reduced, which causes an impedance bandwidth enhancement.

- The band-gap structures can be used as a high impedance ground plane to enhance radiation performances, such as gain, patterns, side-lobes, among others.

An example of GPS antenna using EGB technology compared with a conventional choke ring approach is depicted in figure 1.32. Choke rings antenna provide excellent performances for GPS, such as axial ratio and phase center stability. However this antenna is large, heavy and expensive. The EGB solution uses printed circuit technology, improving dimensions, weight, and manufacturing cost [20].

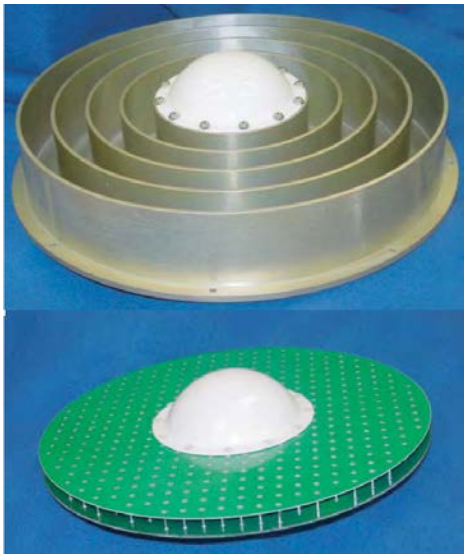

Figure 1.32: Example of GPS antenna made with EBG technology (bottom) in comparison to conventional choke ring approach (top) [20, 16]

1.5.2.2 Metasurfaces for antenna miniaturization and bandwidth enhancement

Mosallaei and Sarabandi conducted a study on bandwidth improvement and miniaturization in their publication on reactive impedance surfaces [19]. They compared a patch placed over a PEC surface and a patch over a RIS, as depicts in Figure 1.33. The patches and ground planes had the same size. To achieve the same resonance in both cases they varied the permittivity of the substrate for the PEC version. The results obtained for the classical structure were bandwidth equal to 0.6% and efficiency of 70%, while the RIS-based structure resulted on bandwidth 6.7% and efficiency 90%. This results demonstrates that a patch over a RIS ground can be miniaturized if it were placed over the same substrate as the classic patch case. RIS can store magnetic energy to compensate near-field electric energy of the radiating patch, wich helps for antenna miniaturization.

As the results shown, bandwidth for RIS is 8 times larger than for the conventional patch antenna. This is because RIS spatially distributes the metallic pieces on the ground plan, which contributes reducing the mutual coupling between antenna and radiator, allowing a wider bandwidth.

1.5.3 Metasurfaces in cavity

Resonator cavities and the effect of backing a patch antenna into a cavity aperture have already been exposed. What is the interest of embedding a metasurfaces in a cavity?

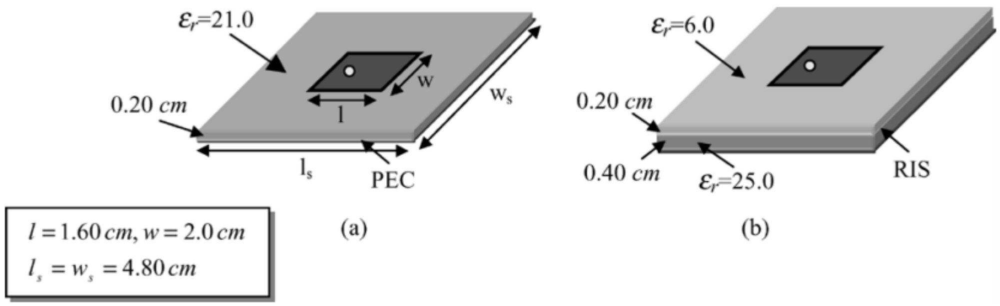

Figure 1.33: (a) Patch antenna over a conventional substrate (b) Patch antenna over a RIS substrate formed by a 4x4 array printed on a dielectric material [19]

It has been seen in previous sections that the problem of bordering a patch antenna with a metallic wall (cavity), causes a deterioration of the bandwidth (especially for small cavity size), as Martinis [3] represents in the graph of Figure 1.34.

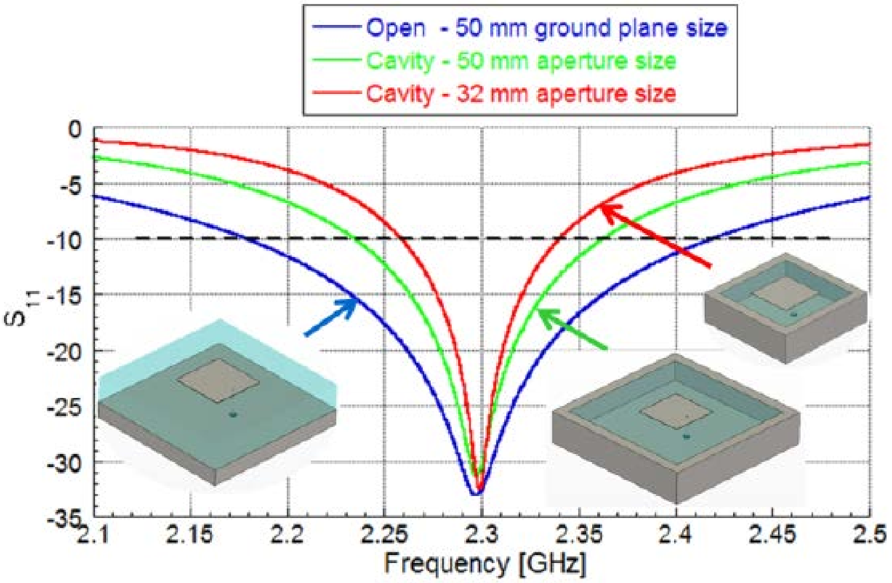

Figure 1.34: Bandwidth reduction due to cavity enclosure patch antennas

Martinis also studies theoretically, numerically and experimentally that a small cavity patch antenna does not reach the maximum bandwidth limits, which can be assessed by the method proposed by Gustafsson *et al.* in [133]. A new type of antennas that could be closer to the predicted maximum bandwidth needed to be proposed. The model for a simple cavity was modified with the addition of a parasitic capacitive reactance at the aperture. With this modification, analytically the maximum predicted bandwidth is reached. As shown above, metasurfaces have the characteristic of increasing bandwidth. Therefore, metasurfaces are a good candidate to solve bandwidth issues for antenna cavity.

The circuit model of an antenna that can reach the maximum expected bandwidth is presented in

Figure 1.35. Comparing with the model of a single cavity presented in subsection 1.4.1, a capacitor has been added. In this case, the condition of resonance is,

$$jB_{AP}(k) - j\frac{k_{TE}}{k\eta_0}\cot\left(k_{TE}h\right) + jc_0kC = 0 \tag{1.50}$$

where k is the wavenumber and c_0 is the speed of light in vacuum. Fixing the permittivity ε_r to a known value, the capacitance C may be considered like a function of cavity height h. Martinis concludes that for any value of h the maximum optimal results will be obtained for a cavity filled with air, i.e. $\varepsilon_r = 1$.

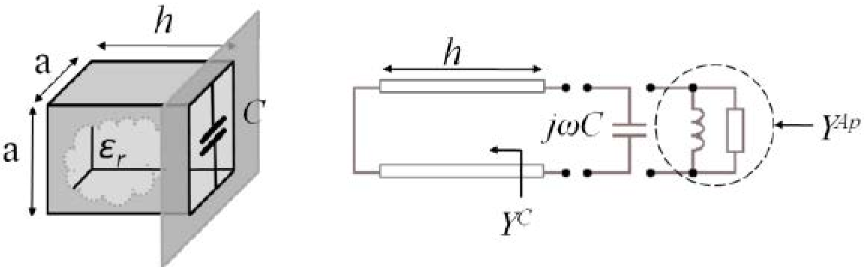

Figure 1.35: Cavity-backed antenna with a parasitic capacitance in the aperture and the corresponding transmission line model [21]

How is the capacitance C obtained at the opening of the cavity? Arranging several small parts instead of a large one produces a decrease in inductance, which makes the desired capacitance more pure, with no real part. The process of "cutting" the patch is illustrated in Figure 1.36.

This study determined that elements smaller than $\lambda_0/13$ are needed to properly approximate a capacitance in the aperture of a cavity. The criteria of the metamaterials establishes that the size of the elements must be less than $\lambda_0/10$. Therefore, this structure can be considered a metasurface. It should be noted that the directivity and gain of this type of antennas is similar to the one of a classic patch antenna. The design of this structure will be better detailed and analyzed in Chapter 2.

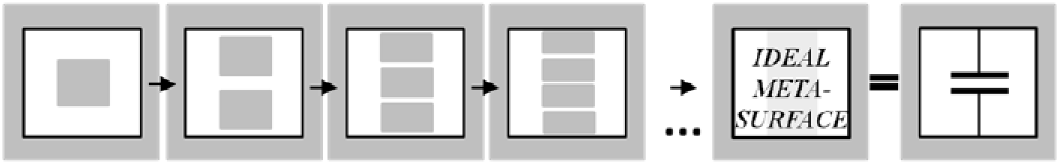

Figure 1.36: Evolution from a microstrip patch antenna into a metasurface antenna in cavity [3]

1.5.4 Other applications with metasurfaces

Aside from the advantages of its use in antennas, metasurfaces can be used in a plethora of applications in electromagnetism, like perfect absorbers, lenses, cloaking, scattering reduction or energy harvesting. Below are briefly exposed some of the most widely researches today.

Absorbers

Absorbers and reflectors have been heavily investigated since it was shown that a device was capable of absorbing electromagnetic waves. The search for the perfect absorber is based on independent polarization and independent angle of incidence at a large frequency range. Classic absorbers [134, 135] have the advantage of being wide bands. However, they are massive because of their one-quarter-wavelength thickness, and usually composed of lossy materials. Today, more compact and lightweight elements are sought. The interesting characteristics of metasurfaces make them attractive for the conception of absorbers. Metasurface-based absorbers may increase the electric field on the surface and, as a consequence, finer absorbers can be designed. Research about absorbers has a big interest for THz and optical applications, as bolometers, infrared detectors, plasmonic sensor, etc [136, 137, 138, 139].

Modulators and polarizers

An advantage of metasurfaces is the possibility of manipulating amplitude, phase and polarization response over wavelength scales due to the ease of controlling both the electric and magnetic fields. Polarizers are mainly based on the control of the electrical response. However, controlling in addition the magnetic variation can improve the devices. Although the modulators and polarizers manufactured today are robust enough for current technology but research is focused on their use in THz regime.

[140] and [141] are some examples of metasurface inspired modulators. The first is based on a metasurface formed by periodic split ring resonators and the second one uses a doped graphene layer, which is a topic of great interest in research.

Metasurface lenses

Lens antennas are antennas that are designed using lenses. These types of antennas were interesting in research but the technology advancement became them too massive and expensive to manufacture for low frequencies. The arrival of the metasurfaces allows the creation of cheaper and low-profile lens antennas. The interest in metasurfaces lenses came due to their negative index materials. This property allows focusing light even without curved lenses, which solves the problem of spherical aberrations.

A popular metasurface lens design is the bases on gradual variations of patches size. The example of Figure 1.37 presents the gradual reduction of circular patches where the variation of the radii controls the surface impedance. Others patch shapes than circles are also used to create surfaces with spatial variation of refractive indices [142].

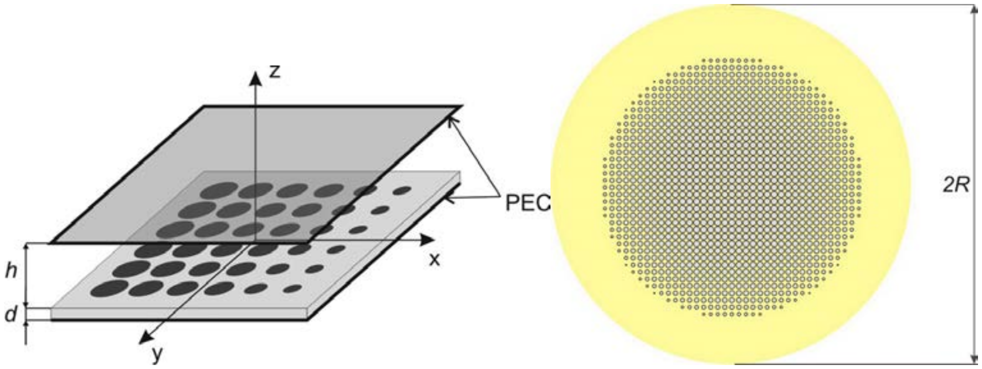

Figure 1.37: Gradually-varying circular patches with the surface impedance profile corresponding to the Luneburg lens [13]

1.6 Antenna array

An array of antennas is defined as a regrouping of several elementary sources, generally identical. The union of these devices allows to combine their radiation capabilities to increase the gain in a particular direction according to the principle of superposition. Because of its versatility, arrays are used to obtain results than can not be achieved with a single element. One of the most important applications of antenna arrays is in mobile phone base stations. In these cases the beamwidth in the vertical plane (typically between 6° - 7°) is given by the array structure, while the beamwidth in the horizontal plane (65° or 90°) is fixed by the radiating element. However, there are applications in which electrically-large antennas are grouped, such as the huge interferometry radio telescopes formed by large reflective antennas, which achieve extremely narrow beams. Arrays are also used for space applications or radars. In general, the main advantage compared to reflective antennas is that they allow electronic beam orientation. By contrast, the main disadvantage is the higher manufacturing cost. Microstrip patch antennas [143, 144], dipoles [145, 146], monopoles [147, 148] or helix antennas [149, 150] are some of the most common elements in arrays.

Most of the arrays can be divided in two groups based on how the elements axis is related to the direction of radiation.

- When the main lobe is perpendicular to the plane where the antennas are placed is called broadside array. To achieve perpendicular radiation, the antennas have to be fed in phase.
- On the contrary, if the radiation direction is along the antenna line, it is called endfire array. It is a linear array in which the elements must be fed with a phase shift equal to the separation of adjacent antennas.

However, there are other types of arrays, such as phased arrays, where the radiation direction has an angle other than those mentioned above.

Ideally, an antenna belonging to an array should work in the same way as if considered as a single element. The intrinsic properties of each element are modified by the neighbor antennas and a coupling is created between them. This coupling depends on the shape, the layout and the distance between elements. This phenomenon causes the deformation of the radiation pattern and the antenna mismatch.

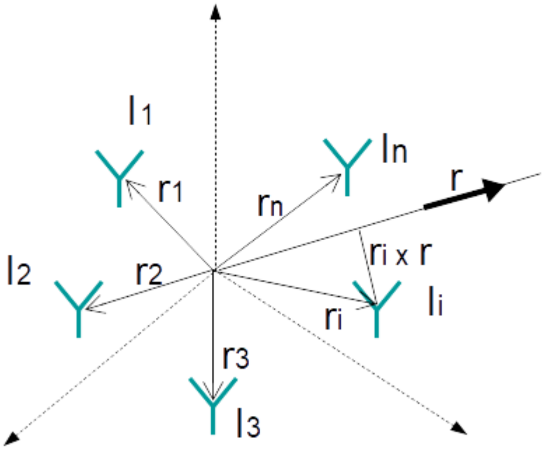

Figure 1.38: Array general configuration

1.6.1 Radiation of arrays

1.6.1.1 Array with identical antennas

Thus, considering an array with identical elements, five main parameters control the performances of the array: the geometrical configuration of the set, the distance between elements, and amplitude, phase and pattern of the unit element.

As mentioned above, the total array radiation is inferred from the radiation of each cell by applying the principle of superposition. If all sources are considered equal and oriented in the same way, that calculation is simplified using the array factor (AF). The AF is the complex-valued radiation pattern obtain of an array made up of isotropic elements. Since the radiation patterns of each element of the network are identical and the cells are oriented in the same spatial direction, the array radiation pattern can be obtained by multiplying the AF by the radiation pattern of a single element. Figure 1.38 shows an array of identical antennas where each element i is pointed by the position vector $\overrightarrow{r_i}$. The radiated field is obtain from Equation (1.51).

$$\overrightarrow{E_i}\left(r,\theta,\phi\right)=\overrightarrow{E_e}\left(r,\theta,\phi\right)\frac{I_i}{I_o}e^{jk_0 r\hat{\overrightarrow{r_i}}} \tag{1.51}$$

where $\overrightarrow{E_e}$ is the radiation of the reference unit cell. If in Equation (1.52), $\overrightarrow{E_e}$ is taken as a common factor, the results is the product of $\overrightarrow{E_e}$ by a summation. This summation that includes the position and feeding effects of the whole set, is the array factor Equation (1.53). The AF depends on the directions θ and ϕ, and on the frequency given by the propagation constant or wave-number, k_0.

$$\overrightarrow{E_i}\left(r,\theta,\phi\right)=\sum\overrightarrow{E_{ii}}=\overrightarrow{E_e}\left(r,\theta,\phi\right)\sum_i\frac{I_i}{I_o}e^{jk_0 r\hat{\overrightarrow{r_i}}}=\overrightarrow{E_e}\left(r,\theta,\phi\right)AF(\theta,\phi) \tag{1.52}$$

where

$$AF(\theta,\phi)=\sum_i\frac{I_i}{I_o}e^{jk_0 r\hat{\overrightarrow{r_i}}} \tag{1.53}$$

This property is called principle of pattern multiplication. It permits to analyze how radiating element and array geometry influences are independent. The total radiation pattern of the field (modulus of the radiated field) is the product of the radiation pattern of a single element by the modulus of the AF. Likewise, the polarization of the total radiated field depends only on the radiating element used, because the AF is a scalar. In large arrays, the AF may vary faster than the single element pattern for certain planes. Because of this, the AF can be considered as the total pattern of the array for these planes.

1.6.1.2 Array with complex geometry

For the complex geometries the general array configuration is considered, Figure 1.39 [22]. The total field of the array is given by Equation (1.54) regardless of the position of the elements.

$$E\left(\theta,\phi\right)=\sum_i\sum_n\frac{I_{i,n}}{I_o}E_{i,n}\left(r,\theta,\phi\right)e^{jk_0 r\hat{\overrightarrow{r_{i,n}}}} \tag{1.54}$$

where n represents the number of elements and i the number of stages in the array. In that way, $\frac{I_{i,n}}{I_o}$ is the amplitude apply to the nth element at the ith stage, and $E_{i,n}\left(r,\theta,\phi\right)$ is the radiation pattern of the reference element, that is the nith element.

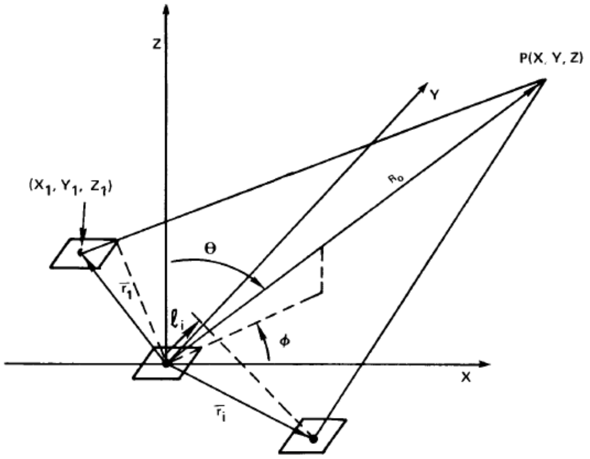

Figure 1.39: General array configuration [22]

1.6.2 Array for GNSS and anti-jamming solutions

Arrays to solve GNSS problems are constantly growing. The accuracy enhancement and characteristics of GNSS systems demands the development of new technologies. The current dependence on GNSS systems, makes them critical target of electronic warfare. Because of this, one of the main lines of action today is to develop anti-jamming devices. Jamming is the transmission of signals deliberately to alter or cancel the transmission over another signal. An adversary may use several jammers over a part or entire GNSS system to create chaos in critical infrastructures. For the military, a jammed GNSS signal can have serious repercussions and conventional nulling antennas are unreasonably large for many military and aviation applications. This problem can be solved by using antenna arrays that employ space-time or space-frequency adaptive processing. Arrays can be controlled to activate or deactivate certain elements to created nulls in the interference directions while it keeps emitting in the rest of them.

1.6.2.1 Planar array (CRPA)

Arrays can also be classified according to the way in which their elements are arranged. Therefore, a planar array is a flat two-dimensional array where the element are distributed in a plane. This plane has different shapes as circular, rectangular, triangular, etc. Planar arrays can be created with different types of antennas, such as reflective arrays, curtain array or microstrip antenna array, the most used today. Some examples of GNSS arrays over a square planes are given in [151, 152]. However, the most chosen configuration for GNSS applications due to its characteristics is the circular one. Figure 1.40 shows an example of array forming a circular plane. This configuration is extensively used for many applications, such as anti-jamming [153, 154], mutual coupling reduction [155], radiation pattern enhancement [62], among other.

Taking into account the GNSS application of arrays, it is worth mentioning the Planar-Controlled Reception Pattern Antenna (CRPA) arrays. They are very effective in mitigation the interference problem by spatially filtering the desired signal based on an adaptive algorithm. Thus, their radiation pattern is adapted to place nulls in the direction of the incident interfering plane waves [23].

Volakis *et al.* gather in [156] different miniaturized adaptive planar arrays for GNSS whose provide jamming rejection capabilities.

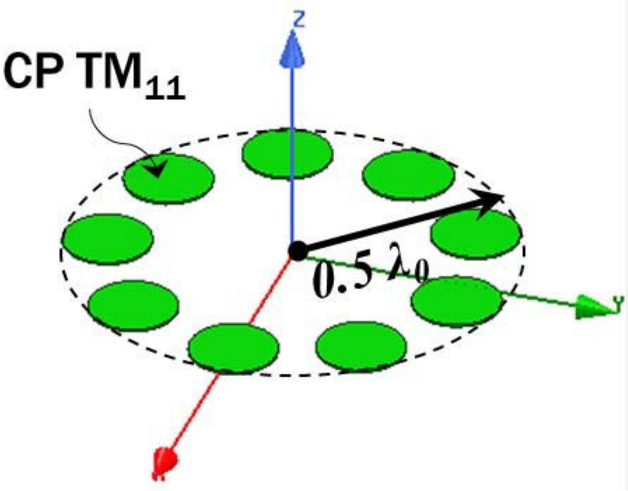

Figure 1.40: Planar array forming a circular surface [23]

1.6.2.2 Conformal array

Many times, the form and application of the carrier require the use of a conformal array. This type of array is a three-dimensional array which is conform to some curved surface. The antennas are placed over a volume, as a semi-sphere, cone or cylinder.

For example, in [157], an array conformed around a revolving cylinder is presented. These types of arrays are often integrated into the curving skin of aircraft and missiles, to reduce aerodynamic drag. Other example of this type of arrays is given in [158]. Yinusa *et al.* present a conformal array consists of 7 elements which are arranged on a half sphere. A stable gain and axial ratio performance over the whole upper hemisphere is achieved with this geometry.

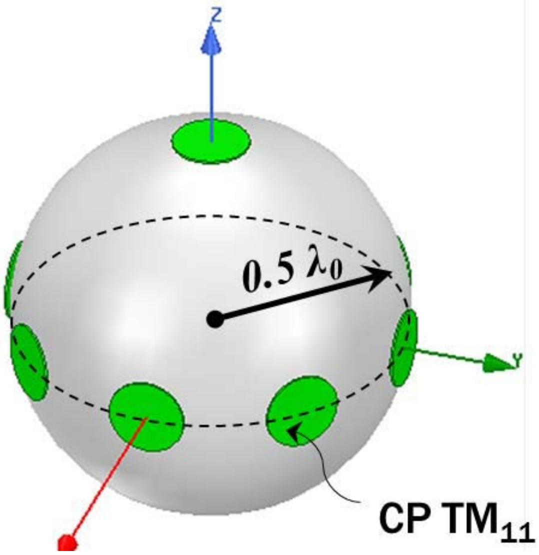

Figure 1.41: Conformal array [23]

1.6.3 Mutual coupling in arrays

Along the subsection 1.2.4 about multiport antennas, we concluded that the performance of an antenna depends not only on the current of a port but also on the current of the neighboring ports. Similarly in arrays when the antennas are near each other, the performances of the single element depends also on the neighboring elements. This effect is called mutual coupling. The amount of energy that ends up at the other port depends on three parameters: the radiation characteristics of each antenna, the relative separation between them and the relative orientation of the elements [5]. This interchange of energy is sometimes difficult to predict analytically but it is important to take into account. Scattering parameters instead of mutual impedance is used to research the mutual coupling effect between array elements. Similarly to TARC exposed in the previous section, in this case the ARC (Active Reflection Coefficient) is used to calculate the ratio of forward to back waves from each antenna [159].

$$\mathit{\Gamma}_a = \sum_n S_{_{1n}} \left(\frac{E_n}{E_1} \right) \tag{1.55}$$

where E_0 is the incident wave on the transmission line going to the nth element and $S_{_{0n}}$ is the coupling between the referent and the nth element.

Considering an identical elements array with equal distance d, the ARC at any element is the summation of its passive mismatch (S_{11}) plus the product of each element drive E_n normalized and multiplied by the mutual coupling coefficient S_{1n}. Vulgarizing, the ARC of an array may be defined as the linear superposition of passive reflection coefficient S_{11} of the elements and the mutual coupling S_{12} from the adjacent elements.

Even if it is important to take into account carefully the effect of both coupling between elements and coupling between ports (in multiport antenna cases), this can be used advantageously. In [160], Wang *et al.* utilize mutual coupling to obtain bandwidth enhancement. Instead of focusing the bandwidth optimization on mutual impedance analysis, the optimization has been guided by the ARC. This theoretical analysis demonstrates that the bandwidth enhancement of the whole array set can be obtained when the passive S_{11} of the element and the mutual coupling S_{12} are well canceled.

1.7 Conclusion

This chapter gathers the theoretical basis essential for the development of this thesis work, including Global Navigation Satellite Systems (GNSS), microstrip antennas, cavity antennas, metasurfaces and multiband antennas.

The properties of geolocation systems have been presented in this chapter. Understanding the properties of the navigation systems allow the proper conception of antennas adapted to GNSS applications. Also, a brief compilation of the state of the art on the antennas used for GNSS applications has been shown.

Microstrip antennas presents an interesting solution for antenna miniaturization and cost reduction. However, the confinement of a microstrip antenna into a cavity has drawbacks, such as bandwidth reduction. The use of metasurfaces may enhance the bandwidth when the printed antenna is located at the aperture of a cavity. Microstrip antennas, cavity antennas and metasurface antennas are the three main axes of this research. The low cost and compactness of microstrip antennas, the miniaturization offered by the use of metasurfaces, and the isolation and robustness of the integration into cavities, make their combination an interesting subject of study.

Other applications such as multiband antennas or antenna arrays have been treated.

Chapter 2

Linearly-polarized antennas for GNSS

The advantages and disadvantages of microstrip, metasurface and cavity antennas have been explained and discussed during the state-of-the-art (Chapter 1). The purpose of the present chapter is to introduce some examples of antennas that can satisfy the particular case of this study. Recalling the objectives to achieve, the conception of an antenna able to cover at least three GNSS bands is demanded. However, due to its subsequent integration into a projectile, the insertion of the antenna into a metal cavity is required. This cavity has to be as small as possible because the diameter of the carrier is fixed to 155 mm. Taking into account the curvature of the metal cylindrical carrier, the dimensions of the cavity are limited to $50 \times 50 \times 20$ $(a \times a \times h)$ mm^3, where a is the dimension of the aperture and h the height of the cavity (Figure 2.1). As shown in Figure 1.2, to cover the bands GPS L1, Galileo E1 and Glonass G1 an antenna with a bandwidth of at least 60 MHz is necessary (theoretically 51 MHz plus a small margin band). The central frequency is considered at 1.578 GHz. Microstrip antennas, metasurfaces and cavity-backed antennas are mixed with the aim to designing a metasurface-inspired cavity-backed microstrip antennas in linear polarization.

Firstly, cavity antennas formed by a single square patch (section 2.1) and stacked patches (section 2.2) are exposed. These two sections are intended to determine the limits of these microstrip designs and why they will be discarded for the purposes of this work.

Then, section 2.3 discusses about the use of metasurfaces in lineal polarization to confront the problem stated above. Two different antennas are designed and manufactured throughout this section. The first antenna has maximum aperture dimensions of 50×50 mm^2. A miniaturization will be carried out for the second one, which has a rectangular shape with aperture dimensions 40×45 mm^2. In the mentioned section are presented the design process and the simulation results for this category of antennas. Both structures are manufactured and measured. The manufacturing process of the prototypes is developed in section 2.4. Then, section 2.5 exposes the experimental results obtained for both prototypes compared to the numerical results. Finally, the integration of the antenna into the carrier is study in section 2.6. In this last section, a brief analysis that studies the influence of a radome on the antenna performances is carried out.

2.1 Single square patch in cavity

The simplest case of a microstrip antenna is a single square patch. In this section, a single patch microstrip antenna embedded in a metal cavity is studied. The goal of this study is to verity if it is possible to reach a bandwidth of 60 MHz using a single patch antenna integrated in a $50 \times 50 \times 20$ mm^3 metal cavity. If the central frequency is considered at 1.578 GHz, the dimensions in wavelength are $0.26\lambda_0 \times 0.26\lambda_0 \times 0.11\lambda_0$ mm^3. In a second term, the dimensions of the aperture will be modified to find the smallest size for a 60MHz-bandwidth antenna.

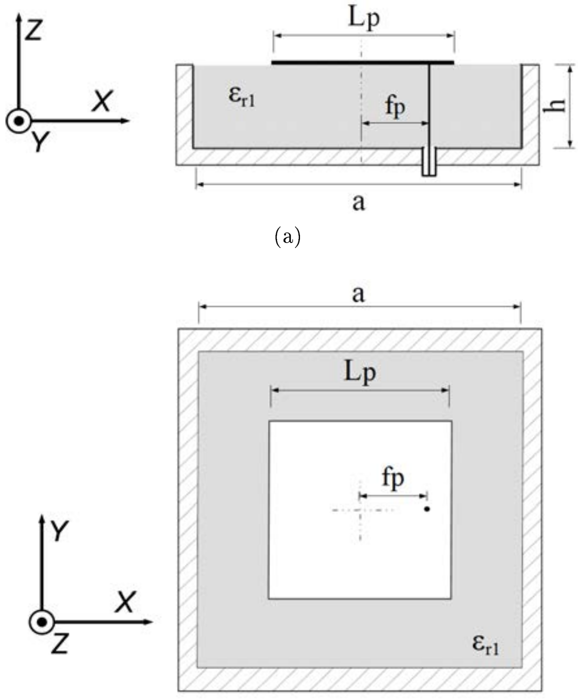

(a)

(b)

Figure 2.1: Schematic of a cavity-backed single patch microstrip antenna. (a) Cross-section view. (b) Top view

2.1.1 Antenna description

The design, schematized in Figure 2.1, consists of a finite metal cavity with 5 mm wall thickness, depth set at h =20 mm and square aperture size of $a \times a\ mm^2$. The cavity acts as the ground plane and it is filled with a high permittivity dielectrics material (ε_{r1}). The square patch of dimensions $L_p \times L_p\ mm^2$ is made of a PEC material and it is printed on the top of the dielectrics. The patch radiates in vertical direction (z-axis). The antenna is fed through a coaxial probe. The coaxial cable inner conductor of diameter 0.5 mm is connected directly to the radiator at a distance f_p from the center of the patch. This inner cylinder is covered by a Teflon® ($\varepsilon_{r_{teflon}} = 2.1$) coating of diameter 1.7 mm and an outer metal sheet of 2.2 mm. These dimensions allow to have a characteristic impedance of 50Ω in the port.

2.1.2 Simulation results and parametric study

The study with the single patch starts from the following premises:

- The depth of the cavity is fixed to 20 mm. It is easier to obtain better bandwidth when the substrate thickness is larger. However, the cavity depth is set at 20 mm to match with the above-mentioned requirements.

- The desired match frequency is 1.578 GHz to cover all three bands with a 60 MHz-bandwidth antenna.
- The chosen dielectrics substrate is a Roger material [31] with permittivity $\varepsilon_{r1} = 3.66$, to make it possible to obtain a patch that fits the aperture. With the aim of simplifying the study, a known material with low permittivity available in the laboratory is chosen.
- Variations on the patch size and feed position are performed to well match the antenna.

To match the antenna to the resonant frequency, the following parameters are modified: the distance of the feeding point from the center of the antenna (f_p) and the length of the patch (L_p). The position of the feeding point determines the adaptation level of the reflection coefficient as represented in Figure 2.2a. Furthermore, the variation of the patch dimension will allow a frequency shift, as shown in Figure 2.2b.

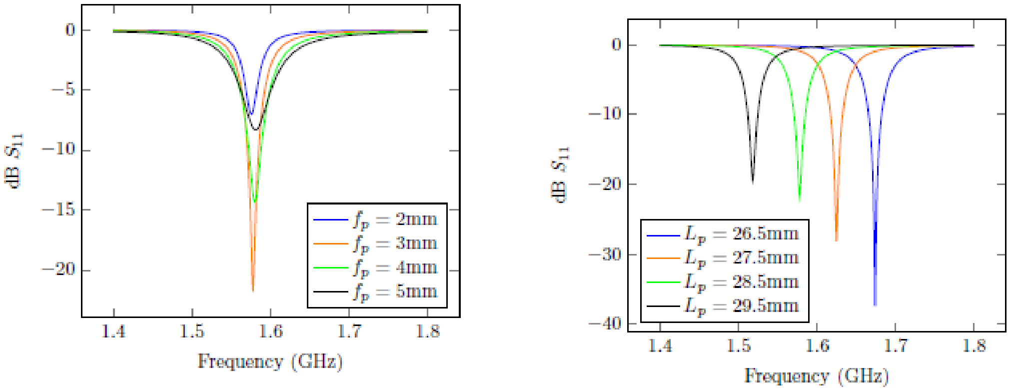

(a) Effect of f_p on resonance frequency

(b) Effect of L_p on the resonance frequency

Figure 2.2: Parametric study for a single patch antenna in cavity

Although the height of the substrate (cavity depth) has been set to 20 mm for this study, Table 2.1 shows that as the thickness of the substrate increases, the bandwidth increases. However, with a cavity depth of 20 mm, the bandwidth needed is clearly not reached.

h (mm)	L_p (mm)	f_p (mm)	BW (MHz)
2.54	28.8	2.5	8
5.08	27.6	3.5	12.6
7.62	26.4	3	18.7
10.16	25	3.7	23.1
15	22	5	30
20	18.4	6	31

Table 2.1: Bandwidth achieved for different cavity height when the aperture size is fixed to 40 mm

2.1.3 Discussion

It has been demonstrated that it is not possible to obtain the above-mentioned requirements with a standard patch antenna due to the effect of the cavity: cavities reduce antenna bandwidth. Another option to achieve the desired bandwidth consists in using stacked patches. The behavior of a stacked-patches configuration in cavity is studied in next section.

2.2 Stacked patch in cavity

Microstrip antennas composed of stacked patches is a widely used configuration for bandwidth improvement when increasing dielectric thickness is not an option. The principle of this configuration is to create two resonances close to each other. This fact causes both to merge and create a larger bandwidth. Long shows in [47] an example of bandwidth improvement using stacked circular patches. Also, Martinis writes about bandwidth enhancement of stacked patches in cavity in [21]. In this study, Martinis compares with a metasurface-inspired antenna, which will be under study in later sections.

In our case, the antenna based on stacked patches also must be integrated into a metal cavity. Like the case with a single patch, the requirements and specifications of the study must be followed, i.e., if an antenna based on stacked patches could reach a bandwidth of 60 MHz at the central frequency of 1.578 GHz. In the opposite case, if the antenna does not reach 60 MHz with the maximum cavity size ($50 \times 50 \times 20\ mm^3$), the minimum dimension to obtain that bandwidth will be searched.

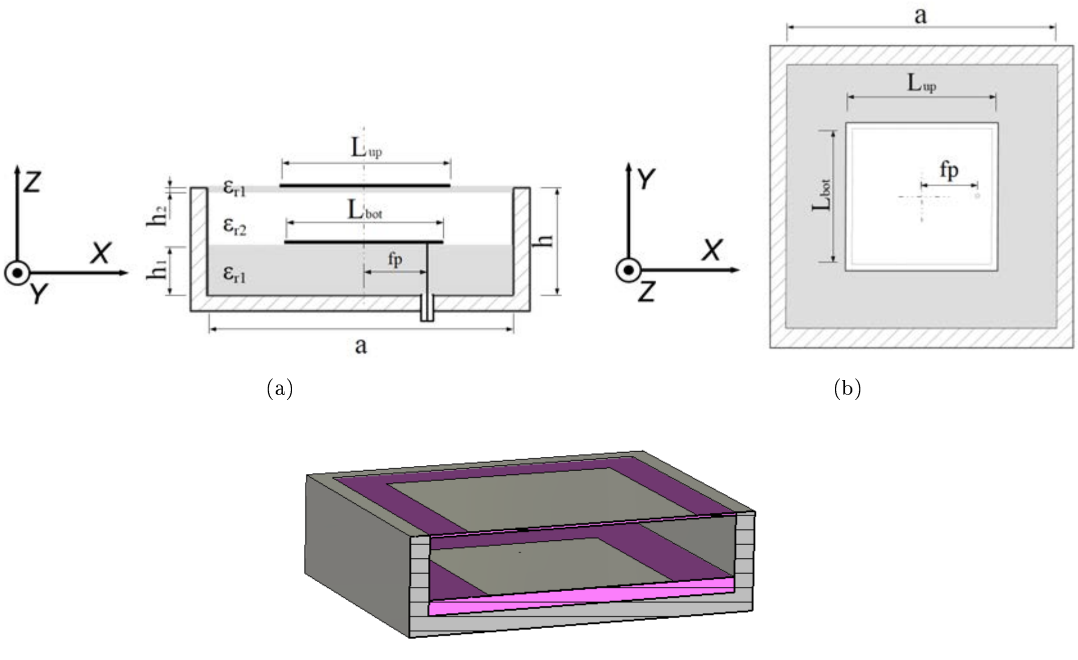

(a) (b)

(c)

Figure 2.3: Schematic of a cavity-backed stacked patches microstrip antenna. (a) Cross-section view. (b) Top view. (c) 3D model

2.2.1 Design procedure

Figure 2.3 shows the cross-section view and top view of a square cavity antenna based on two stacked patches with a cavity size $a \times a \times h$, with a the aperture size and h the cavity depth. In general, the stacked-patches antenna structure consists of two stacked parallel microstrip antennas separated by an air layer. Top radiator is slightly larger than bottom radiator ($L_{up} > L_{bot}$) and both patches are printed on a dielectric material, generally the same. The bottom antenna is active and fed by a coaxial probe and the upper patch acts as a parasitic antenna.

The structure of the antenna for this example is composed as follows. The height of the cavity has a fixed value, $h = 20$ mm, and the patches (lengths L_{up} and L_{bot}) are printed on a $h_2 = 0.64$ mm and $h_1 = 16$ mm dielectrics substrate, respectively, with the same relative permittivity $\varepsilon_{r1} = 3.66$. It should be noted that $h_1 > h_2$ and $L_{up} > L_{bot}$. The volume between both patches is filled with air ($\varepsilon_{r2} = 1$). The antenna is fed by a coaxial probe attached to the bottom patch through the cavity. The feed point is displaced from the center of the cavity the distance f_p.

Similarly with the first section, the objective is to achieve the smallest cavity aperture size for a bandwidth of 60 MHz.

2.2.2 Simulation results

To determine if the stacked patches cavity geometry is valid or not for the requirements of this antenna, a comparative study has been performed. The simulations are performed with the commercial software CST Studio Suite [114]. The objective of the study carried out is to find the maximum bandwidth obtained for different square aperture sizes a: from 40 mm ($0.2\lambda_0$ at 1578 MHz) to 100 mm ($0.53\lambda_0$ at 1578 MHz). For each cavity size a, the structure is optimized to maximize the bandwidth and matched to the central frequency of 1.578 GHz. Table 2.2 summarized the behavior of these parameters in the antenna performances.

Parameter	Resonance frequency	S11
$f_p \nearrow$	$\nearrow$	$\nearrow$
$L_{up} \nearrow$	$\searrow$	$=$
$L_{bot} \nearrow$	$\searrow$	$\nearrow$

Table 2.2: Parametric analysis for stacked patch antennas

Figure 2.4 shows the maximum achievable bandwidth versus the aperture size of the cavity in wavelength. These results conclude that it is not possible to use a stack-based design to reach the desired 60 MHz bandwidth at 1.578 GHz with aperture dimensions lower than 0.43 λ_0 ($a = 81$ mm). In other words, for aperture dimensions less than $0.43\lambda_0 \times 0.43\lambda_0$ the maximum bandwidth for an optimized antenna is less than 60 MHz. It should be added that, for dimensions lower than 0.24 λ_0, it is not possible to match this antenna at the determined frequency of 1.578 GHz.

2.2.3 Discussion

The antenna based on stacked patches is a well-known solution to increase the bandwidth of a certain system. For the specific case of compact metallic cavities, the stack up of two microstrip antennas do not give satisfying results to reach enough bandwidth to cover L1, G1 and E1 (60 MHz). Increasing the aperture (cavity) size is essential to enlarge the BW to achieve the specifications. The numerical results have shown that a length of at least 0.43 λ_0 ($a = 81$ mm) was necessary, which is not compatible with the dimension requirements (width of 0.26 λ_0 and length of 0.31 λ_0). In this case, the problem comes when the dimensions of the antenna are limited by a small cavity. Due to the size of this metallic cavity, the layers cannot have sufficient separation to resonate without coupling.

One solution to solve bandwidth issues is the use of metasurfaces. Martinis demonstrates in [3] that the use of metasurfaces in the aperture of a cavity has numerous advantages such as bandwidth enhancement.

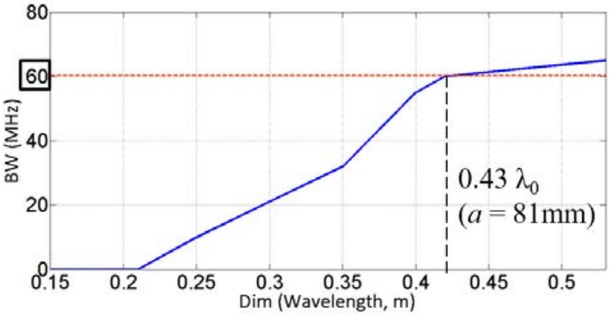

Figure 2.4: Antenna bandwidth as a function of the aperture size for stacked patches microstrip antenna embedded on a square cavity

2.3 Metasurface antenna in cavity

Throughout this section, two different antennas in a cavity metasurface-based will be presented. The objective of the study is to find the antenna as small as possible that obeys the exposed requirements. The first antenna has a square opening of 40×40 mm^2 ($0.21\lambda_0 \times 0.21\lambda_0$). As we will see, this antenna does not reach the required bandwidth, therefore, a 50×50 mm^2 ($0.26\lambda_0 \times 0.26\lambda_0$) has been studied. In order to reduce the size and do not loose the maximum bandwidth, a rectangular solution of 40×45 mm^2 ($0.21\lambda_0 \times 0.24\lambda_0$) is proposed. All of them are based on a parametric study that will be shown during the section.

2.3.1 Design procedure

By including a parasitic capacitive reactance at the aperture of a cavity, the maximum bandwidth can be achieved in relation to a simple open cavity. A metasurface behaves like a capacitive element and at the same time produces an increase in bandwidth (reduced by the cavity confinement of the antenna). In other words, a simple patch also may acts as a capacitor, but does not offer the desired results due to the inductance it also provides. Martinis [3] demonstrates the good performances of creating a series of small patches instead of a single one as the physical conception of the capacitor. The inductance is reduced and the “pure” capacitance approaches (Figure 1.36). This geometry would be translated as a series connection of capacitors. The design of the metasurface antenna in linear polarization to solve the problem of this thesis, it will be based on this concept. The conception procedure to design this type of antennas is described in section 1.5.3.

2.3.1.1 Antenna composition, materials and excitation

The cavity-backed antenna geometry, provided in Figure 2.5a, is embedded in a square cavity whose dimensions $a \times b \times h$ depend on the flying platform diameter (around 150 mm). The metallic cavity is filled as follow:

- A thick (h_1) polypropylene layer ($\varepsilon_r = 2.25$; $\tan(\delta) = 0.001$ [161]) at the bottom of the cavity selected to ensure an adequate robustness to the structure, especially due to the strong acceleration constraints supported by the flying platforms (several thousands of g) given in the introduction of this manuscript (Figure 19). Due to its low permittivity, polypropylene hardly interferes with the electromagnetic properties of the antenna and slightly helps to miniaturize the antenna.

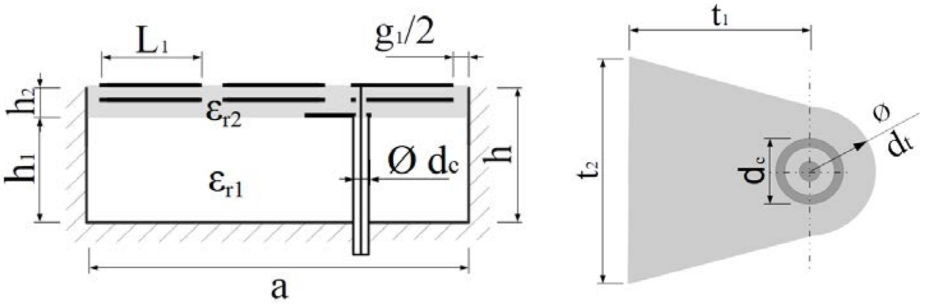

(a) (b)

Figure 2.5: (a) Cross section of the metasurface-inspired cavity antenna. (b) Details of the metal part welded to the feeding point

- A thin (h_2) lamination of two Rogers RO3210 substrates ($\varepsilon_r = 10.2$; $\tan(\delta) = 0.0027$ [31]) with three metallic levels: the lowest one is the feeding layer with a trapezoidal shape transmission line (Figure 2.5b), while the metasurface-inspired radiating element is printed on the two upper layers; the layer of substrate is thin enough (0,64 mm) to provide the requested capacitive effect. Two metasurface layers have been overlapped to further increase the capacitance. Only the upper radiator is directly fed.
- Finally, the excitation of the antenna is made by a coaxial cable located a distance f_p from the center of the cavity, on one of the side patches. In addition, a small metal part (Figure 2.5b) is added to the bottom of the high permittivity substrate to match the antenna and facilitate soldering in the manufacturing process. The antenna matching level can be varied by tuning the parameters of this excitation section, t_1 and t_2. The diameter of the coaxial cable is $d_c = 2.2mm$.

2.3.1.2 Metasurface design

Cutting the large patch into smaller patches causes a jump (cut) in the current crossing the patch. These small pieces contribute less to the antenna inductance.

According to a study carried out in [3], a surface with three rectangular elements provides good results for cavities between 0.2 λ_0 and 0.3 λ_0 (at 1578 MHz), which is our case. With only two elements a satisfactory bandwidth is not obtained. If the aperture is larger than 0.3 λ_0, a fourth element could be added. If the aperture is larger, more patches can be added to obtain the same capacitance. In conclusion, elements with dimensions below 1/13 λ_0 are necessary to correctly approximate the capacitor to the aperture [3]. In general, a metasurface must be made up of sub-wavelength elements, commonly the element size used is smaller than $1/10\lambda_0$ ("rule of thumb"). Therefore, this surface meets the metamaterial criteria.

Briefing, the metasurface study throughout the whole work in linear polarization is made of three rectangular strips of equal size ($L_1 \times L_2$), as depicted in Figure 2.6. Moreover, the capacitance loading the radiating aperture is adjusted by tuning the gap values g_1 and g_2. It should be noted that we consider the small gap between the end of the patch set and the cavity edge as $g_1/2$.

2.3.2 Simulation results

The key parameters used to optimize the antenna performances are the following: the position of the feed point (f_p), the gap between patches (g_1) which defines L_1, the gap between the edge of the patch

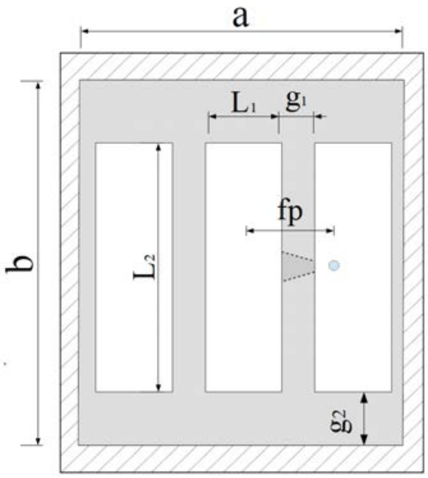

Figure 2.6: Top view of the metasurface in cavity

and the cavity (g_2) which sets L_2 and the dimensions of the small trapezoidal piece (t_1, t_2).

2.3.2.1 Parametric study

A parametric study has been performed to evaluate the influence of some parameters on antenna performances. It should be noted that the parametric study has been performed for a frequency range independent of the GNSS central frequency considered in this work. The objective is to see the evolution of the resonance with the variation of the parameters.

As already mentioned above, putting two layers of metasurface greatly increases the capacitance in the aperture. The following parametric study aims to see the evolution of the antenna matching result when more layers of metasurface are added. Regardless of matching frequency, the number of layers has been increased between three and six layers. Figure 2.7 shows the frequency decreasing when there are more layers. This may be interesting for frequency reduction, but the bandwidth is also degraded. Therefore, an agreement between bandwidth and number of layers should be sought when it comes to designing antennas.

For the second case, the variation of the gap g_1 between patches has been studied. In this case the parameters g_2, t_1, t_2 and f_p remains constant. As a explanation, the width of the strips (L_1) changes when g varies, since the size of the aperture is fixed. The gap between patches is one of the most important parameters to design a metasurface. The distance (the coupling) between the cells allows a correct antenna matching to the frequency needed, i.e., to get the proper capacitance. Using an antenna backed in a metallic cavity (similar to Figure 2.5a) composed of 4 cells (patches), the effect of the gap in the reflection coefficient S11 has been tested. The gap has been varied between 0.5 mm ($0.004\lambda_0$) and 5 mm ($0.04\lambda_0$), and only the feeding point has been changed to obtain a good level of adaptation. As can be seen in the graph of Figure 2.8, the matching frequency is lower when the gap is smaller, that is, when the coupling between becomes more important. However, if the gap is too small (0.5 mm and 1 mm in this case, depending on the aperture size), the patches are fully coupled, the searched capacitance is lost and it behaves as a standard patch. For a gap equals to 0 the metasurface is lost becoming a single patch and the capacitive effect becomes null, because the patch covers the entire aperture.

The following Table 2.3 summarizes the influence of each parameter on the antenna characteristics.

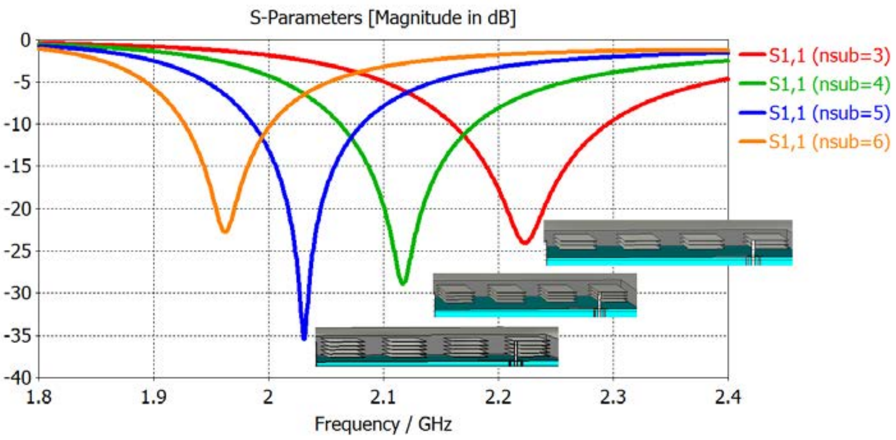

Figure 2.7: Variation of number of layers (metasurfaces). Result of having 3, 4, 5 and 6 layers

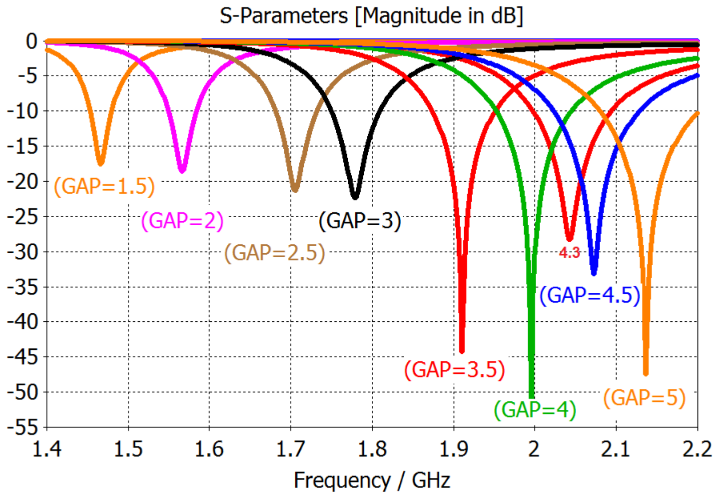

Figure 2.8: Variation of gap between patches. When the distance also varies the size of the strips

Parameter	Resonance frequency	S11 parameter	BW
f_p ↗	↗	↘	↗
g_1 ↗	↗	↘	↘
t_1 ↗	↘	↗	↗
t_2 ↗	↘	↗	↗
L_2 ↗	↘	=	=
N. layers	↘	↗	↘

Table 2.3: Parametric analysis for the metasurface described in Figure 2.6

2.3.2.2 Square cavity

The idea is to develop an antenna that meets the exposed requirements being as small as possible. The smallest structure in this case would be a 40×40 mm square opening (0.21 $\lambda_0\times$ 0.21 λ_0 at 1.578 GHz).

The objective is to evaluate whether this structure reaches a bandwidth of 60 MHz or not.

Square cavity 40 × 40

To carry out a preliminary study to match the metasurface structure to GNSS frequencies, a scale factor has been applied to a previous design [3, 21]. To obtain a resonant frequency at 1578 MHz with 60 MHz bandwidth, the FBW (Fractional Bandwidth) would be 3.7%. Therefore, to be able to perform the scale factor, an antenna that has the same percentage of FBW is researched. The above-mentioned starting structure is adapted at 2300 MHz with 87 MHz bandwidth, so FBW $\simeq$ 3.7%. Applying a scale factor to all dimensions, the minimum cavity dimensions should be 46.4×46.4×28.9 mm^3 to obtain a maximum bandwidth of 60 MHz using this design, Figure 2.9. These dimensions are slightly higher than desired (40×40×20 mm^3). However, the main problem is the cavity height, which must be fixed at 20 mm due to the shape of the carrier (a hollow cylinder with diameter 155 mm).

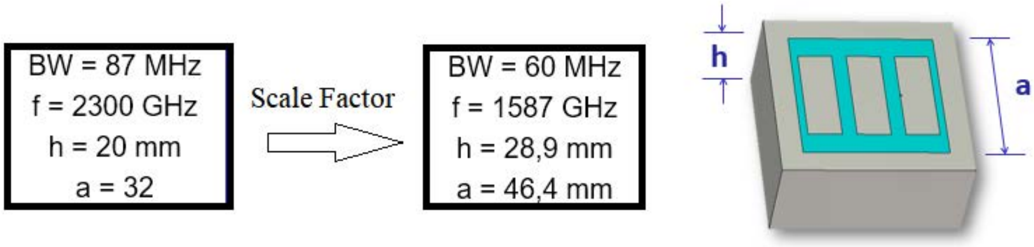

Figure 2.9: Scale factor application for cavity antenna

Therefore, the above structure has been simulated with a cavity of 40×40×20 mm^3. The results reveal that 60 MHz of bandwidth cannot be achieved for an antenna with these dimensions. The simulated reflection coefficient shows in Figure 2.10 the maximum bandwidth achieved with this antenna, 52 MHz.

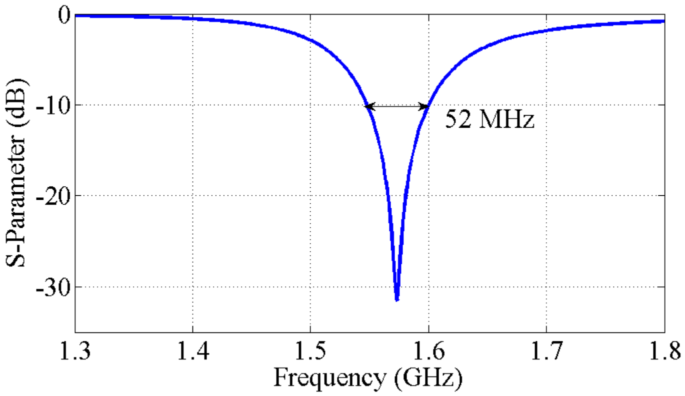

Figure 2.10: Simulated S11 for metasurface-inspired rectangular cavity antenna of dimensions $0.21\lambda_0 \times 0.21\lambda_0 \times 0.11\lambda_0$ at 1.578 GHz (40 × 40 × 20 mm^3)

In this context, the immediate solution is to slightly increase the aperture size. The analysis and simulation results for a 50×50×20 mm^3 cavity antenna is studied below.

Square cavity 50 × 50

After the previous results, an increase of the cavity aperture up to 50×50 mm^2 (0.26 $\lambda_0 \times$ 0.26 λ_0) has been chosen. This structure is presented in [33]. The cavity antenna follows the structure presented in the previous section which is recalling below. A thick polypropylene layer is place on the bottom of the cavity. A thin lamination of two Rogers RO3210 substrates with three metallic levels: the lowest one is the feeding layer with a trapezoidal shape transmission line (Figure 2.11c), the two upper metallic layers are the metasurfaces, both have identical patterns made of three rectangular strips of equal size. The antenna is fed by a coaxial cable, whose central conductor is connected to the upper patch and the outer conductor connected to the metal cavity. Moreover, the capacitance loading of the radiating aperture can be adjusted by tuning the gap values g_1 and g_2 (Figure 2.11a and Figure 2.11b). Considering the future manufacture of the antenna, the fine glue layer applied (estimated to ε_r = 3.5, tan(δ) = 0.01, $h = 0.1mm$) to glue all the antenna elements together has been taken into account in simulations

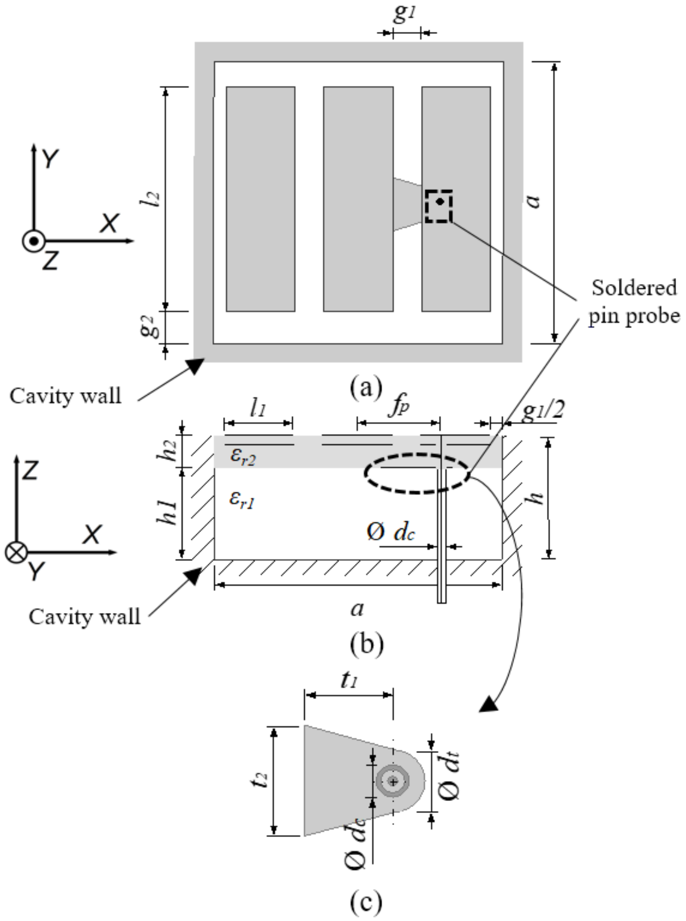

Figure 2.11: LP antenna embedded in a square cavity 50×50×20 mm^3. (a) Top view. (b) Cross-section view. (c) Feeding system.

As design guidelines, first, the strip width (l_1) is chosen to be about $\lambda_0/13$ (which also determines g_1), and l_2 is fixed to 0.77 × a to get a wide enough bandwidth. The antenna center frequency and matching level are then tuned by the variables f_p and finely optimized by adjusting the dimensions t_1 and t_2 (Figure 2.11c). The final dimensions are provided in Table 2.4 and the numerical model is depicted in Figure 2.12.

Parameter	Value	Parameter	Value
a	50 mm	l_2	26.8 mm
h_1	18.8 mm	ε_{r1}	23.5
h_2	1.92 mm	ε_{r2}	10.2
f_p	13.2 mm	t_1	8.8 mm
g_1	3.83 mm	t_2	8.2 mm
g_2	5.6 mm	d_t	4.22 mm
l_1	12.77 mm	d_c	2.2 mm

Table 2.4: Optimized dimensions of the 50x50 mm square cavity-backed antenna

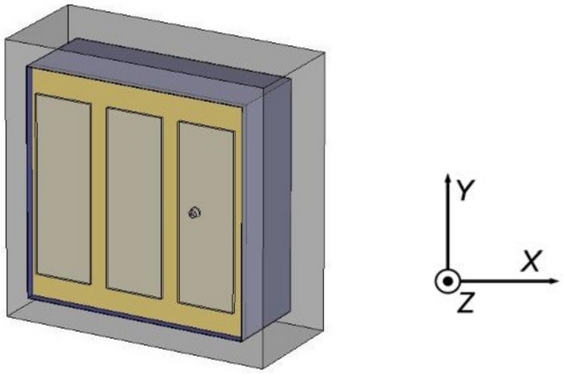

Figure 2.12: 3D view of the numerical model for the metasurface cavity antenna of cavity dimensions 50×50×20 mm^3

The simulation results are shown below. Figure 2.13a shows the transmission coefficient S11. The bandwidth measured at -10 dB is 87 MHz, which matches the minimum 60 MHz required. So, the antenna is well matched over the three aimed GNSS bands. The peak gain reaches 4 dBi Figure 2.13b. Radiation patterns for H and E planes are represented in Figure 2.14 and the half power beam width (HPBW) is 129° for $\varphi = 0°$ and 104° for $\varphi = 90°$.

Briefing, this antenna fulfills all the requirements set forth at the beginning of this chapter. However, the aperture size is larger than desired, although valid. The next question is asked, could the opening be reduced since the bandwidth is larger than required? As the objectives are not achieved with a 40×40 mm^2 aperture, a rectangular cavity has been considered, as it is known that the carrier is a long cylinder. Figure 2.15 shows a diagram of the rectangular cavity in the metal hollow cylinder. Increasing the length presents fewer drawbacks because there is a margin of space along the cylinder. However, due to the future implementation of a ring-shaped antenna array around the carrier, the increase in width should be avoided. Because of that, an extension of 5 mm in one cavity length is tested. Therefore, the antenna is backed in a aperture size of 40×45 mm^2.

2.3.2.3 Rectangular cavity 40 × 45

First, a study was carried out to see what would be the smallest possible dimension for the rectangular cavity. The cavity width has been fixed to 40 and the length has been progressively increased. According

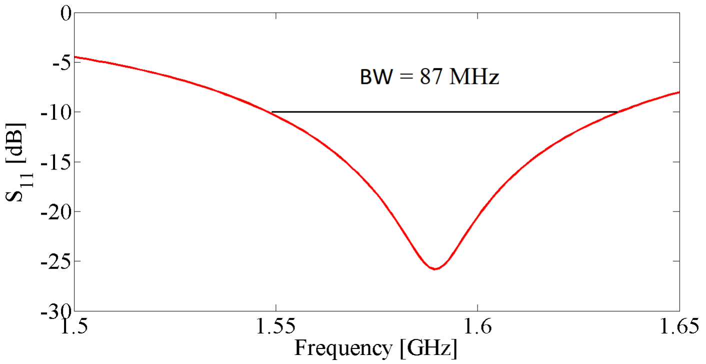

(a) Simulated reflection coefficient of the LP cavity backed metasurface antenna

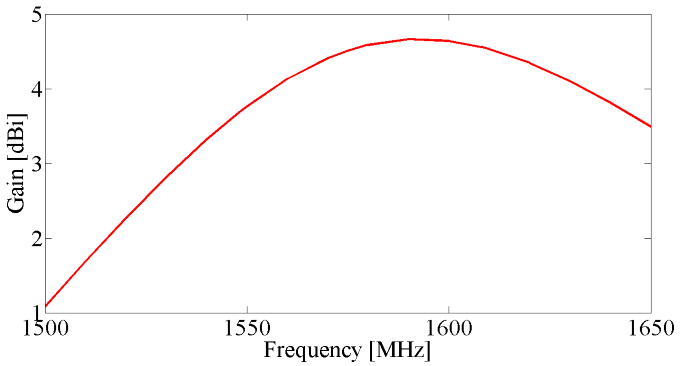

(b) Simulated gain of the LP cavity backed metasurface antenna

Figure 2.13: Simulated results for a linearly-polarized metasurface-inspired cavity antenna with aperture dimensions 50 x 50

to Figure 2.16, from a cavity length of 45 mm, the antenna will reach 60 MHz bandwidth. For each value of the length, the antenna has been optimized to obtain the maximum bandwidth.

Parameter	Value	Parameter	Value
$a \times b$	40 × 45 mm^2	l_2	22 mm
h_1	18.08 mm	ε_{r1}	2.25
h_2	1.92 mm	ε_{r2}	10.2
f_p	9 mm	d_t	4.22 mm
l_1	10.93 mm	d_c	2.2 mm

Table 2.5: Optimized dimensions of the 40×45 mm^2 square cavity-backed antenna

The conception of this antenna is similar to previous designs and the cavity is composed as explained before. Summarizing, the design is based on a metal cavity with a depth h = 20 mm (0.11 λ_0) and with a rectangular aperture of 40×45 (a×b) mm^2 (0.21 λ_0× 0.24 λ_0). Most of the cavity, 90%, can be ideally filled of air (h_1), or of a solid material with low permittivity, as polypropylene, which will be finally used in the manufacturing process for mechanical issues. The two metasurface layers are composed of three rectangular patches of equal size; $l_1 \times l_2$. Each layer is printed on a thin substrate (0.67 mm) of high

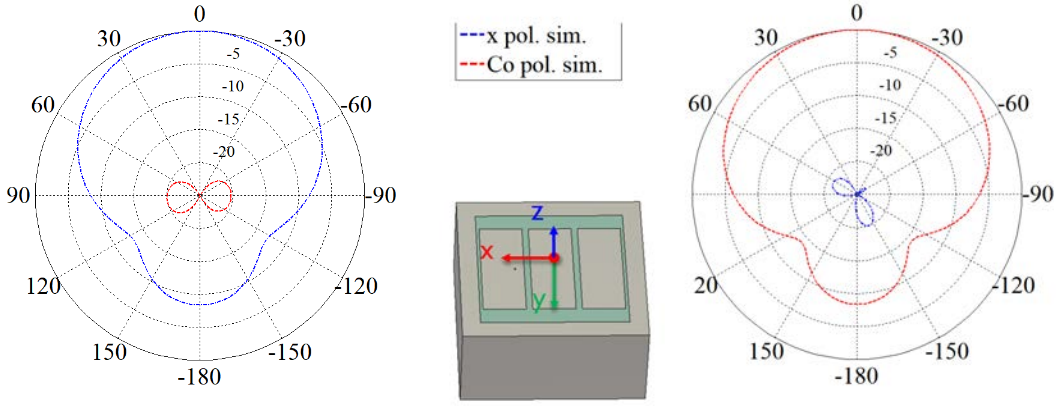

(a) H-plane ($\varphi = 0°$)

(b) E-plane ($\varphi = 90°$)

Figure 2.14: Simulated radiation patterns for a linearly-polarized metasurface-inspired cavity antenna with aperture dimensions 50×50 mm^2 at 1578 MHz

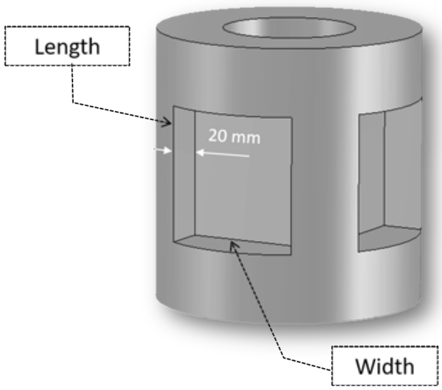

Figure 2.15: Cylindrical carrier schema with rectangular cavities

permittivity ($\varepsilon_r = 10.2$). The antenna is fed by a coaxial cable located f_p mm from the center, on one of the upper side patches. In addition, a small metal part (similar to the square antenna one) is added to the bottom of the high permittivity substrate to match the antenna and facilitate soldering in the manufacturing process. The key parameters tuned to optimize the antenna performance are t_1, t_2, g_1 and f_p. The values of the parameters for the optimized solution are given in Table 2.5.

Figure 2.17 shows the reflection coefficient obtained in simulation for cavity rectangular metasurface antenna. The BW is 68 MHz (FBW = 4.1% at the center of 1.578 GHz) around the central frequency which gives us a slightly higher bandwidth than the minimum required.

The radiation patterns computed at the central frequency (1.578 GHz) and at two frequencies over 68 MHz (1.548 GHz and 1.608 GHz) are represented in Figure 2.18. The HPBW at is between 130° (at 1548 MHz) and 136° (at 1608 MHz) for the plane $\varphi = 0°$, and between 105° (at 1548 MHz) and 106° (at 1608 MHz) for $\varphi = 90°$. Even if the HPBW are wide due to the small size of the antenna, it is an advantage for GNSS reception. In both linear and circular polarization, a wide HPBW enables the capture of more

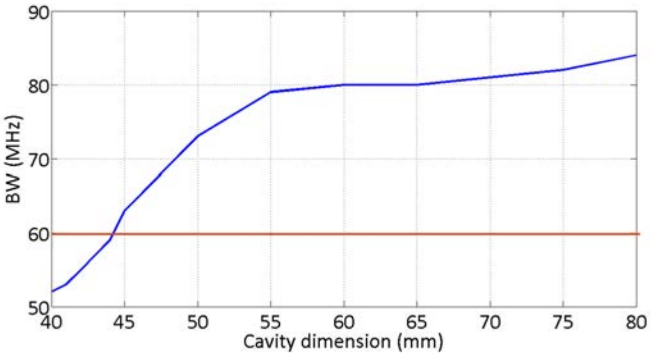

Figure 2.16: Study on the effect of length for a fixed a to 40 mm

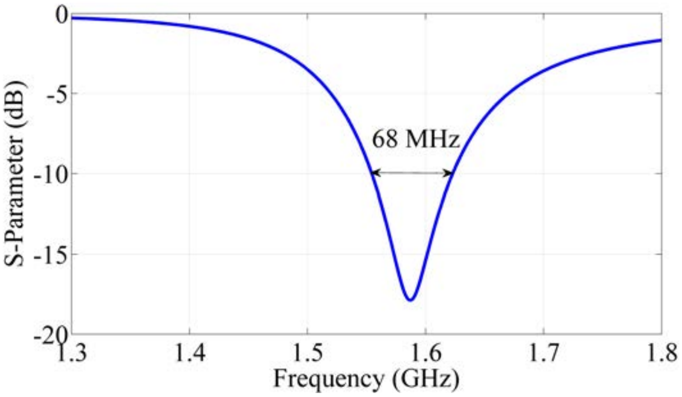

Figure 2.17: Simulated S11 for metasurface-inspired rectangular cavity antenna of dimensions 40×45×20 mm^3 ($0.21\lambda_0\times$ $0.24\lambda_0\times$ $0.11\lambda_0$ at 1.578 GHz)

satellites in one hemisphere. If the antenna has too narrow HPBW, signals from low elevation satellites will not be captured.

Figure 2.19a represents how the maximum efficiency matches at the central frequency 1.578 GHz. This antenna presents a good performances regarding the total efficiency of $\eta = 96.5\%$. The gain made in simulation is plotted in Figure 2.19b. The maximum gain value is 4.54 dBi which corresponds to the center frequency. If a priori gain may seem quite low, it is more than enough for the GNSS criteria, as explained in the dedicated section of chapter 1. The small gain is due to the smallness of the cavity and the coupling between close elements.

Due to the good results, both the 50 mm square aperture cavity and the rectangular one, several prototypes have been manufactured and measured. Then, compared with simulation results. This rectangular structure was communicated in [32].

2.4 Prototyping

Due to the good results obtained in simulation for the rectangular aperture and the 50 mm square aperture antenna, several prototypes have been manufactured and measured. The prototypes of both antennas have been entirely manufactured by ISL technicians.

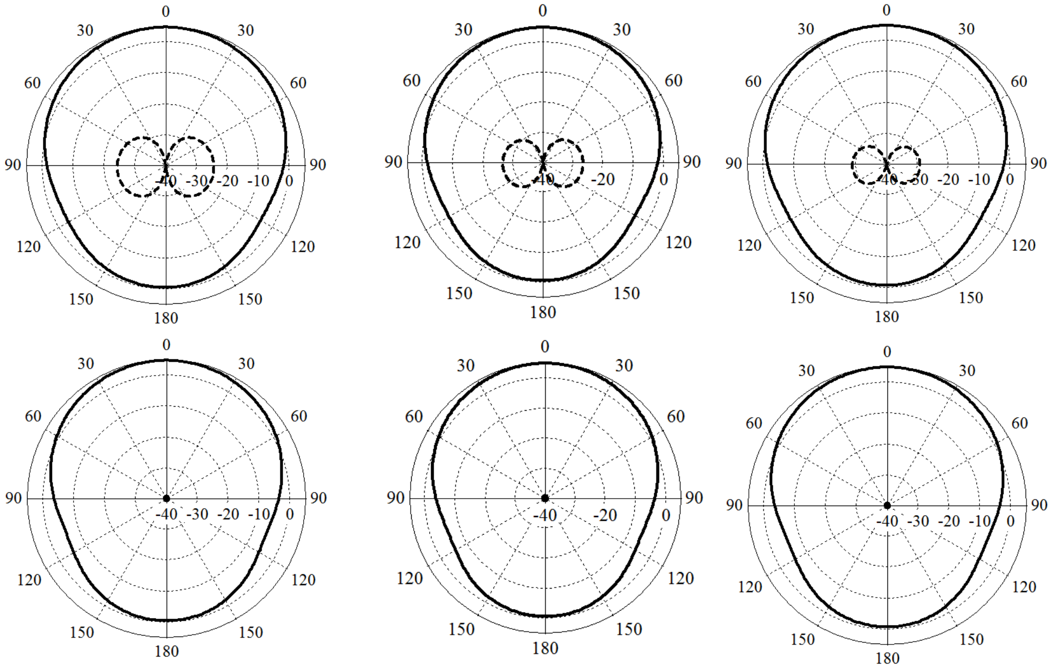

(a) 1548 MHz (b) 1578 MHz (c) 1608 MHz

Figure 2.18: Simulated radiation patterns at several frequencies for metasurface-inspired rectangular cavity antenna of dimensions 40×45×20 mm^3 ($0.21\lambda_0\times$ $0.24\lambda_0\times$ $0.11\lambda_0$ at 1.578 GHz). Solid line for co-polarization and dotted line for cross-polarization. H-plane (φ = 0°) on the top row and E-plane (φ = 90°) on the bottom row

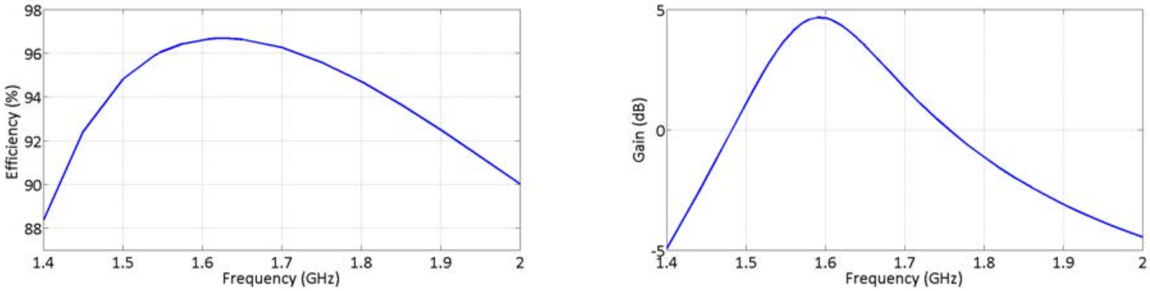

(a) (b)

Figure 2.19: (a) Simulated efficiency and (b) simulated realized gain for the rectangular cavity-backed metasurface antenna of 40 x 45.

2.4.1 Part by part presentation

Figure 2.20 presents the different parts that the prototype is made of. At the top is the copper plate that serves as closure of the cavity. On your right you can see the trapezoidal metallization printed on the Rogers 3210 dielectric. The metallization layers will go on a polypropylene block that fills the rest of the cavity. Finally, a coaxial cable with SMC connector. The assembly of all the parts is explained in a dedicated section.

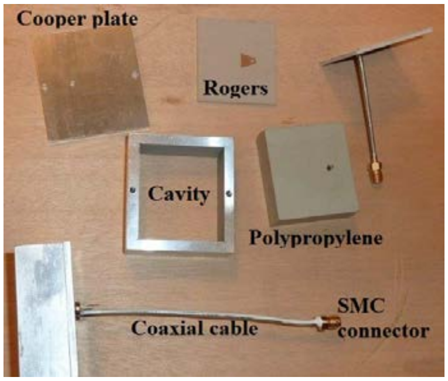

Figure 2.20: Pieces breakdown of a metasurface-inspired LP prototype

Cavity

The prototype cavity is formed by four walls of 5 mm thick forming a quadrilateral with 90° angles. As the image shows, the metal cavity is made as a frame, without the bottom. The design has been designed to facilitate the inclusion of the rest of the elements and the coaxial cable. The cavity frame is closed in the bottom by a copper plate.

Figure 2.21: Two versions of the metal cavity used for the prototypes

Two different versions of the cavity have been manufactured and photographed in Figure 2.21. The cavity on the right is the first conceived model. In this case the frame is fixed and the copper plate can be fixed with two screws. There are two problems with this model: the difficulty of inserting and fixing the antenna elements and the electrical contact with the copper plate with only two screws. Because of this, the cavity on the left is used for the second version of the prototypes. This improved version includes a removable side opening to insert the elements through the side of the cavity. Also, the electrical contact of the copper foil is ensured by more screw points.

Polypropylene

As explained in previous sections, polypropylene (PP) has been chosen to provide robustness to the antenna. Ideally, the best results are obtained if the bottom of the cavity is filled with air. However, its manufacture is not possible because the metasurfaces must be held by some support. Polypropylene is a thermoplastic polymer belongs to the group of polyolefins and is partially crystalline and non-polar. Polyethylene has similar characteristics, but polypropylene is slightly harder, more heat resistant and mechanically rugger.

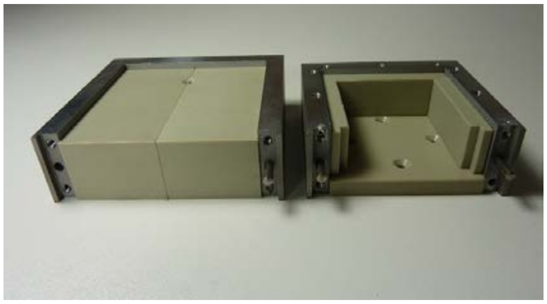

Figure 2.22: Two versions of the polypropylene blocks inside the cavity

As the metal cavities case, two versions of the polypropylene blocks have been manufactured, both shown in figure 2.22. At the beginning it was decided to make a compact block (divided into two to facilitate the insertion) as shown in figure 2.22 (left). However, to ensure the stability of the antenna, it is not necessary to fill the entire cavity with polypropylene. For this reason, five smaller pieces of polypropylene (4 sides and one upper) as shown in figure 2.22 (right) have been designed. With this second design, the total permittivity inside the antenna is reduced and thus adjusted to the ideal case (cavity filled with air). Another benefit is the saving of material and the ease of insertion of the coaxial cables, which have to cross the cavity to reach the patch.

Microstrip manufacturing

The two layers of metasurface and the microstrip connection line have been manufactured independently following the technique of microstrip antennas. Each design has been printed on a 0.63 mm thick dielectric layer and relative permittivity 10.2. The dielectric belongs to the Rogers 3200 series and it is a ceramic-filled laminates reinforced with woven fiberglass. The three are glued together with the metallization face down in the case of the connection line. The layers are depicted in Figure 2.23.

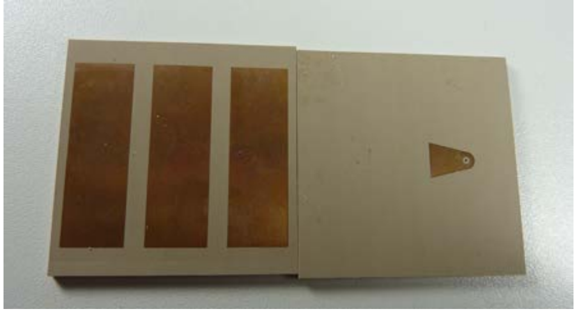

Figure 2.23: Metallization design of microstrip layers

2.4.2 Antenna feeding

The antenna is fed by an coaxial cable in 50Ω characteristic impedance with a SMC type connector at the end. The inner conductor is connected in one of the side sheet of the upper patch. The outer connector is welded to the microstrip connection line and to the copper plate (bottom part of the cavity), to use the cavity as a ground plane. The cable utilized has the following dimensions:

- Diameter inner conductor: 0.5 mm
- Diameter dielectric material, Teflon®: 1.7mm
- Diameter outer conductor: 2.2 mm

2.4.3 Assembly

The assembly process of the above mentioned pieces must be precise due to the small margin of error caused by the small dimensions of the antenna. First of all, the coaxial cable is inserted through the holes made in both the polypropylene and the copper plate. The coaxial cable crosses the entire cavity until it reaches the upper patch, where the inner connector is soldered. Next, the polypropylene side blocks and the aforementioned elements (except the plate) are introduced and joined inside the cavity, from the side in the case of the second model cavity. The microstrip layers are placed on top of the polypropylene blocks that act as a stop for the metasurface. The rectangular patches of the meta surface are outward the aperture, while the connection line keeps inside the cavity. The cavity is closed at the bottom by a copper foil screwed to the walls.

Despite the compactness of the set, it is glued to avoid movements of the pieces. The glue used (estimated to $\varepsilon_r = 3.5$, $\tan(\delta) = 0.01$, $h = 0.1mm$) is more liquid than usual to also covers the possible microscopic holes. In such a millimeter prototype, small air gaps can cause a frequency shift.

Figure 2.24 presents both complete prototypes (rectangular 40×45 mm^2 and square 50×50 mm^2). The antenna in a square cavity on the right and the antenna in a rectangular cavity on the left.

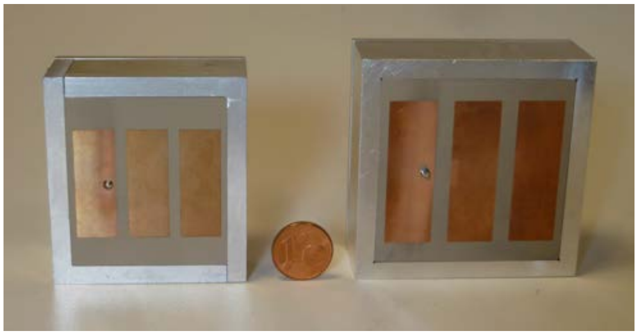

Figure 2.24: Final prototypes for the cavity-backed metasurface-inspired antenna for GNSS: Rectangular aperture (left) and square aperture (right)

2.5 Measurements and experimental results

After manufacture, the prototypes have been measured using the vector analyzer (VNA) and the anechoic chamber for farfield. Two prototypes will be presented from each of the antennas. The first one does not provide the correct results due to manufacturing problems. Therefore, a second prototype that meets the objectives is presented.

2.5.1 Square cavity

Two versions of the linear polarization cavity-backed 50×50×20 mm^3 (0.26 $\lambda_0\times$ 0.26 $\lambda_0\times$ 0.11 λ_0 at 1578 MHz) antenna have been manufactured and measured. The results for both are set out below.

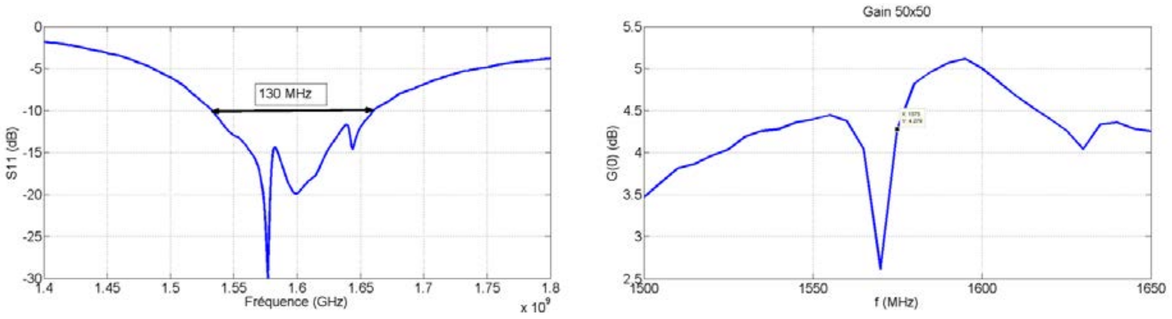

(a) Measured reflection coefficient

(b) Measured gain

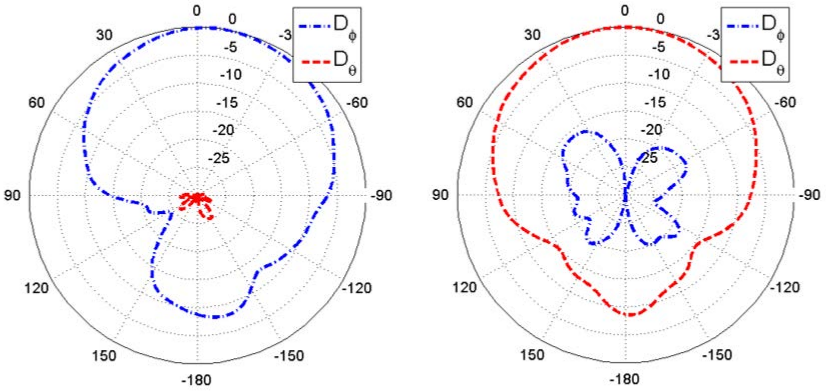

(c) Measured radiation patterns

Figure 2.25: First prototype measurement results for the antenna on a square aperture of 50×50 mm^2

2.5.1.1 First prototype

Results of the first prototype of the cavity-backed metasurface antenna in a square cavity are presented below. As the image presents, the prototype has a manufacturing problem due to the presence of a drop at 1570 MHz in the gain (Figure 2.25b) and in the radiation patters (Figure 2.25c). Even if the bandwidth of 130 MHz (Figure 2.25a) is a good result, the matching is not correct.

As the graphs show, the drop can be seen in all the results. An empirical explanation has not been found, however it may be due to the existence of an air gap that has not been covered by the glue or due to a poor contact of the copper foil with any part of the cavity. Therefore, this prototype is discarded. To solve the problems presented by this manufacturing, a new prototype has been created. This new prototype utilized the second version of the cavity presented above.

2.5.1.2 Second prototype

The simulated and measured reflection coefficients, gains and radiation patterns are in good agreement with each other as confirmed by Figure 2.26a, Figure 2.26b and respectively. The antenna is well matched

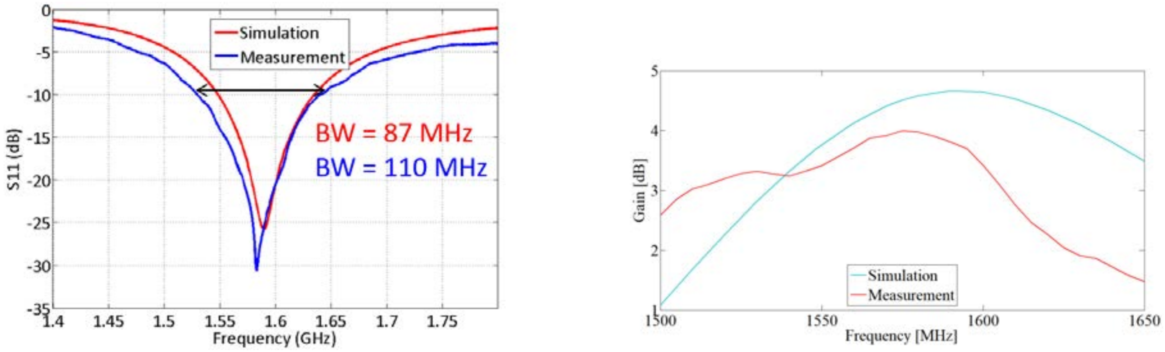

(a) Reflection coefficient (b) Measured gain

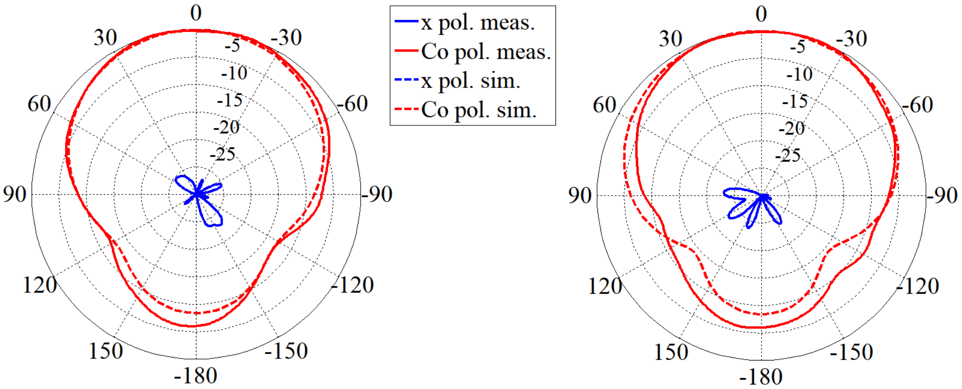

(c) Measured radiation patterns. H-plane ($\varphi = 0°$) on the left and E-plane ($\varphi = 90°$) on the right Figure 2.26c

Figure 2.26: Comparison between measurement and simulation results for the antenna on a square aperture of 50×50 mm^2

over the three aimed GNSS bands. The radiation results at the central frequency reaches a gain of 4 dBi. The half power beamwidth (HPBW) is 129° ($\varphi = 0°$) and 104° ($\varphi = 90°$) in simulation, and 118° ($\varphi = 0°$) and 120° ($\varphi = 90°$) for the measurement. The measured bandwidth is 110 MHz, even greater than the simulation bandwidth, 87 MHz. This may be due to some coupling or losses in the manufacturing or measurement process.

2.5.2 Rectangular cavity

2.5.2.1 First prototype

The first manufactured prototype has a slight frequency shift and, therefore, a decrease in bandwidth. This means that the requirements of the GNSS bands are not met. Figure 2.27a shows a bandwidth of 40 MHz, compared to 68 MHz obtained in simulation. The gain is also lower, does not exceed 4 dBi, while in simulation it exceeds 4.5 dBi (Figure 2.27b). Despite this, the radiation diagrams presents good performances (Figure 2.27c).

The failure of the first prototype can be caused by a gap not covered by the glue or some mismatch in manufacturing. Therefore, a new prototype with the same measurements was made to check if the

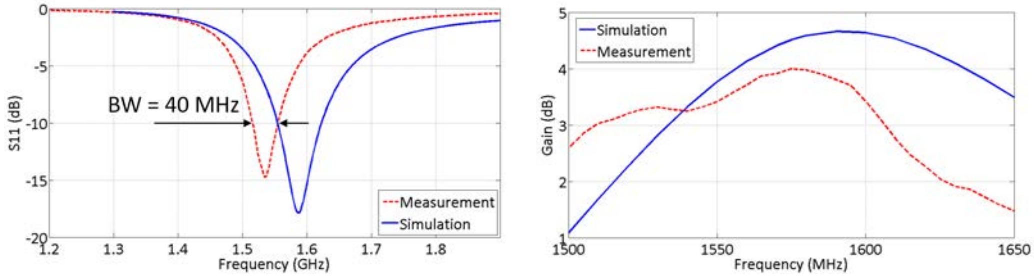

(a) Reflection coefficient (b) Gain

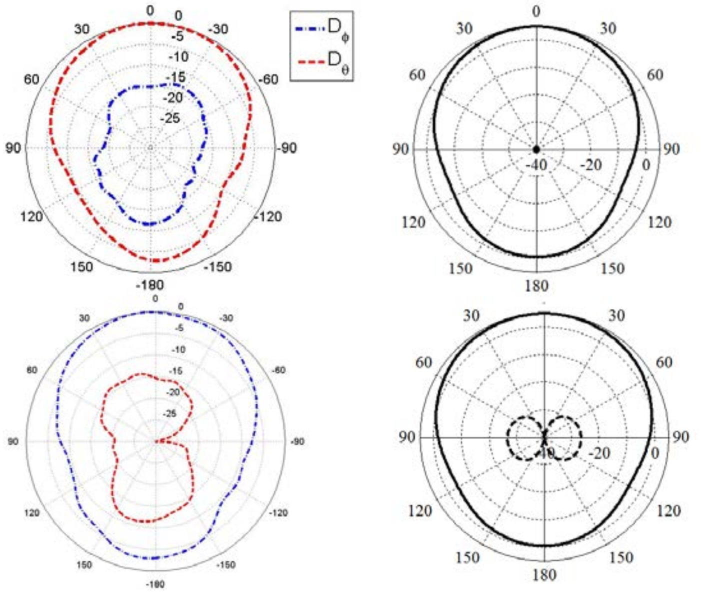

(c) Measured (left) and simulated (right) radiation patterns

Figure 2.27: First prototype. Measurement and simulation results for the antenna on a rectangular aperture of 40×45 mm^2

structure works correctly. In the case of obtaining the same results as in the first prototype, the simulation should be reviewed.

2.5.2.2 Second prototype

In this case, the bandwidth exceeds 60 MHz (62 MHz) so it matches the results obtained in simulation Figure 2.28a. However, the bandwidth does not cover the required GNSS bands (L1, E1 and G1), since it does not reach 1.61 GHz which is the end of the G1 band. The gain is low (Figure 2.28b), but it is sufficient for the application of the antenna, since GNSS does not require a large gain (minimum gain for GNSS, -4.5 dBi). The half power beamwidth (HPBW) is 131° ($\varphi = 0°$) and 106° ($\varphi = 90°$) in simulation, and 110° ($\varphi = 0°$) and 120° ($\varphi = 90°$) for the measurement. As it happened in the previous prototype, the radiation patterns show good results matching with the simulation results (Figure 2.28c).

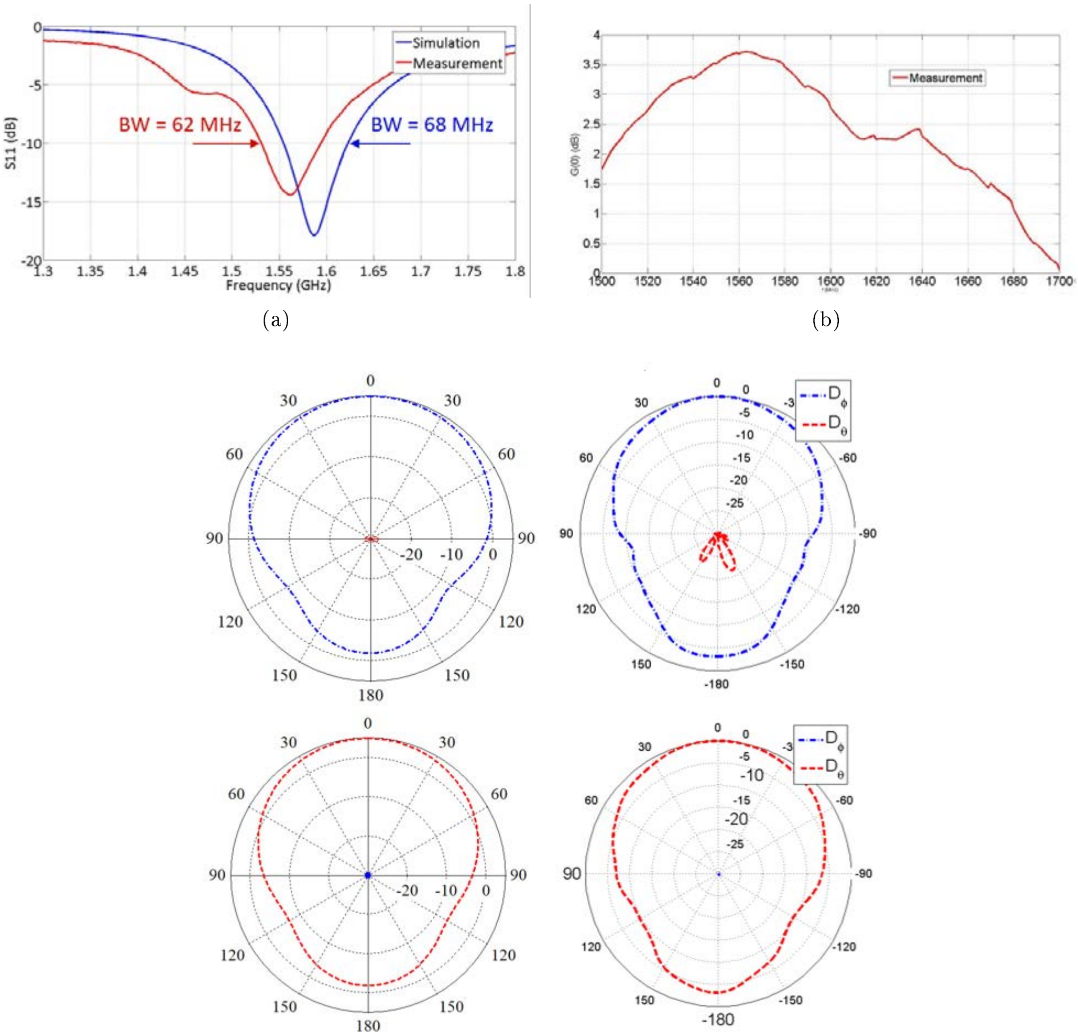

(a)

(b)

(c) H-plane ($\varphi = 0°$) on the top row and E-plane ($\varphi = 90°$) on the bottom row

Figure 2.28: Measurement and simulation results for the antenna on square aperture of 40×45 mm^2. (a) Reflection coefficient. (b) Gain. (c) Simulated (left) and measured (right) radiation patterns.

2.6 Antenna integration

As previously mentioned, the objective of this work is the design of an antenna with certain characteristics for GNSS applications and integrated in a cavity. This cavity is part of the body of a projectile made of metal. This confinement produces benefits and disadvantages for the antenna and imposes the maximum size that it must have. In this case it is a hollow cylinder with a diameter of 155 mm where the antenna is placed on the external face. In this section the effect of the integration of the antenna in the cylinder is studied.

The final objective of the project, to which this thesis belongs, is the conception of a ring-shaped conformal array around the cylinder. The number of elements that make up the array will depend on the final size of the antenna aperture. Figure 2.29 shows an example of the arrangement of 5 metasurface antennas around the carrier. The conception and analysis of the array is not part of topic of this thesis. Figure 2.30a depicted the cylinder modeling and Figure 2.30b the conformal frame to hold the antenna in the aperture. The cylinder from Figure 2.30a is modeled with a single cavity because the objective is study the effect of the carrier on the designed antenna and not to investigate the effect between array elements.

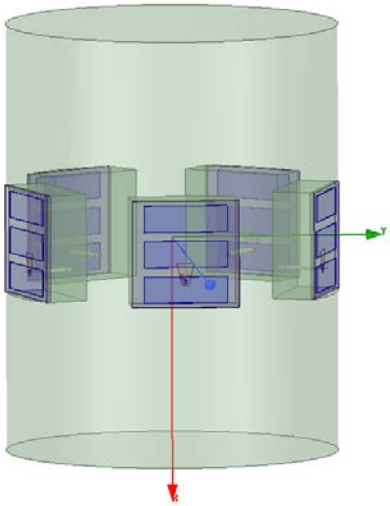

Figure 2.29: Five antennas ring array conformed around a metallic cylinder of 155mm diameter

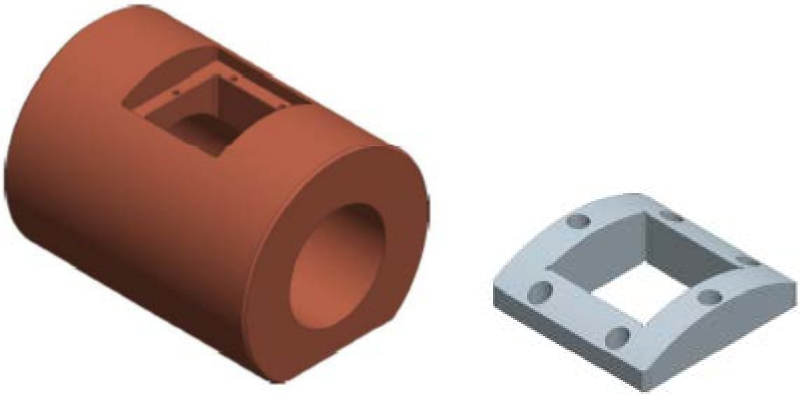

(a) (b)

Figure 2.30: (a) Metal cylindrical carrier in simulation. (b) Metal frame to hold the antenna in simulation

2.6.1 Carrier integration for metasurface-based antenna

The effect of integrating the linearly-polarized metasurface antennas designed in this chapter have been analyzed in this section. The simulation have been performed with a metallic cylinder of 155 mm diameter. The main interest is to observe the behavior of the antenna performances when the aperture is surrounded by a curved plane. In this case the antenna keeps the usual flat design, taking into account that the antenna height is completely confined on the cylinder.

The integration of both the 40×45 mm^2 rectangular antenna and the 50×50 mm^2 square antenna presented in previous sections are studied. In the case of the rectangular cavity two circumstances are considered: the length of the opening in the direction of the y-axis or the x-axis. That is, if the opening is placed in the 45×40 mm^2 position or rotated to the 40×45 mm^2. The simulation model of the last case is depicted in Figure 2.31a and the square antenna in Figure 2.31b.

The three structures have been simulated without introducing any change in their parameters. In this way it is possible to check if the bandwidth and the matching frequency are disturbed. The results are summarized in Table 2.6 and discussed below.

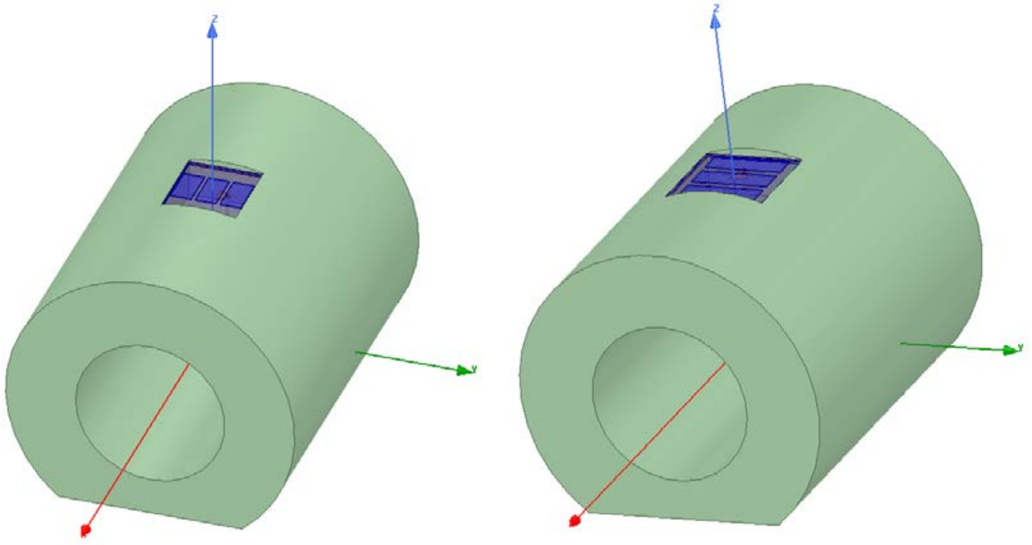

(a) Rectangular cavity (b) 50x50

Figure 2.31: Metasurface integrated into the cylindrical carrier

Aperture size	BW (MHz)	f_c (MHz)	Gain (dB)	HPBW (°)
$40 \times 45\ mm^2$	74	1579	4.24	107
$45 \times 40\ mm^2$	54	1578	4.35	95
$50 \times 50\ mm^2$	101	1574	4.47	102

Table 2.6: Metasurface-inspired antennas results after integration into a cylindrical carrier

The results obtained show that both the 50×50 mm^2 square antenna and the 40×45 mm^2 rectangular antenna have a bandwidth greater than 60 MHz, an essential requirement to cover the L1, E1 and G1 bands. However, the version of the rectangular antenna rotated 90° undergoes a degradation of the bandwidth, so it does not meet the requirements of this work. The most interesting aspect of these results is the increase of the HPBW. This means that the cylinder causes an lobe extension. This feature is beneficial for GNSS applications, since the antenna can reach more satellites in one hemisphere, even those located at lower altitudes. An example of the radiation patterns in two orthogonal planes caused by the integration of the antenna in the carrier cavity is given in Figure 2.32.

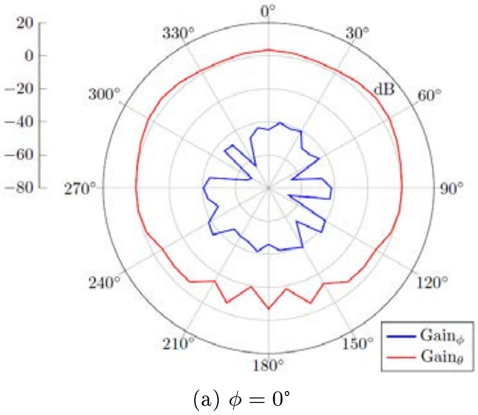

(a) $\phi = 0°$ (b) $\phi = 90°$

Figure 2.32: Radiation pattern for the metasurface antenna in a cavity of 40×45×20 mm^3 embedded into a metal cylinder with diameter 155 mm

For future research outside this thesis, it would be interesting the conception of an antenna using flexible substrates and patches to fit the antenna to the shape of the cylinder. An example of an array of antennas with flexible substrates for projectile applications is presented in [162].

2.6.2 Influence of a protective radome

Usually, microstrip patch antennas are not directly in contact with the environment to protect them from external agents. A radome is used for this purpose. For the integration of an antenna into a projectile, the radome prevents the antenna from being damaged in the shooting and from the air speed during flight. The radome is made of a material that affects as little as possible the electromagnetic properties of the antenna.

In our case, the chosen radome is made by polypropylene ($\varepsilon_r = 2.25$; $\tan(\delta) = 0.001$) [161], because it is the available material that has less influence on the antenna properties. The effect of the radome is simulated for two cavity sizes analyzed before, such as $40 \times 45 \times 20mm^3$ and $50 \times 50 \times 20mm^3$. Figure 2.33 shows the placement of the radome on the antenna after the integration into the carrier. The plastic piece has a curved surface that conforms to the curvature of the cylinder.

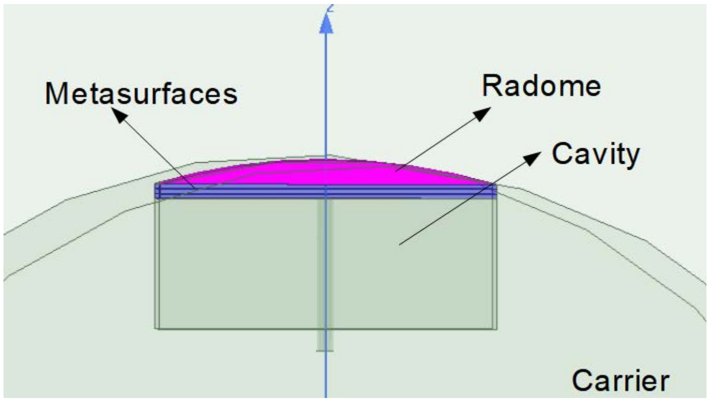

Figure 2.33: Simulation placement of the radome protecting the antenna

2.6.2.1 Radome for metasurface antennas in square cavity 50×50 mm^2

A numerical study has been carried out using the 50×50 mm^2 square aperture antenna and a radome placed on it. The numerical results for the reflection coefficient with and without radome are gathered in Figure 2.34. A re-optimization of the antenna by varying parameter g_1 (gap between patches) has been performed because the radome causes a slight resonance shift. The variation of this parameter is shown in the Table 2.7. Once the antenna matches to the central frequency 1578 MHz, the bandwidth hardly varies (3 MHz) compared to the radome-free antenna. The bandwidth with radome is 98 MHz and without radome 101 MHz.

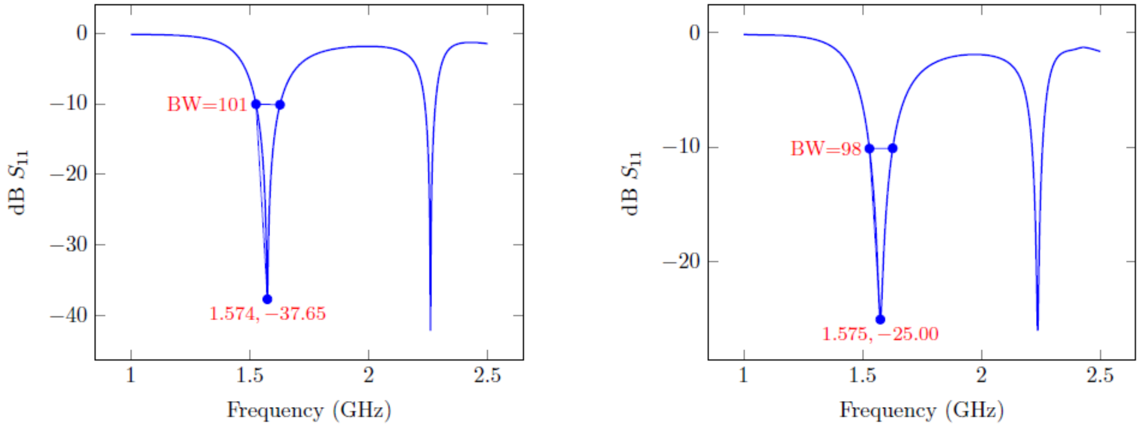

Figure 2.34: Simulate S11 parameter for metasurface antenna backed in a square aperture ($50 \times 50mm^2$) without (left) and with (right) radome

Regarding other parameters, the radome causes the gain to be slightly decreased and the HPBW increases. It can be concluded that this antenna maintains similar performances with and without radome. Therefore it is valid to cover 60 MHz to capture signals L1, G1 and E1 from GNSS satellites.

	f_p (mm)	g_1 (mm)	t_1 (mm)	t_2 (mm)	BW (MHz)	f_c (MHz)	Gain (dB)	HPBW (°)
No radome	13	4.3	8.5	8	101	1574	4.47	102
Radome	13	4.8	8.5	8	98	1575	4.21	115

Table 2.7: Comparison between metasurface antenna performances with and without radome for a square cavity

2.6.2.2 Radome for metasurface antennas in rectangular cavity 40×45 mm^2

A similar procedure to the previous one has been performed. The effect of a radome has been analyzed numerically on the 40×45 mm^2 rectangular antenna integrated in the metal cylinder.

Figure 2.35 represents simulated S11 parameter of the antenna integrated in the metal cylinder. Left-placed one corresponds to the simulation without radome and right-placed one the simulation with radome. The antenna bandwidth without radome is 74 MHz while with radome it is 61 MHz. This study shows that radome leads to slightly shift the resonance frequency. However, a readjustment of the gap between patches (g_1) allows the antenna to be matched to 1575 MHz. Therefore, it can be concluded that the bandwidth suffers a quite remarkable decrease, but it valid to cover the required bands. Table 2.8 represents the values of the variables and the final results of both simulations. As with the previous case, the gain is slightly decreased and the HPBW increased, reaching 123º for this antenna.

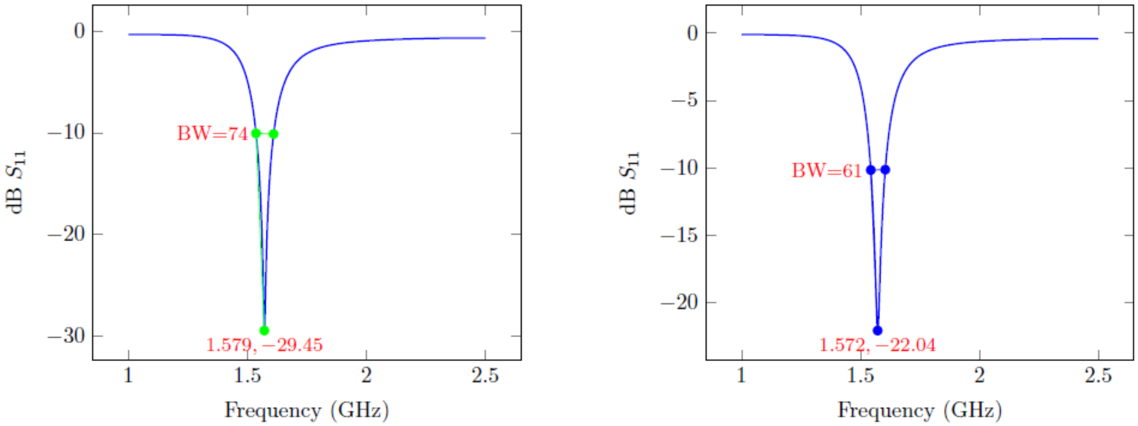

Figure 2.35: Simulate S11 parameter for metasurface antenna backed in a rectangular aperture ($40 \times 45mm^2$) without (left) and with (right) radome

	f_p (mm)	g_1 (mm)	t_1 (mm)	t_2 (mm)	BW (MHz)	f_c (MHz)	Gain (dB)	HPBW (°)
No radome	9	2.28	5	8	74	1579	4.29	107
Radome	9	2.57	5	8	61	1573	4.20	123

Table 2.8: Comparison between metasurface antenna performances with and without radome for a rectangular cavity

2.6.2.3 Discussion

The two studies carried out prove that the radome slightly affects the bandwidth of the antenna. However, the antennas still have sufficient bandwidth to cover the L1, E1 and G1 bands. The gain is slightly decreased in both cases but its value is enough for the correct operation of the antenna. A very beneficial result to get GNSS signals is the increase in HPBW, which causes a lobe opening and signals from a big number of satellites can be received.

2.7 Conclusion

This chapter has discussed the linearly-polarization antennas for GNSS applications. Specifically, an antenna that is capable of integration g into a metal cavity with a specified dimensions.

First, it has been proven that a microstrip antenna composed of a single patch does not meet the requirements. Similarly, the configuration based on two stacked patches also does not adapt to the expected dimensions and with the necessary bandwidth.

Two solutions based on metasurfaces have been presented. In this case it has been possible to obtain more than 60 MHz bandwidth with an aperture size of $0.21\lambda_0 \times 0.24\lambda_0$ and $0.26\lambda_0 \times 0.26\lambda_0$. This allows to cover E1, L1 and G1 with a small and compact antenna. Several prototypes have been manufactured that allow to verify the results obtained in simulation. The studied structure has smaller dimensions than the cavity antennas studied in the literature. The use of a metasurface loading the aperture reduces the dimensions of the antenna and the required bandwidth is achieved.

The changes produced by the carrier integration and the use of a radome have also been analyzed. GNSS required circular polarization antennas, however linear polarization antenna can be used for on-board flying platforms in multipath-free-environments. Although, circularly-polarized versions provides a better carrier-to-noise ratio (C_0/N_0), which is also required for ground purposes.

Chapter 3

Circularly-polarized metasurface antennas for GNSS

Linear polarization (LP) is the easier solution for an antenna design; because it can be achieved with simpler feeding techniques, simpler structures where the symmetry is not critical. However, some applications require circular polarization (CP). The antennas dedicated to receive the signals from GNSS systems should be designed in CP because the GNSS satellites antennas emit in CP, specifically in RHCP (Right-Handed Circular Polarization). LP antenna can be also used onboard flying platforms in multipath-free-environments, but the CP version provides a better carrier-to-noise ratio (C/N), which is also required for ground purposes.

In this chapter, a new metasurface-based design will be proposed to match with the CP criteria (axial ratio $<$ 3 dB for the entire frequency band). In addition to the criteria for obtaining circular polarization, the general requirements of this study set out in the introduction must be met. In short, the three bands of GNSS G1, L1 and E1 have to be covered, which implies a bandwidth of at least 60 MHz for an antenna backed in a metal cavity. Therefore, the designed-structure is a cavity-backed metasurface-inspired antenna in circular polarization.

In this chapter we discuss first the possible ways to obtain circular polarization applied to this case. A new metasurface design that allows to obtain circular polarization is presented in Section 3.1. This section includes the antenna composition and the feeding system which plays an important role for circular polarization. Then, two different aperture sizes are presented. A larger square aperture of 50×50 mm^2 and a smaller one of 40×40 mm^2. The simulation results for different number of excitation points are presented and discussed. The antennas that have presented better characteristics in simulation have been manufactured. Several prototypes are shown and analyzed during Section 3.2. Finally, the antennas are measured and compared with the simulation results in Section 3.3, and conclusions are drawn at the end.

3.1 Circularly-polarized metasurface antennas in cavity

As mentioned earlier in Chapter 1, the correct polarization of the antenna capturing geolocation signals is important. The use of circular polarization makes it possible to distinguish between signals coming directly from the satellite and multipath signals rebounded from Earth's surface. Therefore, these reflected signals can be mitigated by the system and avoid erroneous information. Taking into account the proper functioning of the antenna designed in Chapter 2, an update to circular polarization must be performed. The best way to start designing a circular polarized antenna is to look for geometric symmetry to excite two orthogonal TE modes. For them, the shape of the above-designed metasurface must be modified, because it does not have orthogonal symmetry. The antenna in square cavity is taken as a reference because of the adapted geometry. However, obtaining the circular polarization in the rectangular aperture antenna will be studied.

3.1.1 Circular polarization methods

If in linear polarization only the fundamental mode is excited, in circular polarization two modes are excited in two orthogonal directions with a phase difference of 90° between them. The two main ways to excited both modes are as following:

- A single feed point exciting an anisotropic surface, which couples the two modes together

In the case of a single feeding point, the metasurface becomes anisotropic by inserting a slot in each patch. Two examples of this type of metasurfaces are depicted in Figure 3.1. This introduces coupling between the two excited modes. Due to this coupling, two close resonances appear on S_{11} parameter, which causes a wide bandwidth. However, circular polarization is only achieved in the band between the two resonances. Therefore, in this investigations we will not use this technique because we need the circular polarization in the entire band. An example of this type of circular polarization generation embedded in aperture with an infinite ground plane is presented in [163], where the author shows an anisotropic metasurface composed of nine rectangular patches divided in two by a slot. The geometry of this metasurface (9 patches) is taken as an inspiration for the research presented in this chapter. There are another circularly-polarized structures using a single excitation point (presented in Chapter 1), such as trimmed patches or patches with a slot.

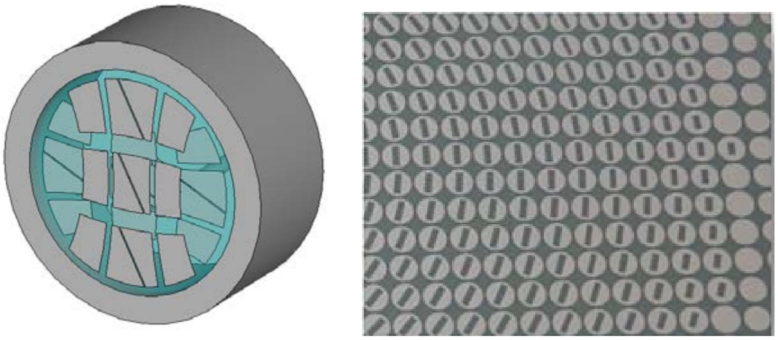
(a) (b)

Figure 3.1: (a) Finite ground plane circular cavity having an anisotropic two layer metasurface at the aperture [3]. (b) Anisotropic metasurface formed by circular patches with slots inside [24]

- Two uncoupled feed points, orthogonal in position and quadrature in phase shift

Circular polarization with two feeding points is based on the use of two phase quadrature sources that excite two orthogonal modes at the same time. Figure 3.2a depicts the arrangement of the feeding points for a patch antenna. The feed points are physically separated 90° from each other and are excited in phase quadrature by an external device (e.g., Wilkinson splitter, hybrid, etc.) which creates an offset of 90° on one of the two points.

Circular polarization can also be carried out with four excitation points, arranged as shown in Figure 3.2b. In this case, the symmetry of the antenna is improved and consequently, the axial ratio is enhanced. However, the required polarization circuit increases in complexity.

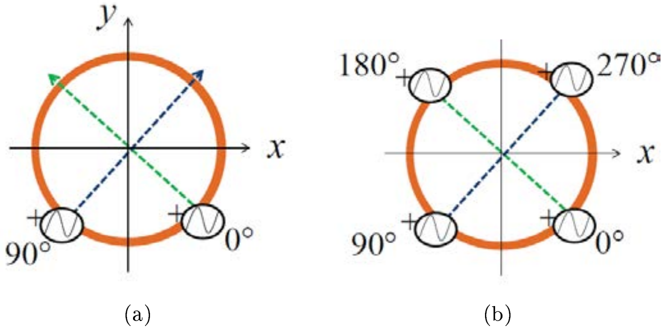

Figure 3.2: Circular polarization generation with (a) two and (b) four feeding points [25]

3.1.2 Antenna design in circular polarization

As mentioned above, the single-point feeding technique will not be used. Therefore, an antenna with multiple excitations will be designed. To this, the metasurface is adapted to excite the two orthogonal modes correctly and achieve the correct capacitance. The antenna structure, which is backed with a metallic cavity will be detailed in this section.

3.1.2.1 Preliminary studies for a rectangular aperture

Ideally, a square cavity offers better symmetry to obtain circular polarization. Moreover, in Chapter 1, the miniaturization to the rectangular aperture gave good results. Could CP be achieved with a structure similar to the LP rectangular aperture? To excite the orthogonal modes, two feed points 90° out of phase have been added. To obtain an identical structure for both polarization, we have also added a second metasurface layer rotated 90° compared to the first one. Figure 3.3 shows the 3D model of the solution proposed for the rectangular antenna in circular polarization. After many efforts to adapt the structure, we finally found that the circular polarization cannot be obtained because of the asymmetry presented by the structure. In addition, the bandwidth is reduced compared to the linear polarization counterpart. Therefore, this design is set aside, because it does not allow to achieve circular polarization. To ensure the symmetry, the cavity aperture is chosen to be square for the rest of the study.

For next studies, the 50×50 square aperture size antenna in linear polarized as defined in Chapter 2, is the starting point for the future designs, because it offers better symmetry to get circular polarization.

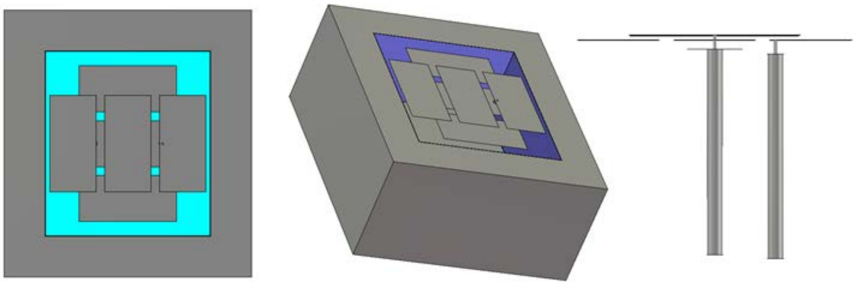

Figure 3.3: Metasurface inspired antenna backed on a rectangular cavity

3.1.2.2 Antenna structure for square aperture

Metasurface design

The LP antenna design is extended to circular polarization (CP) by replacing the rectangular strips loading the radiating aperture exposed in Chapter 2 by a matrix of 3×3 capacitively-coupled square patches (dimensions $L \times L$).

In other words, the surface is broken into pieces in both directions, forming an array of small patches, as shown in Figure 3.4. As in the LP case, the antenna have two layer of metasurfaces. Multiple layers make the metasurface a good capacitor allowing to reduce the cavity height or the thickness of the substrate. However, too many layers may decrease the bandwidth performances because the capacitance is “buried” into the cavity and cannot be regarded as being strictly at the aperture.

If a second excitation should be added to generate the circular polarization, the first excitation is duplicated and rotated 90° respect to the antenna center to excite the orthogonal mode. These two excitations should be 90° out of phase with respect to each other. Dimensions of the small patches L and the gap g between them ensure the same resonance frequency for both polarization modes.

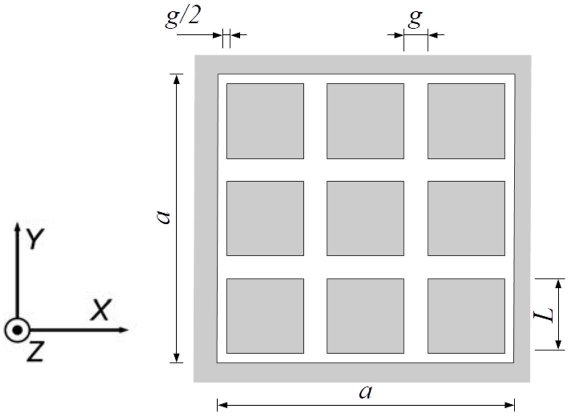

Figure 3.4: Metasurface design to achieve circular polarization for a square cavity

Antenna composition and materials

The metallic cavity is filled with two different materials, similar to the LP version presented in previous chapter. A general version without tanking into account the number of feeding points is depicted in Figure 3.5:

- A thick polypropylene layer ($\varepsilon_{r1} = 2.25$, $\tan(\delta) = 0.001$, $h_1 = 18.08$ mm, [161]) is selected to guaranty an adequate robustness to the structure, especially to satisfy the strong acceleration constraints supported by the flying platforms (several thousands of g),
- A thin lamination of three Rogers RO3210 substrates ($\varepsilon_{r2} = 10.2$, $\tan(\delta) = 0.0027$, $h_2 = 3 \times 0.64$ mm, [31]) with three metallic levels is included: the lowest one is the feeding layer, while the metasurface-inspired radiating element is printed on the two upper metallic layers; the upper substrate is thin enough (0.64 mm) to provide the requested capacitive effect and thus to enlarge the antenna bandwidth; both upper metallic layers have identical patterns. The dimension of the elements (L) is smaller than $\lambda_0/10$, which satisfies the metasurface criteria. Moreover, the loading capacitance of the radiating aperture can be adjusted by tuning the gap value g.

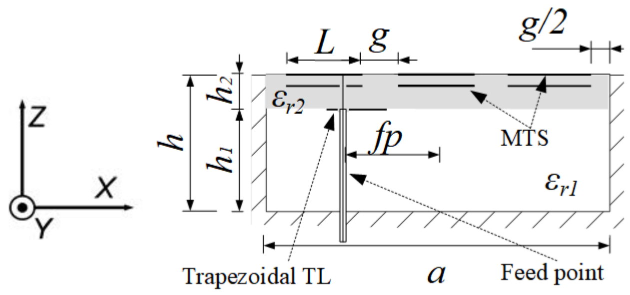

Figure 3.5: Cross-section view a CP antenna embedded in a square cavity

Antenna feeding

The trapezoidal transmission line (Figure 3.6) soldered to the coaxial feed which was used for the linear polarization antenna, is maintained here also. Each coaxial probe is provided with of one of these elements. The dimensions of this element allow adjusting the antenna matching, therefore, it will suffer variations depending on the number of excitations of the structure. In this chapter the cases of two and four excitations are presented. The variation of the piece shape for each model will be exposed in the section dedicated to each structure.

The excitation used is made of a coaxial probe adapted to 50 Ω with an outside diameter of 2.2 mm.

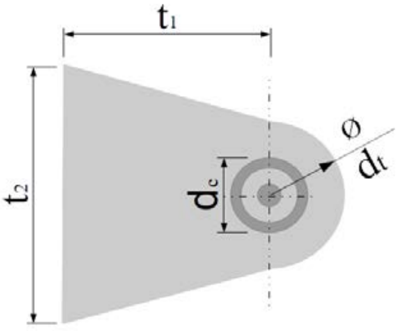

Figure 3.6: Trapezoidal transmission line is printed on the substrate to help its soldering to the coaxial cable

Design guidelines and parametric study

The gap g between the square patches is a fundamental design parameter since it allows tuning the metasurface capacitance loading the radiating aperture, and therefore the resonant frequency of the antenna and its efficiency. The feed parameters (f_p, t_1, t_2, Figures 3.5 and 3.6) are also optimized to improve the antenna matching level and impedance bandwidth, where f_p is the feed point position from the center of the antenna. A parametric study showing the influence of g and f_p is developed below.

Figures 3.7 and 3.8 illustrate the influence of these two critical design parameters (g and f_p respectively) on the reflection coefficient at one of the input ports, assuming that all other dimensions are fixed and equal to their optimal values specified. Note that, by symmetry, the reflection coefficients are the same at each input port ($S_{11} = S_{22}$). Figure 3.7 confirms the very strong impact of g on the resonance frequency, while Figure 3.8 shows that f_p has a less important effect on the resonance frequency values, but a stronger impact on the matching level.

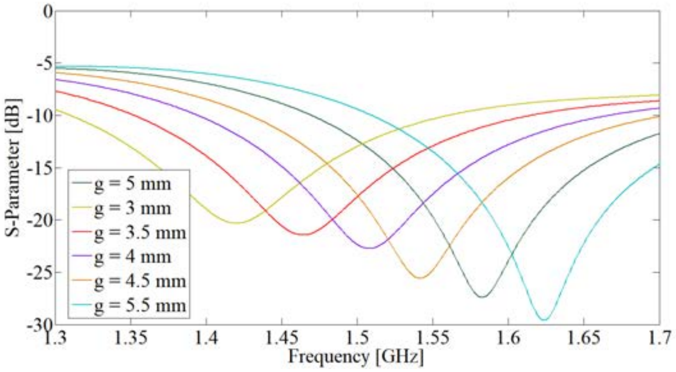

Figure 3.7: S11 parameter variations when g parameter varies and f_p, t_1, t_2 are fixed

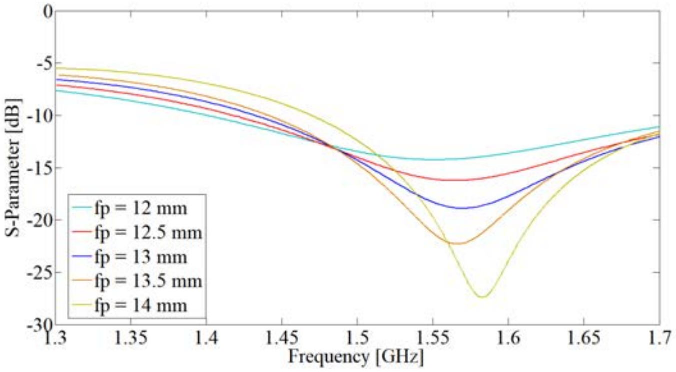

Figure 3.8: S11 parameter variations when f_p parameter varies and g, t_1, t_2 are fixed

3.1.3 Simulation results for a square cavity

The numerical results and the final structure for two different aperture sizes are presented below. Firstly, the results of the 50×50 aperture will be developed in two cases: with 2 and 4 feeding points. Secondly, simulation results for a smaller aperture size (40×40) are displayed. In this second case, the study is only performed for an antenna with 4 feeding points.

3.1.3.1 Aperture size of 50×50

As mentioned above, two different cases will be treated in this part. First, a study with two feeding points has been carried out. The initial goal is to simplify the design, since two 90°-shifted feeding points offer a simple structure to create circular polarization. After the results obtained for two feeding points, the creation of a sequential polarization with 4 excitations has been investigated. The numerical results for both structures are presented below.

Two feeding points

A design with two feeding points consists in a structure with only the port #1 and #2 as described in Figure 3.9. This design presents a similar structure to the one mentioned in the previous chapter. The metallic cavity is almost completely filled by polypropylene as shown in Figure 3.9b. On the top, as in

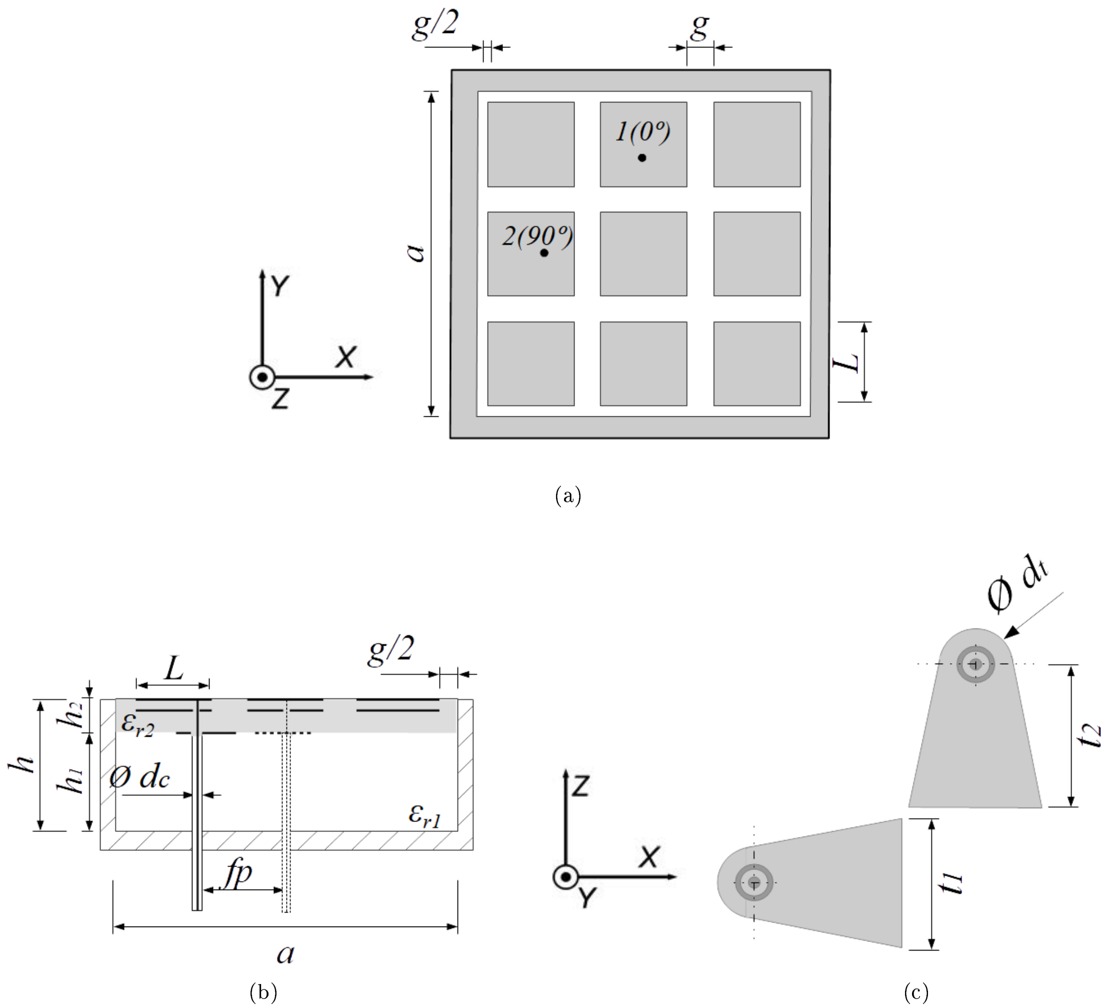

(a)

(b)

(c)

Figure 3.9: Circularly-polarized antenna backed in a square cavity with two feeding points. (a) Top view. (b) Cross section. (c) Feeding layer formed by two metallic pieces

linearly-polarized structure, two metasurface layers composed each of nine square patches with length L are etched on a thin layer of Rogers 3210 substrate. Finally, the third layer consists of two fin shape metallizations soldered to the outer connector of the feeding coaxial cables. These shapes are orthogonal to each other to contain both coaxial probes, as shown in Figure 3.9c.

In this case, the gap g between square patches is one of the fundamental parameters. The variation of this parameter allows to increase or decrease the capacitive effect of the metasurface to adjust the antenna matching. As mentioned before, the distance between the feed point to the center of the aperture (f_p), as well as the dimensions of the trapezoidal transmission lines (t_1 and t_2) are the key parameters for optimization. The antenna is designed tanking into account the behavior of g and f_p exposed in the previous parametric study. Parameters t_1 and t_2 are then adjusted to obtain a good matching level. Table 3.1 shows the values of these parameters, among the others, for the optimized design.

After matching the antenna and in spite of the two feeding points in phase-quadrature, the axial ratio could not be reduced enough. It remains greater than 3 dB at the central frequency (1578 MHz) and for

Parameter	Value	Parameter	Value
a	50 mm	t_1	7.8 mm
h_1	18.08 mm	t_2	1.9 mm
h_2	1.92 mm	ε_{r1}	2.25
f_p	14 mm	ε_{r2}	10.2
L	13.6 mm	d_t	4.5 mm
g	6.25 mm	d_c	2.2 mm

Table 3.1: Optimized dimensions of the 50×50 mm^2 square cavity-backed antenna with two excitation points

the frequencies below 1600 MHz. The plot for the axial ratio is depicted in Figure 3.10. Due to the axial ratio drawback of this structure, a new design with four feeding points is proposed which is presented in the following section.

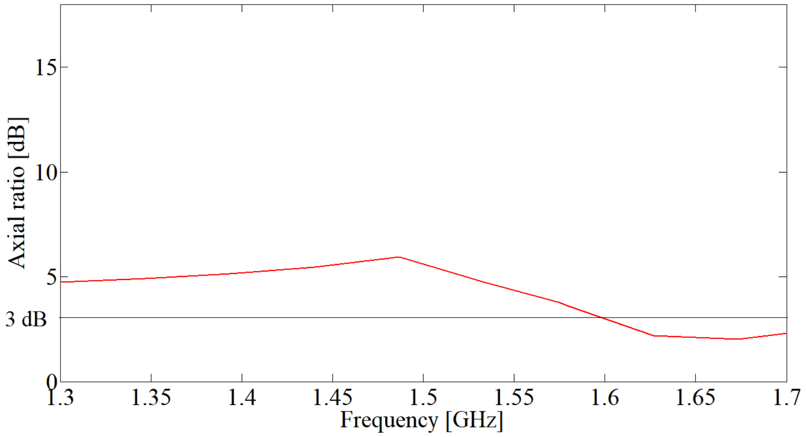

Figure 3.10: Axial ratio of the CP antenna feeds by 2 ports

Four feeding points

Due to the poor axial ratio obtained using two excitations, a new structure with four has been designed. Having four feeding points causes a sequential polarization that ensures the circular polarization. However, the risk of coupling between the ports is greater.

The design guidelines described above has been used for the optimization of this antenna. As in the previous case, the metasurface is composed of nine square patches of area L×L arranged in a 3×3 matrix. The main change of this structure with respect to the previous one is the feeding system. Firstly, the feeding points have been doubled to 4. The excitations are arranged forming a "circle" with 90° shift between ports, i.e., in 0°, 90°, 180° and 270° positions. As mentioned above, each coaxial probe is connected to a trapezoidal metal piece (transmission line), therefore 4 pieces are needed in this case. For the 2 excitation structure, the two transmission lines are not connected to each other. However, in this circumstance it has been decided to join them creating a 4-pointed star shape lamination (Figure 3.11c). This change helps to increase the capacitive effect of the antenna, thus the bandwidth. Likewise, the dimensions of this metallization are used to fine-tune the antenna matching.

Figure 3.12 shows the 3D model of the structure to obtain the numerical results. The dielectric on

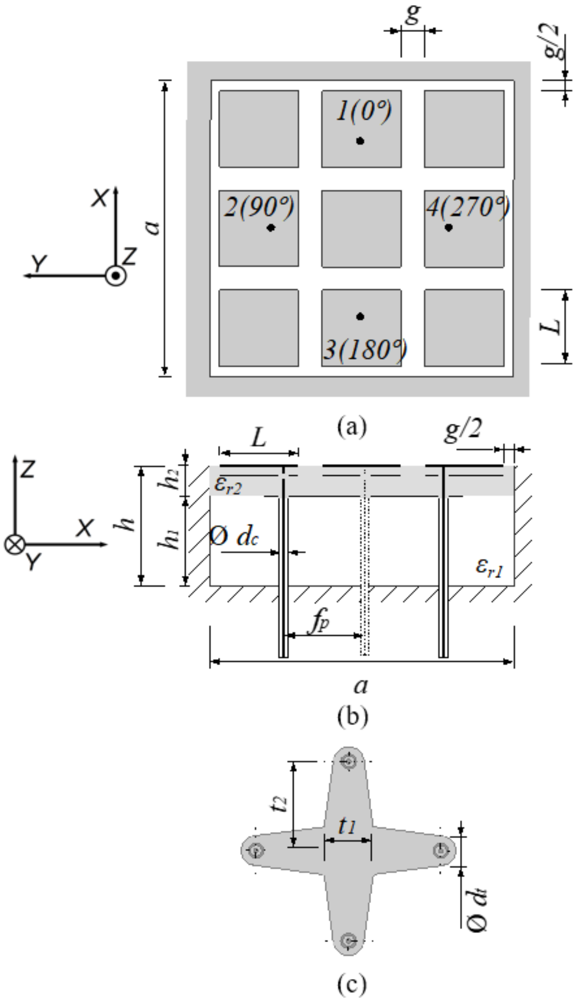

Figure 3.11: CP antenna embedded in a square cavity of 50×50×20 mm^3. (a) Top view. (b) Cross-section view. (c) Feeding metallization

which the patches are printed has been set on transparency to appreciate the different layers. Polypropylene has been included in the cavity since the use of an empty cavity is not possible for mechanical reasons. However, trying to adapt as much as possible to the original idea (cavity filled with air), the minimum amount of polypropylene to ensure robustness has been placed. Polypropylene has been chosen for being a resistant plastic, accessible, light and having little electromagnetic interference. In Figure 3.12 the yellow part (polypropylene) can be distinguished from the blue block (air). The purple layer between polypropylene and the cavity corresponds to the glue used to sick the layers. This glue (estimated to $\varepsilon_r = 3.5$, $\tan(\delta) = 0.01$, $h = 0.1mm$) has been taken into account in the simulation results.

The final dimensions of the optimized design are provided in Table 3.2. The results obtained with these dimensions are presented below.

The results obtained for bandwidth are discussed below. The structure achieves 280 MHz bandwidth as shown in Figure 3.13a, which means 16% bandwidth. Due to the perfect symmetry of the antenna, the simulated reflection coefficients are the same on each port ($S_{11} = S_{22} = S_{33} = S_{44}$). However,

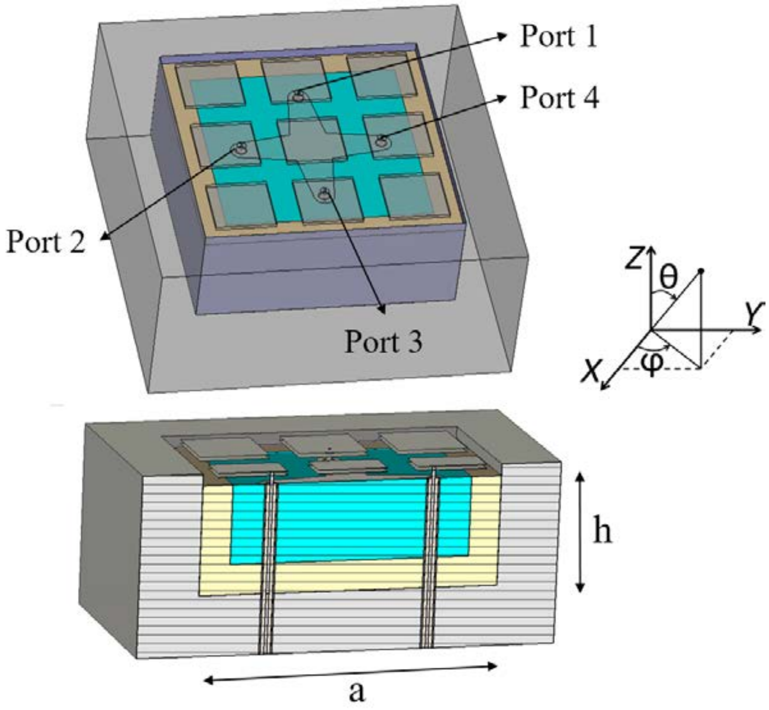

Figure 3.12: Simulation design in CST of the circular polarization CP antenna backed in a metallic cavity with four feeding points

Parameter	Value	Parameter	Value
a	50 mm	t_1	8 mm
h_1	18.08 mm	t_2	13.5 mm
h_2	1.92 mm	ε_{r1}	2.25
f_p	13.5 mm	ε_{r2}	10.2
L	11.6 mm	d_t	4 mm
g	5 mm	d_c	2.2 mm

Table 3.2: Optimized dimensions of the 50×50 mm^2 square cavity-backed antenna with four excitation points

this configuration presents a strong coupling, especially for the ports facing each other. Figure 3.13b represents the coupling between ports where $S_{ij} = S_{ji}$. The lower line (green) corresponds to the transmission coefficients of the contiguous ports ($S_{12} = S_{14} = S_{23} = S_{34}$) where the coupling is not so considerable. The upper curve (pink) shows the strong coupling between opposite ports, where the transmission coefficient is approximately -4 dB. The bandwidth increase is attributed mainly to this coupling. Multiport coupling will be discussed in more detail in Chapter 4.

The gain is presented in Figure 3.14. This antenna offers a simulated realized gain lower than 3 dBic. However, it is enough for GNSS applications. The axial ratio obtained in simulation is ideal, practically zero for the whole band. This is due to the use of an ideal phase difference between ports and the perfect symmetry of the structure. In the experimental results section, the axial ratio obtained for a real case

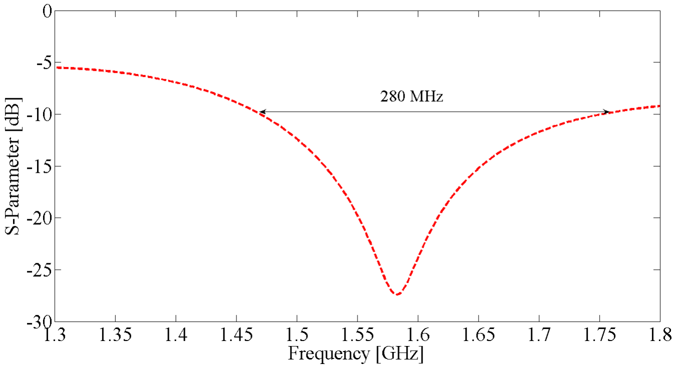

(a) Sii

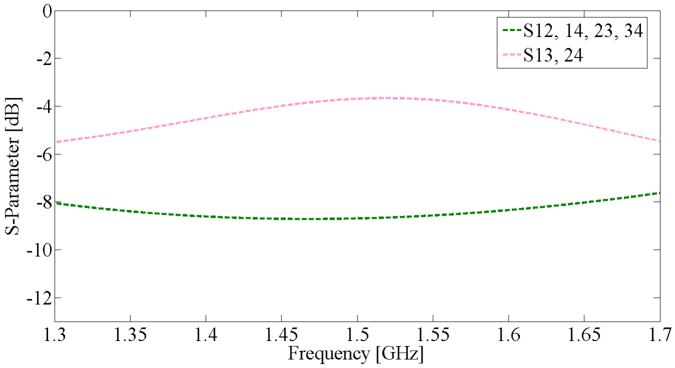

(b) Sij

Figure 3.13: Reflection and transmission coefficients of the metasurface-inspired cavity antenna with four excitations

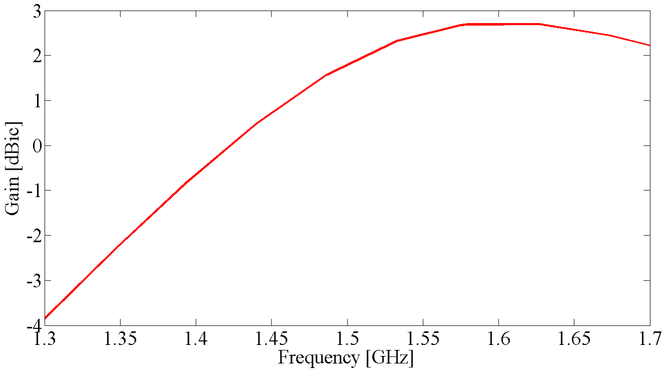

Figure 3.14: Simulated gain of the square metasurface antenna in circular polarization

will be shown.

The radiation patterns for two different cut-planes are presented in Figure 3.15, where Figure 3.15a

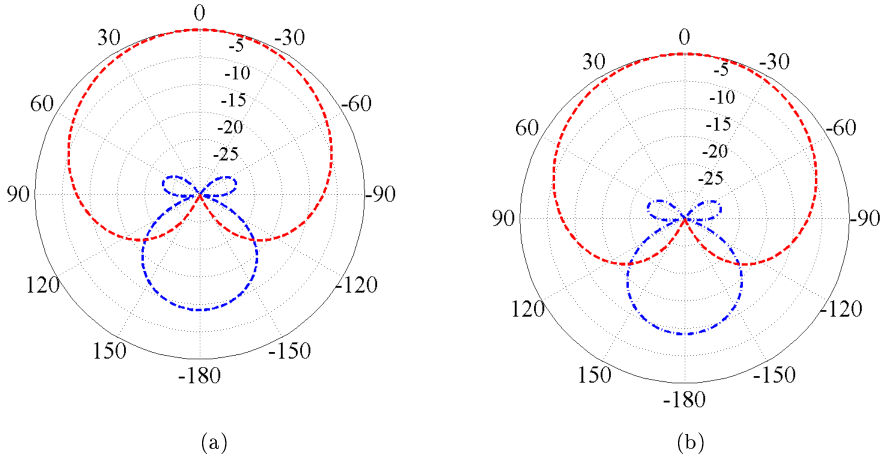

Figure 3.15: Computed normalized radiation patterns in dBic at 1578 MHz in two vertical cut planes: (a) φ=0°, (b) φ=90°. RHCP in red, and LHCP in blue

correspond to the plane $\varphi = 0°$ and Figure 3.15b to the plane $\varphi = 90°$. Radiation pattern offers good results with very low cross-polarization discrimination level ($<$ 18 dB for elevation angles smaller than 60°). Due to the symmetry of the antenna, both planes are identical. The half power beamwidth (HPBW) is 120° for both planes.

3.1.3.2 Aperture size of 40×40

The previous results show that the bandwidth obtained for the 50×50 antenna is much larger than the 60MHz needed to cover the GNSS bands. Therefore, a miniaturization at 40×40 seems to be a better choice for smaller carriers and projectiles. Due to the inconclusive results of the previous structure with 2 feeding points, miniaturization at 40×40 will only be studied in the case of 4 excitations. The antenna structure is exactly the same as shown in the Figure 3.11. But some parameter values change because of the structure miniaturization.

Parameter	Value	Parameter	Value
a	40 mm	t_1	8 mm
h_1	18.08 mm	t_2	12.5 mm
h_2	1.92 mm	ε_{r1}	2.25
f_p	12.5 mm	ε_{r2}	10.2
L	11.37 mm	d_t	4 mm
g	1.9 mm	d_c	2.2 mm

Table 3.3: Optimized dimensions of the 40×40 mm^2 square cavity-backed antenna with two excitation points

The main parameters used to optimize the antenna performance at 1578 MHz are the following: gap between the square patches g, which also depends on the patch dimensions L for a fixed cavity edge a; dimensions of the star around the feeding points (t_1, t_2); finally, the distance between these feed points and the center of the aperture (f_p). The optimization criteria is to minimize the reflection coefficient at the frequency of 1578 MHz. The optimized values for all the parameters are given in Table 3.3.

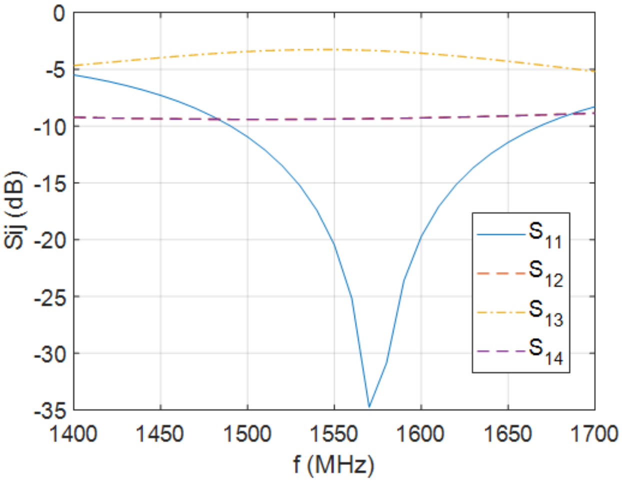

Figure 3.16: Simulated reflection coefficient and mutual coupling between adjacent and opposite ports of the 40×40 CP antenna with four excitations

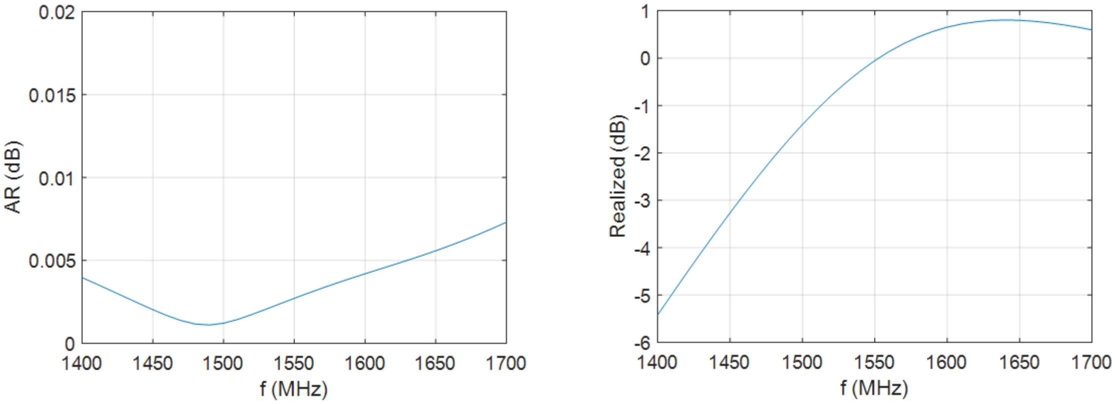

(a) (b)

Figure 3.17: (a) Simulated axial ratio (AR) and (b) realized gain

The simulated S-parameters of the optimized structure are represented in Figure 3.16 (for symmetry reasons, only part of the S-matrix coefficients are plotted). The achieved -10 dB BW is equals to 180 MHz. Due to the short distance between feed points, a strong mutual coupling is observed, especially between opposite ports (1-3 and 2-4). The antenna axial ratio (AR) and realized gain are represented as a function of frequency in Figure 3.17a and Figure 3.17b, respectively. As expected, RHCP quality is almost ideal due to the ideal sequential rotation excitation law. The maximum realized gain is about 0.8 dB (maximum achieved at 1630 MHz); this moderate low value originates from the small cavity size ($0.21\lambda_0 \times 0.21\ \lambda_0$). The radiation patterns computed at the center frequency are presented in Figure 3.18 in co- and cross-polarizations. The full half power beamwidth equals 112° in both principal planes.

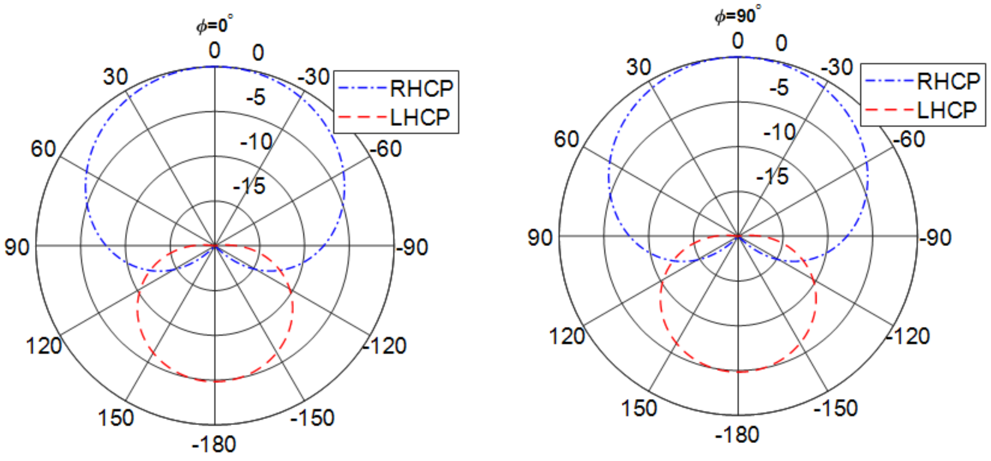

(a)

(b)

Figure 3.18: Simulated radiation patterns at 1578 MHz in both principal planes. φ =0° (a) and φ=90° (b).

3.1.4 Discussion

Two aperture sizes have been presented for the circularly-polarized antenna based on metasurfaces: 40×40 mm^2 and 50×50 mm^2.

In the first case, the antenna with 50×50×20 mm^3 cavity has been analyzed in two different cases: two and four feeding points. Using two orthogonal feeding points is a simple way to generate circular polarization in a patch antenna. However, in this case, circular polarization is not good enough for the required frequency range (155 MHz - 1610 MHz). To solve this problem, an antenna with 4 excitations has been studied. Due to the generation of a sequential excitation, circular polarization is almost ideal for the entire frequency range. The bandwidth of this simulated antenna is 280 MHz. Despite having a wide bandwidth, the existing coupling between the ports in a small cavity is considerable. Precisely this coupling could be the cause of the large bandwidth.

Due to the good results obtained for the above-mentioned antenna, a structure integrated in a smaller cavity (40×40×20 mm^3) has been studied. After readjusting the dimensions of the antenna, a strong coupling between ports is also observed for this design. The bandwidth is wide enough (180 MHz) to cover the GNSS bands between 1550 MHz and 1610 MHz. It could be thought that the antenna could be even more miniaturized because the obtained bandwidth is twice the required one. However, if the antenna is too small, the separation between ports is even smaller and the resulting coupling could cause an inefficient antenna.

3.2 Prototyping

To verify the good results obtained in simulation, the two antennas with 4 feeding points have been manufactured at ISL laboratories. The photograph in the Figure 3.19 depicts a sample of the prototypes made. Two versions of this model have been manufactured and tested: aperture sizes 40×40 and 50×50.

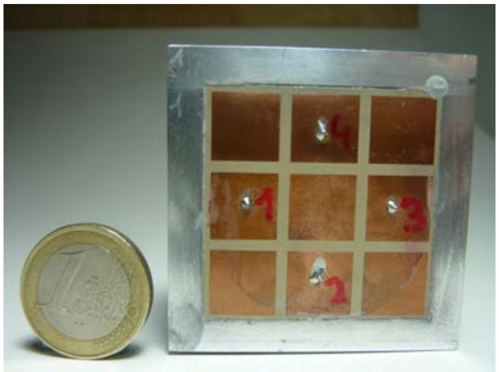

Figure 3.19: Prototype manufactured for the circularly-polarized metasurface antenna for GNSS with cavity dimensions 40×40×20 mm^3

3.2.1 Part by part presentation

3.2.1.1 Cavity

The prototype cavity is formed by four walls of 5 mm thick forming a quadrilateral with 90° angles. As Figure 3.20a shows, the metal cavity is made as a frame, without the bottom. The design has been designed to facilitate the inclusion of the rest of the elements and the coaxial cable. The cavity frame is closed in the bottom by a FR4 plate with double copper face, as depicted in Figure 3.20b.

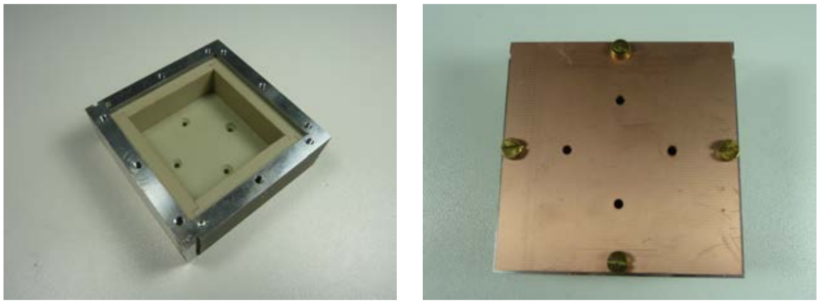

(a) (b)

Figure 3.20: (a) Cavity with polypropylene blocks. (b) Bottom cooper part of the cavity

3.2.1.2 Dielectrics materials

As explained in previous sections, polypropylene has been chosen to provide robustness to the antenna. Ideally, the best results are obtained if the bottom of the cavity is filled with air. However, its manufacture is not possible because the metasurfaces must be held strongly by something. Polypropylene is a thermoplastic polymer belonging to the group of polyolefins and is partially crystalline and non-polar. Polyethylene has similar characteristics, but it is slightly harder, more heat resistant and mechanically rugger. The polypropylene has been inserted by blocks forming a wall around the cavity and a base at the bottom, as the Figure 3.20a presents.

Figure 3.21: Star-shape metallization for coaxial probes connection

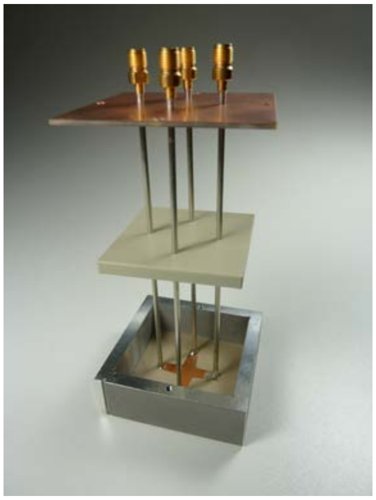

Figure 3.22: Assembly of the different parts of the antenna

3.2.1.3 Microstrip layers

The two layers of metasurface and the microstrip connection line have been manufactured independently following the technique of microstrip antennas. Each design has been printed on a 0.63 mm thick dielectric layer and relative permittivity 10.2. The dielectric belongs to the Rogers 3200 series and it is a ceramic-filled laminates reinforced with woven fiberglass. The three are glued together with the metallization face down in the case of the connection line. The layers of the metasurface are depicted in Figure 3.19 and the star-shape metallization to welded the coaxial cable is shown in Figure 3.21.

Finally every part is assembled inside the cavity as the Figure 3.22 shows. The coaxial cables are welded to the patches and to the FR4. This plate is screwed with the cavity to ensure good contact. A liquid glue is applied to seal all components and cover small holes that may remain.

3.2.2 Antenna feeding circuit

A microwave circuit is designed to ensure the required phase shift between feed of this antenna. A synoptic schema describes it in Figure 3.23a and a photograph is given in Figure 3.23b. The signals received by the four-port antenna are combined by the commercial splitter SCQ-4-1650+ [164] that ensures the RHCP of the antenna by applying a phase shift of 90° between the adjacent input ports. The next element in the signal chain is a BGA725L6 low noise amplifier (LNA) [165] for GNSS applications. The circuit contains also a TCBT-6G+ bias tee [166] component used to deliver DC current to the LNA. The circuit is assembled in a 60×60 mm^2 plate (Figure 3.23b) where the coaxial cables are placed in the opposite side of the feeding points. Measured magnitude and phase of the transmission coefficient for the whole polarization circuit are given in Figures 3.23c and 3.23d, respectively. The whole feeding circuit adds between 9 dB and 10 dB of gain to the antenna for the working frequency range (1550-1610 MHz). Figure 3.23d shows the phase difference of $\Delta\phi = 90° \pm \delta$ between two adjacent ports at the circuit output (point a in Figure 3.23a).

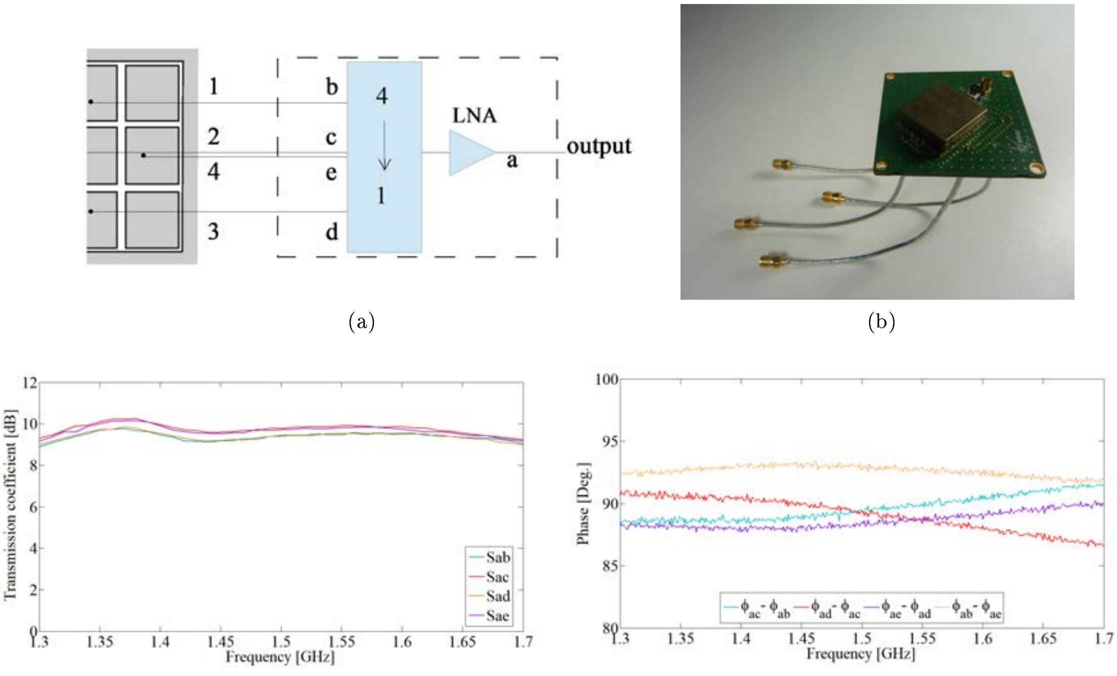

(a) (b)

(c) (d)

Figure 3.23: (a) Synoptic schema of the polarization circuit. (b) Real polarization circuit on a 60×60 mm plate. Transmission coefficient amplitude (c) and phase (d) of the whole polarization circuit.

3.3 Measurements and experimental results

The manufactured prototypes have been measured using the VNA and the anechoic chamber for the farfield, as is depicted in Figure 3.24.The results for both the larger cavity (50×50) and the small cavity (40×40) are shown below.

3.3.1 Larger aperture

The experimental results obtained for 50×50 aperture antenna are presented below. The antenna prototype (Figure 3.24) has been manufactured and measured. As for the LP antenna, thin layers of liquid dielectric glue have been used to assemble both dielectric layers and attach the antenna stack-up to

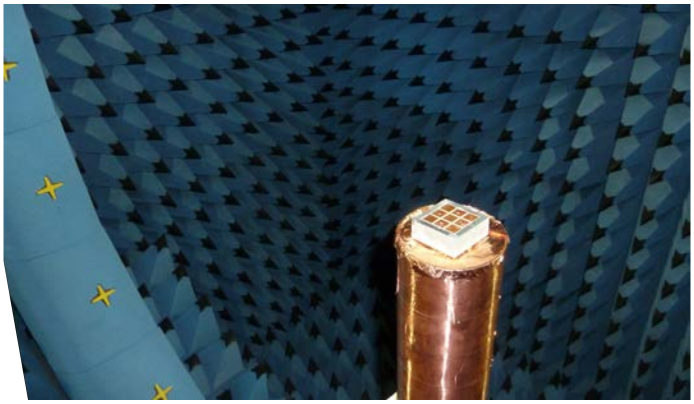

Figure 3.24: Photograph of the manufactured prototype in a Satimo Stargate anechoic chamber

the cavity walls. The four coaxial probes used to excite the antenna module are soldered as defined in Figure 3.11.

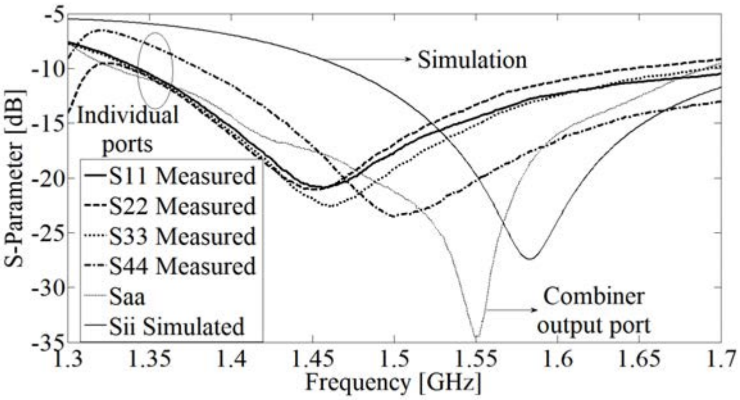

Figure 3.25: Reflection coefficients measured at each input port of the CP antenna, and comparison with the simulated data. The reflection coefficient measured at the combiner out port is also shown

The measured and computed scattering parameters are represented in Figure 3.25. S_{11}, S_{22}, S_{33} and S_{44} represent the measured reflection coefficients at each antenna port, while S_{ii} represents the simulated result. S_{aa} corresponds to the measured reflection coefficient at the output of the active combiner circuit connected to the antenna ports (see section 3.2.2). The antenna is well matched at each port, and the frequency shift observed between simulations and measurements is attributed to mechanical tolerances and material characteristics (e.g. losses in glue among others). The measured -10-dB reflection bandwidth is about 260 MHz. This quite large bandwidth (compared to the LP antenna) is attributed to the strong mutual coupling between ports, especially between two opposite ports, as shown in [69].

The total gain of the antenna module, including the LNA gain, is plotted in Figure 3.26 (left scale). Its average value is around 15 dBic at the center frequency. The axial ratio measured at broadside (Figure 3.26, right scale) remains below 3 dB between 1380 MHz and more than 1700 MHz, and below 2 dB between 1540 MHz and 1655 MHz. The axial ratio value at 45° in elevation remains below 3 dB between 1500 MHz and 1650 MHz. The normalized radiation patterns measured and simulated at 1578 MHz are plotted in Figure 3.27 in RHCP (co-polarization) and LHCP (cross-polarization). The agreement

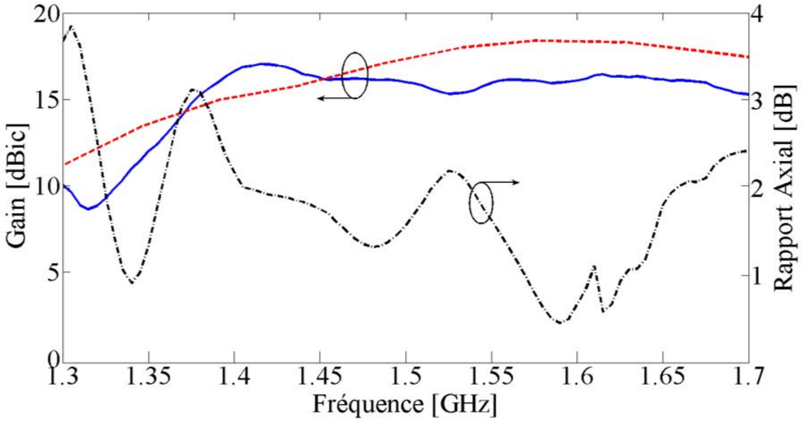

Figure 3.26: Performance of the antenna module with its feeding system (Figure 3.23b). Left: measured and computed gain. Right: measured axial ratio

between simulations and experiments is very good, with a very low cross-polarization discrimination level (< 18 dB for elevation angles smaller than 60°). The HPBW is 105° for plane $\varphi = 0°$ and 115° for plane $\varphi = 90°$.

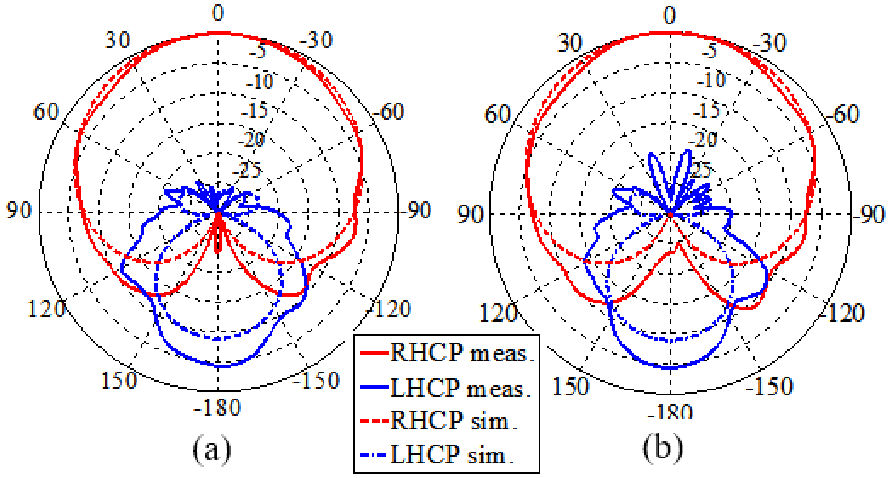

Figure 3.27: CP antenna: measured (solid line) and computed (dotted line) normalized radiation patterns in dBic at 1578 MHz in two vertical cut planes: (a) $\varphi = 0°$, (b) $\varphi = 90°$. RHCP in red, and LHCP in blue

3.3.2 Smaller aperture

The experimental results obtained for 40×40 aperture antenna are presented below.

The measured reflection and mutual coupling coefficients are represented in Figure 3.28. Despite the slight frequency shift (< 55 MHz), the antenna is well matched on all ports, and the measured -10-dB is broader (~120 MHz) than requested (60 MHz), although it is narrower than expected (180 MHz).

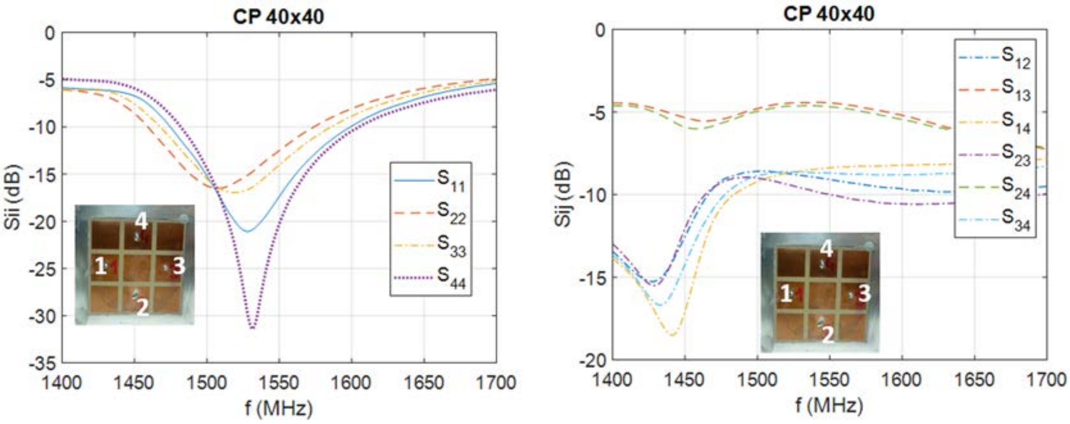

(a)

(b)

Figure 3.28: Measured reflection coefficients (a) and coupling between adjacent ports and between opposite ports (b)

Port	f_{min} (MHz)	$S_{ii}@f_{min}$ (dB)	BW (MHz)
1	1528	-21	124
2	1507	-16.5	113
3	1519	-16.9	119
4	1532	-31.3	123

Table 3.4: Measured resonance frequency, matching level, and -10dB bandwidth

As expected from the simulation, the coupling between opposite ports is high (around -5dB), whereas the coupling between two adjacent ports is around -9dB. Table 3.4 summarizes the results obtained after analyzing the reflection coefficient at each port. The matching frequency slightly differ between the different ports. This may be due to the manufacturing process where some asymmetries may have occurred in the glue or weld process.

The radiation patterns measured at 1578 MHz are given in Figure 3.29, and the measured HPBW (110°) is in good agreement with the expected value (112°) for both planes. The measured axial ratio is given in Figure 3.30; its values is lower than 3 dB between 1300 MHz and 1670 MHz. These results validate the principle of this small CP antenna.

3.3.3 Discussion

In conclusion, both prototypes (sizes 50×50 and 40×40 with four excitations) present good agreement comparing with the results obtained in simulation. The antennas have been measured including a polarization circuit which generates the phase shift between ports by means of a 4-ports combiner. Due to possible asymmetries during manufacturing processes, ports have slightly different reflection coefficients. However GNSS bands are covered in both cases. Both structures offer good RHCP radiation for the upper hemisphere, although LHCP is stronger in experimental results than in numerical results.

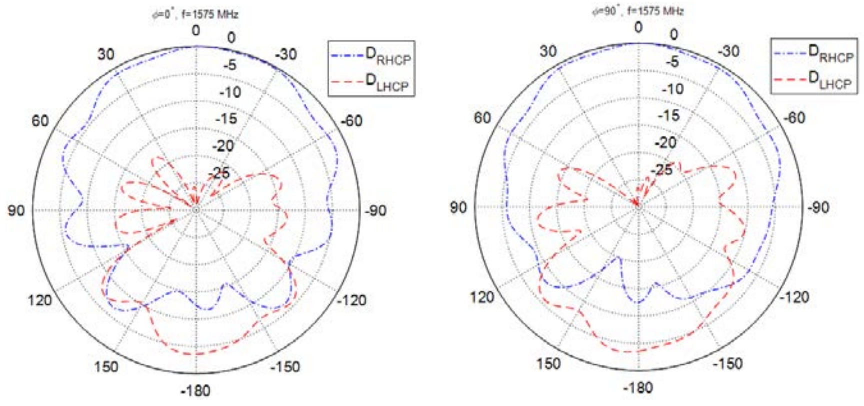

(a) (b)

Figure 3.29: Measured radiation patterns at 1578 MHz in both principal planes. $\varphi = 0°$ (a) and $\varphi = 90°$ (b).

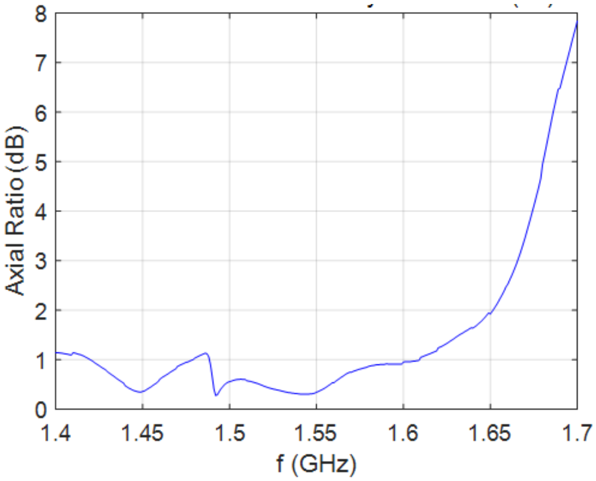

Figure 3.30: Measured axial ratio

3.4 Conclusion

In this chapter a solution in circular polarization has been introduced. Following the same criteria as in the previous chapter, two functional structures have been designed

First, it has been shown that with a symmetrical structure circular polarization is easier to generate, so the square cavity has been chosen to continue the study. The use of two or four feeding points has been investigated. However, the antennas with four excitations have given acceptable results.

A compact RHCP cavity-backed metasurface-inspired antenna with cavity dimensions $0.26\lambda_0 \times 0.26\lambda_0 \times 0.11\lambda_0$ ($50 \times 50 \times 20$ mm^3), covering three different GNSS bands with a single radiating aperture, has been proposed at 1578 MHz. The radiating aperture is loaded by a two-layer array of square patches excited by four feed ports in phase quadrature. This antenna concept has been introduced by first studying a similar antenna system, but operating in linear polarization. The LP antenna can be used onboard flying platforms in multipath-free-environments, while the CP version provides a better carrier-to-noise ratio (C/N), which is also required for ground purposes. The experimental results obtained in RHCP have shown an excellent agreement with the numerical predictions. The proposed antenna is able to sufficiently cover the three GNSS bands (L1, E1, G1) with an active gain of 16 dBic and an axial ratio lower than 1.6 dB over this frequency range ([1550 – 1610] MHz).

Due to the good results obtained for the previous antenna, a miniaturization has been carried out. A structure of dimensions $0.21\lambda_0 \times 0.21\lambda_0 \times 0.11\lambda_0$ ($40 \times 40 \times 20$ mm^3) has been presented. This new, more compact structure also offers very good results in both simulation and experimentation. However, the coupling of the ports is larger due to the small size of the cavity, which makes it lose in efficiency.

Therefore, both antennas are valid for GNSS applications by uploading the bands E1, L1 and G1. Could the rest of the GNSS bands (E5, E6, G2, G3, L2 and L5) be covered with a similar antenna? This case will be studied in the next chapter.

Chapter 4

Multiband antennas for GNSS

In Chapters 2 and 3 different designs of linear polarization and circular polarization antennas have been presented. These structures cover the GNSS bands E1, L1 and G1 located in the upper L-band, concretely between 1559 MHz and 1610 MHz (Figure 4.1). However, Galileo, Glonass and GPS constellations have other bands in the lower L-band, as presented in the GNSS-dedicated section of Chapter 1. Therefore, this chapter aims to create an antenna able to cover the whole set of GNSS bands, i.e. from 1164 MHz to 1610 MHz. Capturing more signals from different systems with a single antenna allows obtaining geolocation information in a faster, more accurate and secure way, as well as accessing other services. This configuration offers extended capacity in case of the jamming of one system.

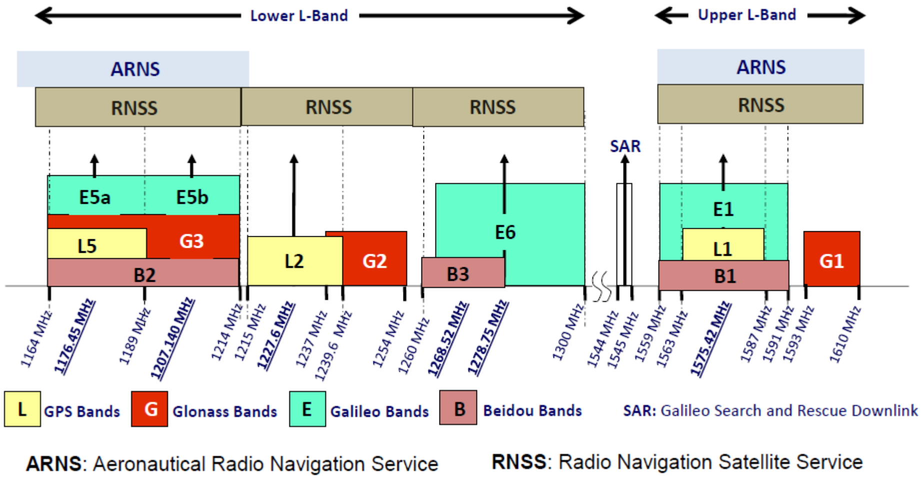

Figure 4.1: GNSS frequency bands distribution [1]

Similar to the cases presented in the previous chapters, the antenna must be integrated into a metal cavity, which causes bandwidth reduction. However, the confinement provides isolation and robustness, necessary for the integration in fast-flying vehicles, as projectiles. The final support of the antenna will be a cylinder with diameter 155mm, so the dimensions of the antenna are limited: ideally the cavity should not have dimensions greater than 50×50×20 mm^3. The goal is to design an antenna as small as possible that can meet these specifications. Circular polarization is chosen to adapt the antenna to the characteristics of the GNSS signals. However, some preliminary studies on linear polarization can be performed.

The ideal situation to obtain a multiband antenna is to create a resonance close to the resonance already obtained for the upper L-band. The union of these two bands would create a broadband that covers all systems. Another option is to get two bands a little more straight; one for the upper L-band and the other one for the lower L-band.

Different techniques to achieve the goals have been tested. The simulation results for the selected structure will be presented in this chapter. Afterwards, a prototype is manufactured and measured. Some problems such as coupling and miniaturization are discussed in this chapter.

4.1 Structures to achieve multiband performances

Maci and Gentili compile in [7] different ways to create a double resonance in patch antennas. Figure 1.36 presents these techniques divided in three groups: orthogonal-modes, multi-patch and reactively loaded. However, in the case of an antenna integrated in a cavity acting as a ground plane, the cavity can also be modified to obtain a multiband structure. In this section some techniques will be studied both in linear polarization and in circular polarization.

A preliminary study of different linear polarization structures inspired by designs from the literature is exposed. The objective of starting the research in linear polarization is its less complexity. However, the final goal is the conception of the antenna in circular polarization for the correct operation in GNSS applications. The conception and results of one structure in linear polarization and another in circular polarization obtaining double resonance are presented below.

4.1.1 Cavity modification by inserting rods

Previous analysis have shown that the variation of the cavity shape causes the appearance of other resonances. One idea to obtain double resonance is the insertion of metal rods through the cavity. Adding these elements causes the appearance of a second resonance because the internal cavity shape has changed. Following this premise, an investigation is performed introducing two rods to create a resonance covering the GNSS bands placed at the lower L-band. Figure 4.2a shows a side view of the antenna metasurface confined into a cavity. The two horizontal elements correspond to the metal rods, which are connected to the cavity only by one side. The central vertical element is the feeding point and the metasurfaces are on the top. The shape of the metasurface corresponds to the one used in Chapter 2 for linear polarization (two microstrip layers with three rectangular strips).

Summarizing, in this section an analysis about antennas in small cavities is performed in order to check if it is possible to have two different resonance frequencies such as:

- a resonance frequency centered at 1227 MHz, with a bandwidth of at least 140 MHz. This aims to cover GPS L2 and L5, Galileo E5 and E6, Glonass G2 and G3.
- a resonance frequency with a bandwidth of at least 60 MHz at 1575 MHz.

In order to reach the above mentioned requirements metallic rods have been inserted inside the cavity. As mentioned above, the linearly-polarized antenna embedded in a 40×45 mm^2 ($a \times b$; $0.21\lambda_0 \times 0.24\lambda_0$) rectangular cavity (Chapter 2), is the one used for the realization of this study.

The results obtained after simulation for this structure show two resonances centered at the required frequencies. However, it is not possible to obtain enough bandwidth to cover all the bands, as depicted in the reflection coefficient of Figure 4.2b. Therefore, these types of structures have been discarded.

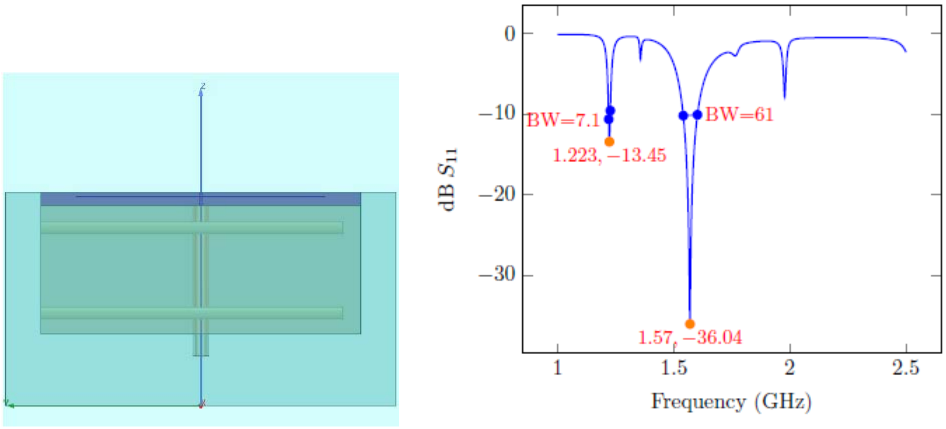

(a) (b)

Figure 4.2: (a) Side view for a metasurface antenna in rectangular aperture cavity with the insertion of two metallic rods. (b) Reflection coefficient of the antenna with 2 rods

4.1.2 Double ground plane structure

A new design capable of generating double resonance is presented below. The modification of the metallic cavity allows to change the way of propagation of the wave and to excite new ways. In the previous case above, several metal rods caused the appearance of a second resonance. In this case, a circular polarization antenna is designed in which a metallic plate will divide the cavity in two creating a "double" ground plane. This plane creates two horizontal sub-cavities, as depicted in Figure 4.3. This design generates a second cavity forced by the insertion of a metal plate. Due to the good elementary results, this structure will be developed in depth in the following sections.

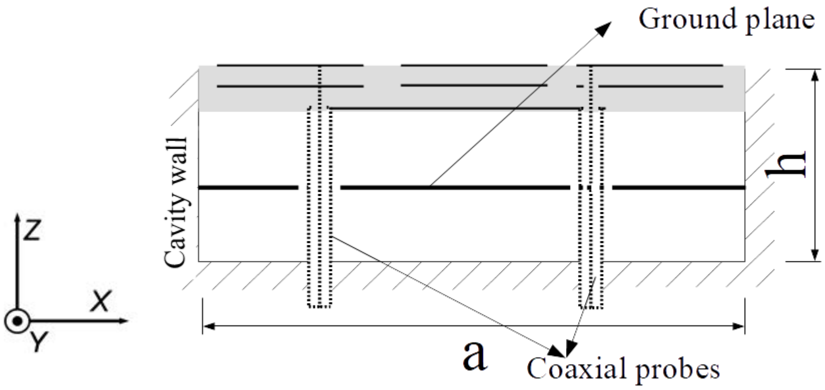

Figure 4.3: Position of the additional ground plane in the cavity

4.2 Design and simulation of the double ground plane structure

A metal plate in the middle of the cavity causes a second resonance close to the previously obtained resonance. This section shows the process of design and adaptation to the requirements of this thesis work. If the first three designs shown in the previous section were in linear polarization, this design will be done in circular polarization. The in-depth analysis has been performed in circular polarization for better adaptability to GNSS applications.

Therefore, the structure obtained in Chapter 3 formed by two layers of 9 square patches has been chosen as the starting point. However, the design of the multiband antenna starts from the cavity dimensions 50 × 50 × 20 mm^3, to ensure a larger bandwidth than the smaller cavity.

4.2.1 Design procedure

4.2.1.1 First design

The general structure of the antenna is similar to the circularly-polarization antenna exposed in Chapter 3. It is summarized as follows:

- Two metasurface layers composed of nine L×L square-shape patches organized as a 3×3 matrix. The patches are printed over a dielectric material with permittivity 10.2.
- Four feeding points rotated 90° between them. Coaxial cables are attached to a third layer of 4-pointed star-shaped microstrip.
- Most of the cavity is filled with air except some polypropylene (PP) blocks to ensure mechanical stability.
- A thin layer of glue is taken into account in simulations.

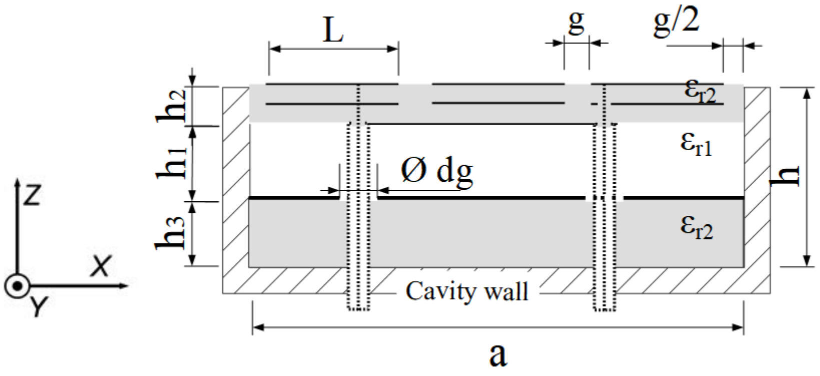

Figure 4.4: Cross-section configuration of the cavity-backed multiband antenna with a second ground plane

In this case, a 0.6 mm thick metal plate has been placed at a height h_3 mm from the bottom of the cavity. The metal plate, called second ground plane in this section, has direct contact with the cavity walls. The plate has holes placed in the position of the coaxial cables. The perforations in the metal plate allow the non-isolation of one sub-cavity and the non-reduction of total cavity height. The circular holes have a diameter d_g larger than the diameter of the coaxial probe to avoid contact. Finally, the lower sub-cavity is filled with a high permittivity (ε_{r2} =10.2) dielectric material to make the sub-cavity resonate. The total cavity size is 50 × 50 × 20 mm^3 ($0.23\lambda_0 \times 0.23\lambda_0 \times 0.09\lambda_0$ at 1400 MHz). In summary, the cavity is composed of the following two sub-cavities (Figure 4.4):

1. The lower sub-cavity (height h_3) composed of a dielectric block (ε_{r2}) and a metal plate with holes around the feeding points, as shown in Figure 4.5. This cavity has a depth of 11 mm. The two halves do not have the same depth with the intention of resonating two different frequencies.

2. The upper sub-cavity has a height of $h_1 + h_2$ represented in figure 4.4. This part contains the aforementioned metasurfaces and polypropylene substrate (in one block), i.e., the same elements as the circularly-polarized antennas in Chapter 3.

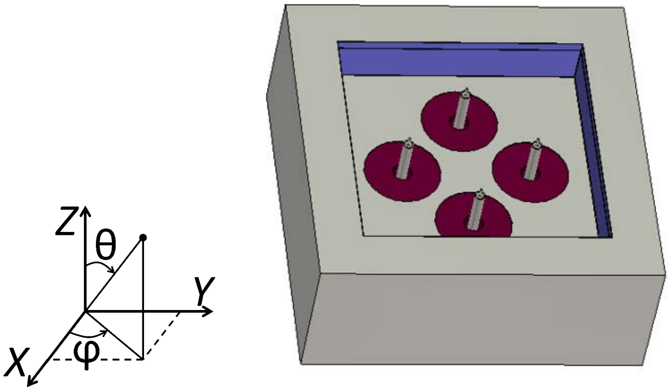

Figure 4.5: View of the metal plate inside the cavity

As Figure 4.6 shows that this design effectively provides a second resonance around the lower L-band frequencies. These first results have been carried out without changing the parameters of the circular polarization antenna on which it has been based. The values of each parameter are listed in Table 4.1. The total height of the cavity is h =20 mm divided by the second ground plane into two sub-cavities of different sizes: 11 mm the lower half and 9 mm the upper half. The diameter of the circles on the sheet is 12.5 mm, surrounding each of the 4 cables. Both the plane and the two metasurfaces are on a Rogers material RO3210 with permittivity ε_{r2} = 10.2. The upper half is made up of a two-layer metasurface with 9 square patches measuring 11.6×11.6 mm^2 and separated by a gap of 5 mm.

The low resonance obtained is centered at 1310 MHz and has a bandwidth of 183 MHz. Despite having a sufficient bandwidth, it is shifted and only include E6 band. This structure does not cover anymore the bands L5, E5 and G3 located between 1164 MHz and 1214 MHz. On the other hand, the upper resonance has been shifted from 1578 MHz to 1600 MHz, so E1 and L1 are not totally covered. Although the required bands are not completely included, this structure offers two close resonances in the L-band, which is interesting for this study.

A parametric study is presented below to understand the influence of some antenna parameters on the matching performances. This study evaluates the parameters to be modified in the design in order to cover the entire GNSS band.

4.2.1.2 Parametric study

The influence of three different parameters on the antenna behavior are studied in this section: the aperture size, the position of the holes in the second ground plane and the position of the metal plate in the cavity.

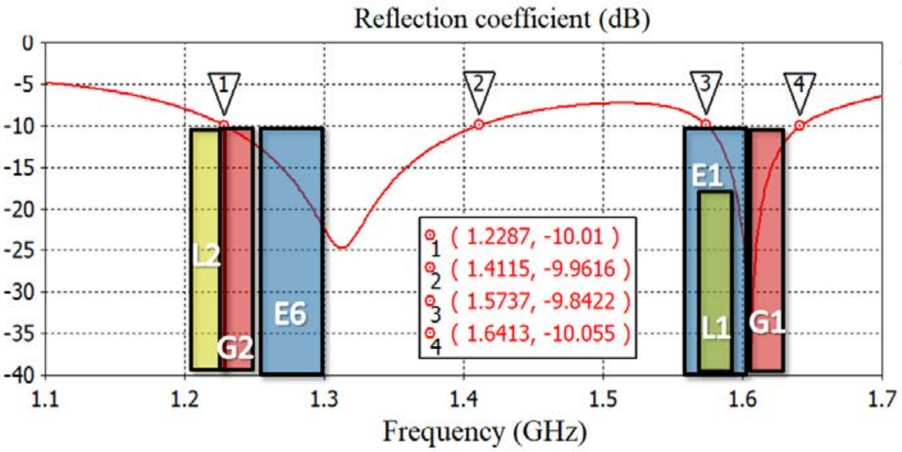

Figure 4.6: Reflection coefficient for the multiband antenna (50×50×20 mm^3) with a metal plate in the middle of the cavity

Parameter	Value	Parameter	Value
a	50 mm	t_1	8 mm
h	20 mm	t_2	13.5 mm
h_2	1.92 mm	ε_{r1}	2.25
h_3	11 mm	d_g	12.5 mm
f_p	13.5 mm	ε_{r2}	10.2
L	11.6 mm	g	5 mm

Table 4.1: Optimized dimensions of the 60×60 mm^2 square cavity-backed multiband antenna with four excitation points

Aperture size

One solution to enhance the resonance bandwidth is increasing the aperture size. The goal of this parametric study is to find the minimum aperture value allowing resonances to be located in the designated frequency bands: lower L-band for the lower resonance ([1164-1300 MHz) and upper L-band for the upper resonance ([1554-1610 MHz). The height, on the contrary, remains unchanged to 20 mm. The objective of this parametric study is to find a way to cover the lower bands, that is, E5, L5 and G3 that are in the range between 1164 MHz and 1214 MHz.

The graph of Figure 4.7 shows the reflection coefficient S_{11} for square aperture sizes (a) between 50 mm and 60 mm in steps of 2 mm. These results reveals that the two resonances tend to shift to lower frequencies when the aperture size is larger. This is a positive result to capture the bands mentioned above. However, the upper resonance is also shifted down.

According to the study, the 60×60 aperture antenna is the only one that covers the lowest band of GNSS. Therefore, a cavity of 60×60×20 mm^3 ($0.28\lambda_0 \times 0.28\lambda_0 \times 0.09\lambda_0$ at 1400 MHz) is the one chosen for future investigations. Nevertheless, a shift towards higher frequencies must be performed for the upper band since it is displaced more than 100 MHz (the end of the band is at 1491 MHz instead of 1610 MHz).

Ground plane holes

With the aim of not enlarging the cavity, other parameters that can shift the resonance frequency are searched. The shape of the new ground plane can be modified. It has been obtained in simulation that if

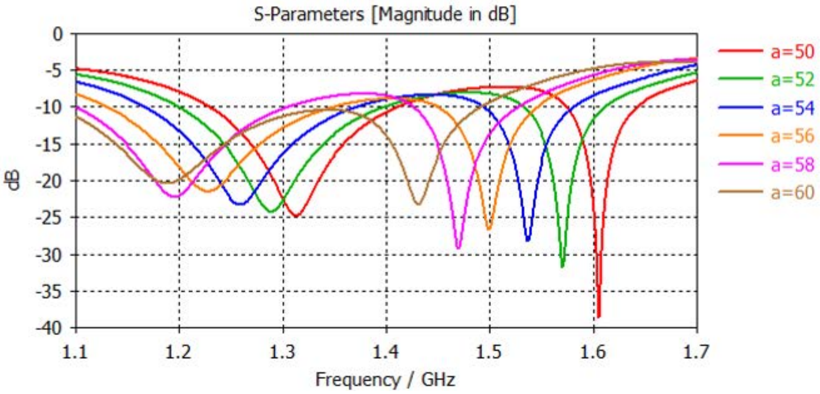

Figure 4.7: Parametric study on the influence of the aperture size for the multiband antenna (a value in mm)

the plate holes are smaller, the resonances tend to move towards higher frequencies. Placing this ground plane in the center of the cavity prevents waves from traveling to the bottom of the cavity. However, the holes allow some of those waves to reach the bottom and excite a second resonance.

In one of the tests performed, the circular notches have been moved to the center of the sheet, as shown in Figure 4.8. This change creates a single larger hole in the center instead of four separate circles. In all cases, coaxial outer conductor have not contact with the intermediate ground plane.

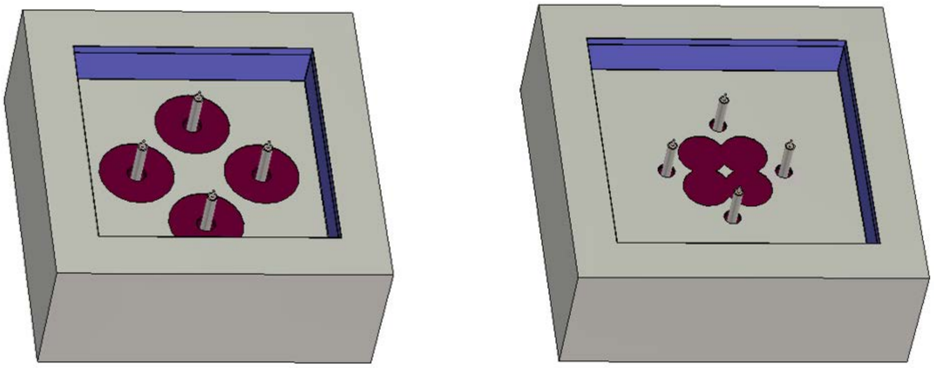

Figure 4.8: Plate holes places around the coaxial probes (left) and plate holes moved to the center of the ground plane (right)

Figure 4.9 represents the reflection coefficient for both cases, holes in the center of the metal plane (green) and holes around the coaxial cables (red). The fact is that arranging the circular holes in the center of the sheet produces a separation of the resonance frequencies. However, if the circles are kept around the coaxial cables, the two resonances tend to become closer to each other. The lower resonance drops from 1180 MHz (holes located around the coaxial) to 1160 MHz (holes located in the center), and the upper resonance goes up from 1430 MHz to 1480 MHz. This result is interesting, since it allows moving the upper resonance towards higher frequencies, and the lower resonance towards lower frequencies.

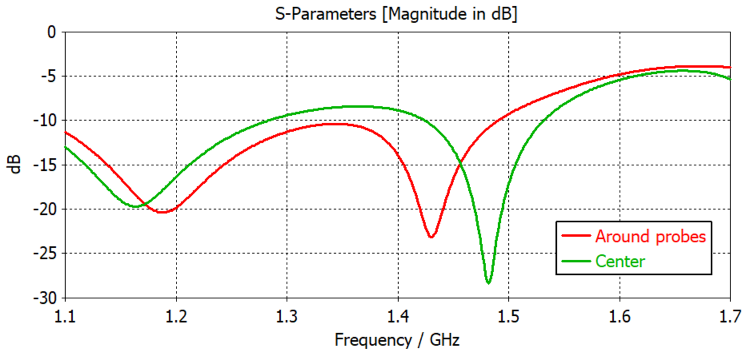

Figure 4.9: Reflection coefficient difference between both structures: circular gap around the probes and in the center of the plate

Ground plane position

The idea is to create two cavities of different sizes. In this case the total depth of the cavity (20 mm) is divided into two sub-cavities of 9 mm and 11 mm. Despite the good results obtained in the last parametric study with this configuration, the influence of the position of the plate (h_3 in figure 4.4) is studied further to be sure of the best configuration. Figure 4.10 shows the influence of the position of the plate with respect to the bottom of the cavity. Distances are marked in millimeters.

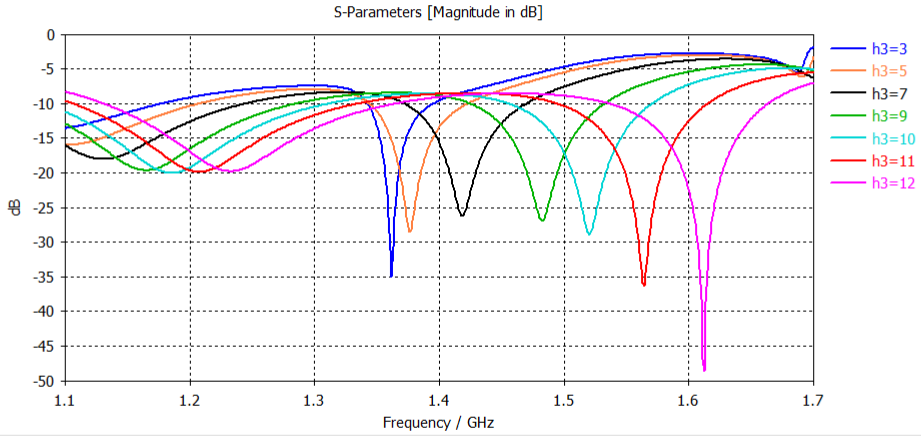

Figure 4.10: Study on the influence of the metal plate position (values in mm)

The position of the metal plate inside the cavity results in a frequency shift. If the sheet is closer to the bottom of the cavity (h_3 is lower), the resonances moves towards higher frequencies. However, the shift is greater in the upper resonance than in the lower one. The simulation confirms that the best case for GNSS bands occurs when the plate is h_3=11 mm from the bottom of the cavity (red curve).

Discussion

The first factor to consider to design an optimized multiband antenna in circular polarization using the structure presented, is the size of the aperture. A larger aperture size, if possible, allows the resonances to be shifted to lower frequencies. The second parameter is the position of the second ground plane in the cavity. If the plane is closer to the bottom of the cavity the resonances are displaced at lower frequencies, mainly affecting the location of the upper resonance. Finally, the metasurface parameters studied in Chapter 3 (the gap between patches g, the feeding point position f_p, and the dimensions of the connection line, t_1 and t_2) are necessary to adjust the resonances to the required frequencies.

4.2.1.3 Final design

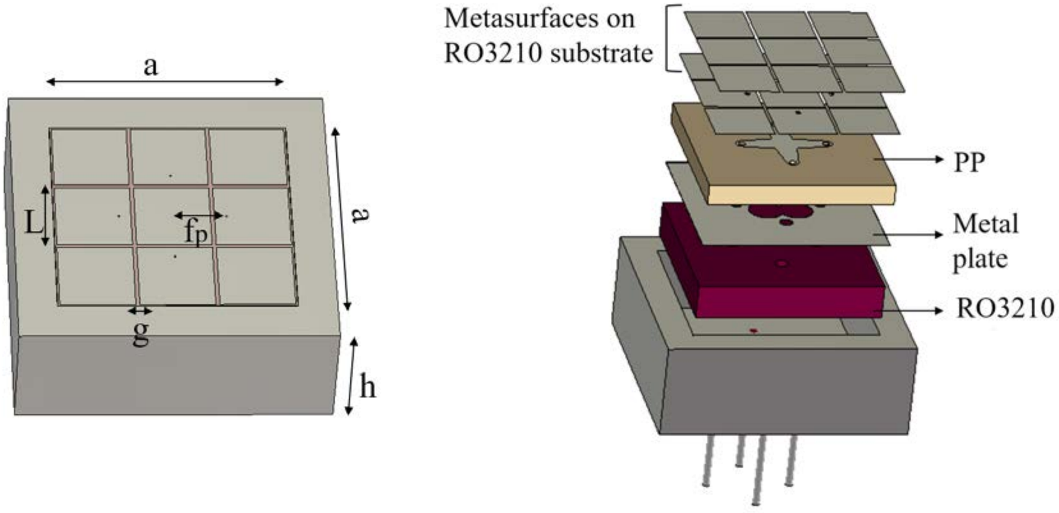

(a) (b)

Figure 4.11: Simulation model of the cavity-backed metasurface-inspired multiband antenna. (a) Metasurface top view. (b) Disassembled view

Taking into account the results obtained in the different parametric studies, the best structure obtained is represented in Figure 4.11. The selection criteria have been the following:

- Cavity dimensions 60×60×20 mm^3 ($0.28\lambda_0 \times 0.28\lambda_0 \times 0.09\lambda_0$ at 1400 MHz)
- Circular holes in the center of the plate: position and shape of the plate are depicted in Figure 4.12
- There is no contact between the outer coating of the coaxial and the metal sheet
- The plate has contact with the walls of the cavity and is located 11 mm from the bottom and 9 mm from the surface

All parameters after optimization, including those of the metasurface, are listed in Table 4.2. Simulation results are developed in next section.

4.2.2 Simulation results

Figure 4.13 shows the reflection coefficient of the circularly-polarized multiband antenna. Two resonances are obtained. The lower resonance is centered at 1220 MHz with bandwidth of 223 MHz (between 1112 and 1335 MHz). This allows capturing signals from all GNSS systems in the lower L-band [1164-1300 MHz]. In the other hand, the upper resonance is centered at 1569 MHz and with a bandwidth of 110

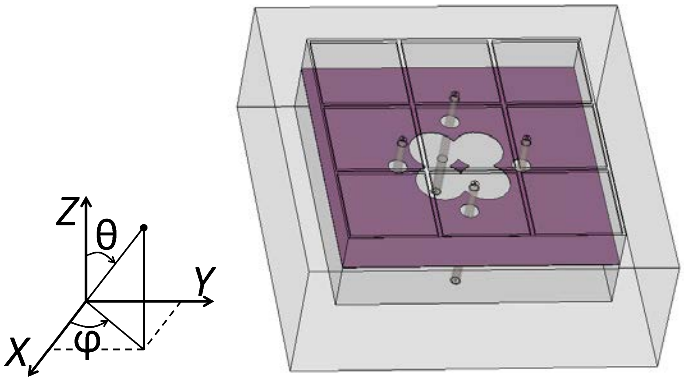

Figure 4.12: Ground plane position and shape for the cavity-backed multiband antenna

Parameter	Value	Parameter	Value
a	60 mm	t_1	8 mm
h	20 mm	t_2	13.5 mm
h_2	1.92 mm	ε_{r1}	2.25
h_3	11 mm	d_g	11 mm
f_p	13.5 mm	ε_{r2}	10.2
L	18.9 mm	d_t	4 mm
g	1 mm	d_c	2.2 mm

Table 4.2: Optimized dimensions of the 60×60 mm^2 square cavity-backed multiband antenna with four excitation points

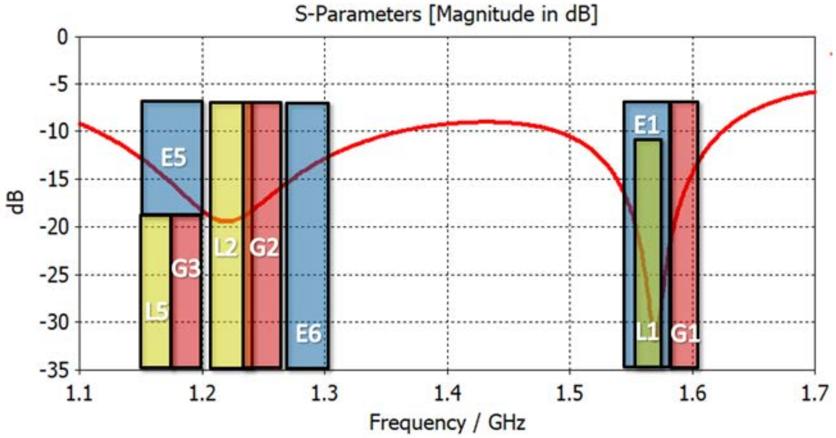

Figure 4.13: Reflection coefficient for the multiband antenna of 60×60 and GNSS bands

MHz (between 1508 and 1618 MHz), receiving signals from Galileo, Glonass and GPS bands located at the upper L-band [1559-1610 MHz].

The transmission coefficients S_{ij} are represented in Figure 4.14. The green curve (S_{12}) shows the coupling produced between adjacent ports. The result applies to any port due to antenna symmetry. The blue curve (S_{13}) shows the transmission coefficient between opposite ports. It can be seen that the coupling is more important (around -3 dB) between opposite ports than between adjacent ports (-8 dB). A strong coupling may degrade the antenna efficiency. This issue will be addressed in the next section.

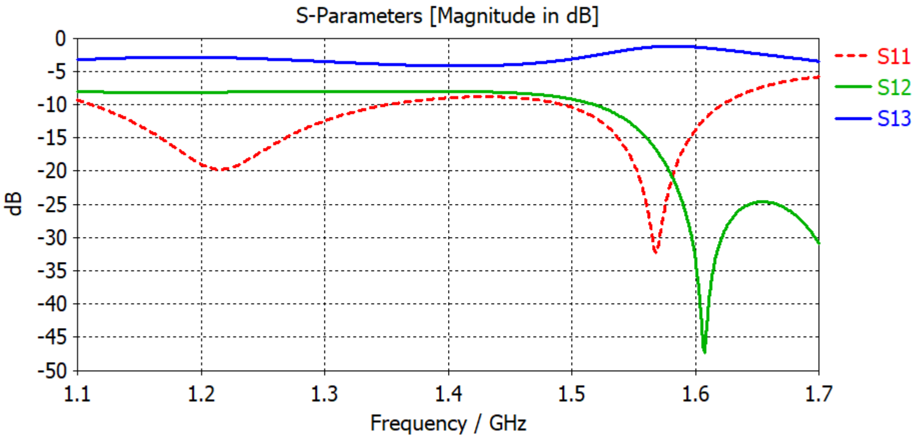

Figure 4.14: Transmission coefficients between adjacent (S12) and opposite (S13) ports

The antenna gain (dBic) is represented in Figure 4.15a. Due to the proximity between ports and the small size of the cavity, the antenna gain is very weak. However, these values are sufficient for GNSS signals. As discussed in Chapter 1, for GNSS antennas the minimum gain considered is -4.5 dBic. The use of four feeding points separated 90° between them makes the axial ratio practically ideal in simulation. Figure 4.15b shows how the axial ratio across the entire band of interest is below 3 dB.

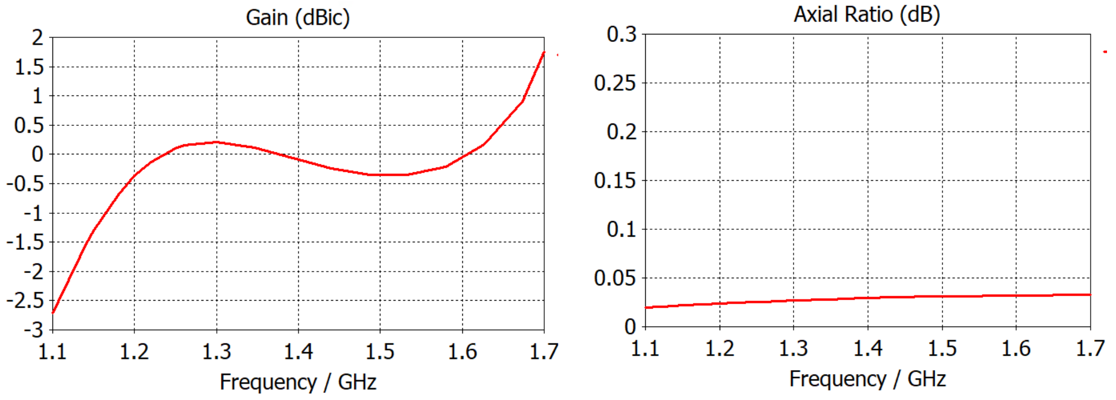

(a) (b)

Figure 4.15: Numerical results for (a) Gain and (b) Axial ratio of the multiband antenna in circular polarization

Three radiation patterns in circular polarization for three different frequencies of the band of interest are shown in Figure 4.16. Radiation pattern are represented for the plane $\varphi = 0°$ (first row), identical in simulation to the plane $\varphi = 90°$ (second row) due to the perfect symmetry of the antenna. The half power beamwidth is around 112° for the whole band. The radiation has a good behavior especially for low frequencies. As the frequency goes higher, the cross polarization (LHCP) start to present higher levels. GNSS signals are emitted in RHCP, so high LHCP would cause multipath interference to appear in the signal. However, in this case, RHCP has still much higher levels than LHCP.

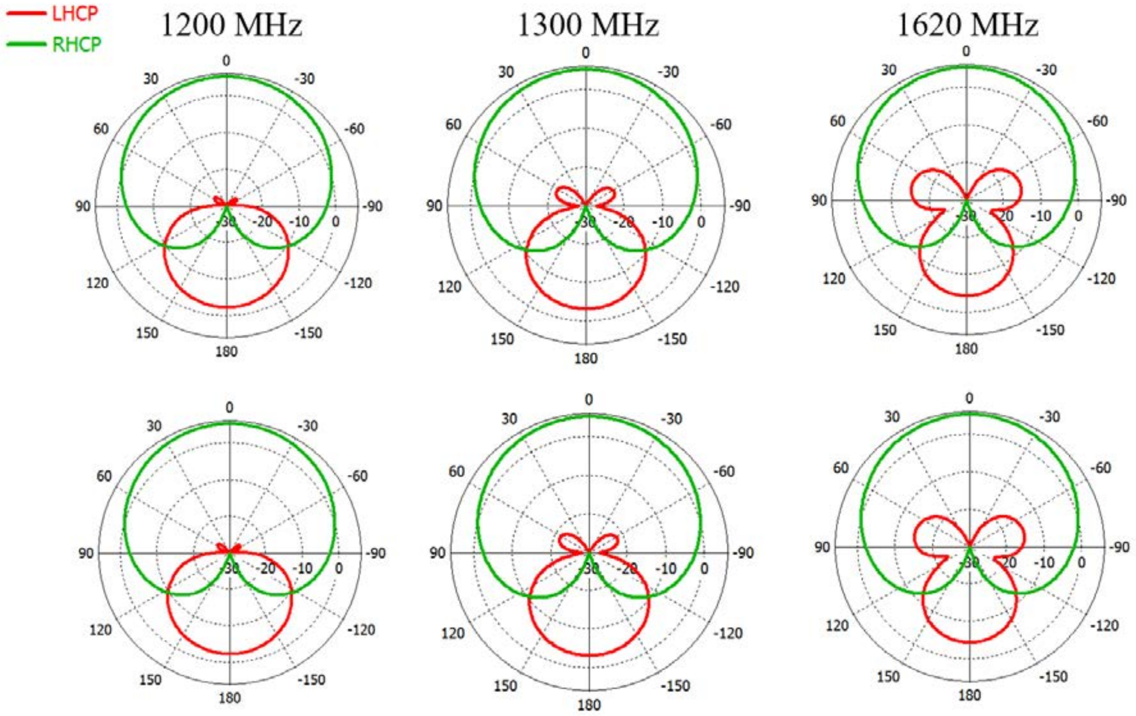

Figure 4.16: Simulated radiation patterns for a circularly polarized multiband antenna at three different frequencies. Red line for LHCP and green line for RHCP. Firt row represents the plane $\varphi = 0°$ and second row the plane $\varphi = 90°$

Due to the strong coupling mentioned above, the total efficiency is approximately 30% in the entire GNSS band which is low, as shown in Figure 4.17. Even if the gain obtained is valid for GNSS applications, improving antenna efficiency is an interesting point to investigate.

The reduction of the coupling is now targeted, despite achieving a structure which is able to cover all GNSS bands. A strong coupling can degrade the performances of the antenna. Different design techniques to reduce coupling have been tested, such as meander lines between patches, notched patches or suppression of the central patch. However, none of them offered positive results for this structure. Therefore, it has been decided to carry out the study of an external decoupling network.

4.3 Decoupling network

The small aperture size of $0.28\lambda_0 \times 0.28\lambda_0$ and the electrically small cavity height of $0.09\lambda_0$ present an important design challenge. The antenna is powered by 4 ports close to each other to generate circular polarization and it is embedded in a metal cavity. This produces an important coupling, which become even stronger between opposite ports. Therefore, an external decoupling network has been proposed to circumvent the coupling issue.

To design this network (Figure 4.18) the software ADS [167] has been used. The scattering matrix extracted from the simulation results in CST has been introduced in a box with 4 ports. Between the

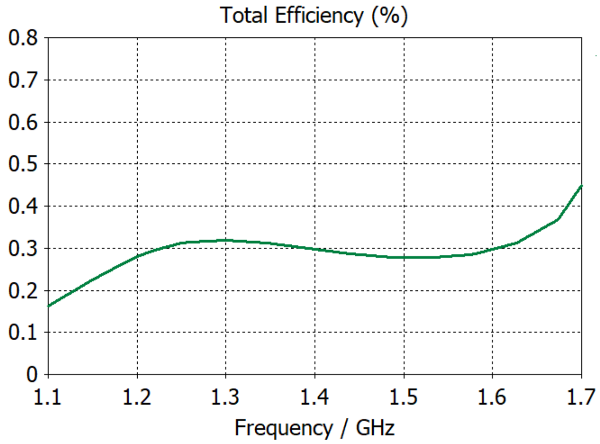

Figure 4.17: Total efficiency for the multiband antenna

passive S-parameters results and each port, the following elements have been placed:

- A transmission line (marked as TLIN [1-4] in Figure 4.18) matched to 50 Ω with electric length of θ to control the phase. One transmission line per port is placed at the output of the S-matrix. This parameter has been evaluated in simulation.
- A Parallel LC circuit to adapt the output terminal (named as PLC in Figure 4.18), where L is the inductance and C the capacitance.

To reduce coupling, the phase of mutual admittance is tuned using transmission lines and a LC circuit to cancel mutual coupling between ports. To define the values of the circuit components, an optimization have been performed. The first step is to find the optimal value of θ to tune the phase of the transmission line, which is designed at the central frequency of the GNSS band (1387 MHz). Next, the capacity value of the LC circuit is optimized to match the output. For simplicity, the inductance has been set at L =50 μH.

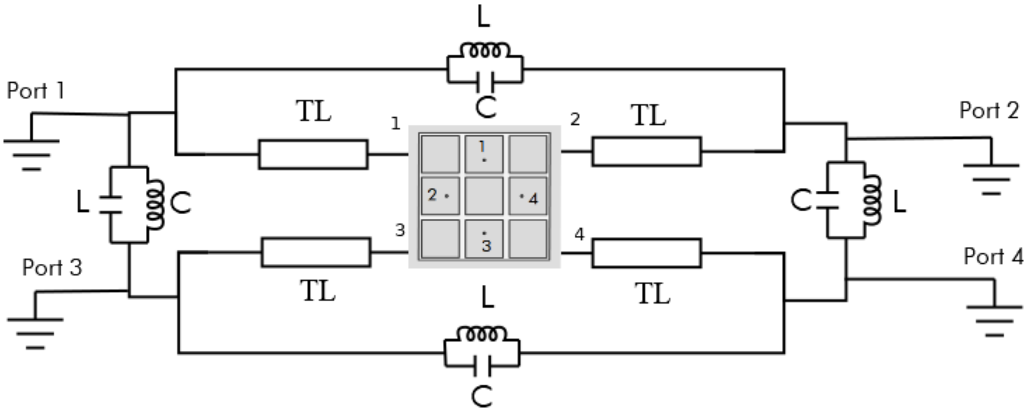

Figure 4.18: External decoupling network for the 4-ports multiband antenna

After optimization, the values for the angle theta is $\theta = 172.57°$ and the capacitance slightly variable around 40 nF. Figure 4.19 represents the S-parameters obtained at the output of the decoupling circuit.

The red line corresponds to the reflection coefficient at one of the port S11 and the blue and pink lines (overlapped between them) are the transmission coefficients between opposite ports (S13) and adjacent ports (S12), respectively. These results show a clear decrease in both couplings, between adjacent ports (S12) and opposite ports (S13). The markers *m1* and *m2* indicate the center of the two GNSS frequency ranges to be covered, 1164-1300 MHz and 1559-1610 MHz. The coupling for the lower frequency is -29 dB, while the coupling for the upper band is -25 dB. Despite these good results of the decoupling network around 1200 MHz and 1578 MHz, it has been found that the antenna has undergone a mismatch (S11 in Figure 4.19). Therefore, a matching network has been added to the circuit to solve this problem.

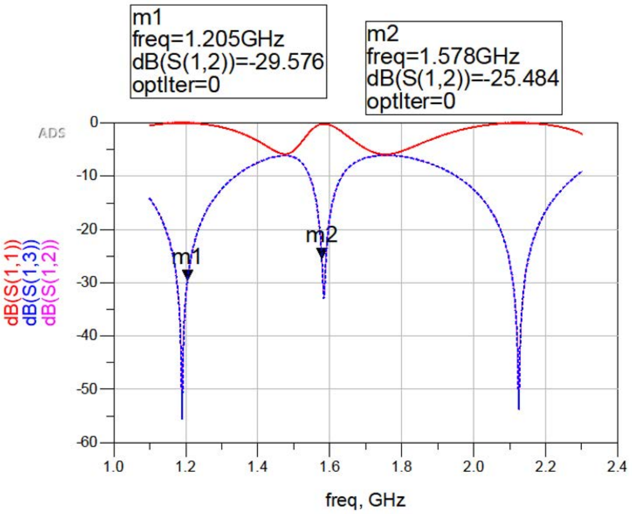

Figure 4.19: S-parameters of the antenna with the external decoupling network

The matching network is depicted in Figure 4.20. The following elements have been added to the four output of the previous decoupling network:

- A transmission line marked in Figure 4.20 as TLN [5-8] with variable electric length (E) and impedance (Z)

- A stub (named as MRSTUB in Figure 4.20) at the end of the circuit with variable dimensions (length L and width W) and angle

The matching network has been designed taking into account the position of the output admittance of the decoupling network. The stub can match the admittance to the load without using lumped elements. An optimization process has been carried out in the same way as in the previous model. The transmission line and stub parameter values have been optimized. These values are listed in Table 4.3.

Element name	E	Z	Element name	W	L	Angle
TL 5	31.35°	25 Ω	Stub 1	918μm	3.74mm	113.8°
TL 6	48.42°	48 Ω	Stub 2	324μm	1.25mm	12.27°
TL 7	26.84°	27 Ω	Stub 3	318μm	1.9mm	10°
TL 8	25.37°	25 Ω	Stub 4	436μm	3.75mm	164°

Table 4.3: Optimized dimensions for the matching network elements

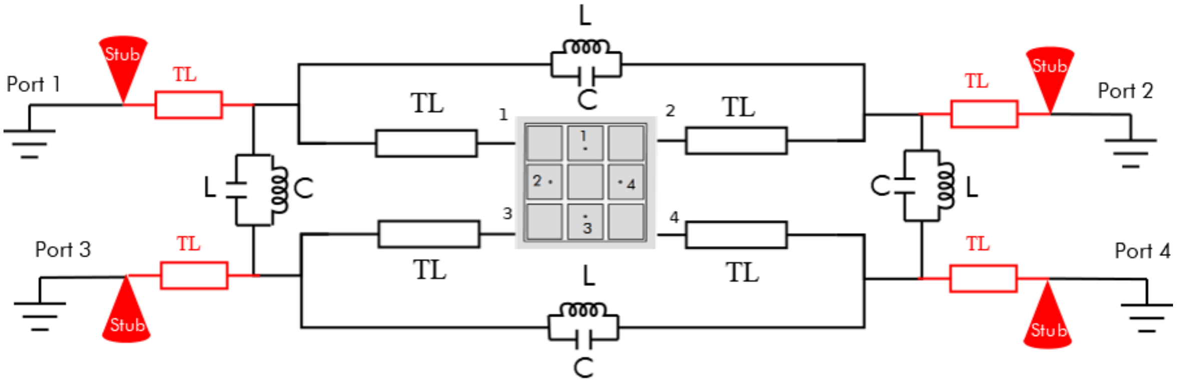

Figure 4.20: External decoupling and matching network for the 4-ports multiband antenna

Figure 4.19 represents the S-parameters obtained at the output of the matching network. The red line corresponds to the reflection coefficient S11 and the pink and blue lines are the transmission coefficients between opposite ports (S13) and adjacent ports (S12), respectively. Despite using an automatic optimization process in the software, the results have not been satisfactory. The antenna is not correctly matched over the whole bandwidth [1164-1610] MHz, as S11 parameter of Figure 4.21 shows. This matching network even causes a degradation of the previous decoupling results.

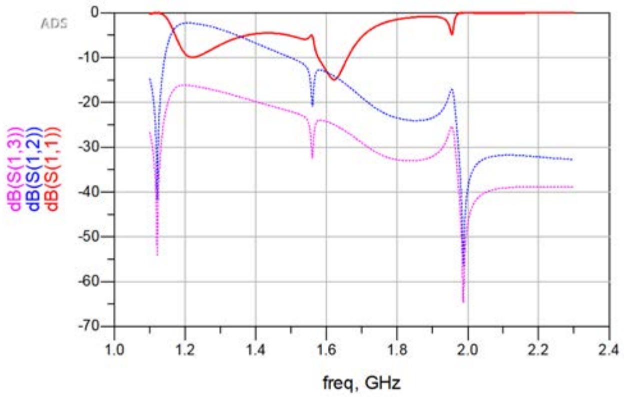

Figure 4.21: S-parameters after external decoupling and matching networks

One possible solution is to use the same matching network for a single frequency range. That is, perform a separate matching for the lower resonance (from 1164 to 1300 MHz) and another for the upper resonance (from 1559 to 1610 MHz). Figure 4.22a shows a correct matching and a coupling reduction from 1157 MHz to 1329 MHz, including the whole lower GNSS range. In the same way, Figure 4.22b presents good matching and low coupling from 1503 MHz to 1610 MHz, including the full upper GNSS band. However, this study demonstrates that it is possible to apply this method to independent frequency bands, but does not provide good results when this technique is applied to all GNSS frequencies.

Despite the unsuccessful result of the decoupling and matching network for the whole GNSS range, a prototype has been manufactured without the external networks. The objective is to validate if the simulation results are matching with measurements. The results are presented below.

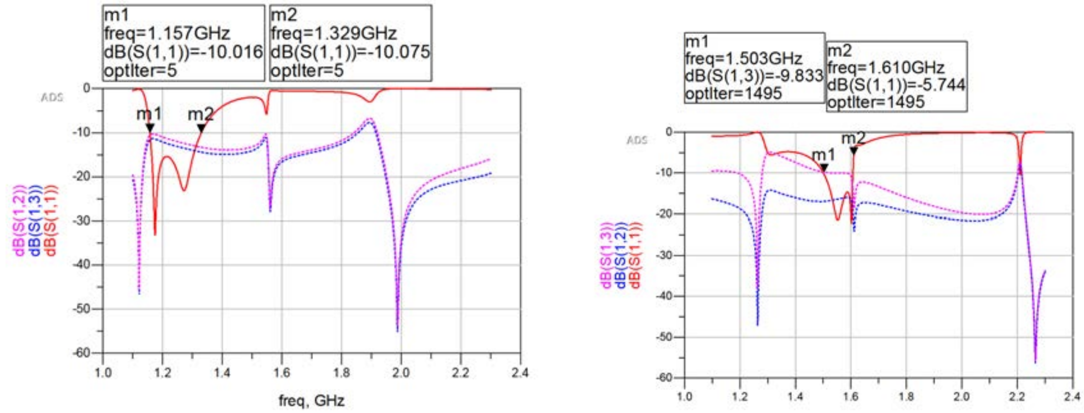

(a) (b)

Figure 4.22: (a) Result of matching only the lower frequencies and (b) only the upper frequencies

4.4 Experimental results

In this section a prototype that verifies the simulation results is manufactured and measured. The manufacturing process of the antenna is similar to those described in Chapters 2 and 3. The main difference is the insertion of the second ground plane with holes inside the cavity of dimensions 60×60×20 mm^3 ($0.28\lambda_0 \times 0.28\lambda_0 \times 0.09\lambda_0$ at 1400 MHz). The results of measurements obtained are also presented in this section.

4.4.1 Prototyping

A single prototype has been produced. Its parts are broken down and shown below.

4.4.1.1 Part by part presentation

Cavity
The main element of the antenna is the metal cavity. As in previous prototypes, the rest of the elements will be embedded inside. The particularity of this cavity is the incision that presents in one of its walls. The cavity frame is photographed in Figure 4.23a. A slit of height 0.6 mm is used to introduce the metal sheet that separates the cavity into two sub-cavities. Figure 4.23b depicts the copper plate to close and screw the bottom of the cavity. This element closes the cavity and allows welding the coaxial probes with the cavity.

Ground plane
The intermediate ground plane that divides the cavity is formed by a 0.6 mm thick copper plate. As photograph of Figure 4.24 shows, the plate has been milled to extract the circular elements from the center of the sheet. Small circles have also been extracted to introduce the coaxial cables through them.

Metasurface and dielectrics elements
The realization of the two metasurface layers follows the same manufacturing procedure as those set forth in previous chapters. The metallization of both the metasurface and the connecting cross are photographed in the figure. They are printed on a sheet of Roger3210 of 0.63 mm thick.

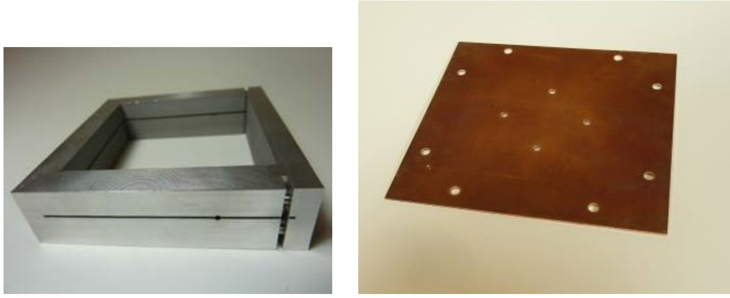

(a) (b)

Figure 4.23: Parts composing the metal cavity. (a) Cavity frame with the slit to place the metal sheet. (b) Copper plate to close the bottom of the cavity

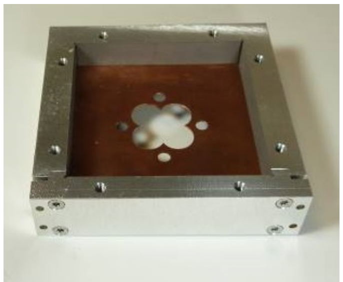

Figure 4.24: Picture of the intermediate ground plane metal plate embedded into the cavity

Figure 4.25b depicts the dielectrics block placed at the bottom of the cavity. This material is the single element that makes up the lower sub-cavity.

4.4.1.2 Whole Prototype

All the above elements are carefully introduced into the cavity making a compact and rigid antenna. This makes the antenna robust, although it increases in weight compared to the previous prototypes. To avoid possible small air gaps caused by the movement of the pieces, everything has been glued with a liquid glue (estimated to $\varepsilon_r = 3.5$, $\tan(\delta) = 0.01$, $h = 0.1mm$). The prototype is presented in Figure 4.26a

The bottom part of the prototype is photographed in Figure 4.26b. Coaxial cables pass through the cavity to be welded into the bottom plate to make perfect electrical contact with the cavity.

4.4.2 Measurement results

The measurements obtained with the VNA and in the anechoic chamber on the prototype are presented below.

The reflection coefficients for each port of the first prototype are presented in Figure 4.27. The results show that the expected double resonance is well obtained despite the slightly frequency shift. However, the coefficient differs one port to another and all GNSS bands are not covered. Even if it is not the expected result in this first prototype, obtaining two resonances is an important step. As in the simulation results, a strong coupling is observed in Figure 4.28, especially between the ports that are face to face, #1 - #3 and #2 - #4 (dotted lines).

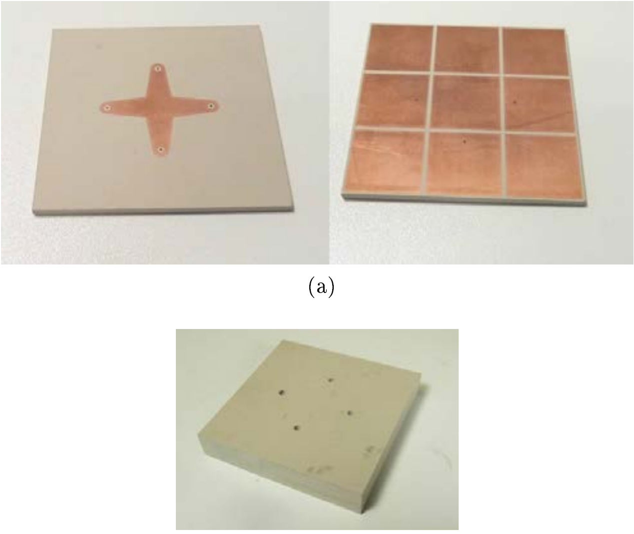

(a)

(b)

Figure 4.25: (a) Metasurface layers and connection cross metallizations. (b) Dielectrics block

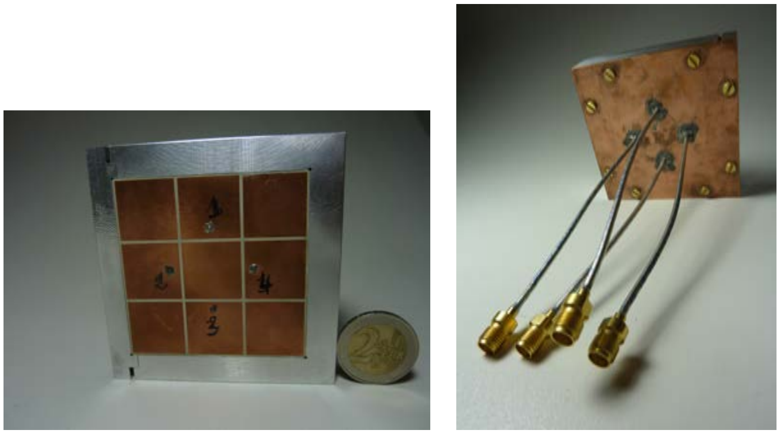

(a)

(b)

Figure 4.26: (a) Top view and (b) bottom view of the cavity-backed multiband antenna prototype. Cavity dimensions 60×60×20 mm^3 ($0.28\lambda_0 \times 0.28\lambda_0 \times 0.09\lambda_0$ at 1400 MHz)

The measured realized gain versus the frequency is shown in Figure 4.29a. Due to the use of the active polarization circuit explained in Chapter 3, the antenna shows a higher gain compared to the simulation. The difference in gain between the low and high frequencies is due to the fact that the polarizer used to perform these measurements is designed for the range 1500 to 1600 MHz. Figure 4.29b represents the axial ratio as a function of frequency. The prototype has a good axial ratio in virtually the entire frequency band. However, from 1570 the circular polarization is degraded. The cause of this degradation has not been found at present. Manufacturing new prototypes may help to test if the problem is due to manufacturing or design flaw. At the time of writing this document, no new prototypes have been made due to time constraints.

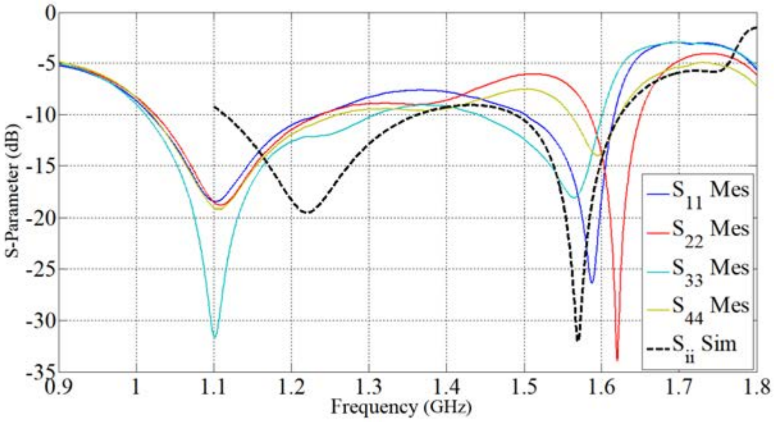

Figure 4.27: Measured reflection coefficient at all ports for the multiband antenna of 60×60

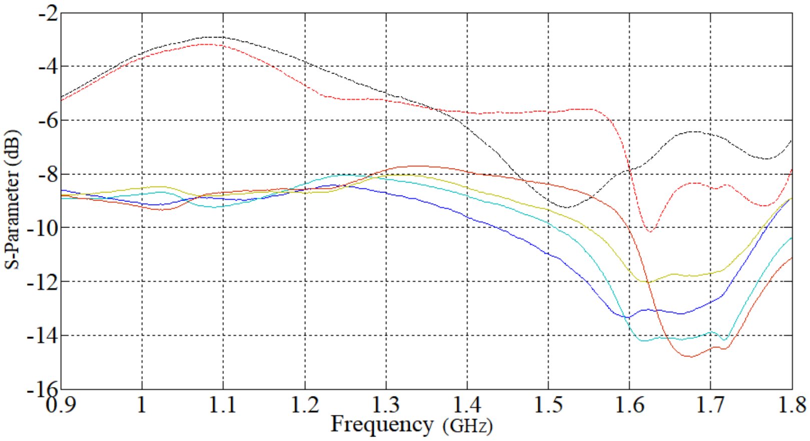

Figure 4.28: Measured transmission coefficients for the multiband antenna of 60×60. Adjacent ports in solid lines and face to face ports

In Figure 4.30 radiation patterns for four three different frequencies (1200, 1300, 1570 and 1610 MHz) are represented, two in the lower resonance and two in the upper resonance. The half power bandwidth is 111° at 1200 MHz, 120° at 1300 MHz, 100° at 1570 MHz and 115° at 1610 MHz. The antenna radiation has good agreement with the simulation results. The lower frequencies present a lower cross polarization (LHCP) than the higher frequencies. In this last case, the degradation of the circular polarization can also be seen.

4.5 Conclusion

The creation of a multiband structure is essential to cover all GNSS bands. In this chapter a multiband design has been proposed.

Multiple methods such as the insertion of rods and the insertion of a second ground plane have been investigated. Finally, the double resonance is created by the division of the cavity into two sub-cavities.

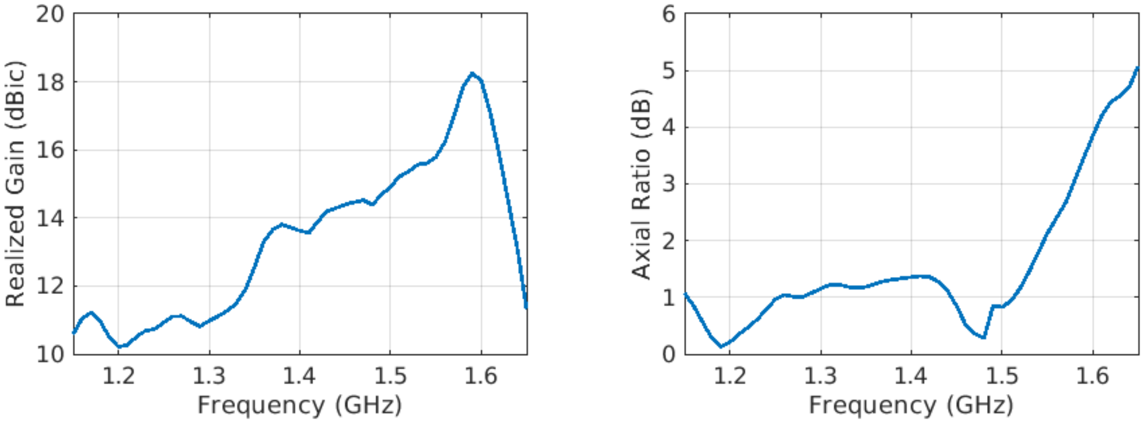

(a)

(b)

Figure 4.29: Measured (a) gain and (b) axial ratio

For this purpose, a metal plate has been introduced in the center of the cavity. The antenna can cover all GNSS bands, however, a strong coupling has been found. Despite the realization of a decoupling circuit, the simulation results in this direction have not been satisfactory.

A prototype has been manufacture to verify the results obtained in simulation. However, the measurements show a degradation of the circular polarization for the upper L band. The rest of the measures present a good agreement with the results obtained in simulation.

In future works new research will be carry out to reduce the coupling conceiving a new symmetric decoupling network and find the problem in polarization at upper parts of the band. A new version of the prototype will be studied.

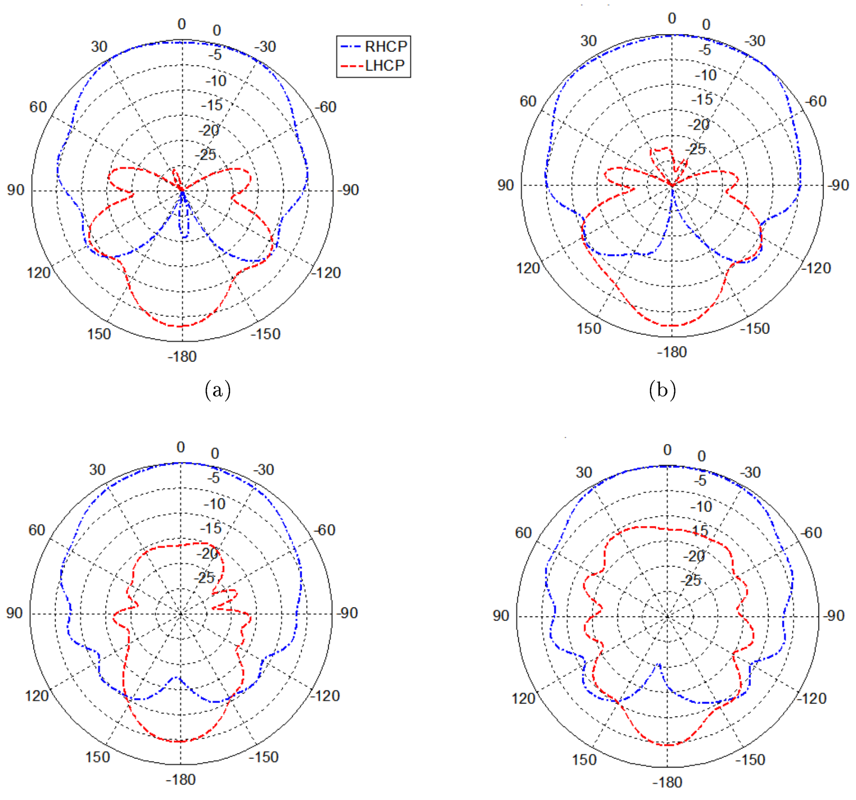

(a) (b)

(c) (d)

Figure 4.30: Measured radiation patterns with RHCP and LHCP polarization at four frequencies. (a) 1200 MHz, (b) 1300 MHz, (c) 1570 MHz and (d) 1610 MHz

General conclusion and perspectives

The aim of this thesis is the analysis and development of antennas able to cover the upper GNSS bands (1550-1610 MHz) and the whole GNSS system (1164-1610 MHz). These antenna are dedicated to the reception of GNSS signals in order to assess the geolocation of flying objects, such as projectiles. The work presented in this thesis focus on the design of antennas to be integrated into projectiles of large caliber (120-155 mm caliber typically). These carriers are very often made of steel, which means that the antenna must be embedded in a metallic cavity. The main drawback of this environment is the strong bandwidth reduction and hence covering multiple GNSS bands is a challenge. Similarly, the antenna dimensions are imposed by the geometry and size of the carrier. An initial width limit of 50 mm was set, corresponding to 0.26 λ_0 at 1578 MHz. Various techniques and structures have been studied to solve the problem. Firstly an antenna exciting a single resonance but presenting a relative wide bandwidth in spite of its small dimensions has been studied. This antenna aims to cover the L1, E1 and G1 bands (from 1559 MHz to 1610 MHz). Secondly, the objective is extended to a multiband antenna that covers all GNSS bands.

Chapter 1 gathers the theoretical basis necessary for the correct development of this thesis work. A section dedicated to the composition, development and operation of the geolocation systems has been explained. Also, a brief compilation of the state of the art on the antennas used for GNSS applications has been given. To design compact GNSS antennas, multiple antenna structures have been considered during this study. Each of these techniques are presented in this chapter. Microstrip antennas, cavity antennas and metasurface antennas are the three main axes of this research. The low cost and compactness of microstrip antennas, the miniaturization offered by the use of metasurfaces, and the isolation and robustness of the integration into cavities, make their combination an interesting subject of study. Metasurfaces have multiples applications. Some of them are exposed during Chapter 1. In the present work, metasurfaces are considered under very specific conditions in comparison to the very numerous publications on this topic; indeed, metasurfaces are employed here at the aperture of a very small metallic cavity. As the ultimate goal is to create an array around the carrier, arrays and their characteristics are shown at the end of this chapter. Arrays are very important in GNSS, especially for anti-jamming applications. Nevertheless this last topic is not treated in this work, but the capacities of jammer rejection with an array constituted of the designed antennas could be characterized in a future work.

Chapter 2 discussed the design of linearly-polarized antennas covering the upper GNSS bands L1, E1 and G1. Although GNSS signals are emitted in circular polarization, a first version in linear polarization is designed. Linear polarization is easier to generate and can be efficiently used in environments without multipath rejections as it is the case for flying platforms. However, lower carrier to noise ratio can be obtained in comparison to a circularly-polarized receiving antenna.

First, it has been proven that a microstrip antenna composed of a single patch does not meet the requirements of 60 MHz of bandwidth. Similarly, the configuration based on two stacked patches doesn't reach the specified bandwidth within the required dimensions.

Two solutions based on metasurfaces have then been introduced. In this case it has been possible to obtain more than 60 MHz bandwidth with an aperture size of 0.21 $\lambda_0\times$ 0.24 λ_0 for a rectangular cavity and $0.26\lambda_0 \times 0.26\ \lambda_0$ for a square cavity. This allows to cover E1, L1 and G1 with a small and compact antenna. The advantage of a rectangular cavity in regards to a square cavity is the aperture surface, which is smaller, and also to facilitate the antenna integration when constraints are stronger on one dimension. Several prototypes have been manufactured that allow to verify the results obtained in simulation. The changes produced by the integration into the whole carrier in regards to the single cavity and the use of a radome have also been analyzed. Small changes on the metasurface parameters have to be made, but it is not a hard point.

GNSS required circular polarization antennas, however linearly-polarized antennas can be used for onboard flying platforms in multipath-free-environments. Circularly-polarized antenna designs are presented in the next chapter.

In Chapter 3 a solution in circular polarization has been introduced. Circular polarization allows to obtain a better carrier-to-noise ratio and to differentiate real signals with multipath reflections.

First, it has been shown that the investigations to get circular polarization from a rectangular cavity were not fruitful, so the square cavity has been chosen to continue the study. The use of two or four feeding points has been investigated. However, the antennas with four excitations have given better results.

A compact RHCP metasurface-inspired cavity antenna of size $0.26\lambda_0 \times 0.26\lambda_0 \times 0.11\lambda_0$ ($50 \times 50 \times 20$ mm^3), covering three different GNSS bands around 1578 MHz with a single radiating aperture, has been proposed. The radiating aperture is loaded by a two-layer metasurface, constituted of square patches excited by four feed ports in phase quadrature. The experimental results obtained in RHCP have shown an excellent agreement with the numerical predictions. The proposed antenna, associated to an active feeding network (splitter with 4 outputs and phase increment, filter, LNA), is able to sufficiently cover the three GNSS bands (L1, E1, G1) with an active gain of 16 dBic and an axial ratio lower than 1.6 dB over this frequency range ([1550 – 1610] MHz).

Due to the good results obtained for the previous antenna, a miniaturization has been carried out. A structure of dimensions $0.21\lambda_0 \times 0.21\lambda_0 \times 0.11\lambda_0$ ($40 \times 40 \times 20$ mm^3) has been presented. This new, more compact structure also offers very good results in both simulation and experimentation. However, in addition to its smaller radiating surface, the coupling of the ports is strong due to the small size of the cavity, which makes it lose in efficiency.

Chapter 4 is focused on the conception of a multiband structure which is essential to cover all GNSS bands from 1164 MHz to 1610 MHz. Multiple methods such as the insertion of rods have been investigated. Finally, the double resonance is created by the division of the cavity into two sub-cavities. For this, a metal plate has been introduced in the center of the cavity. In this chapter a multiband design has been proposed with an intern second ground plane (presenting openings), which forms a double cavity and which results in offering two resonances. Its dimensions are increased to $60 \times 60 \times 20$ mm^3 ($0.28\lambda_0 \times 0.28\lambda_0 \times 0.09\lambda_0$ at 1400 MHz), because the results with smaller cavity were not satisfying. The antenna can cover all GNSS bands, however, a strong coupling between the ports, and in particular ports face to face, has been found.

A prototype has been manufactured to verify the results obtained in simulation. However, the measurements show a degradation of the circular polarization for the upper L band. Apart from this upper band, the AR is low over the whole GNSS bands and in good agreement with the numerical results. The rest of the measures present a good agreement with the results obtained in simulation. The completion of a decoupling network showed the effective enhancement on narrow bands; unfortunately, it was not possible to reduce the coupling between ports over the whole GNSS band. The principle of presenting two resonances in circular polarization with a compact antenna has been numerically and experimentally demonstrated. Nevertheless, further investigations are required to enhance its performances.

To conclude, this work focused on the design of antennas in compact cavity for GNSS applications. The concept of metasurface antennas in cavity was successfully employed with rectangular and square cavity for linear polarization. The work has then be extended to circular polarization and was experimentally validated by designs of antenna covering the GNSS bands L1, E1 and G1. Furthermore, a circularly-polarized structure presenting two resonances has been introduced and the principle demonstrated both in simulations and experiments. This work open several perspectives, which are given below.

Perspectives

The main work to keep on this research is the improvement of the multiband antenna. The prototype manufactured in this thesis presents good circular polarization, however the polarization is slightly degraded for high frequencies. The main novelty of this study is the use of the cavity to create multi-resonances. New investigations could be carried out in this sense, such as the use of a conical cavity (for cylindrical antenna) or pyramid (for square antenna) to obtain a maximum bandwidth. In other words, the cavity could have an exponential profile whenever its height allows it. Another aspect to improve is the reduction of the coupling. A new symmetric decoupling network offering less coupling between ports and/or a more efficient and wide band have to be investigated. Finally, the miniaturization of the multiband antenna is essential, since this antenna passes the desired dimensions at the beginning of the study. We could think also to allow larger dimensions of this structure for ground usages on larger carrier than projectiles: by increasing the dimensions, we could expect to reduce the coupling between the port and hence to enhance the performances.

The principle of having two ground planes (and two sub-cavities) could be studied also for linear polarization, both for square and rectangular cavities. This configuration would be adapted to be integrated into flying projectiles or UAVs. Furthermore, we could think to investigate magneto-electric structure, and potentially to mix magneto-electric with metasurface elements to enlarge the bandwidth.

Another aspect to improve is related to the integration of the antenna into the projectile. A structure using a flexible substrate or 3D-printing dielectric substrate could be studied to make conformal surfaces. This technology could solve the problems of manual mechanical manufacturing and optimize the location for the antenna in the carrier.

Bibliography

[1] J. Sanz Subirana, J. J. Zornoza, and M. Hernández-Pajares, "GNSS Data Processing. vol. i: Fundamentals and Algorithms," *Noordwijk: European Space Agency Communications*, 2013.

[2] M. Martinis, K. Mahdjoubi, R. Sauleau, S. Collardey, and L. Bernard, "Bandwidth behavior of miniature square cavity microstrip antennas," in *Antennas and Propagation in Wireless Communications (APWC), 2013 IEEE-APS Topical Conference on*, pp. 479–482, IEEE, 2013.

[3] M. Martinis, *Development and Characterization of Metamaterials in Cavities.* PhD thesis, University of Rennes 1, 2014.

[4] G. Seeber, "Satellite geodesy. foundations, methods and applications," 2009.

[5] C. A. Balanis, *Antenna theory: analysis and design.* John wiley & sons, 1997.

[6] B. R. Rao, W. Kunysz, and K. McDonald, *GPS/GNSS Antennas.* Artech House, 2013.

[7] S. Maci and G. B. Gentili, "Dual-frequency patch antennas," *IEEE Antennas and Propagation Magazine*, vol. 39, no. 6, pp. 13–20, 1997.

[8] J. B. Benavides, R. A. Lituma, P. A. Chasi, and L. F. Guerrero, "A novel modified hexagonal shaped fractal antenna with multi band notch characteristics for uwb applications," in *2018 IEEE-APS Topical Conference on Antennas and Propagation in Wireless Communications (APWC)*, pp. 830–833, IEEE, 2018.

[9] S. S. Gao, Q. Luo, and F. Zhu, *Circularly polarized antennas.* John Wiley & Sons, 2013.

[10] X. Chen, P.-Y. Qin, Y. J. Guo, and G. Fu, "Low-profile and wide-beamwidth dual-polarized distributed microstrip antenna," *IEEE Access*, vol. 5, pp. 2272–2280, 2017.

[11] A. Kumar and H. D. Hristov, "Microwave cavity antennas," *Norwood, MA, Artech House, 1989, 483 p.*, 1989.

[12] S. Wang, A. Feresidis, G. Goussetis, and J. Vardaxoglou, "Low-profile resonant cavity antenna with artificial magnetic conductor ground plane," *Electronics Letters*, vol. 40, no. 7, pp. 405–406, 2004.

[13] A. Feresidis and J. Vardaxoglou, "A broadband high-gain resonant cavity antenna with single feed," in *Antennas and Propagation, 2006. EuCAP 2006. First European Conference on*, pp. 1–5, IEEE, 2006.

[14] L. Ge and K. M. Luk, "A low-profile magneto-electric dipole antenna," *IEEE Transactions on Antennas and Propagation*, vol. 60, no. 4, pp. 1684–1689, 2012.

[15] M. Martinis, K. Mahdjoubi, R. Sauleau, S. Collardey, and L. Bernard, “Circuit models explaining bandwidth behavior of small circular cavity backed patch antennas,” in *Antennas and Propagation (EuCAP), 2014 8th European Conference on*, pp. 3652–3656, IEEE, 2014.

[16] N. Engheta and R. W. Ziolkowski, *Metamaterials: physics and engineering explorations.* John Wiley & Sons, 2006.

[17] R. A. Shelby, D. R. Smith, and S. Schultz, “Experimental verification of a negative index of refraction,” *science*, vol. 292, no. 5514, pp. 77–79, 2001.

[18] D. Sievenpiper, L. Zhang, R. F. Broas, N. G. Alexopolous, and E. Yablonovitch, “High-impedance electromagnetic surfaces with a forbidden frequency band,” *IEEE Transactions on Microwave Theory and techniques*, vol. 47, no. 11, pp. 2059–2074, 1999.

[19] H. Mosallaei and K. Sarabandi, “Antenna miniaturization and bandwidth enhancement using a reactive impedance substrate,” *IEEE Transactions on antennas and propagation*, vol. 52, no. 9, pp. 2403–2414, 2004.

[20] R. Hurtado, W. Klimczak, W. McKinzie, and A. Humen, “Artificial magnetic conductor technology reduces weight and size for precision gps antennas,” in *Navigational National Technical Meeting, San Diego, CA*, pp. 28–30, 2002.

[21] M. Martinis, K. Mahdjoubi, R. Sauleau, S. Collardey, and L. Bernard, “Bandwidth behavior and improvement of miniature cavity antennas with broadside radiation pattern using a metasurface,” *IEEE Transactions on Antennas and Propagation*, vol. 63, pp. 1899–1908, May 2015.

[22] R. J. Mailloux, *Phased array antenna handbook.* Artech house, 2017.

[23] N. Rezazadeh and L. Shafai, “A controlled reception pattern antenna array with dual-mode circular microstrip antenna elements for increased angular availability,” *IEEE Transactions on Antennas and Propagation*, vol. 66, no. 5, pp. 2594–2598, 2018.

[24] E. Martini, M. Mencagli Jr, and S. Maci, “Metasurface transformation for surface wave control,” *Philosophical Transactions of the Royal Society A: Mathematical, Physical and Engineering Sciences*, vol. 373, no. 2049, p. 20140355, 2015.

[25] M. Ramirez-Acedo, *Antennas Microstrip con Polarizacion Circular para Sistemas de Posicionamiento por Satelite y aplicaciones RFID.* PhD thesis, Universidad Autonoma de Barcelona, 2013.

[26] N. C. Karmakar, “Investigations into a cavity-backed circular-patch antenna,” *IEEE Transactions on Antennas and Propagation*, vol. 50, no. 12, pp. 1706–1715, 2002.

[27] M. Martinis, L. Bernard, K. Mahdjoubi, R. Sauleau, and S. Collardey, “Wideband antenna in cavity based on metasurfaces,” *IEEE Antennas and Wireless Propagation Letters*, vol. 15, pp. 1053–1056, 2016.

[28] M. H. Cohen, “On the band width of cavity antennas,” *Journal of Applied Physics*, vol. 25, no. 5, pp. 582–587, 1954.

[29] V. Counter, “Miniature cavity antenna,” *Microw. Lab., Stanford Univ., Stanford, CA, USA, Tech. Rep*, vol. 2, pp. W28–099, 1948.

[30] A. Li, S. Singh, and D. Sievenpiper, “Metasurfaces and their applications,” *Nanophotonics*, vol. 7, no. 6, pp. 989–1011, 2018.

[31] R. Corporation, "Rogers Corporation, www.rogerscorpo.com," 2019.

[32] L. Garcia-Gamez, L. Bernard, R. Sauleau, S. Collardey, K. Mahdjoubi, P. Pouliguen, and P. Potier, "Metasurface-inspired antenna in cavity for gnss applications," in *2018 12th European Conference on Antennas and Propagation (EuCAP)*, IEEE, 2018.

[33] L. Garcia-Gamez, L. Bernard, S. Collardey, H. Covic, R. Sauleau, K. Mahdjoubi, P. Potier, and P. Pouliguen, "Compact gnss metasurface-inspired cavity antennas," *IEEE Antennas and Wireless Propagation Letters*, vol. 18, no. 12, pp. 2652–2656, 2019.

[34] L. Garcia-Gamez, L. Bernard, R. Sauleau, S. Collardey, K. Mahdjoubi, P. Pouliguen, and P. Potier, "Circularly-polarized metasurface antenna in cavity for gnss applications," in *2019 13th European Conference on Antennas and Propagation (EuCAP)*, pp. 1–5, IEEE, 2019.

[35] M. Martinis, K. Mahdjoubi, R. Sauleau, S. Collardey, and L. Bernard, "Comparison of a cavity antenna with stacked patches and a metasurface-inspired design," in *Antennas and Propagation (EuCAP), 2015 9th European Conference on*, pp. 1–3, IEEE, 2015.

[36] D. Sullivan, "Time and frequency measurement at nist: The first 100 years," in *Proceedings of the 2001 IEEE International Frequency Control Symposium and PDA Exhibition (Cat. No. 01CH37218)*, pp. 4–17, IEEE, 2001.

[37] E. Kaplan and C. Hegarty, *Understanding GPS: principles and applications.* Artech house, 2005.

[38] J. Rabemanantsoa and A. Sharaiha, "Size reduced multi-band printed quadrifilar helical antenna," *IEEE Transactions on Antennas and Propagation*, vol. 59, no. 9, pp. 3138–3143, 2011.

[39] Y.-S. Wang and S.-J. Chung, "A miniature quadrifilar helix antenna for global positioning satellite reception," *IEEE transactions on antennas and propagation*, vol. 57, no. 12, pp. 3746–3751, 2009.

[40] B. Kaswarra, W. Quddus, F. Scire, S. N. Makarov, *et al.*, "Circular polarization bandwidth for a bowtie turnstile over a ground plane," in *2007 IEEE Antennas and Propagation Society International Symposium*, pp. 3544–3547, IEEE, 2007.

[41] S. N. Makarov, F. Scire'Scappuzzo, B. Kaswarra, and W. Quddus, "Circular polarization bandwidth of a planar turnstile antenna," in *2007 IEEE Antennas and Propagation Society International Symposium*, pp. 2646–2649, IEEE, 2007.

[42] M.-J. Chiang, S. Wang, and C.-C. Hsu, "Compact multifrequency slot antenna design incorporating embedded arc-strip," *IEEE Antennas and Wireless Propagation Letters*, vol. 11, pp. 834–837, 2012.

[43] K.-F. Lee, S. L. S. Yang, and A. A. Kishk, "Dual-and multiband u-slot patch antennas," *IEEE Antennas and Wireless Propagation Letters*, vol. 7, pp. 645–647, 2008.

[44] M. Chen and C.-C. Chen, "A compact dual-band gps antenna design," *IEEE Antennas Wireless Propag. Lett*, vol. 12, pp. 245–248, 2013.

[45] J. Zhang, Y. Li, Z. Liang, S. Zheng, and Y. Long, "Design of a multifrequency one-quarter-rings microstrip antenna," *IEEE Antennas and Wireless Propagation Letters*, vol. 14, pp. 209–212, 2015.

[46] S. Maci, G. B. Gentili, P. Piazzesi, and C. Salvador, "Dual-band slot-loaded patch antenna," *IEE Proceedings-Microwaves, Antennas and Propagation*, vol. 142, no. 3, pp. 225–232, 1995.

[47] S. Long and M. Walton, "A dual-frequency stacked circular-disc antenna," *IEEE Transactions on Antennas and propagation*, vol. 27, no. 2, pp. 270–273, 1979.

[48] J. Dahele, K.-F. Lee, and D. Wong, “Dual-frequency stacked annular-ring microstrip antenna,” *IEEE Transactions on Antennas and Propagation*, vol. 35, no. 11, pp. 1281–1285, 1987.

[49] A. A. Savochkin and A. Nudga, “The multiband antenna,” in *2011 VIII International Conference on Antenna Theory and Techniques*, pp. 182–184, IEEE, 2011.

[50] G. Avitabile, S. Maci, F. Bonifacio, and C. Salvador, “Dual band circularly polarized patch antenna,” in *Proceedings of IEEE Antennas and Propagation Society International Symposium and URSI National Radio Science Meeting*, vol. 1, pp. 290–293, IEEE, 1994.

[51] A. Siblini, B. Jecko, and E. Arnaud, “Multimode reconfigurable nano-satellite antenna for pdtm application,” in *2017 11th European Conference on Antennas and Propagation (EUCAP)*, pp. 542–545, IEEE, 2017.

[52] R.-S. Chu, K. M. Lee, and A. T. Wang, “Multiband phased-array antenna with interleaved tapered-elements and waveguide radiators,” in *IEEE Antennas and Propagation Society International Symposium. 1996 Digest*, vol. 3, pp. 1616–1619, IEEE, 1996.

[53] S. F. Jilani and A. Alomainy, “A multiband millimeter-wave 2-d array based on enhanced franklin antenna for 5g wireless systems,” *IEEE Antennas and Wireless Propagation Letters*, vol. 16, pp. 2983–2986, 2017.

[54] Y. Yao, X. Shao, Y. Li, J. Yu, and X. Chen, “Design of multiband circularly polarized antenna arrays for gnss applications,” 2018.

[55] B. B. Mandelbrot, *The fractal geometry of nature*, vol. 173. WH freeman New York, 1983.

[56] T. Hong, S.-X. Gong, Y. Liu, and W. Jiang, “Monopole antenna with quasi-fractal slotted ground plane for dual-band applications,” *IEEE Antennas and Wireless Propagation Letters*, vol. 9, pp. 595–598, 2010.

[57] A. Azari, “Super wideband fractal antenna design,” in *2009 3rd IEEE International Symposium on Microwave, Antenna, Propagation and EMC Technologies for Wireless Communications*, pp. 242–245, IEEE, 2009.

[58] A. Azari, “A new super wideband fractal microstrip antenna,” *IEEE transactions on antennas and propagation*, vol. 59, no. 5, pp. 1724–1727, 2011.

[59] H. Oraizi and S. Hedayati, “Microstrip multiband fractal dipole antennas using the combination of sierpinski, hilbert and giuseppe peano fractals,” in *Proceedings of 2014 Mediterranean Microwave Symposium (MMS2014)*, pp. 1–4, IEEE, 2014.

[60] M. Ibraheam, S. Irteza, S. Caizzone, A. Dreher, R. Stephan, and M. A. Hein, “Compact dual-band dual-polarized antenna array for robust satellite navigation receivers,” in *2015 9th European Conference on Antennas and Propagation (EuCAP)*, pp. 1–5, IEEE, 2015.

[61] K. A. Yinusa, L. A. Greda, and A. Dreher, “A conformal multi-frequency antenna array for safety-of-life satellite navigation,” in *Radar Conference (EURAD), 2017 European*, pp. 363–366, IEEE, 2017.

[62] M. Smith, G. Sole, and R. Thomas, “Dual frequency circularly polarised antennas and arrays for satellite navigation,” in *IEE Colloquium on Circularly Polarised Elements and Arrays*, pp. 3–1, IET, 1991.

[63] J. J. Wang and V. K. Tripp, "Design of multioctave spiral-mode microstrip antennas," *IEEE Transactions on Antennas and Propagation*, vol. 39, no. 3, pp. 332–335, 1991.

[64] J. J. Wang, "Spiral-mode microstrip (smm) antennas and associated methods for exciting, extracting and multiplexing the various spiral modes," Apr. 15 1997. US Patent 5,621,422.

[65] S. Yun, D. Chang, and I. Yom, "Wideband receive antennas of sensor stations for gps/galileo satellite," in *2008 4th Advanced Satellite Mobile Systems*, pp. 210–212, IEEE, 2008.

[66] F. Scire-Scappuzzo and S. N. Makarov, "A low-multipath wideband gps antenna with cutoff or non-cutoff corrugated ground plane," *IEEE transactions on antennas and propagation*, vol. 57, no. 1, pp. 33–46, 2009.

[67] E. Krantz, S. Riley, and P. Large, "Gps antenna design and performance advancements: The trimble zephyr," *Trimble Navigation Limited*, 2001.

[68] J.-M. Baracco, L. Salghetti-Drioli, and P. de Maagt, "Amc low profile wideband reference antenna for gps and galileo systems," *IEEE Transactions on Antennas and Propagation*, vol. 56, no. 8, pp. 2540–2547, 2008.

[69] M. Manteghi and Y. Rahmat-Samii, "Multiport characteristics of a wide-band cavity backed annular patch antenna for multipolarization operations," *IEEE Transactions on Antennas and Propagation*, vol. 53, no. 1, pp. 466–474, 2005.

[70] D. M. Pozar, *Microwave engineering*. John Wiley & Sons, 2009.

[71] G. A. Deschamps, "Microstrip microwave antennas," in *Proceedings of the Third Symposium on the USAF Antenna Research and Development Program, Oct*, pp. 18–22, 1953.

[72] I. J. Bahl and P. Bhartia, *Microstrip antennas*. Artech house, 1980.

[73] F. Zavosh and J. T. Aberle, "Single and stacked circular microstrip patch antennas backed by a circular cavity," *IEEE Transactions on Antennas and Propagation*, vol. 43, no. 7, pp. 746–750, 1995.

[74] F. Zavosh and J. T. Aberle, "Improving the performance of microstrip-patch antennas," *IEEE Antennas and Propagation Magazine*, vol. 38, no. 4, pp. 7–12, 1996.

[75] L. Shen, S. Long, M. Allerding, and M. Walton, "Resonant frequency of a circular disc, printed-circuit antenna," *IEEE Transactions on antennas and propagation*, vol. 25, no. 4, pp. 595–596, 1977.

[76] A. Derneryd, "Analysis of the microstrip disk antenna element," *IEEE Transactions on Antennas and Propagation*, vol. 27, no. 5, pp. 660–664, 1979.

[77] F. Zavosh and J. T. Aberle, "Infinite phased arrays of cavity-backed patches," *IEEE transactions on antennas and propagation*, vol. 42, no. 3, pp. 390–398, 1994.

[78] S. C. Pavone, M. Faenzi, E. Martini, M. Albani, and S. Maci, "Closed form basis function fourier spectra for dispersion calculation of metasurfaces made by circular and elliptical ring patches," 2018.

[79] C. A. Balanis, *Advanced engineering electromagnetics*. John Wiley & Sons, 1989.

[80] K. Carver and J. Mink, "Microstrip antenna technology," *IEEE transactions on antennas and propagation*, vol. 29, no. 1, pp. 2–24, 1981.

[81] W. F. Richards, J. R. Zinecker, R. D. Clark, and S. A. Long, "Experimental and theoretical investigation of the inductance associated with a microstrip antenna feed," *Electromagnetics*, vol. 3, no. 3-4, pp. 327–346, 1983.

[82] Y. Lo, D. Solomon, F. Ore, D. Harrison, and G. Deschamps, "Study of microstrip antennas, microstrip phased arrays, and microstrip feed networks.," tech. rep., ILLINOIS UNIV AT URBANA-CHAMPAIGN ELECTROMAGNETICS LAB, 1977.

[83] J. R. James, P. S. Hall, *et al.*, *Handbook of microstrip antennas*, vol. 1. IET, 1989.

[84] E. A. Hajlaoui and H. Trabelsi, "Improvement of circularly polarized slot-patch antenna parameters by using electromagnetic band gap structures," *Journal of Microwaves, Optoelectronics and Electromagnetic Applications*, vol. 15, no. 4, pp. 428–440, 2016.

[85] A. Siblini, H. A. Taam, B. Jecko, M. Rammal, and A. Bellion, "Pixel and patch comparison circular polarization: For arma new agile circularly polarized approach," in *2017 Sensors Networks Smart and Emerging Technologies (SENSET)*, pp. 1–4, IEEE, 2017.

[86] H. A. Wheeler, "Fundamental limitations of small antennas," *Proceedings of the IRE*, vol. 35, no. 12, pp. 1479–1484, 1947.

[87] L. J. Roca, M. Martinez-Vasquez, and R. Serrano, *Handbook on small antennas.* EurAAP AISBL, 2012.

[88] L. J. Chu, "Physical limitations of omni-directional antennas," *Journal of applied physics*, vol. 19, no. 12, pp. 1163–1175, 1948.

[89] R. M. Fano, "Theoretical limitations on the broadband matching of arbitrary impedances," *Journal of the Franklin Institute*, vol. 249, no. 1, pp. 57–83, 1950.

[90] R. Collin and S. Rothschild, "Evaluation of antenna q," *IEEE Transactions on Antennas and Propagation*, vol. 12, no. 1, pp. 23–27, 1964.

[91] R. Fante, "Quality factor of general ideal antennas," *IEEE Transactions on Antennas and Propagation*, vol. 17, no. 2, pp. 151–155, 1969.

[92] J. S. McLean, "A re-examination of the fundamental limits on the radiation q of electrically small antennas," *IEEE Transactions on antennas and propagation*, vol. 44, no. 5, p. 672, 1996.

[93] R. Harrington, "On the gain and beamwidth of directional antennas," *IRE Transactions on Antennas and Propagation*, vol. 6, no. 3, pp. 219–225, 1958.

[94] G. Smith, *Antenna engineering handbook.* McGraw Hill, 1984.

[95] D. H. Lee, A. Chauraya, Y. Vardaxoglou, and W. S. Park, "A compact and low-profile tunable loop antenna integrated with inductors," *IEEE Antennas and Wireless Propagation Letters*, vol. 7, pp. 621–624, 2008.

[96] P. Turalchuk, I. Munina, M. Derkach, O. Vendik, and I. Vendik, "Electrically small loop antennas for rfid applications," *IEEE Antennas and Wireless Propagation Letters*, vol. 14, pp. 1786–1789, 2015.

[97] P. Eratuuli, P. Haapala, and P. Vainikainen, "Dual frequency wire antennas," *Electronics Letters*, vol. 32, no. 12, pp. 1051–1052, 1996.

[98] P.-L. Teng and K.-L. Wong, “Planar monopole folded into a compact structure for very-low-profile multiband mobile-phone antenna,” *Microwave and optical technology letters*, vol. 33, no. 1, pp. 22–25, 2002.

[99] G. W. Pierce, *Electric Oscillations and Electric Waves: With Application to Radiotelegraphy and Incidental Application to Telephony and Optics.* McGraw-Hill Book Company, 1920.

[100] T. Taga, K. Hirasawa, and M. Haneishi, “Analysis of planar inverted-f antennas and antenna design for portable radio equipment,” *Analysis, Design, and Measurement of Small and Low Profile Antennas*, pp. 161–180, 1992.

[101] T.-Y. Wu and K.-L. Wong, “On the impedance bandwidth of a planar inverted-f antenna for mobile handsets,” *Microwave and optical technology letters*, vol. 32, no. 4, pp. 249–251, 2002.

[102] M.-C. Huynh and W. Stutzman, “Ground plane effects on planar inverted-f antenna (pifa) performance,” *IEE Proceedings-Microwaves, Antennas and Propagation*, vol. 150, no. 4, pp. 209–213, 2003.

[103] F. Mariottini, M. Albani, E. Toniolo, D. Amatori, and S. Maci, “Design of a compact gps and sdars integrated antenna for automotive applications,” *IEEE Antennas and Wireless Propagation Letters*, vol. 9, pp. 405–408, 2010.

[104] X. Qing, Z. N. Chen, *et al.*, “A compact circularly polarized slotted patch antenna for gnss applications,” *IEEE Transactions on Antennas and Propagation*, vol. 62, no. 12, pp. 6506–6509, 2014.

[105] Y. Anjani, A. Alphones, *et al.*, “A wide-beam circularly polarized asymmetric-microstrip antenna,” *IEEE Transactions on Antennas and Propagation*, vol. 63, no. 8, pp. 3764–3768, 2015.

[106] A. Lalbakhsh and K. P. Esselle, “Design of an improved resonant cavity antenna,” in *Electromagnetics in Advanced Applications (ICEAA), 2017 International Conference on*, pp. 1658–1660, IEEE, 2017.

[107] C. Cheype, C. Serier, M. Thèvenot, T. Monédière, A. Reineix, and B. Jecko, “An electromagnetic bandgap resonator antenna,” *IEEE Transactions on Antennas and Propagation*, vol. 50, no. 9, pp. 1285–1290, 2002.

[108] K. Agarwal, A. Alphones, *et al.*, “Wideband circularly polarized amc reflector backed aperture antenna,” *IEEE Transactions on Antennas and Propagation*, vol. 61, no. 3, pp. 1456–1461, 2013.

[109] L. Siu, H. Wong, and K.-M. Luk, “A dual-polarized magneto-electric dipole with dielectric loading,” *IEEE Transactions on antennas and propagation*, vol. 57, no. 3, pp. 616–623, 2009.

[110] F. Wu and K. M. Luk, “Wideband tri-polarization reconfigurable magneto-electric dipole antenna,” *IEEE Transactions on Antennas and Propagation*, vol. 65, no. 4, pp. 1633–1641, 2017.

[111] A.-S. Kaddour, S. Bories, A. Bellion, and C. Delaveaud, “Compact frequency reconfigurable magneto-electric crossed dipole in vhf band,” 2018.

[112] W. Yang and J. Zhou, “Wideband circularly polarized cavity-backed aperture antenna with a parasitic square patch,” *IEEE Antennas and Wireless Propagation Letters*, vol. 13, pp. 197–200, 2014.

[113] M. H. Cohen, *The normal modes of cavity antennas.* PhD thesis, Antenna Laboratory, Department of Electrical Engineering, Ohio State University Research Foundation, 1952.

[114] D. S. Simula, “CST Studio Suite,” 2019.

[115] Ansys, “Ansys HFSS,” 2019.

[116] M. H. Awida, S. H. Suleiman, and A. E. Fathy, “Substrate-integrated cavity-backed patch arrays: A low-cost approach for bandwidth enhancement,” *IEEE transactions on antennas and propagation*, vol. 59, no. 4, pp. 1155–1163, 2011.

[117] P. Singhal and S. Banerjee, “A cavity backed rectangular patch antenna,” in *6th International SYmposium on Antennas, Propagation and EM Theory, 2003. Proceedings. 2003*, pp. 112–115, IEEE, 2003.

[118] M. Martinis, R. Sauleau, K. Mahdjoubi, S. Collardey, and L. Bernard, “Bandwidth behavior of miniature cavity antennas,” in *Journées JCGE'2014-SEEDS*, 2014.

[119] R. M. Walser, “Electromagnetic metamaterials,” in *Complex Mediums II: Beyond Linear Isotropic Dielectrics*, vol. 4467, pp. 1–15, International Society for Optics and Photonics, 2001.

[120] V. Veselago, “Electrodynamics of substances with simultaneously negative values of epsilon and mu,” *Usp. Fiz. Nauk*, vol. 92, p. 517, 1967.

[121] Y. Rahmat-Samii and H. Mosallaei, “Electromagnetic band-gap structures: classification, characterization, and applications,” 2001.

[122] C. Caloz, T. Itoh, and A. Rennings, “Crlh metamaterial leaky-wave and resonant antennas,” *IEEE Antennas and Propagation Magazine*, vol. 50, no. 5, pp. 25–39, 2008.

[123] P.-L. Chi and Y.-S. Shih, “Compact and bandwidth-enhanced zeroth-order resonant antenna,” *IEEE Antennas and Wireless Propagation Letters*, vol. 14, pp. 285–288, 2014.

[124] A. Alù, F. Bilotti, N. Engheta, and L. Vegni, “Subwavelength, compact, resonant patch antennas loaded with metamaterials,” *IEEE Transactions on Antennas and Propagation*, vol. 55, no. 1, pp. 13–25, 2007.

[125] J. L. Volakis and K. Sertel, “Narrowband and wideband metamaterial antennas based on degenerate band edge and magnetic photonic crystals,” *Proceedings of the IEEE*, vol. 99, no. 10, pp. 1732–1745, 2011.

[126] R. W. Ziolkowski and A. Erentok, “Metamaterial-based efficient electrically small antennas,” *IEEE Transactions on antennas and propagation*, vol. 54, no. 7, pp. 2113–2130, 2006.

[127] Y. Dong, H. Toyao, and T. Itoh, “Compact circularly-polarized patch antenna loaded with metamaterial structures,” *IEEE transactions on antennas and propagation*, vol. 59, no. 11, pp. 4329–4333, 2011.

[128] K. B. Alici and E. Ozbay, “Electrically small split ring resonator antennas,” *Journal of applied physics*, vol. 101, no. 8, p. 083104, 2007.

[129] O. S. Kim and O. Breinbjerg, “Miniaturised self-resonant split-ring resonator antenna,” *Electronics letters*, vol. 45, no. 4, pp. 196–197, 2009.

[130] Y. Dong, H. Toyao, and T. Itoh, “Design and characterization of miniaturized patch antennas loaded with complementary split-ring resonators,” *IEEE Transactions on antennas and propagation*, vol. 60, no. 2, pp. 772–785, 2011.

[131] O. Quevedo-Teruel, H. Chen, A. Díaz-Rubio, G. Gok, A. Grbic, G. Minatti, E. Martini, S. Maci, G. V. Eleftheriades, M. Chen, *et al.*, “Roadmap on metasurfaces,” *Journal of Optics*, vol. 21, no. 7, p. 073002, 2019.

[132] D. Sievenpiper, *High-impedance electromagnetic surfaces.* PhD thesis, Dept. Elect. Eng., Univ. California, Los Angeles CA, 1999.

[133] M. Gustafsson, C. Sohl, and G. Kristensson, "Physical limitations on antennas of arbitrary shape," *Proceedings of the Royal Society A: Mathematical, Physical and Engineering Sciences*, vol. 463, no. 2086, pp. 2589–2607, 2007.

[134] W. Dallenbach and W. Kleinsteuber, "Reflection and absorption of decimeter-waves by plane dielectric layers," *Hochfreq. u Elektroak*, vol. 51, pp. 152–156, 1938.

[135] W. W. Salisbury, "Absorbent body for electromagnetic waves," June 10 1952. US Patent 2,599,944.

[136] L. Chen, S.-W. Qu, B.-J. Chen, X. Bai, K.-B. Ng, and C. H. Chan, "Terahertz metasurfaces for absorber or reflectarray applications," *IEEE Transactions on Antennas and Propagation*, vol. 65, no. 1, pp. 234–241, 2016.

[137] A. K. Azad, W. J. Kort-Kamp, M. Sykora, N. R. Weisse-Bernstein, T. S. Luk, A. J. Taylor, D. A. Dalvit, and H.-T. Chen, "Metasurface broadband solar absorber," *Scientific reports*, vol. 6, p. 20347, 2016.

[138] X. Liu, K. Fan, I. V. Shadrivov, and W. J. Padilla, "Experimental realization of a terahertz all-dielectric metasurface absorber," *Optics express*, vol. 25, no. 1, pp. 191–201, 2017.

[139] N. Liu, M. Mesch, T. Weiss, M. Hentschel, and H. Giessen, "Infrared perfect absorber and its application as plasmonic sensor," *Nano letters*, vol. 10, no. 7, pp. 2342–2348, 2010.

[140] H.-T. Chen, W. J. Padilla, M. J. Cich, A. K. Azad, R. D. Averitt, and A. J. Taylor, "A metamaterial solid-state terahertz phase modulator," *Nature photonics*, vol. 3, no. 3, p. 148, 2009.

[141] Z. Miao, Q. Wu, X. Li, Q. He, K. Ding, Z. An, Y. Zhang, and L. Zhou, "Widely tunable terahertz phase modulation with gate-controlled graphene metasurfaces," *Physical Review X*, vol. 5, no. 4, p. 041027, 2015.

[142] J. Lee and D. F. Sievenpiper, "Patterning technique for generating arbitrary anisotropic impedance surfaces," *IEEE Transactions on Antennas and Propagation*, vol. 64, no. 11, pp. 4725–4732, 2016.

[143] D. M. Pozar, "Analysis of an infinite phased array of aperture coupled microstrip patches," *IEEE Transactions on Antennas and Propagation*, vol. 37, no. 4, pp. 418–425, 1989.

[144] W. K. Toh, X. Qing, and Z. N. Chen, "A planar dualband antenna array," *IEEE Transactions on Antennas and Propagation*, vol. 59, no. 3, pp. 833–838, 2010.

[145] R. Milne, "Dipole array lens antenna," *IEEE Transactions on Antennas and Propagation*, vol. 30, no. 4, pp. 704–712, 1982.

[146] A. J. Fenn, P. T. Hurst, J. D. Krieger, J. S. Sandora, and L. I. Parad, "Ultrawideband vhf/uhf dipole array antenna," in *2010 IEEE International Symposium on Phased Array Systems and Technology*, pp. 79–82, IEEE, 2010.

[147] P. Green and P. Mayes, "50-ohm log-periodic monopole array with modulated-impedance microstrip feeder," *IEEE Transactions on Antennas and Propagation*, vol. 22, no. 2, pp. 332–334, 1974.

[148] X. Wei, J. Liu, and Y. Long, "Printed log-periodic monopole array antenna with a simple feeding structure," *IEEE Antennas and Wireless Propagation Letters*, vol. 17, no. 1, pp. 58–61, 2017.

[149] A. Sharma and J. Ramirez, "3-d printed waveguide-fed x-band helix antenna array," in *2016 IEEE International Symposium on Antennas and Propagation (APSURSI)*, pp. 479–480, IEEE, 2016.

[150] A. Palomares-Caballero, A. Alex-Amor, J. F. Valenzuela-Valdes, and P. Padilla, "Helix antenna array based on higher symmetries for antenna miniaturization and mutual coupling reduction," in *2019 IEEE-APS Topical Conference on Antennas and Propagation in Wireless Communications (APWC)*, pp. 272–275, 2019.

[151] S. Caizzone, "Miniaturized e5a/e1 antenna array for robust gnss navigation," *IEEE Antennas and Wireless Propagation Letters*, vol. 16, pp. 485–488, 2016.

[152] S. Y. Martynyuk, D. O. Vasylenko, F. F. Dubrovka, and A. G. Laush, "A novel dual band microstrip antenna array for receiving of satellite navigational signals gps/glonass/galileo," in *2015 International Conference on Antenna Theory and Techniques (ICATT)*, pp. 1–5, IEEE, 2015.

[153] Q. Li, W. Wang, D. Xu, and X. Wang, "A robust anti-jamming navigation receiver with antenna array and gps/sins," *IEEE Communications Letters*, vol. 18, no. 3, pp. 467–470, 2014.

[154] C. Kuester, H. Chaloupka, and J. Knauth, "A high temperature superconducting anti-jam gps antenna array," in *MILCOM 1999. IEEE Military Communications. Conference Proceedings (Cat. No. 99CH36341)*, vol. 1, pp. 671–674, IEEE, 1999.

[155] K. Zhang, H. Chen, X. Zhu, and G. Sun, "Miniaturized antenna arrays based on a switch for gnss," in *2015 4th International Conference on Computer Science and Network Technology (ICCSNT)*, vol. 1, pp. 977–980, IEEE, 2015.

[156] J. L. Volakis, A. J. O'Brien, and C.-C. Chen, "Small and adaptive antennas and arrays for gnss applications," *Proceedings of the IEEE*, vol. 104, no. 6, pp. 1221–1232, 2016.

[157] Z. Lingling, Q. Jinghui, and S. Bo, "Design of gps antenna array on revolving cylinder," in *2007 Asia-Pacific Microwave Conference*, pp. 1–4, IEEE, 2007.

[158] K. A. Yinusa, L. A. Greda, and A. Dreher, "A conformal multi-frequency antenna array for safety-of-life satellite navigation," in *2017 European Radar Conference (EURAD)*, pp. 363–366, IEEE, 2017.

[159] L. Lechtreck, "Cumulative coupling in antenna arrays," in *1965 Antennas and Propagation Society International Symposium*, vol. 3, pp. 144–149, IEEE, 1965.

[160] M. Wang, W. Wu, and Z. Shen, "Bandwidth enhancement of antenna arrays utilizing mutual coupling between antenna elements," *International Journal of Antennas and Propagation*, vol. 2010, 2010.

[161] M. De Cos and F. Las-Heras, "Polypropylene-based dual-band cpw-fed monopole antenna," *IEEE Antennas and Propagation Magazine*, vol. 55, no. 3, pp. 264–273, 2013.

[162] V. Jaeck, *Development of reconfigurable communication antennas in C band for smart ammunition.* PhD thesis, University of Rennes 1, 2016.

[163] M. Martinis, K. Mahdjoubi, R. Sauleau, S. Collardey, L. Bernard, and A. Schneider, "Miniature rectangular cavity antennas with circular polarization," 2016.

[164] Mini-circuits, *Power Spliter/Combiner.*

[165] Infineon Technologies AG, *Silicon Germanium Low Noise Amplifier for Global Navigation Satellite Systems (GNSS) in ultra small package with 0.77 mm2 footprint*, 6 2011. Revised Mars 2012.

[166] Mini-circuits, *Bias-Tee*.

[167] K. T. Keysight EEsof EDA, “ADS,” 2019.

Appendix A

Publications and communications related to the thesis

Publication in peer review journal

- L. Garcia-Gamez, L. Bernard, S. Collardey, H. Covic, R. Sauleau, K. Mahdjoubi, P. Poitier, P. Pouliguen, “Compact GNSS Metasurface-Inspired Cavity Antennas”, IEEE AWPL, Antennas and Wireless Propagation Letters, Vol. 18, Issue : 12, pp.2652-2656, 2019.

Publication in international conference proceedings

- L. Garcia-Gamez, L. Bernard, R. Sauleau, S. Collardey, K. Mahdjoubi, P. Pouliguen, P. Potier, “Circularly-Polarized Metasurface Antenna in Cavity for GNSS Applications”, 13th European Conference on Antennas and Propagation, Cracovie, Pologne, Avril 2019.
- L. Garcia-Gamez, R. Sauleau, S. Collardey, L. Bernard, K. Mahdjoubi, P. Pouliguen, P. Poitier, “Metasurface-inspired Antenna in Cavity for GNSS Applications”, 12th European Conference on Antennas and Propagation, Londres, Royaume-Uni, Avril 2018.

Communications

- L. Garcia-Gamez, L. Bernard, R. Sauleau, S. Collardey, K. Mahdjoubi, P. Pouliguen, P. Potier, “Antenne metasurface en cavité à polarisation circulaire pour applications GNSS”, XXIèmes Journées Nationales Microondes, Caen, France, Mai 2019. (Poster)
- L. Garcia-Gamez, R. Sauleau, S. Collardey, L. Bernard, K. Mahdjoubi, P. Pouliguen, P. Potier, “Antennes compactes en cavité pour applications GNSS”, Journées Scientifiques URSI, Paris, France, Mars 2018. (Oral presentation)
- L. Garcia-Gamez, M. Martinis, R. Sauleau, S. Collardey, L. Bernard, K. Mahdjoubi, P. Pouliguen, P. Potier, “Antenne miniature en cavité circulaire à base de métasurfaces”, XXèmes Journées Nationales Microondes, Saint-Malo, France, Mai 2017. (Poster)

UNIVERSITÉ DE RENNES 1

Titre : Analyse et conception d'antennes compactes en cavités basées sur des métasurfaces pour des applications GNSS multi-bandes

Mots clés : GNSS, antenne compacte, métasurface, polarisation circulaire, cavité

Résumé : Les systèmes de navigation par satellites globaux (GNSS) sont aujourd'hui largement utilisés pour pléthore d'applications civiles ou pour la défense, incluant la navigation de plateformes volantes ou roulantes. Galileo, GPS ou Glonass sont trois des constellations GNSS considérées dans cette thèse.

L'objectif de ce travail est de développer des antennes compactes capables de couvrir plusieurs bandes GNSS ; trois autour de 1575 MHz dans un premier temps (L1, G1, E1), puis la totalité de la bande GNSS ([1164-1610] MHz). Ces antennes sont destinées à être intégrées dans des projectiles, constitués principalement de métal. Pour cette raison, l'antenne doit être intégrée dans une cavité métallique pour ne pas affecter les propriétés aérodynamiques ni la stabilité mécanique du porteur. Intégrer des antennes imprimées dans des cavités métalliques offre plusieurs avantages : la miniaturisation, l'isolation ou la réduction des ondes de surface. Néanmoins, cela amène également une réduction importante de la bande passante. La solution immédiate pour limiter cet effet est d'agrandir la dimension de la cavité. Cependant, cette approche ne peut pas être appliquée aux nombreux cas où le porteur impose des limitations d'encombrement. Au vu des spécifications ci-dessus, l'emploi d'une antenne imprimée basée de métasurfaces est proposé et étudié, d'autant plus que des résultats antérieurs ont montré que des structures d'antennes classiques ne peuvent répondre aux spécifications demandées.

Les objectifs de cette thèse sont de concevoir et de caractériser des antennes à polarisation linéaire et à polarisation circulaire couvrant plusieurs bandes GNSS. La polarisation linéaire est considérée pour les premières études, car ces antennes ne sont pas destinées à être utilisées dans un environnement souffrant de trajets multiples. La polarisation circulaire est considérée dans un second temps. Finalement, l'extension de la bande passante à la globalité de la bande GNSS est considérée.

Title: Analysis and Design of Compact Antennas in Cavity based on Metasurfaces for Multiband GNSS Applications

Keywords: GNSS, compact antenna, metasurface, circular polarization, cavity

Abstract: Global Navigation Satellite Systems (GNSS) are widely used today for a plethora of civil and defense applications, including navigation of flying or moving platforms. Galileo, GPS or Glonass are three of the GNSS constellations considered in this thesis.

The aim of this work is to develop a compact antenna, which is able to cover multiple GNSS bands: three around 1578 MHz (L1, G1, E1) in a first time and the whole band ([1164-1610] MHz) in a second time. These antennas are intended to be integrated into projectiles mainly constituted of metal. For this reason, the antenna must be embedded in a metallic cavity to not affect the carrier aerodynamic properties and nor its mechanical stability.

Integrating microstrip antennas in metallic cavities offers several advantages, like miniaturization, isolation or surface wave reduction; however, this leads to a drastic reduction of the antenna bandwidth.

The most straightforward solution to circumvent this limitation consist in enlarging the metal cavity size. Nonetheless, this approach cannot be applied in many cases when the carrier imposes stringent dimensional limitations. Owing to the above-mentioned specifications, the use of a metasurface-inspired microstrip antenna is proposed and investigated, since previous results have demonstrated that classical antenna structures do not comply with the requirements.

The objectives of the thesis are to design and characterize linearly-polarized and circularly-polarized antennas covering multiple bands of GNSS. Linear polarization is considered for the first studies, as these antennas are not intended to be used in an environment with multi-path signals. Circular polarization is addressed in a second time. Finally, the extension of the bandwidth to the whole GNSS bands is considered.